

TERNARY PHASE EQUILIBRIA IN TRANSITION METAL-
BORON-CARBON-SILICON SYSTEMS

Part II. Ternary Systems

Volume XIII. Phase Diagrams of the
Systems Ti-B-C, Zr-B-C,
and Hf-B-C

E. Rudy
St. Windisch

~~This document is subject to special export controls, and each transmittal to foreign governments or foreign nationals may be made only with prior approval of Metals and Ceramics Division, Air Force Materials Laboratory, Wright Patterson Air Force Base, Ohio.~~

*This document has been approved for public release and sale; its distribution is unlimited. USAF Systems Command
Letter dated Aug 22, 1968
(Capt Marchbanks)
0837117*

*** Export controls have been removed ***

Approved for Public Release

FOREWORD

The research described in this report was carried out at the Materials Research Laboratory, Aerojet-General Corporation, Sacramento, California, under USAF Contract No. AF 33(615)-1249. The contract was initiated under Project No. 7350, Task No. 735001, and was administered under the direction of the Air Force Materials Laboratory, Research and Technology Division, with Captain R.A. Peterson and Lt. P.J. Marchiando acting as Project Engineers, and Dr. E. Rudy, Aerojet-General Corporation, as Principal Investigator. Professor Dr. H. Nowotny, University of Vienna, served as consultant to the project.

The project, which includes the experimental and theoretical investigations of ternary and related binary systems in the system classes Me_1 - Me_2 -C, Me-B-C, Me_1 - Me_2 -B, Me-Si-B, and Me-Si-C, was initiated on 1 January 1964.

The phase diagram work on the three metal-boron carbon systems described in this report was carried out by E. Rudy and St. Windisch. Assisting in the investigations were: J. Pomodoro (preparation of sample material), J. Hoffman (metallographic preparations), and R. Cobb (X-ray exposures).

Chemical analysis of the alloys was performed under the supervision of Mr. W. E. Trahan, Quality Control Division of Aerojet-General Corporation. The authors wish to thank Mr. R. Cristoni for the preparation of the illustrations, and Mrs. J. Weidner, who typed the report.

The manuscript of this report was released by the authors March 1966, for publication as an RTD Technical Report.

Other reports issued under USAF Contract AF 33(615)-1249 have included:

Part I. Related Binaries

Volume I.	Mo-C System
Volume II.	Ti-C and Zr-C Systems
Volume III.	Systems Mo-B and W-B
Volume IV.	Hf-C System
Volume V.	Ta-C System. Partial Investigations in the Systems V-C and Nb-C
Volume VI.	W-C System. Supplemental Information on the Mo-C System
Volume VII.	Ti-B System
Volume VIII.	Zr-B System
Volume IX.	Hf-B System
Volume X	V-B, Nb-B, and Ta-B Systems

Part II. Ternary Systems

Volume I.	Ta-Hf-C System
Volume II.	Ti-Ta-C System

FOREWORD (Cont'd)

- Volume III. Zr-Ta-C System
- Volume IV. Ti-Zr-C, Ti-Hf-C, and Zr-Hf-C Systems
- Volume V. Ti-Hf-B System
- Volume VI. Zr-Hf-B System
- Volume VII. Systems Ti-Si-C, Nb-Si-C, and W-Si-C
- Volume VIII. Ta-W-C System
- Volume IX. Zr-W-B System. Pseudo-binary System TaB_2 - HfB_2
- Volume X. Systems Zr-Si-C, Hf-Si-C, Zr-Si-B, and Hf-Si-B.
- Volume XI. Systems Hf-Mo-B and Hf-W-B
- Volume XII. Ti-Zr-B System

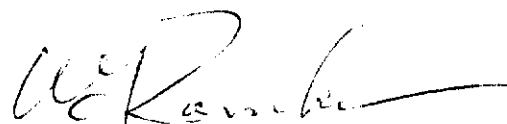
Part III. Special Experimental Techniques

- Volume I. High Temperature Differential Thermal Analysis

Part IV. Thermochemical Calculations

- Volume I. Thermodynamic Properties of Group IV, V, and VI Binary Transition Metal Carbides.
- Volume II. Thermodynamic Interpretation of Ternary Phase Diagrams
- Volume III. Computational Approaches to the Calculation of Ternary Phase Diagrams

This technical report has been reviewed and is approved.



W. G. RAMKE
Chief, Ceramics and Graphite Branch
Metals and Ceramics Division
Air Force Materials Laboratory

ABSTRACT

The ternary alloy systems Ti-B-C, Zr-B-C, and Hf-B-C have been investigated by means of X-ray, metallographic, melting point, and differential-thermoanalytical techniques. The experimental alloy material comprised of hot-pressed and sintered, arc- and electron-beam molten, as well as high temperature equilibrated and quenched, specimens; each phase of the experimental work was supported by chemical analysis.

The results of this investigation are discussed and possible fields of application outlined.

TABLE OF CONTENTS

	PAGE
I. <u>INTRODUCTION AND SUMMARY</u>	1
A. Introduction	1
B. Summary	2
1. Titanium-Boron-Carbon	2
2. Zirconium -Boron-Carbon	12
3. Hafnium-Boron-Carbon	22
II. <u>LITERATURE REVIEW</u>	34
A. Boundary Systems	34
1. Titanium-Carbon	34
2. Zirconium-Carbon	35
3. Hafnium-Carbon	35
4. Titanium-Boron	37
5. Zirconium-Boron	39
6. Hafnium-Boron	42
7. Boron-Carbon	45
B. Ternary Systems	48
1. Titanium-Boron-Carbon	48
2. Zirconium-Boron-Carbon	49
3. Hafnium-Boron-Carbon	50
III. <u>EXPERIMENTAL PROGRAM</u>	51
A. Starting Materials	51
1. Titanium	51
2. Hafnium	51
3. Zirconium and Zirconium Dihydride	52

TABLE OF CONTENTS (Cont'd)

	PAGE
4. Titanium Monocarbide	52
5. Zirconium Monocarbide	52
6. Titanium Diboride	52
7. Zirconium Diboride	53
8. Hafnium Diboride	53
9. Graphite	53
10. Boron	54
B. Alloy Preparation and Heat Treatment	54
C. Melting Temperatures	56
D. Differential Thermal Analysis	58
E. Metallography	60
F. X-ray Analysis	62
G. Chemical Analysis	62
IV. <u>RESULTS</u>	63
A. Titanium-Boron-Carbon	63
1. The Titanium Phase	63
2. Phase Equilibria in the Metal-Rich Portion of the System	63
3. The Pseudobinary Section Diboride-Monocarbide	73
4. The Pseudobinary Section Diboride-Graphite	81
5. The Pseudobinary Section Diboride-Boron Carbide	83
6. Ternary Equilibria in the Composition Region TiC-TiB ₂ -B-C	89
7. Assembly of the Phase Diagram	91

Contrails

TABLE OF CONTENTS (Cont'd)

	PAGE
B. Zirconium-Boron-Carbon	104
1. The Zirconium Phase	104
2. Phase Equilibria in the Metal-Rich Portion of the System	105
3. The Pseudobinary Section Diboride-Monocarbide	117
4. The Pseudobinary Section Zirconium Diboride-Graphite	124
5. The Pseudobinary Section Diboride-Boron Carbide	126
6. Ternary Equilibria in the Composition Region $TiC-TiB_2-B_4C-C$	133
7. Equilibria in the Boron-Corner of the System	137
8. Assembly of the Phase Diagram	140
C. Hafnium-Boron-Carbon	150
1. Equilibria in the Hafnium-Corner of the System	150
2. Phase Equilibria in the Concentration Region $HfB-HfB_2-HfC_{1-x}$	166
3. The Pseudobinary Section Hafnium Diboride-Graphite	180
4. The Pseudobinary Section Diboride-Boron Carbide	184
5. Ternary Equilibria in the Composition Region $HfC-HfB_4-B-C$	189
6. Assembly of the Phase Diagram	193
V. <u>DISCUSSION</u>	205
A. Phases and Phase Equilibria	205
B. High Temperature Applicability of Group IV Metal-Boron-Carbon Alloys	206
References	208

Contrails

LIST OF ILLUSTRATIONS

FIGURE		PAGE
1	Phase Diagram of the System Ti-B-C	4
2	Scheil-Schultz Reaction Diagram for the Titanium-Boron-Carbon System	5
3	Ti-B-C: Isopleth $Ti-B_{0.5}C_{0.5}$	7
4	Ti-B-C: Isopleth $Ti_{0.5}C_{0.5}-B$	8
5	Ti-B-C: Isopleth $Ti_{0.5}B_{0.5}-C$	10
6	Liquidus Projections for the Ti-B-C System	11
7	Phase Diagram of the System Zr-B-C	13
8	Scheil-Schultz Reaction Diagram for the Zirconium-Boron-Carbon System	14
9	Zr-B-C: Isopleth $Zr-B_{0.5}C_{0.5}$	17
10	Zr-B-C: Isopleth $Zr_{0.5}C_{0.5}-B$	19
11	Liquidus Projections for the Zr-B-C System	23
12	Phase Diagram of the System Hf-B-C	24
13	Scheil-Schultz Reaction Diagram for the Hafnium-Boron-Carbon	25
14	Hf-B-C: Isopleth $Hf-B_{0.5}C_{0.5}$.
15	Hf-B-C: Isopleth $Hf_{0.5}B_{0.5}-C$	30
16	Hf-B-C: Isopleth $Hf_{0.5}C_{0.5}-C$	31
17	Liquidus Projections for the Hf-B-C System	33
18	Constitution Diagram Titanium-Carbon	36
19	TiC_{1-x} : Variation of the Lattice Parameter With the Carbon Concentration	37
20.	Constitution Diagram Zirconium-Carbon	38
21	Constitution Diagram Hafnium-Carbon	39
22	Constitution Diagram Titanium-Boron	41
23	Constitution Diagram Zirconium-Boron	43

LIST OF ILLUSTRATIONS (Cont'd)

FIGURE		PAGE
24	Constitution Diagram Hafnium-Boron	44
25	Phase Diagram Boron-Carbon	45
26	Phase Diagram Boron-Carbon	46
27	Section of the Phase Diagram Ti-B-C at 1500°C	48
28	Section of the Phase Diagram Zr-B-C at 1400°C	49
29	Section of the Phase Diagram Hf-B-C at 1500°C	50
30	Temperature Correction Chart for the Pirani Furnace	57
31	Ti-B-C: Location of Samples Investigated by Differential Thermal Analysis	59
32	Zr-B-C: Location of Specimen Investigated by Differential Thermal Analysis	59
33	Hf-B-C: Location of Specimens Investigated by Differential Thermal Analysis	60
34	Ti-B-C (84-10-6 At.%), Cooled from 1550°C	64
35	Ti-B-C (90-6-4 At.%), Cooled at Approximately 15°C per Second from 1515°C	64
36	Ti-B-C (75-10-15 At.%), Cooled at Approximately 10°C per Second from 1710°C	68
37	Ti-B-C (64-29-7 At.%), Cooled at Approximately 20°C per Second from 1600°C	68
38	Ti-B-C: Location and Qualitative Phase Evaluation of the Alloy Series Equilibrated at 1400°C	69
39	Ti-B-C (66-3-31 At.%), Quenched from 1900°C	70
40	Ti-B-C (62-3-35 At.%), Quenched from 2700°C	70
41	Ti-B-C (62-3-35 At.%), Sample from Figure 40 Re-equilibrated for 10 Minutes at 1800°C and Slowly Cooled	71
42	Ti-B-C (51-47-2 At.%), Cooled with Approximately 5°C per Second from 2210°C	71
43	Ti-B-C (55-30-15 At.%), Cooled with Approximately 10°C per Second from 2300°C	72

Contrails

LIST OF ILLUSTRATIONS (Cont'd)

FIGURE		PAGE
44	Ti-B-C (62-12-26 At.%), Melted, Re-equilibrated for 20 Minutes at 2100°C, and Quenched	73
45	Ti-B-C: Pseudobinary Section TiB_2 - $TiC_{\sim 0.92}$	74
46	Ti-B-C (63-10-27 At.%), Quenched from 2850°C	75
47	Ti-B-C (55-10-35 At.%), Rapidly Quenched from 2640°C	75
48	Ti-B-C (44-26-30 At.%), Quenched from 2622°C	76
49	Ti-B-C (44-29-27 At.%), Cooled with Approximately 80°C per Second from 2620°C	76
50	Ti-B-C (42-33-25 At.%), Quenched from 2620°C	77
51	Enlarged View of Sample 50	77
52	Ti-B-C (55-10-35 At.%), Cooled with Approximately 50°C per Second from 2645°C	78
53	Ti-B-C (44-29-27 At.%), Cooled with Approximately 2°C per Second from 2620°C	78
54	Ti-B-C (57-3-40 At.%), Quenched from 2800°C	79
55	Ti-B-C (57-3-40 At.%), Cooled with Approximately 20°C per Second from 2600°C	79
56(a) through 56(c).	Alloy: Ti-B-C (52-3-45 At.%)	80
(a)	Quenched	
(b)	Cooled with Approximately 50°C per Second	
(c)	Cooled with Approximately 30°C per Second	
57	Ti-B-C: Location of Melting Point Samples, and Qualitative Phase Evaluation After Melting	82
58	Pseudobinary Section TiB_2 -C: Melting Temperatures: Qualitative Phase Evaluation of Solid State Equilibrated and Quenched Alloys	83
59	Ti-B-C (28-57-15 At.%), Cooled with 8°C per Second from 2550°C	84
60	Ti-B-C (25-50-25 At.%), Quenched from 2545°C	84
61	Ti-B-C (23-47-30 At.%), Quenched from 2514°C.	85

Contrails

LIST OF ILLUSTRATIONS (Cont'd)

FIGURE		PAGE
62	Ti-B-C (23-45-32 At.%), Quenched from 2507°C	85
63	Ti-B-C (19-36-45 At.%), Quenched from 2517°C	86
64	Ti-B-C (15-30-55 At.%), Cooled with Approximately 20°C per Second from 2640°C	86
65	Pseudobinary Section TiB_2-B_4C	87
66	DTA-Thermogram (Cooling) of a Boron-Carbon Alloy with 10 Atomic Percent Carbon.	88
67	DTA-Thermogram (Cooling) of a Ti-B-C (28-62-10 At.%) Alloy Located Close to the Pseudobinary Section TiB_2-C	90
68	DTA-Thermogram of a Ti-B-C (27-58-15 At.%), Alloy Containing Small Amounts of Excess B_4C	91
69	Ti-B-C (20-63-17 At.%), Cooled with Approximately 15°C per Second from 2300°C	92
70	Ti-B-C (8-64-28 At.%), Quenched from 2246°C	92
71	DTA-Thermograms of a Boron-Carbon Alloy with 30 Atomic Percent Carbon	93
72	DTA-Thermogram of a Ti-B-C (30-35-35 At.%) Alloy, Showing Liquification and Solidification of the $TiB_2+TiC+C$ Eutectic at 2400°C	94
73(a)	Pirani-Melting Point Specimen of a Ti-B-C (34-25-40 At.%) After Reaching 2400°C	95
73(b)	Sample from Figure 73(a), After Sectioning	95
74(a)	Ti-B-C (25-40-35 At.%), Quenched from 2424°C	96
74(b)	Ti-B-C (33-21-46 At.%), Quenched from 2517°C	96
75	Ti-B-C (25-30-45 At.%), Rapidly Cooled from 2550°C	97
76	Ti-B-C (25-40-35 At.%), Cooled at Approximately 10°C per Second from 2430°C	97
77(a) through 77(i),	Isothermal Sections for the Ti-B-C System.	98
	(a) 1500°C (d) 2000°C (g) 2420°C	
	(b) 1600°C (e) 2160°C (h) 2600°C	
	(c) 1700°C (f) 2300°C (i) 2800°C	

Contrails

LIST OF ILLUSTRATIONS (Cont'd)

FIGURE		PAGE
78	Ti-B-C: Melting Troughs and Compositions of the Melt Participating in Nonvariant ($p = \text{const}$) Equilibria	104
79	α - β (hcp \leftrightarrow bcc) Transformation in Crystal Bar Zirconium	105
80	DTA-Thermogram of a Zr-B-C (65-18-17 At.%), Alloy	106
81	Zr-B-C: Location and Qualitative Phase Evaluation of the Alloys Equilibrated at 1400°C	107
82	Zr-B-C (94-3-3 At.%), Cooled with Approximately 20°C per Second from 1700°C	111
83	Zr-B-C (65-18-17 At.%), Cooled at Approximately 10°C per Second from 1800°C	111
84	Zr-B-C (60-25-15 At.%), Cooled at Approximately 30°C per Second from 2050°C	112
85	Zr-B-C (45-47-8 At.%), Cooled with Approximately 30°C per Second from 1800°C	112
86	Zr-B-C (37-58-5 At.%), Cooled at Approximately 40°C per Second from 2800°C	113
87	Zr-B-C (90-6-4 At.%), Quenched from 1750°C	113
88	Zr-B-C (90-8-2 At.%), Quenched from 1700°C	114
89	Zr-B-C (88-10-2 At.%), Quenched from 1615°C	114
90	Zr-B-C (80-15-5 At.%), Quenched from 1650°C	115
91	Zr-B-C (73-20-7 At.%), Quenched from 1700°C	115
92	Zr-B-C (83-10-47 At.%), Quenched from 1690°C	116
93	Zr-B-C (70-10-20 At.%), Quenched from 1800°C	116
94	Melting Temperatures Along the Pseudobinary Section ZrB_2 -ZrC	117
95	Zr-B-C (49-12-39 At.%), Quenched from 3080°C	118
96	Zr-B-C (45-23-32 At.%), Quenched from 2842°C	118
97	Zr-B-C (43-30-27 At.%), Quenched from 2830°C	119
98	Zr-B-C (50-30-20 At.%), Quenched from 2740°C	119

LIST OF ILLUSTRATIONS (Cont'd)

FIGURE		PAGE
99	Zr-B-C (42-37-21 At.%), Quenched from 2830°C	120
100	Zr-B-C (41-42-17 At.%), Cooled at Approximately 80°C per Second from 2835°C	120
101	Zr-B-C (45-23-32 At.%), Cooled at Approximately 30°C per Second from 2840°C	121
102	Zr-B-C (45-23-32 At.%), Cooled at Approximately 5°C per Second from 2840°C	121
103	Zr-B-C: Location of Melting Point Samples, and Qualitative Phase Evaluation After Melting	122
104	Zr-B-C (57-3-40 At.%), Quenched from 3385°C	123
105	Zr-B-C (60-8-32 At.%), Cooled at Approximately 20°C per Second from 2850°C	123
106	Zr-B-C (60-8-32 At.%), Sample from Figure 105 Re-Equilibrated for 15 Minutes at 1700°C, and Cooled to Room Temperature	124
107	Melting Temperatures of Pseudobinary $ZrB_2 + C$ Alloys	125
108	Pseudobinary Eutectic Solidification at 2390°C in a Zr-B-C (31-63-6 At.%) Alloy	126
109	Zr-B-C (26-54-20 At.%), Quenched from 2445°C	127
110	Zr-B-C (23-47-30 At.%), Quenched from 2425°C	127
111	Zr-B-C (22-43-35 At.%), Quenched from 2390°C	128
112	Melting Temperatures of Pseudobinary $ZrB_2 + B_4C$ Alloys	128
113	DTA-Thermogram of a Zr-B-C (5-78-17 At.%) Alloy Showing Pseudobinary Eutectic Melting (Heating) and Solidification (Cooling) Along the Section $ZrB_2 - B_4C$	129
114	Zr-B-C (28-69-3 At.%), Arc Melted and Quenched	130
115	Zr-B-C (23-71-6 At.%), Arc-Melted and Quenched	130
116	Zr-B-C (9-78-13 At.%), Cooled at Approximately 20°C per Second from 2220°C	131
117	Zr-B-C (5-78-17 At.%), Arc-Melted and Quenched	131

LIST OF ILLUSTRATIONS (Cont'd)

FIGURE		PAGE
118(a) and (b).	Sample from Figure 116 Details of the Eutectic Structure $ZrB_2 + B_4C$.	132
119	Zr-B-C (10-50-40 At.%), Cooled at Approximately 40°C per Second from 2460°C	133
120	Zr-B-C (12-66-24 At.%), Cooled at Approximately 20°C per Second from 2180°C	134
121	Zr-B-C (26-43-31 At.%), Quenched from 2490°C	135
122	Zr-B-C (28-35-37 At.%), Quenched from 2385°C	135
123	Zr-B-C (35-20-45 At.%), Quenched from 2500°C	136
124	Zr-B-C (48-5-47 At.%), Quenched from 3160°C	136
125	Qualitative Phase Evaluation on Quenched Alloys Located in the Boron Corner of the Zr-B-C System.	137
126	Binary (A) and Ternary (B, C, and D) Decomposition of ZrB_{12}	138
127	DTA-Thermogram (Cooling) of a Zr-B-C (13-80-7 At.%) Alloy	139
128	Zr-B-C (90-5-5 At.%), Equilibrated for 10 Minutes at 2050°C After Melting, and Quenched	140
129(a) through (h)	Isothermal Sections for the Zr-B-C System	141
	(a) 1400°C	(e) 2400°C
	(b) 1800°C	(f) 2600°C
	(c) 2160°C	(g) 2800°C
	(d) 2300°C	(h) 3000°C
130	Melting Troughs and Nonvariant Melting-Equilibria in the Zr-B-C System.	149
131	Hf-B-C: Location and Qualitative Phase Evaluation of the Alloy Series Equilibrated at 1400°C	150
132	DTA-Thermogram of an Metal-Rich Hf-B-C (86-10-4 At.%) Alloy	156
133	DTA-Thermogram of a Hf-B-C (70-20-10 At.%) Alloy	157
134	Hf-B-C (95-3-2 At.%), Quenched from 2100°C	158

LIST OF ILLUSTRATIONS (Cont'd)

FIGURE		PAGE
135	Hf-B-C (92-6-2 At.%), Quenched from 1900°C	158
136	Hf-B-C (88-10-2 At.%), Quenched from 1860°C	159
137	Hf-B-C (86-12-2 At.%), Quenched from 1850°C	159
138	Hf-B-C (95-3-2 At.%), Equilibrated and Cooled at 1°C per Second from 1850°C	160
139	Hf-B-C (92-3-5 At.%), Equilibrated and Cooled at 1°C per Second from 1850°C	160
140	Hf-B-C (87-3-10 At.%), Heat-Treated at 1800°C and Cooled	161
141	Hf-B-C (85-2-13 At.%), Melted, Re-equilibrated for 30 Minutes at 2300°C, and Cooled at < 1°C per Second	161
142	Hf-B-C (82-2-16 At.%), Melted, Re-equilibrated at 2300°C and Cooled at Approximately 10°C per Second	162
143	Hf-B-C (91-4-5 At.%), Quenched from 2300°C	162
144	Hf-B-C (83-10-7 At.%), Quenched from 1850°C	163
145	Sample from Figure 144, Equilibrated for 15 Minutes in the Liquidus + Solidus Region (1900°C), and Cooled	163
146	Hf-B-C (83-14-3 At.%), Quenched from 2000°C	164
147	Sample from Figure 146, Re-equilibrated for 20 Minutes at 1820°C, and Quenched	164
148	Hf-B-C (68-27-5 At.%), Rapidly Cooled from 2085°C	165
149	Sample from Figure 148, Re-equilibrated for 15 Minutes in the Liquidus + Solidus Region (2000°C), and Cooled	166
150	Hf-B-C (44-48-8 At.%), Cooled at Approximately 15°C per Second from 2940°C	168
151(a) and (b)	Enlarged View of the Specimen Shown in Figure 50	169
152	Hf-B-C: Location of Melting Point Samples, and Qualitative (X-ray) Phase Evaluation After Melting	170
153	Hf-B-C (53-20-27 At.%), Melted, Re-equilibrated at 2200°C, and Quenched	170

LIST OF ILLUSTRATIONS (Cont'd)

FIGURE		PAGE
154	Hf-B-C (51-14-35 At.%), Melted at 3350°C and Cooled at Approximately 20°C per Second After Re-equilibration at 2800°C.	171
155	Melting Temperatures of Alloys Located Along the Pseudo binary Section HfB_2 - $\text{HfC}_{0.90}$	171
156	Hf-B-C (46-20-34 At.%), Rapidly Quenched from 3348°C	172
157	Hf-B-C (41-38-21 At.%), Rapidly Quenched from 3145°C	172
158	Hf-B-C (40-43-17 At.%), Quenched from 3142°C	173
159	Sample from Figure 158, Equilibrated for 40 Seconds at 3100°C, and Quenched	173
160	Magnified Portion of the Specimen Shown in Figure 158	174
161	Hf-B-C (40-45-15 At.%), Quenched from 3145°C	174
162	Hf-B-C (38-49-13 At.%), Quenched from 3145°C	175
163	Hf-B-C (60-8-32 At.%), Quenched from 3350°C	176
164	Hf-B-C (55-4-61 At.%), Quenched at Approximately 60°C per Second from 3200°C	176
165	Hf-B-C (53-4-43 At.%), Quenched at Approximately 60°C per Second from 3200°C	177
166	Hf-B-C (51-4-45 At.%), Quenched at Approximately 80°C per Second from 3200°C	177
167	Hf-B-C (48-4-48 At.%), Quenched at Approximately 80°C per Second from 3200°C	178
168(a) and (b)	Increased Diboride Precipitation from the Monocarbide Solution Following Slow Cooling from 3200°C	179
169	Hf-B-C (57-10-33 At.%), Tin-Quenched from 3100°C After Melting	180
170	Melting in the Pseudobinary System HfB_2 -C.	181
171	DTA-Thermogram (Cooling) of a Hf-B-C (31-63-6 At.%) Alloy, Showing Pseudobinary Eutectic Solidification Along the Section HfB_2 -C	182

LIST OF ILLUSTRATIONS (Cont'd)

FIGURE		PAGE
172	Hf-B-C (18-36-46 At.%), Quenched from 2650°C	182
173	Hf-B-C (20-40-40 At.%), Quenched from 2512°C	183
174	Hf-B-C (22-44-34 At.%), Rapidly Cooled from 2517°C	183
175	Hf-B-C (28-57-15 At.%), Cooled at 2°C per Second from 2580°C	184
176	Melting Along the Pseudobinary Section $\text{HfB}_2\text{-B}_4\text{C}$	185
177	DTA-Thermogram of a Hf-B-C (7-78-15 At.%) Alloy, Showing Eutectic Melting (Heating) and Solidification (Cooling) Along the Section $\text{HfB}_2\text{-B}_4\text{C}$	186
178(a) and (b)	Eutectic Alloy Hf-B-C (7-78-15 At.%): (a) Quenched from 2340°C (b) After Annealing at 2200°C	187
179(a) and (b)	Alloy: Hf-B-C (10-77-13 At.%), Cooled at Approximately 20°C per Second from 2350°C	188
180	Hf-B-C (4-79-17 At.%), Quenched from 2360°C	189
181	DTA-Thermogram of an Hf-B-C (10-70-20 At.%) Alloy. (Melting and Solidification of the Ternary Eutectic $\text{HfB}_2 + \text{B}_4\text{C} + \text{C}$)	190
182	Formation of the Ternary Eutectic $\text{HfB}_2 + \text{HfC} + \text{C}$ in an Hf-B-C (20-15-65 At.%) Alloy	190
183	Hf-B-C (10-67-23 At.%), Quenched from 2270°C	191
184	Hf-B-C (23-40-37 At.%), Quenched from 2500°C	191
185	Hf-B-C (25-35-40 At.%), Quenched from 2507°C	192
186	DTA-Thermogram of an Hf-B-C (4-90-6 At.%) Alloy. Formation of the Ternary Eutectic $\text{HfB}_2 + \text{B}_4\text{C} + \text{C}$ at 1950°C	193
187	Isothermal Sections of the Hf-B-C System (a) 1400°C (e) 2050°C (I) 3100°C (b) 1800°C (f) 2300°C (j) 3200°C (c) 1940°C (g) 2400°C (d) 2000°C (h) 2800°C	194
188	Melting Troughs and Compositions of the Nonvariant (p = const) Melts in the Hf-B-C System.	204

Contrails

LIST OF TABLES

TABLES		PAGE
1	Pseudobinary (Eutectic) Reaction Isotherm $L \leftrightarrow \delta + \rho$ at 2720°C: Compositions of the Equilibrium Phases	3
2	Pseudobinary (Eutectic) Reaction Isotherm $L \leftrightarrow \delta + \kappa$ at 2507°C: Compositions of the Equilibrium Phases	5
3	Class III Four-Phase Equilibrium $L \leftrightarrow \delta + \rho + \kappa$ at 2400°C: Compositions of the Equilibrium Phases.	6
4	Pseudobinary (Eutectic) Reaction Isotherm $L \leftrightarrow \delta + \omega$ at 2310°C: Compositions of the Equilibrium Phases	7
5	Class III Four-Phase Equilibrium $L \leftrightarrow \delta + \omega + \kappa$ at 2240°C: Compositions of the Equilibrium Phases	9
6	Class II Four-Phase Equilibrium $L + \delta \leftrightarrow \rho + \gamma$ at 2160°C: Compositions of the Equilibrium Phases	9
7	Class III Four-Phase Equilibrium $L \leftrightarrow \delta + \omega + \epsilon$ at 2016°C: Compositions of the Equilibrium Phases	11
8	Class II Four-Phase Equilibrium $L \leftrightarrow \beta + \gamma + \rho$ at 1510°C: Compositions of the Equilibrium Phases	12
9	Pseudobinary (Eutectic) Equilibrium $L \leftrightarrow \delta + \rho$ at 2830°C: Compositions of the Equilibrium	15
10	Pseudobinary (Eutectic) Reaction $L \leftrightarrow \delta + \kappa$ at 2390°C: Compositions of the Equilibrium Phases.	16
11	Class II Four-Phase Equilibrium $L \leftrightarrow \delta + \rho + \kappa$ at 2360°C: Compositions of the Equilibrium Phases	17
12	Pseudobinary (Eutectic) Reaction $L \leftrightarrow \delta + \omega$ at 2220°C: Compositions of the Equilibrium Phases	18
Table 13.	Class III Four-Phase Equilibrium $L \leftrightarrow \delta + \omega + \kappa$ at 2165°C: Compositions of the Equilibrium Phases	19
14	Class II Four-Phase Equilibrium $L + \delta \leftrightarrow \gamma + \omega$ at 2160°C: Compositions of the Equilibrium Phases	20
15	Class III Four-Phase Equilibrium $L \leftrightarrow \gamma + \epsilon + \omega$ at 1990°C: Compositions of the Equilibrium Phases	21
16	Class II Four-Phase Equilibrium $\gamma + \omega \leftrightarrow \delta + \epsilon$ at 1800°C: Composition of the Equilibrium Phases	21
17	Class II Four-Phase Equilibrium $L \leftrightarrow \beta + \rho + \delta$ at 1615°C: Compositions of the Equilibrium Phases	22

Contrails

LIST OF TABLES (Cont'd)

TABLE		PAGE
18	Pseudobinary (Eutectic) Reaction $L \leftrightarrow \gamma + \epsilon$ at 3140°C: Compositions of the Equilibrium Phases	26
19	Pseudobinary Eutectic Reaction $L \leftrightarrow \epsilon + \rho$ at 2515°C: Compositions of the Equilibrium Phases	26
20	Class II Four-Phase Equilibrium $L \leftrightarrow \epsilon + \gamma + \rho$ at 2480°C: Compositions of the Equilibrium Phases.	27
21	Pseudobinary (Eutectic) Reaction $L \leftrightarrow \epsilon + \omega$ Isotherm at 2330°C: Compositions of the Equilibrium Phases	28
22	Four-Phase Equilibrium $L \leftrightarrow \epsilon + \omega + \rho$ at 2260°C: Composi- tions of the Equilibrium Phases	29
23	Class II Four-Phase Equilibrium $L + \epsilon \leftrightarrow \delta + \gamma$ at 2050°C: Compositions of the Equilibrium Phases	30
24	Class II Four-Phase Equilibrium $L \leftrightarrow \epsilon + \omega + \kappa$ at 1950°C: Compositions of the Equilibrium Phases	32
25	Class II Four-Phase Equilibrium $L + \gamma \leftrightarrow \delta + \alpha$ at 1950°C: Compositions of the Equilibrium Phases:	32
26	Class III. Four-Phase Equilibrium $L \leftrightarrow \alpha + \beta + \delta$ at 1850°C: Compositions of the Equilibrium Phases	34
27	Structure and Lattice Parameters of Titanium Borides	40
28	Structure and Lattice Parameters of Zirconium Borides	42
29	Structure and Lattice Parameters of Hafnium Borides	43
30	Solid State Homogenization Treatments for Ti-B-C, Zr-B-C and Hf-B-C Alloys	55
31	Etching Procedures for Group IV Metal-Boron-Carbon Alloys	61
32	Melting Temperatures and Phase Evaluation of Titanium- Boron-Carbon Alloys	65
33	Melting Temperatures and Phase Evaluation of Zirconium- Boron-Carbon Alloys	108
34	Melting Temperatures and Phase Evaluation of Hafnium- Boron-Carbon Alloys	152

I. INTRODUCTION AND SUMMARY

A. INTRODUCTION

From the intermediate phases formed between the refractory transition metals and boron, the diborides of the group IV metals, titanium, zirconium, and hafnium, exhibit the highest oxidation resistance and thus have attracted technical interest in recent years. Current efforts, devoted to utilize the beneficial properties of refractory borides, include their use in composite structures, the development of oxidation-resistant graphites, and of protective coating systems for high temperature applications. Their extreme hardness, which compares with those of the carbides, stimulated research directed towards their utilization in cutting materials. Binderless TiC + TiB₂ composites, for example, have shown promise in this direction.

Like the carbides and the other compounds of the transition metals with B-elements, the borides are extremely brittle, and hence sensitive to mechanically or thermally induced stresses. Considerable efforts have therefore been made in the past, to find suitable binder materials to improve their poor mechanical properties. However, with the exception of the metal-boron-carbon alloys, for which lower-temperature phase equilibrium data were established in previous work⁽¹⁻⁴⁾, practically no systematic investigations have been carried out on ternary or higher-order boron-containing alloys.

In view of the need for reliable high temperature phase equilibrium data, a separate task of the present program was devoted to the study of the phase relationships in selected systems Me-Si-B, and Me-C-B, where Me stands for a refractory transition metal. The work on the phase diagrams Me-Si-B, as well as the binary metal-boron systems, has been described in previous reports^(5, 7), whereas the present one covers the investigations of the phase diagrams Ti-B-C, Zr-B-C, and Hf-B-C. In these systems, data of particular interest included the high temperature behavior of the diborides in the presence of graphite and B₄C, and the modification of the metal-rich equilibria by the existence of monoborides in the binary systems Ti-B and Hf-B.

Conclusions

Each individual system was studied in fairly great detail and care was exercised in the experimentations, in order to achieve accurate and reliable results. Difficulties encountered during the course of the work included slow attainment of equilibrium in alloys containing hafnium monoboride, and rapid annealing of the eutectic structures in ternary alloys. Usually, rapid quenching from the molten state was required, in order to obtain representative microstructures.

B. SUMMARY

The ternary alloy systems titanium-boron-carbon, zirconium-boron-carbon, and hafnium-boron-carbon, have been investigated by means of X-ray, melting point, differential-thermoanalytical, and metallographic techniques; complete phase diagrams were established for all three systems. The phase diagram results are summarized as follows:

1. Titanium-Boron-Carbon

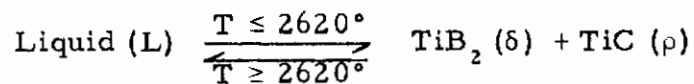
No new ternary phases are formed in the alloy system, and the ternary phase field is dominated by the very stable diboride. Simple eutectic-type pseudobinary equilibria are formed between TiB_2-B_4C , TiB_2-C , and TiB_2-TiC . In the lower temperature ranges, a further two-phase equilibrium exists between the incongruently melting TiB and the monocarbide phase. Eight (8) isothermal ternary reactions occur in the system, of which three are associated with eutectic formation in the above mentioned pseudobinary systems; four Class III ternary reactions are due to the occurrence of ternary eutectica within the three-phase fields $Ti + TiB + TiC$, $TiB_2 + TiC + C$; $TiB_2 + B_4C + C$, and $TiB_2 + B_4C + B$, and the two-phase equilibrium between the monoboride and the monocarbide is terminated in a Class II four-phase reaction at $2160^\circ C$. The assembled phase diagram is illustrated in the isometric drawing shown in Figure 1, while binary and ternary isothermal reactions are summarized in concise form in the familiar Scheil-Schultz reaction diagram (Figure 2). Relevant vertical sections (isopleths) of the system are depicted in Figures 3, 4, and 5. Isothermal sections of the system for the temperature range 1500° to $2800^\circ C$ are given in the result section (IV-A-7) of this report. The diagram shown in Figure 6 depicts the location of the eutectic troughs and provides an approximate temperature mapping of the liquidus surfaces in the Ti-B-C system.

The isothermal ternary reactions, together with the approximate compositions of the equilibrium phases, are as follows:

Contrails

- a. Pseudobinary, Eutectic-Type Reaction
Isotherm at 2620°C.

The reaction proceeding at this temperature
can be presented as:



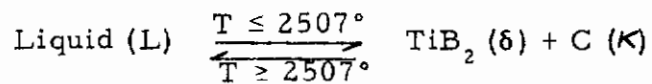
The approximate equilibrium compositions of the phases are given in Table 1.

Table 1. Pseudobinary (Eutectic) Reaction Isotherm $L \rightarrow \delta + \rho$ at
2620°C: Compositions of the Equilibrium Phases.

Phase	Concentrations, At. %		
	Ti	B	C
Melt (L)	45	31	24
TiB ₂ (δ)	~34	~63	<3
TiC (ρ)	53	~6	41

- b. Pseudobinary, Eutectic-Type Reaction
Isotherm at 2507°C.

The reaction can be presented as:



The approximate compositions of the phases are given in Table 2.

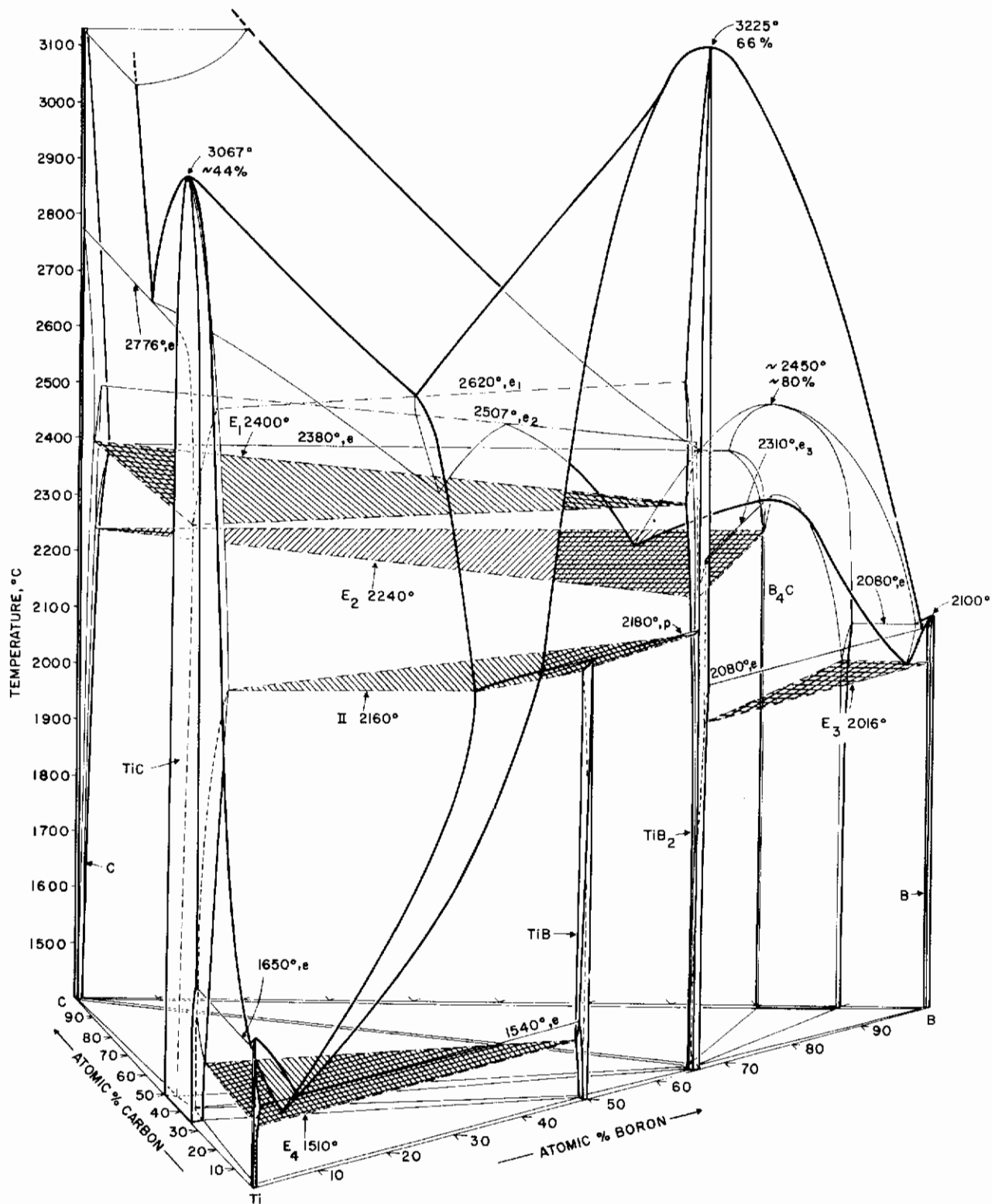


Figure 1. Phase Diagram of the System Ti-B-C.

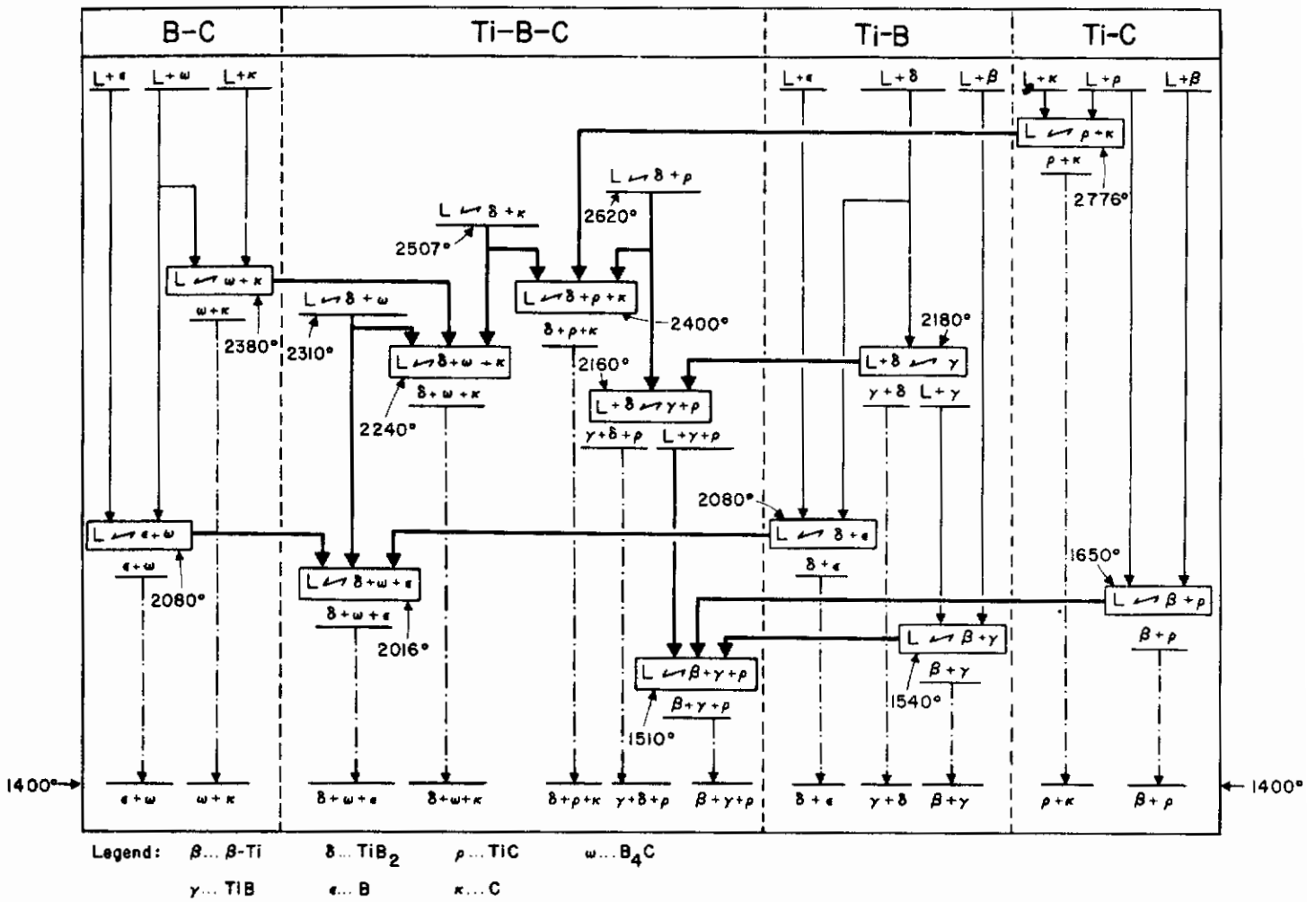


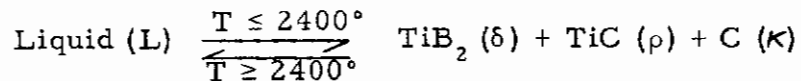
Figure 2. Scheil-Schultz Reaction Diagram for the Titanium-Boron-Carbon System.

Table 2. Pseudobinary (Eutectic) Reaction Isotherm $L \rightarrow \delta + \kappa$ at 2507°C: Compositions of the Equilibrium Phases

Phase	Concentrations, At. %		
	Ti	B	C
Melt (L)	23	45	32
TiB_2 (δ)	~34	~64	<2
C (κ)	<1	~2	>97

c. Class III Four-Phase Equilibrium at 2400°C.

The ternary eutectic reaction proceeding within the composition field $TiB_2 + TiC + C$ can be presented as:



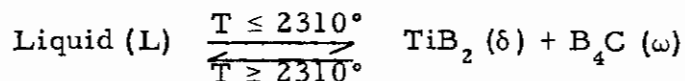
The equilibrium compositions of the phases are listed in Table 3.

Table 3. Class III Four-Phase Equilibrium $L \rightarrow \delta + \rho + \kappa$ at 2400°C: Compositions of the Equilibrium Phases.

Phase	Concentrations, At. %		
	Ti	B	C
Melt (L)	29	37	34
$TiB_2 (\delta)$	34	64	<2
$TiC (\rho)$	52	2	46
$C (\kappa)$	<1	<2	>97

d. Pseudobinary, Eutectic-Type Reaction Isotherm at 2310°C

Eutectic melting or solidification occurring between TiB_2 and B_4C is characterized by the reaction equation:



The approximate equilibrium compositions of the phases are presented in Table 4.

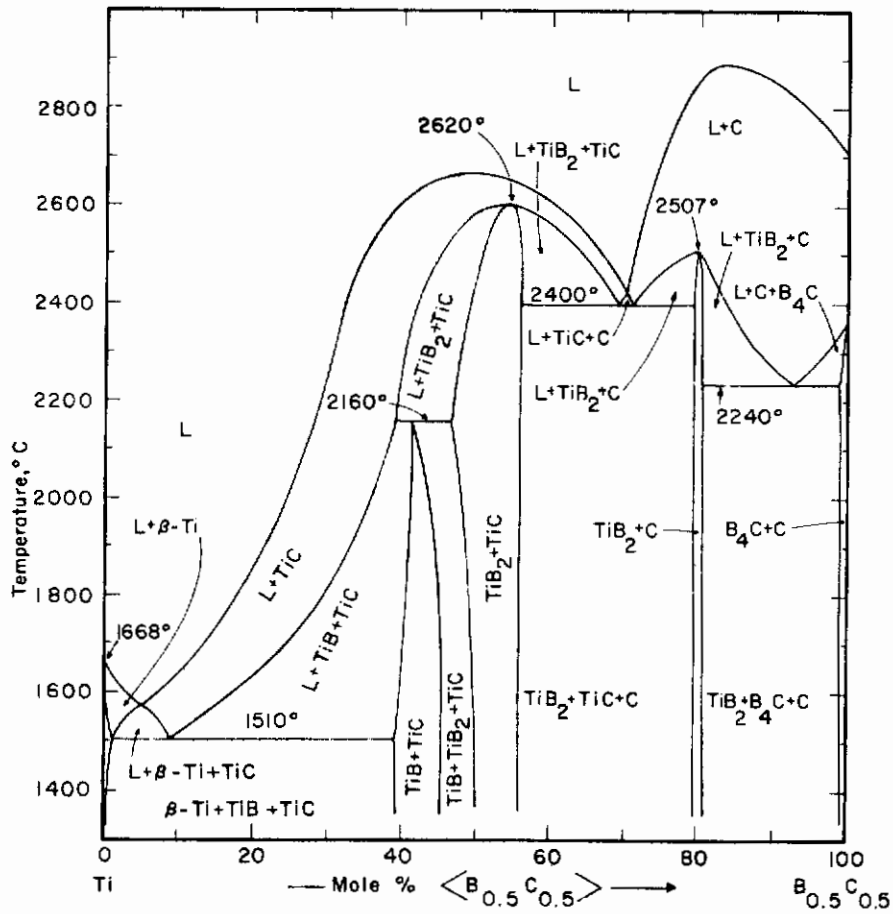


Figure 3. Ti-B-C. Isopleth Ti-B_{0.5}C_{0.5}

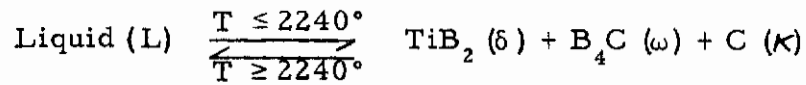
Table 4. Pseudobinary (Eutectic) Reaction Isotherm L → δ + ω at 2310°C: Compositions of the Equilibrium Phases

Phase	Concentrations, At. %		
	Ti	B	C
Melt (L)	~5	80	~15
TiB ₂ (δ)	> 33	~65	< 2
B ₄ C (ω)	< 1	~82	~17

Contrails

e. Class III Four-Phase Equilibrium at 2240°C.

This equilibrium is associated with the formation of a ternary eutectic between the phases TiB_2 , B_4C , and C (graphite), and is represented by the reaction equation:



The approximate equilibrium compositions of the phases are given in Table 5.

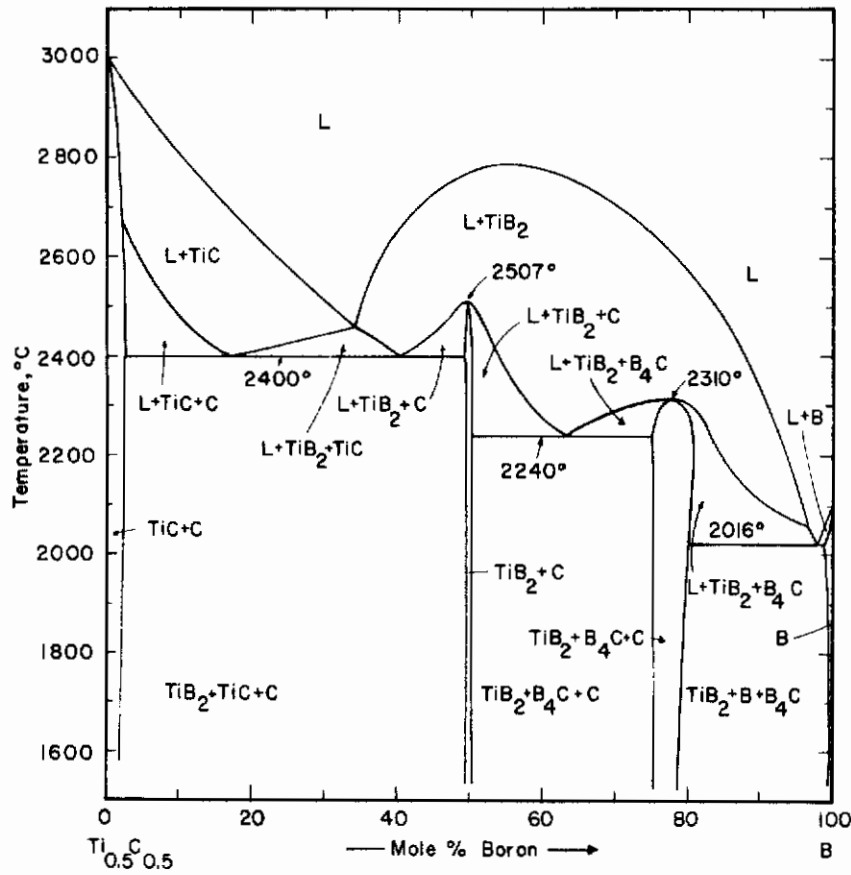


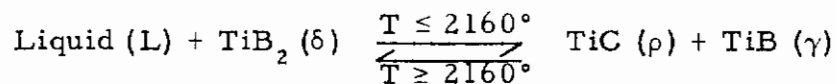
Figure 4. Ti-B-C: Isopleth $Ti_{0.5}C_{0.5}$ -B

Table 5. Class III Four-Phase Equilibrium $L \rightarrow \delta + \omega + \kappa$ at 2240°C : Compositions of the Equilibrium Phases.

Phase	Concentrations, At. %		
	Ti	B	C
Melt (L)	~10	~62	~28
TiB ₂ (δ)	~34	~64	< 2
B ₄ C (ω)	< 1	~80	> 79
C (κ)	< 1	~3	> 96

f. Class II Four-Phase Equilibrium at 2160°C

The overall reaction proceeding at this temperature can be presented as:



The approximate equilibrium compositions of the participant phases are given in Table 6.

Table 6. Class II Four-Phase Equilibrium $L + \delta \rightarrow \rho + \gamma$ at 2160°C : Compositions of the Equilibrium Phases.

Phase	Concentrations, At. %		
	Ti	B	C
Melt (L)	~59	~34	~7
TiB ₂ (δ)	~34	> 64	< 2
TiC (ρ)	~64	~4	~32
TiB (γ)	~50	> 48	< 2

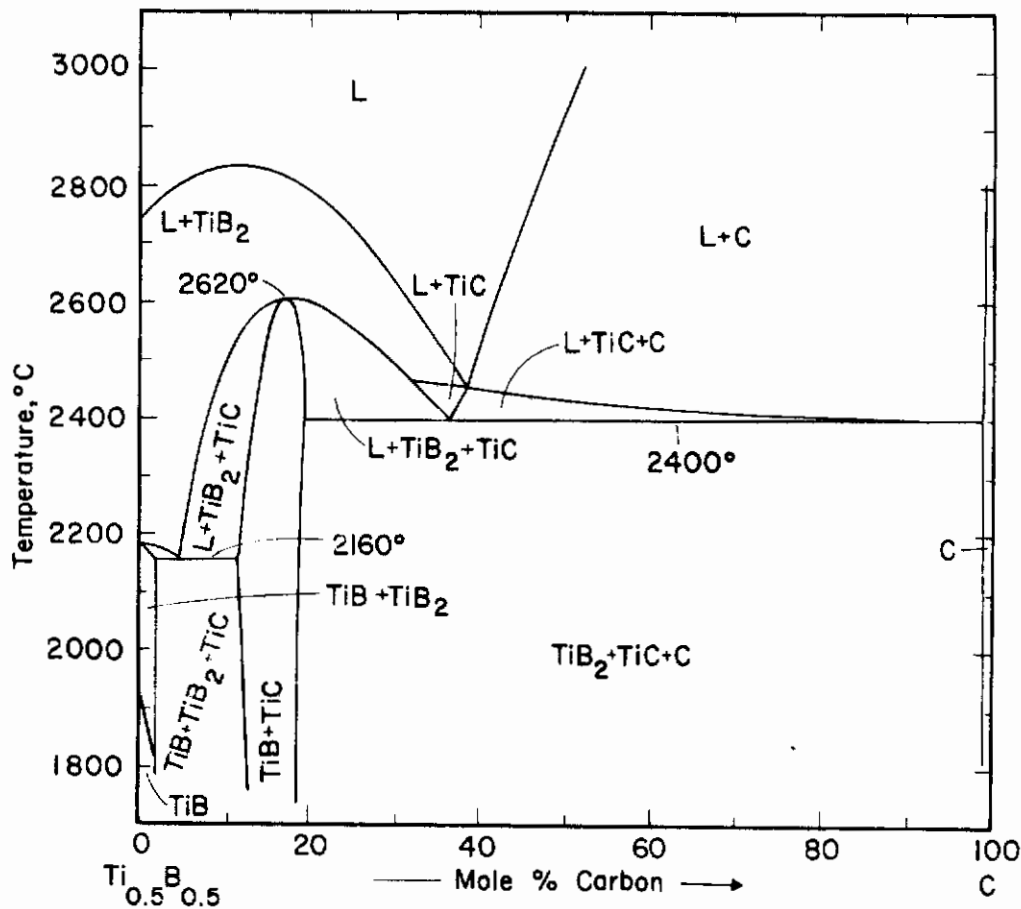
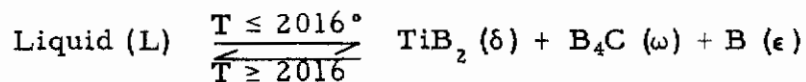


Figure 5. Ti-B-C: Isopleth $Ti_{0.5}B_{0.5}$ -C.

g. Class III Four-Phase Equilibrium at 2016°C.

The isothermal reaction proceeding at this temperature is associated with the formation of a eutectic equilibrium between the phases TiB_2 , B_4C , and B, and can be represented by the reaction equation:



The approximate equilibrium compositions of the phases are given in Table 7.

Table 7. Class III Four-Phase Equilibrium $L \rightarrow \delta + \omega + \epsilon$ at 2016°C:
Compositions of the Equilibrium Phases.

Phase	Concentrations, At. %		
	Ti	B	C
Melt (L)	~1.5	~97	~1.5
TiB ₂ (δ)	~33	~66	~1
B ₄ C (ω)	<1	>88	~11
B (ε)	<1	~99	<1 (?)

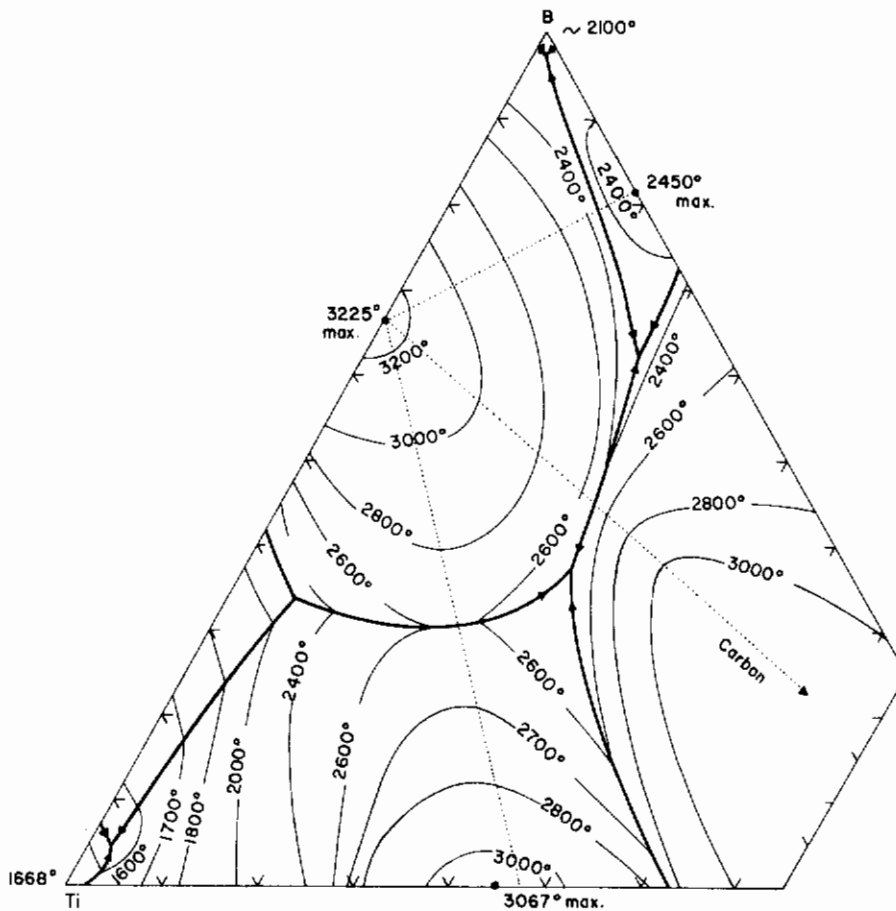
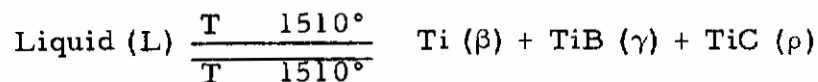


Figure 6. Liquidus Projections for the Ti-B-C System.
(Liquidus Isotherms Approximate)

Confidential

h. Class II Four-Phase Equilibrium at 1510°C.

This reaction isotherm is associated with ternary eutectic formation between β -Ti, TiB, and TiC according to a reaction scheme:



The approximate equilibrium concentrations of the phases are given in Table 8.

Table 8. Class II Four-Phase Equilibrium L — $\beta + \gamma + \rho$ at 1510°C: Compositions of the Equilibrium Phases.

Phase	Concentrations, At. %		
	Ti	B	C
Melt (l)	93	5	2
Ti (β)	>98	~1	~1
TiB (γ)	~51	>48	<1
TiC (ρ)	~68	~2	~30

2. Zirconium-Boron-Carbon

No structure types other than those of the binary phases are found in ternary alloys, i.e. the ternary phase equilibria formed are governed solely by the stability of the binary phases. As in the corresponding system with titanium, the extreme stable diboride dominates the ternary phase field, and forms two-phase equilibria with ZrC_{1-x} , B_4C and graphite. Altogether nine (9) isothermal phase reactions occur in the system: three of them are associated with the formation of eutectic equilibria on the pseudobinary sections ZrB_2 -ZrC, ZrB_2 -C, and ZrB_2 - B_4C . Four Class III four-phase equilibria take account of the occurrence of ternary eutectic equilibria between the phases $\text{Zr} + \text{ZrC} + \text{ZrB}_2$, $\text{ZrB}_2 + \text{ZrC} + \text{C}$, $\text{ZrB}_2 + \text{B}_4\text{C} + \text{C}$, and $\text{ZrB}_{12} + \text{B}_4\text{C} + \text{B}$. A Class II four-phase plane at 2160°C marks the replacement of the solid-state equilibrium $\text{ZrB}_{12} + \text{B}_4\text{C}$ by an equilibrium $\text{ZrB}_2 + \text{liquid}$ towards higher temperatures; a further Class II reaction isotherm at 1800°C, which involves solid phases only, characterizes the lower temperature stability limit of zirconium dodecarbide in the ternary phase field. With the exception of zirconium monocarbide, for which a maximum boron-exchange of ~5 mole percent was determined, the atom exchanges in all other phases are small.

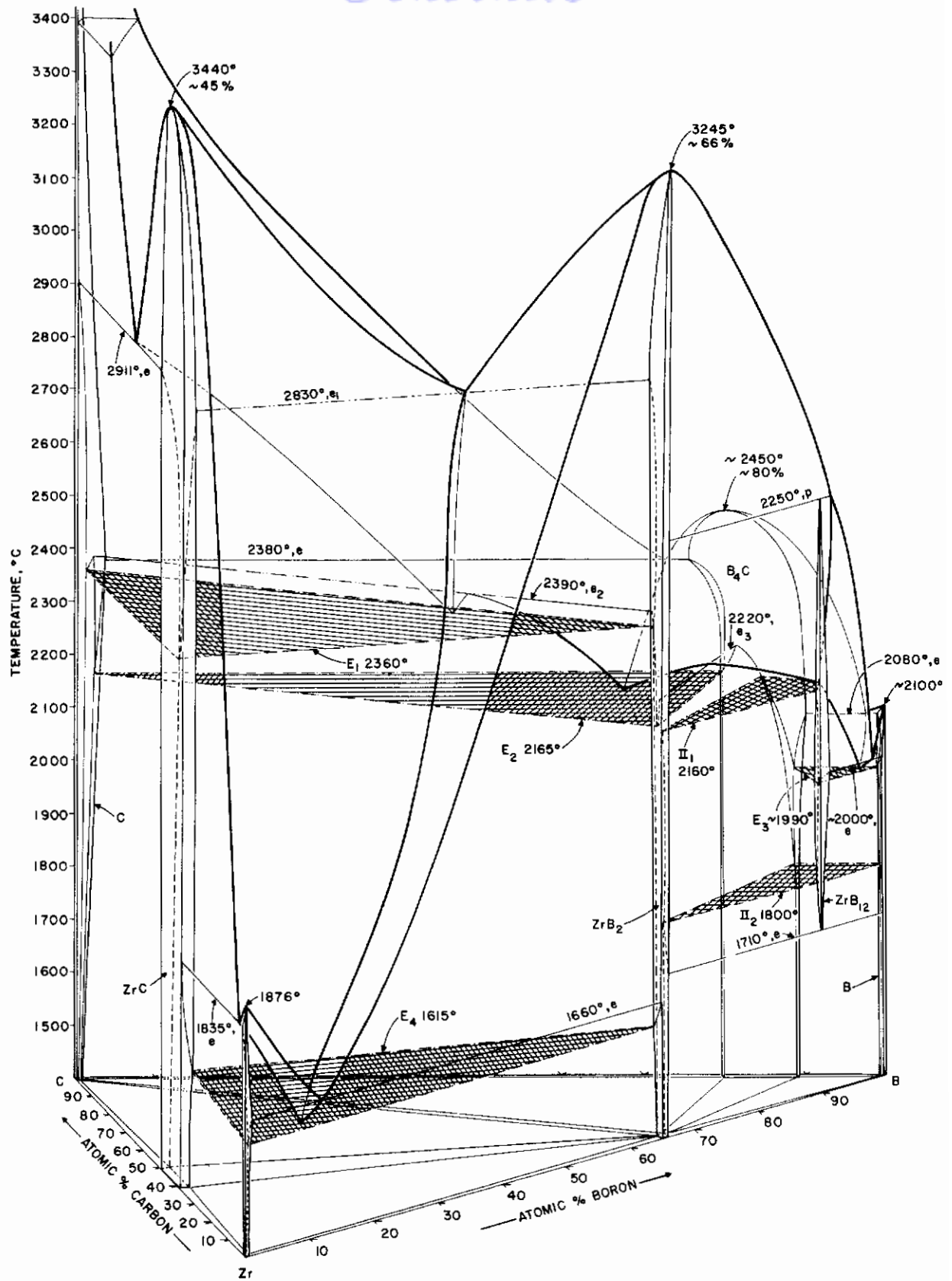


Figure 7. Phase Diagram of the System Zr-B-C.

The phase diagram of the Zr-B-C alloy system is depicted in the isometric drawing of Figure 7, and isothermal binary and ternary reactions are summarized in condensed form in the familiar Scheil-Schultz diagram shown in Figure 8. Two isopleths, one across the composition line Zr-B_{0.5}C_{0.5}, and the other along the concentration line Zr_{0.5}C_{0.5}-B have been prepared from the temperature sections (Chapter IV-B-8), and are shown in Figures 9 and 10. Sections of the quasibinary equilibria are contained in the result section of this report. The locations of the melting troughs, supplemented by liquidus isotherms (approximate) are illustrated in the diagram shown in Figure 11.

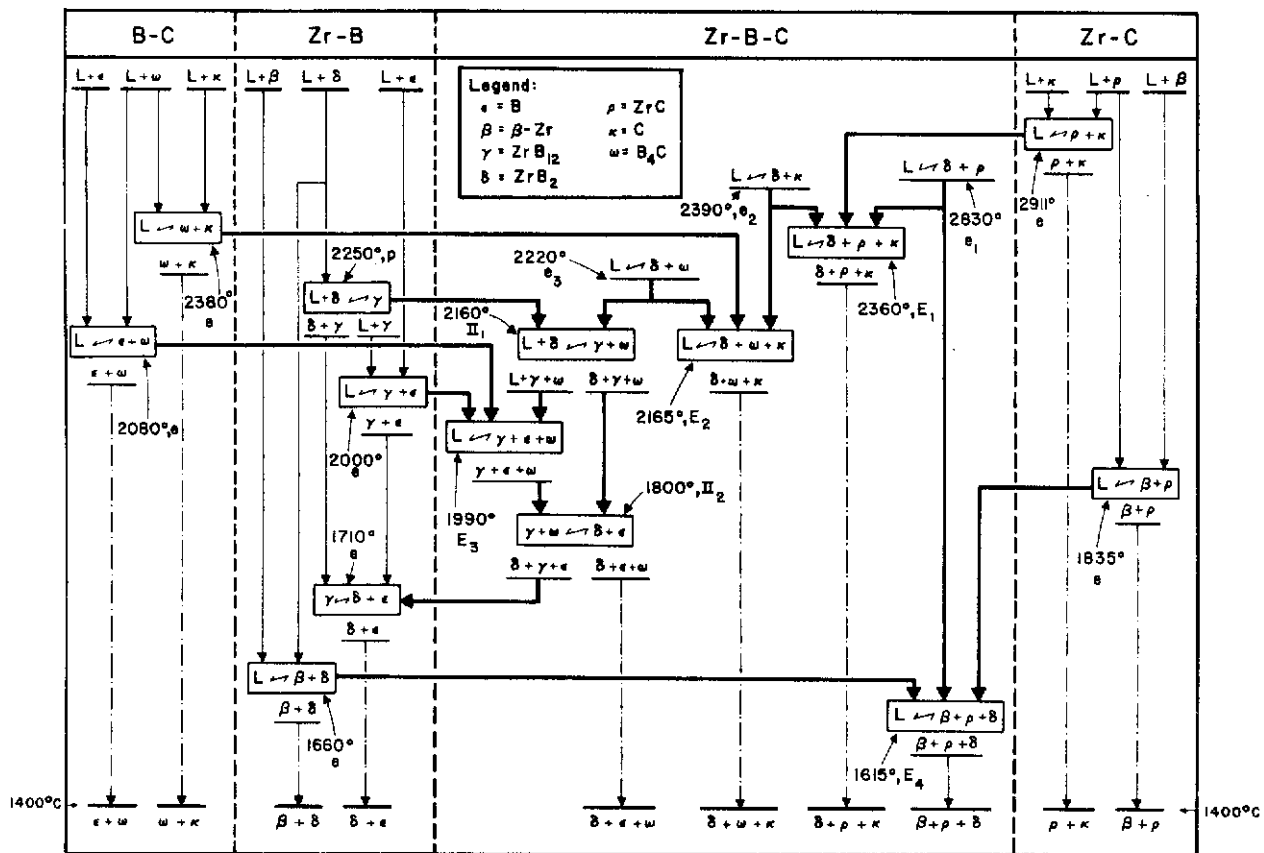
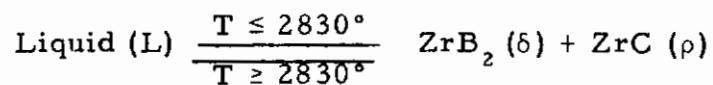


Figure 8. Scheil-Schultz Reaction Diagram for the Zirconium-Boron-Carbon System.

The isothermal ternary reactions, together with the approximate equilibrium compositions of the participant phases, are summarized below.

- a. Pseudobinary, Eutectic-Type Reaction Isotherm at 2830°C.

The eutectic reaction between the diboride and monocarbide can be presented as:



The equilibrium compositions of the participant phases are given in Table 9.

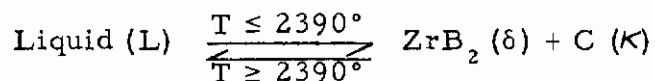
Table 9. Pseudobinary (Eutectic) Equilibrium L — δ + ρ at 2830°C: Compositions of the Equilibrium Phases.

Phase	Concentrations, At. %		
	Zr	B	C
Melt (L)	42	38	20
ZrB ₂ (δ)	~ 33	> 65	< 2
ZrC (ρ)	53	5	42

Contrails

- b. Pseudobinary, Eutectic-Type Reaction Isotherm
2390°C.

This reaction isotherm is associated with eutectic formation between zirconium diboride and graphite:



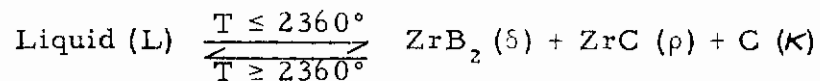
The equilibrium compositions of the phases are given in Table 10.

Table 10. Pseudobinary (Eutectic) Reaction $L \rightarrow \delta + \kappa$ at 2390°C: Compositions of the Equilibrium Phases.

Phase	Concentrations, At. %		
	Zr	B	C
Melt (L)	22	45	33
ZrB ₂ (δ)	~33	>65	<2
Graphite(κ)	<1	~2	>97

- c. Class III Four-Phase Equilibrium at 2360°C.

This reaction isotherm is associated with the formation of a ternary eutectic between ZrB₂, ZrC, and C, according to:



The equilibrium compositions of the participant phases are presented in Table 11.

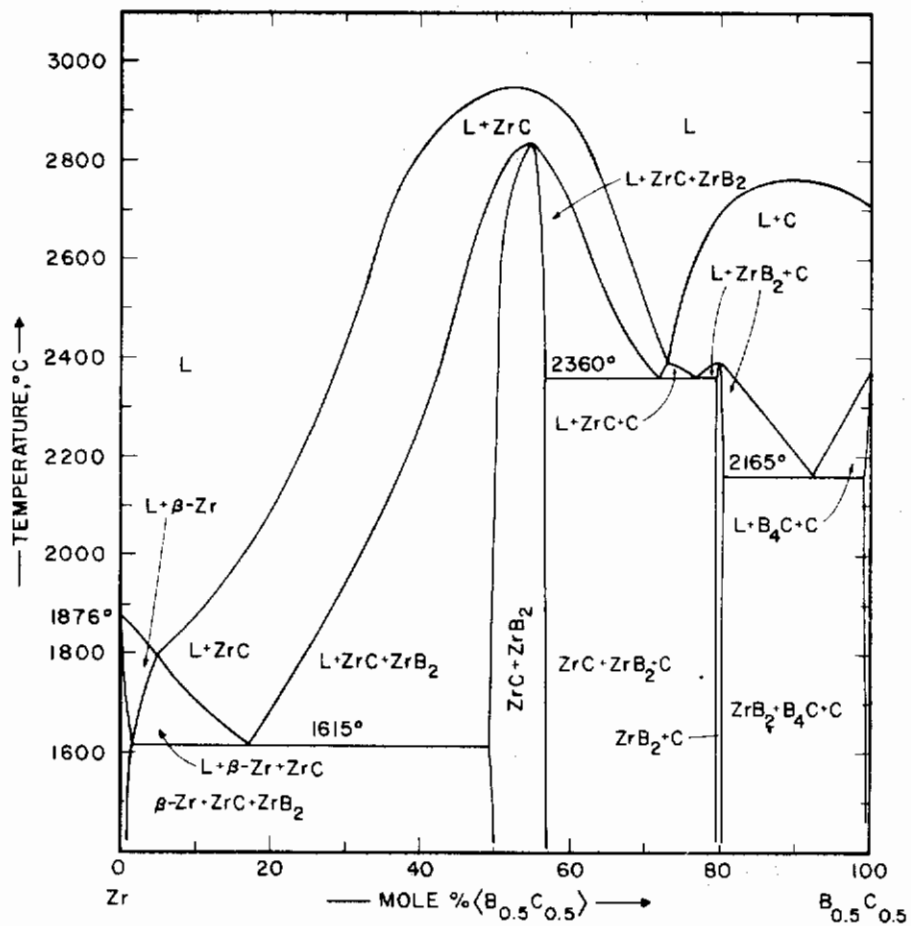


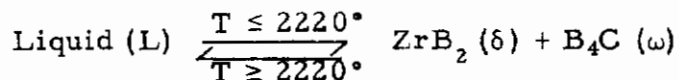
Figure 9. Zr-B-C: Isopleth Zr-B_{0.5}-C_{0.5}

Table 11. Class II Four-Phase Equilibrium $L \rightarrow \delta + \rho + \kappa$ at 2360°C: Compositions of the Equilibrium Phases.

Phase	Concentrations, At. %		
	Zr	B	C
Melt (L)	25	41	34
ZrB ₂ (δ)	~33	>65	<2
ZrC (ρ)	52	~3	45
C (κ)	<1	<2	>97

- d. Pseudobinary, Eutectic-Type Reaction Isotherm at 2220°C.

The eutectic reaction between ZrB_2 and B_4C can be presented by the reaction equation:



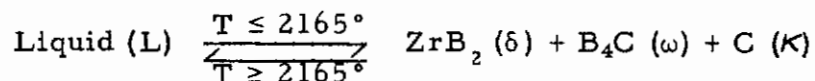
The equilibrium compositions of the participant phases are given in Table 12.

Table 12. Pseudobinary (Eutectic) Reaction $L \rightarrow \delta + \omega$ at 2220°C: Compositions of the Equilibrium Phases.

Phase	Concentrations, At. %		
	Zr	B	C
Melt (L)	~9	~77	~14
ZrB_2 (δ)	> 32	~66	< 2
B_4C (ω)	< 1	> 81	~18

- e. Class II Four-Phase Equilibrium at 2165°C.

This reaction isotherm is associated with the formation of a ternary eutectic between ZrB_2 , B_4C , and graphite, according to:



The equilibrium compositions of the phases are presented in Table 13.

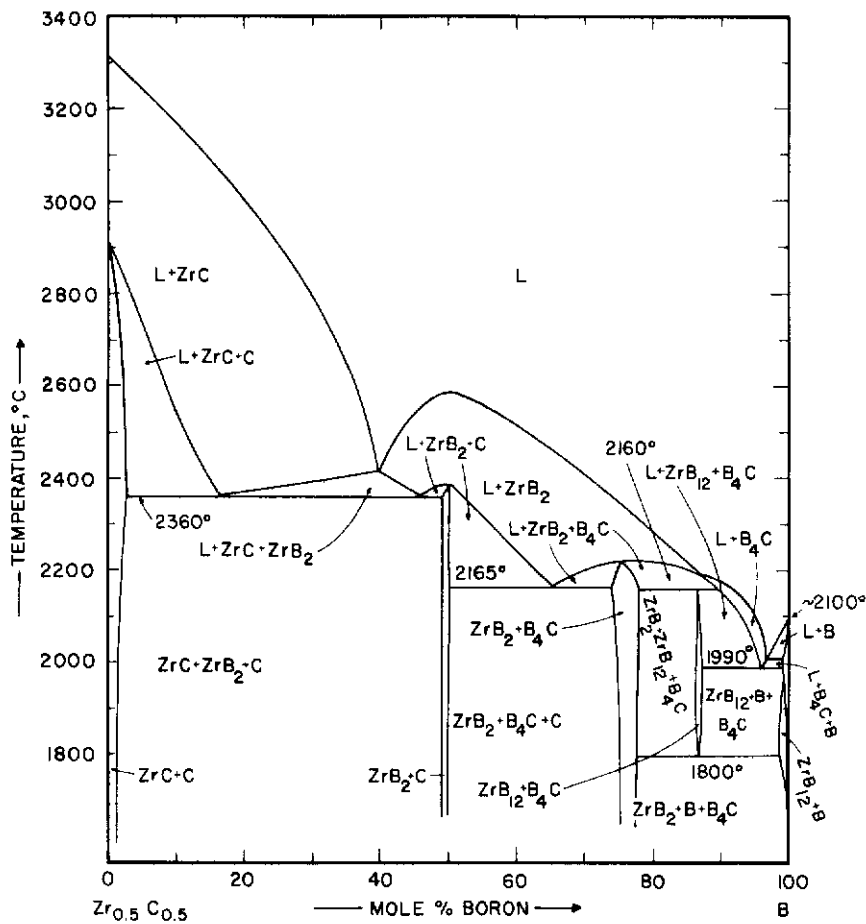


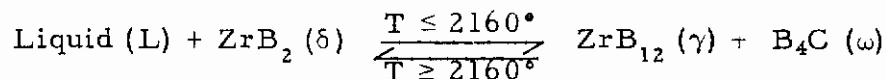
Figure 10. Zr-B-C: Isopleth $Zr_{0.5}C_{0.5}$ -B.

Table 13. Class III Four-Phase Equilibrium $L \rightarrow \delta + \omega + \kappa$ at 2165°C : Compositions of the Equilibrium Phases.

Phase	Concentrations, At. %		
	Zr	B	C
Melt (L)	~11	~66	~23
ZrB_2 (δ)	> 32	~66	< 2
B_4C (ω)	< 1	~79	> 20
Graphite(κ)	< 1	~2	> 97

f. Class II Four-Phase Equilibrium at 2160°C.

This reaction isotherm in essence determines the upper temperature limit for the appearance of ZrB_{12} in the ternary phase field. The reaction can be presented as:



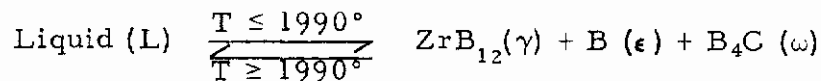
The equilibrium compositions of the phases are listed in Table 14.

Table 14. Class II Four-Phase Equilibrium $L + \delta \rightarrow \gamma + \omega$ at 2160°C: Compositions of the Equilibrium Phases.

Phase	Concentrations, At. %		
	Zr	C	C
Melt (L)	~6	~91	~3
ZrB_2 (δ)	> 32	~67	< 1
ZrB_{12} (γ)	~9	~90	≤ 1
B_4C (ω)	< 1	~84	> 15

g. Class III Four-Phase Equilibrium at ~1990°C.

This reaction isotherm determines eutectic melting (solidification) between the phases ZrB_{12} , B_4C , and C, according to:



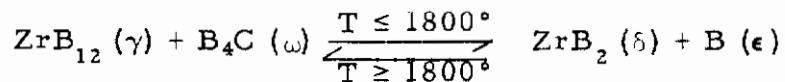
The approximate equilibrium compositions of the participant phases are listed in Table 15.

Table 15. Class III Four-Phase Equilibrium $L \rightarrow \gamma + \epsilon + \omega$ at 1990°C : Compositions of the Equilibrium Phases.

Phase	Concentrations, At. %		
	Zr	B	C
Melt (L)	~2	~2	~96
ZrB_{12} (γ)	>9	~90	<1
B (ϵ)	<1	>98	~1
B_4C (ω)	<1	~88	>11

h. Class II Four-Phase Equilibrium at 1800°C
(Solid State Reaction)

This reaction isotherm in effect determines the low temperature stability limit of ZrB_{12} in the ternary phase field. The overall reaction can be presented as:



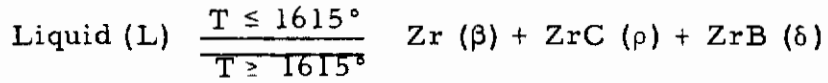
The approximate equilibrium compositions of the phases are listed in Table 16.

Table 16. Class II Four-Phase Equilibrium $\gamma + \omega \rightarrow \delta + \epsilon$ at 1800°C : Composition of the Equilibrium Phases

Phase	Concentrations, At. %		
	Zr	B	C
ZrB_{12} (γ)	~10	~90	<<1
B_4C (ω)	<1	~89	>10
ZrB_2 (δ)	>32	67	<1
B (ϵ)	>98	<1	<1

i. Class III Four-Phase Equilibrium at 1615°C

This reaction isotherm is associated with the formation of a ternary eutectic equilibrium between β -Zr, ZrC, and ZrB₂.



The approximate equilibrium compositions of the phases are listed in Table 17.

Table 17. Class II Four-Phase Equilibrium L — $\beta + \rho + \delta$ at 1615°C: Compositions of the Equilibrium Phases.

Phases	Concentrations, At. %		
	Zr	B	C
Melt (L)	88	10	2
Zr (β)	>98	<1	<1
ZrC (ρ)	61	3	36
ZrB ₂ (δ)	~ 33	>66	<1

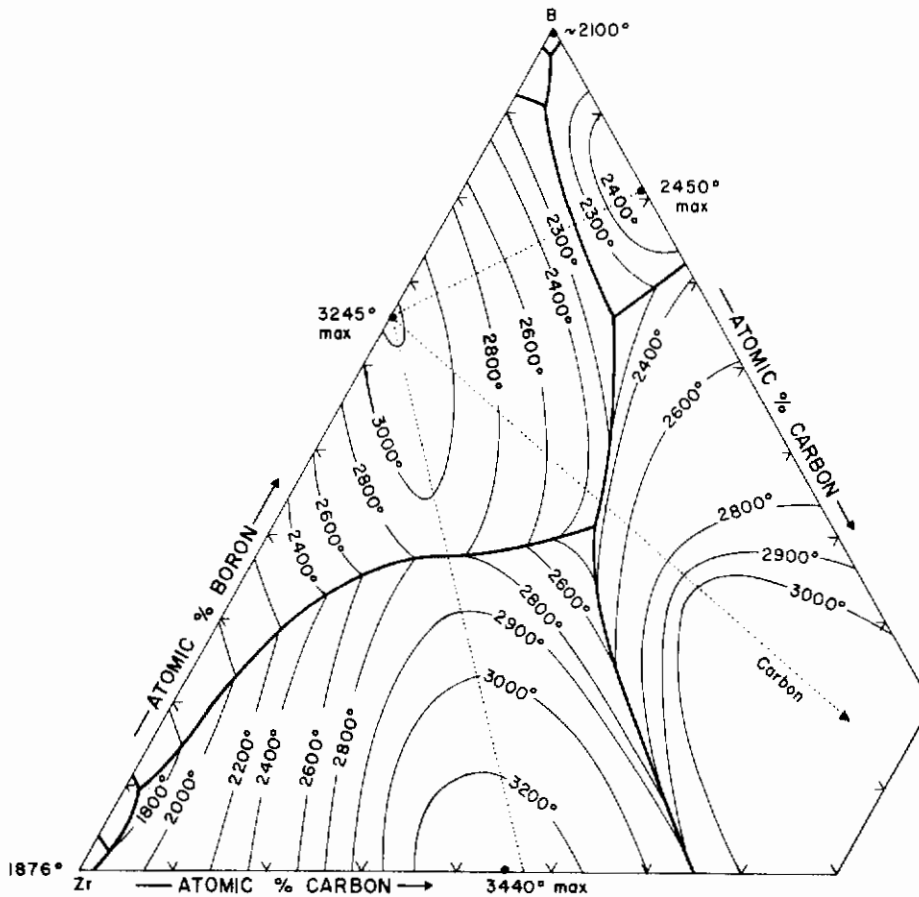


Figure 11. Liquidus Projections for the Zr-B-C System. (Liquidus Isotherms Approximate)

3. Hafnium-Boron-Carbon

No new ternary alloy phases are formed in the system, and the phase distribution in the ternary is governed by the appearance of the extremely stable hafnium diboride HfB_2 , forming pseudobinary systems with B_4C , graphite, and HfC .

Altogether, nine (9) reaction isotherms occur in the ternary phase field. Three of them are associated with the formation of eutectic equilibria in the above-mentioned pseudobinary system sections; ternary eutectic melting between the phases $\alpha\text{-Hf} + \beta\text{-Hf} + \text{HfB}$, $\text{HfC} + \text{HfB}_2 + \text{C}$, $\text{HfB}_2 + \text{B}_4\text{C} + \text{C}$, and $\text{HfB}_2 + \text{B}_4\text{C} + \text{B}$, accounts for further four four-phase temperature planes; one Class II four-phase equilibrium at 1940°C replaces the equilibrium monoboride + $\alpha\text{-Hf-ss}$ by an equilibrium $\text{HfC-ss} + \text{melt}$ towards higher temperatures, and a further Class II equilibrium at 2050°C terminates the appearance of the monoboride in the ternary. Like in the corresponding systems involving titanium and zirconium, the monocarbide is the only phase which shows appreciable solid solubility. The complete phase diagram of the system Hf-B-C in isometric view is shown in Figure 12, while binary and ternary reactions are summarized in condensed form in the Scheil-Schultz reaction diagram, illustrated in Figure 13. Three vertical sections (Figures 14, 15, and 16) were prepared from the temperature sections (Section IV-C-7) and the location of the melting troughs, supplemented by the liquidus isotherms, are shown in Figure 17.

The ternary reaction isotherms, together with the approximate compositions of the phases participating in the non-variant equilibria are summarized below.

- a. Pseudobinary, Eutectic-Type Reaction Isotherm at 3140°C .

This isotherm is associated with the formation of a eutectic equilibrium on the pseudobinary section $\text{HfB}_2 + \text{HfC}$. The reaction can be represented by:

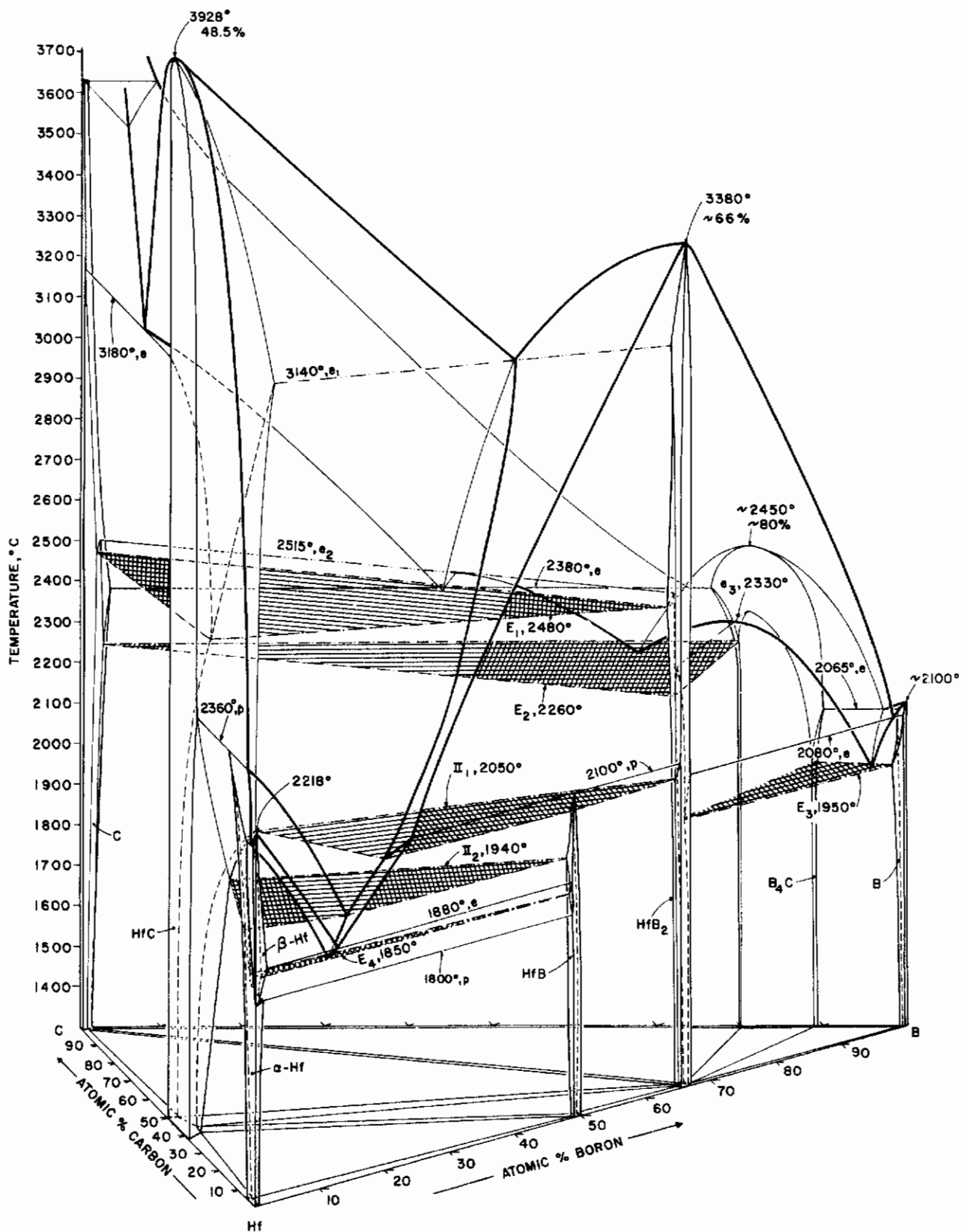


Figure 12. Phase Diagram of the System Hf-B-C.

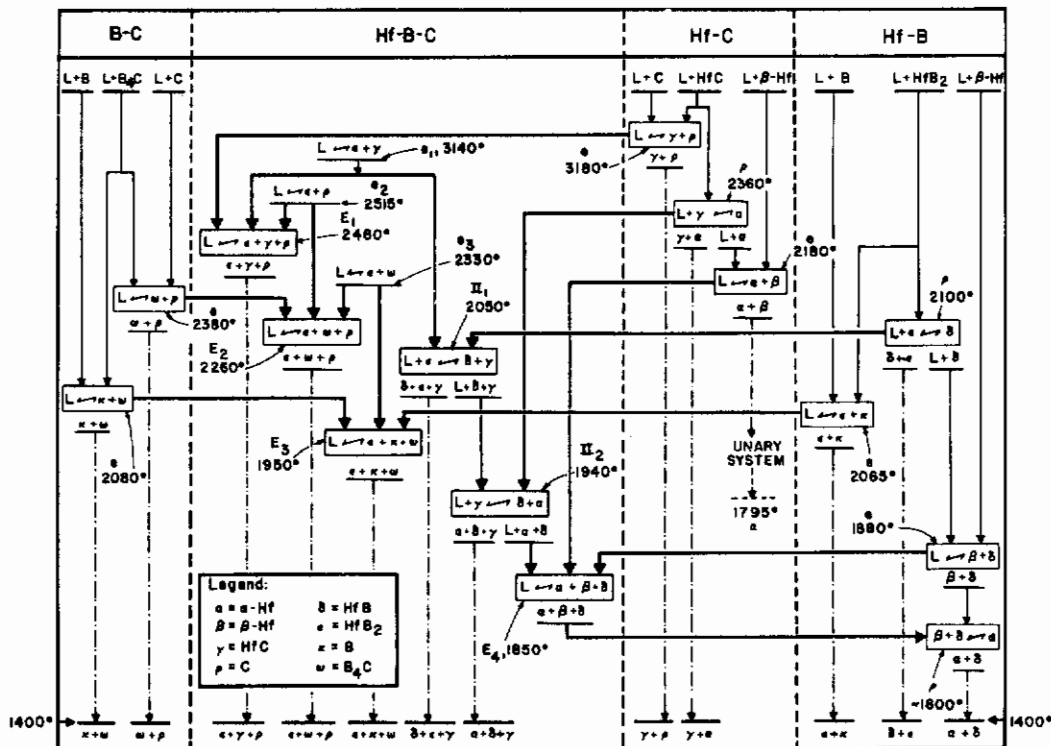
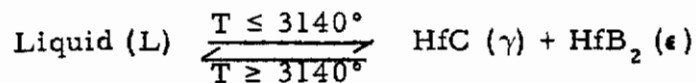


Figure 13. Scheil-Schultz Reaction Diagram for the Hafnium-Boron-Carbon System.



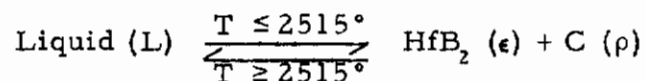
The approximate equilibrium compositions of the participant phases are given in Table 18.

Table 18. Pseudobinary (Eutectic) Reaction $L \rightarrow \gamma + \epsilon$ at 3140°C : Compositions of the Equilibrium Phases

Phase	Concentrations, At. %		
	Hf	B	C
Melt (L)	40	44	16
HfC (γ)	~55	~12	~33
HfB ₂ (ϵ)	~34	>64	<2

b. Pseudobinary, Eutectic-Type Reaction Isotherm at 2515°C .

This isotherm is associated with the occurrence of a eutectic equilibrium along the pseudobinary section diboride + graphite. The equilibrium reaction can be represented by the equation:



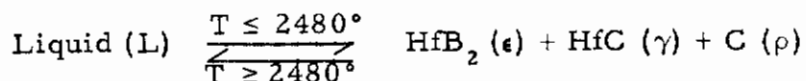
The approximate equilibrium compositions of the phases are given in Table 19.

Table 19. Pseudobinary Eutectic Reaction $L \rightarrow \epsilon + \rho$ at 2515°C : Compositions of the Equilibrium Phases.

Phase	Concentrations, At. %		
	Hf	B	C
Melt (L)	21	42	37
HfB ₂ (ϵ)	>33	>64	<3
C (ρ)	<1	~2	>97

c. Class II Four-Phase Equilibrium at 2480°C.

This reaction isotherm accounts for the occurrence of a eutectic equilibrium between diboride, monocarbide, and graphite:



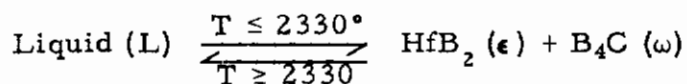
The approximate equilibrium compositions of the phases are listed in Table 20.

Table 20. Class II Four-Phase Equilibrium $L \rightarrow \epsilon + \gamma + \rho$ at 2480°C: Compositions of the Equilibrium Phases.

Phase	Concentrations, At. %		
	Hf	B	C
Melt (L)	24	38	38
HfB ₂ (ε)	~33	>64	<3
HfC (γ)	~51	~5	~44
Graphite(ρ)	<1	~2	>97

d. Pseudobinary, Eutectic-Type Reaction Isotherm at 2330°C.

This isotherm is associated with the formation of a eutectic equilibrium along the pseudobinary section HfB₂-B₄C. The reaction proceeding at 2330°C can be presented as:



The approximate equilibrium compositions of the participant phases are listed in Table 21.

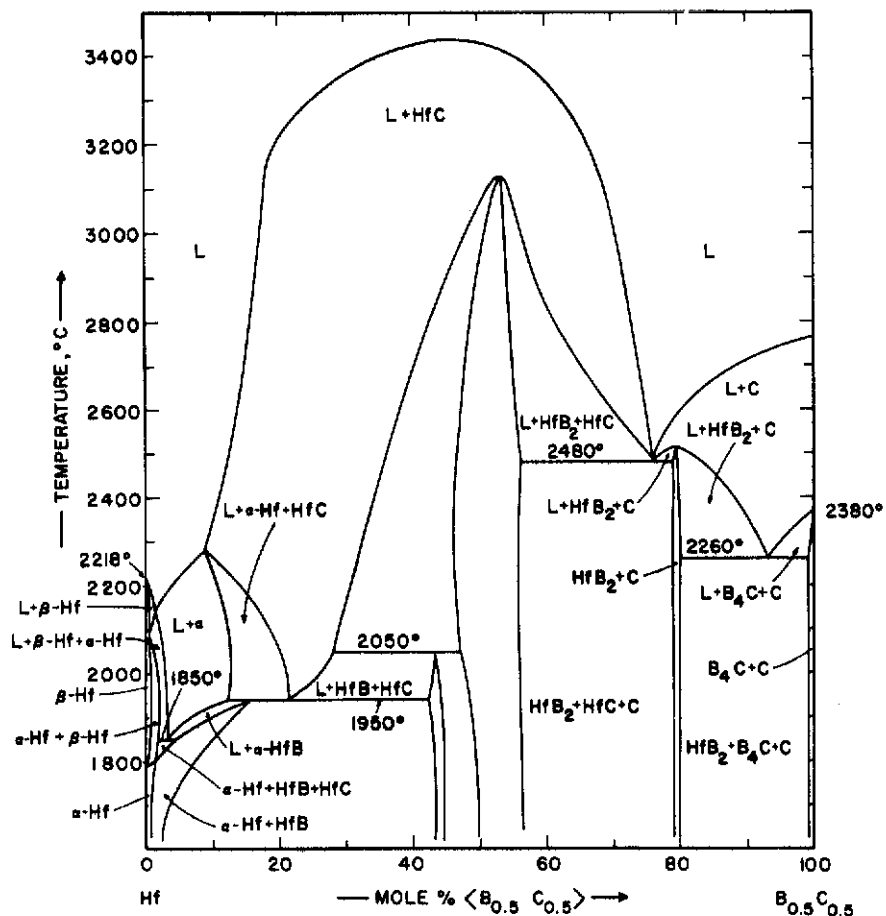


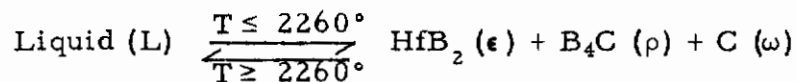
Figure 14. Isopleth Hf-B_{0.5}C_{0.5}.

Table 21. Pseudobinary (Eutectic) Reaction L → ε + ω Isotherm at 2330°C: Compositions of the Equilibrium Phases

Phase	Concentrations, At. %		
	Hf	B	C
Melt (L)	~7	~78	~15
HfB ₂ (ε)	~33	>65	< 2
B ₄ C (ω)	<1	~81	> 18

e. Class II Four-Phase Equilibrium at 2260°C.

The four-phase reaction plane is associated with the formation of a ternary eutectic between the phases HfB_2 , B_4C , and graphite. The eutectic reaction is:



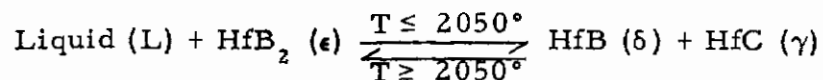
The approximate equilibrium compositions of the phases are presented in Table 22.

Table 22. Four-Phase Equilibrium $\text{L} \rightarrow \epsilon + \omega + \rho$ at 2260°C: Compositions of the Equilibrium Phases

Phase	Concentrations, At. %		
	Hf	B	C
Melt (L)	~9	~66	~25
$\text{HfB}_2 (\epsilon)$	~33	>64	<3
$\text{B}_4\text{C} (\omega)$	<1	~80	>19
C (ρ)	<1	~2	>97

f. Class II Four-Phase Equilibrium at 2050°C

The overall reaction at equilibrium, which essentially describes the ternary decomposition (heating) of the monoboride phase, can be presented as:



The approximate equilibrium compositions of the phases are listed in Table 23.

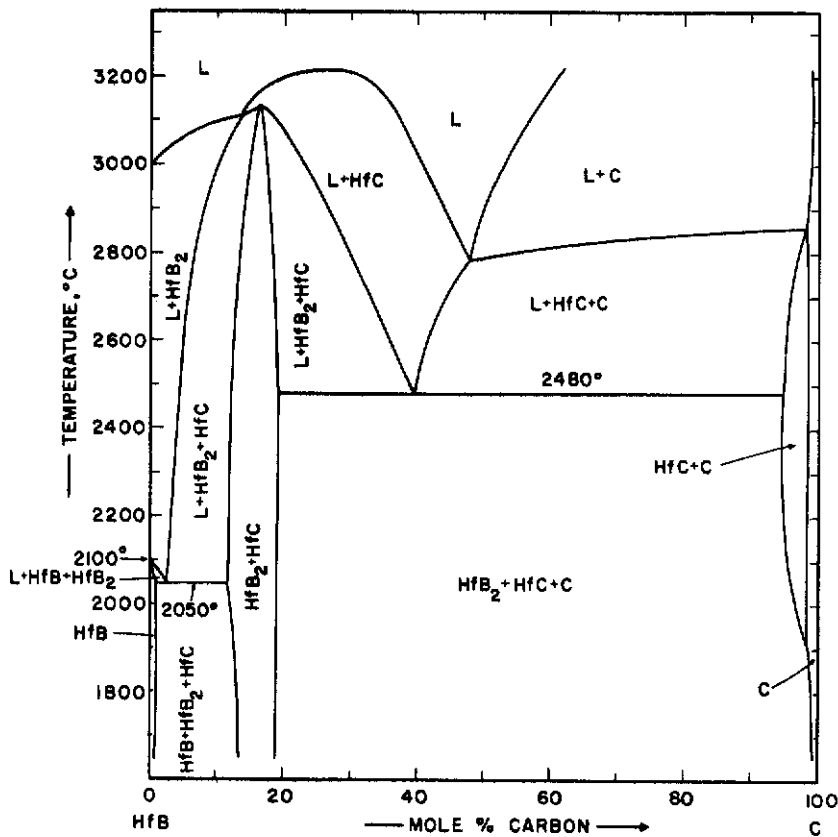


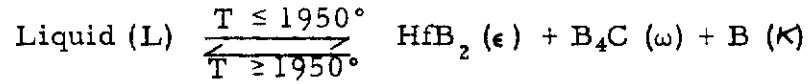
Figure 15. Hf-B-C: Isopleth Hf_{0.5}B_{0.5}-C.

Table 23. Class II Four-Phase Equilibrium L + ε → δ + γ at 2050°C: Compositions of the Equilibrium Phases.

Phase	Concentrations, At. %		
	Hf	B	C
Melt (L)	~79	~18	~3
HfB ₂ (ε)	~34	>64	<2
HfB (δ)	~50	>49	<1
HfC (γ)	~60	~9	~31

g. Class III Four-Phase Equilibrium at 1950°C

The four-phase reaction proceeding at this temperature is associated with the occurrence of a ternary eutectic between HfB_2 , B_4C , and B. The equilibrium can be presented as:



The approximate compositions of the equilibrium phases are summarized in Table 24.

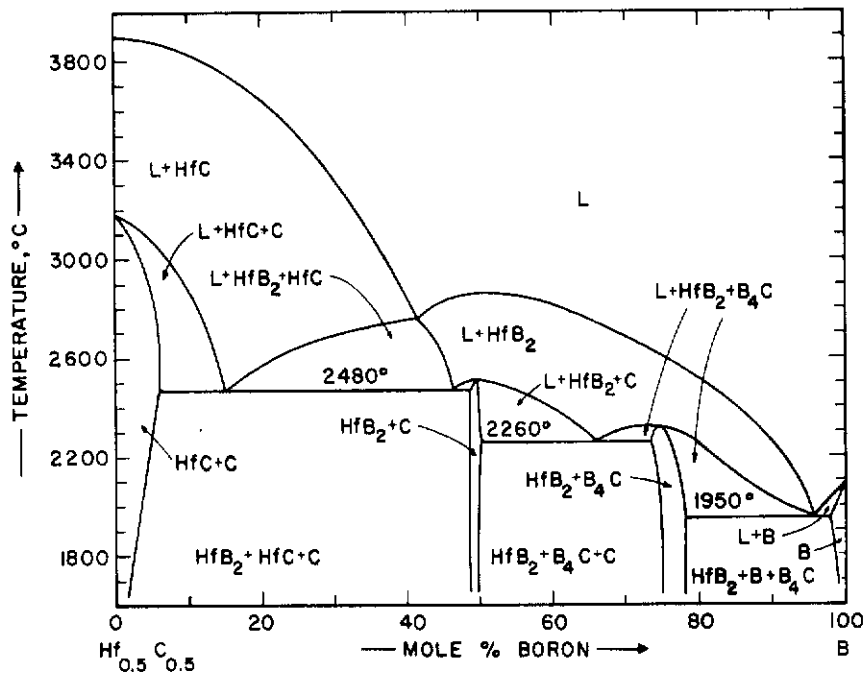


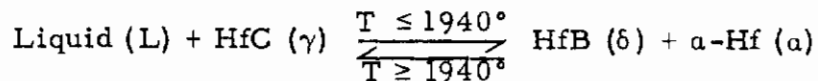
Figure 16. Hf-B-C: Isopleth $\text{Hf}_{0.5}\text{C}_{0.5}$ -C.

Table 24. Class II Four-Phase Equilibrium $L \rightarrow \epsilon + \omega + \kappa$ at 1950°C: Compositions of the Equilibrium Phases.

Phase	Concentrations, At. %		
	Hf	B	C
Melt (L)	~2	~96	~2
HfB ₂ (ε)	~33	>66	<1
B ₄ C (ω)	<1	~89	>10
B (κ)	<1	~98	<1

h. Class II Four-Phase Equilibrium at 1940°C.

The equilibrium characterizes the replacement of the solid state equilibrium $\alpha\text{-Hf-ss} + \text{HfB}$ by an equilibrium melt + monocarbide towards higher temperatures. The equilibrium reaction can be written as:



The approximate equilibrium compositions of the phases are presented in Table 25.

Table 25. Class II Four-Phase Equilibrium $L + \gamma \rightarrow \delta + \alpha$ at 1940°C: Compositions of the Equilibrium Phases.

Phase	Concentrations, At. %		
	Hf	B	C
Melt (L)	~84	~14	~2
HfC (γ)	~62	~6	~32
HfB (δ)	~51	>48	<1
α-Hf (α)	~90	~1	~9

i. Class II Four-Phase Equilibrium at 1850°C.

This reaction isotherm is associated with the occurrence of a ternary eutectic equilibrium between α -Hf, β -Hf, and the monoboride. The overall reaction can be written as:

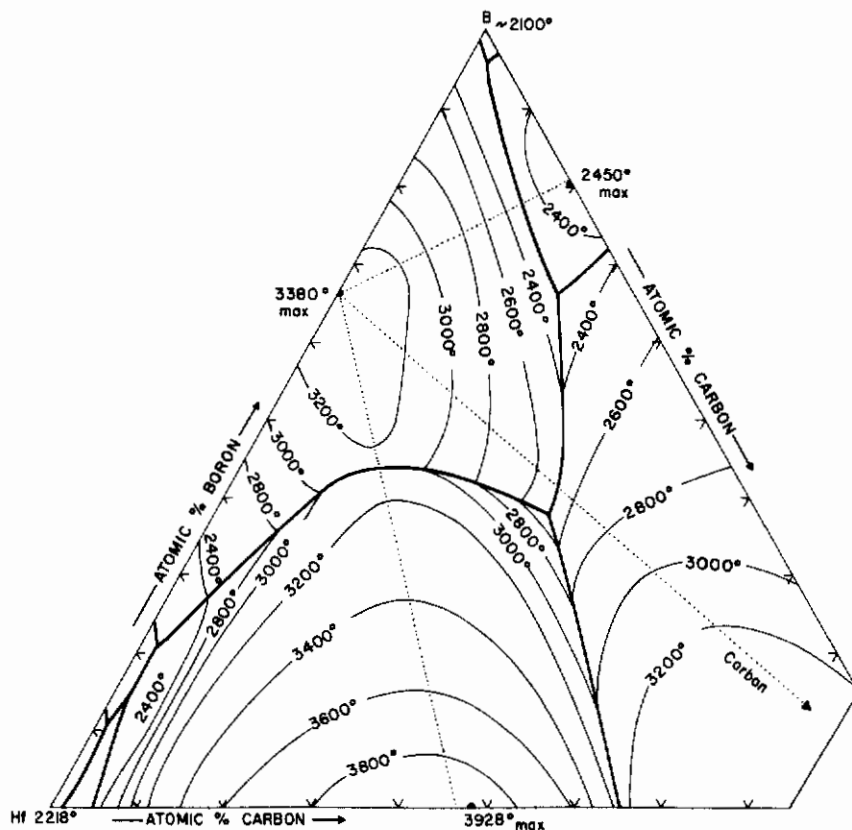
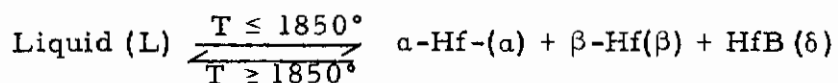


Figure 17. Liquidus Projections for the Hf-B-C System.
(Liquidus Isotherms Approximate)

The approximate equilibrium composition of the phases are listed in Table 26.

Table 26. Class III. Four-Phase Equilibrium L — $\alpha + \beta + \delta$ at 1850°C: Compositions of the Equilibrium Phases.

Phase	Concentrations, At. %		
	Hf	B	C
Melt (l)	~87.5	~11	~1.5
α -Hf (α)	~96	~1	~3
β -Hf (β)	>97.5	~1.5	<1
HfB (δ)	~50	49	<1

II. LITERATURE REVIEW

A. BOUNDARY SYSTEMS

1. Titanium-Carbon

Only one stable intermediate phase is formed in the system: TiC, with a face-centered cubic, B1-type of structure has a wide range of homogeneity⁽⁸⁻¹⁴⁾, which extends at 1650°C from 32 At. % C ($a=3.285 \text{ \AA}$) to ~49 At. % C ($a = 4.330 \text{ \AA}$, Figure 19). According to L. Stone and H. Margolin⁽¹⁶⁾, the exceptionally wide extension of the homogeneity range to the metal-rich region found by P. Ehrlich⁽⁹⁾ is due to oxygen or nitrogen contamination of the alloys. According to more recent investigations^(15, 7) the carbon-rich boundary is located at slightly understoichiometric compositions,

but work by E. K. Storms⁽¹⁴⁾ indicates, that the phase approaches stoichiometry at temperatures close to melting.

The phase relationships in the Ti-C system were investigated by I. Cadoll and J.P. Nielsen⁽¹¹⁾. According to their results, β -Ti decomposes in a peritectic reaction at 1750°C into monocarbide and melt, but later data clearly are in favor of a eutectic reaction isotherm between β -Ti and TiC_{1-x} ^(15, 18). Reported melting temperatures for the monocarbide phase vary between 2940°C⁽¹⁹⁾ and 3250°C⁽²⁰⁻²³⁾, and a congruent melting point of 3067°C at 44 At.% was measured at this laboratory⁽¹⁵⁾. The carbon-rich eutectic point is located at 63 At.% C⁽¹⁵⁾ and a temperature of 2776°C^(14, 15). The phase diagram of the titanium-carbon system, based on a recent re-determination in this laboratory⁽¹⁵⁾ is shown in Figure 18.

2. Zirconium-Carbon

Only one stable intermediate phase, a monocarbide with a face-centered cubic, B1-type of structure and a wide range of homogeneity⁽²⁴⁾ occurs in the system^(13, 14, 24-30). The lower-carbon boundary at 1830°C is located at approximately 38 At.% C ($a = 4.694 \text{ \AA}$ at 38.5 At.% C^(29, 30); $a = 4.686 \text{ \AA}$ at 37.5 At.%⁽¹⁵⁾). The high-carbon boundary was placed by J. Farr⁽²⁸⁾ at 49.4 At.%. Representative lattice parameter data reported for the graphite-saturated phase are: $a_{\text{ZrC}_{0.95}} = 4.6983 \text{ \AA}$ ^(29, 30), and $a = 4.698_5 \text{ \AA}$, measured on a specimen containing excess graphite⁽¹⁵⁾.

The phase diagram (Figure 20) is characterized by a eutectic between β -Zr and the defect monocarbide, and the formation of a eutectic between the very high-melting monocarbide and graphite. In its essential details, the phase diagram data given by R.V. Sara, et al. have been confirmed by work in this laboratory⁽¹⁵⁾.

3. Hafnium-Carbon

In the binary hafnium-carbon system^(13, 27, 31-34) (Figure 6), one intermediate carbide phase with extreme high melting point^(31, 35, 36) and a wide range of defect solid solutions exists^(27, 37).

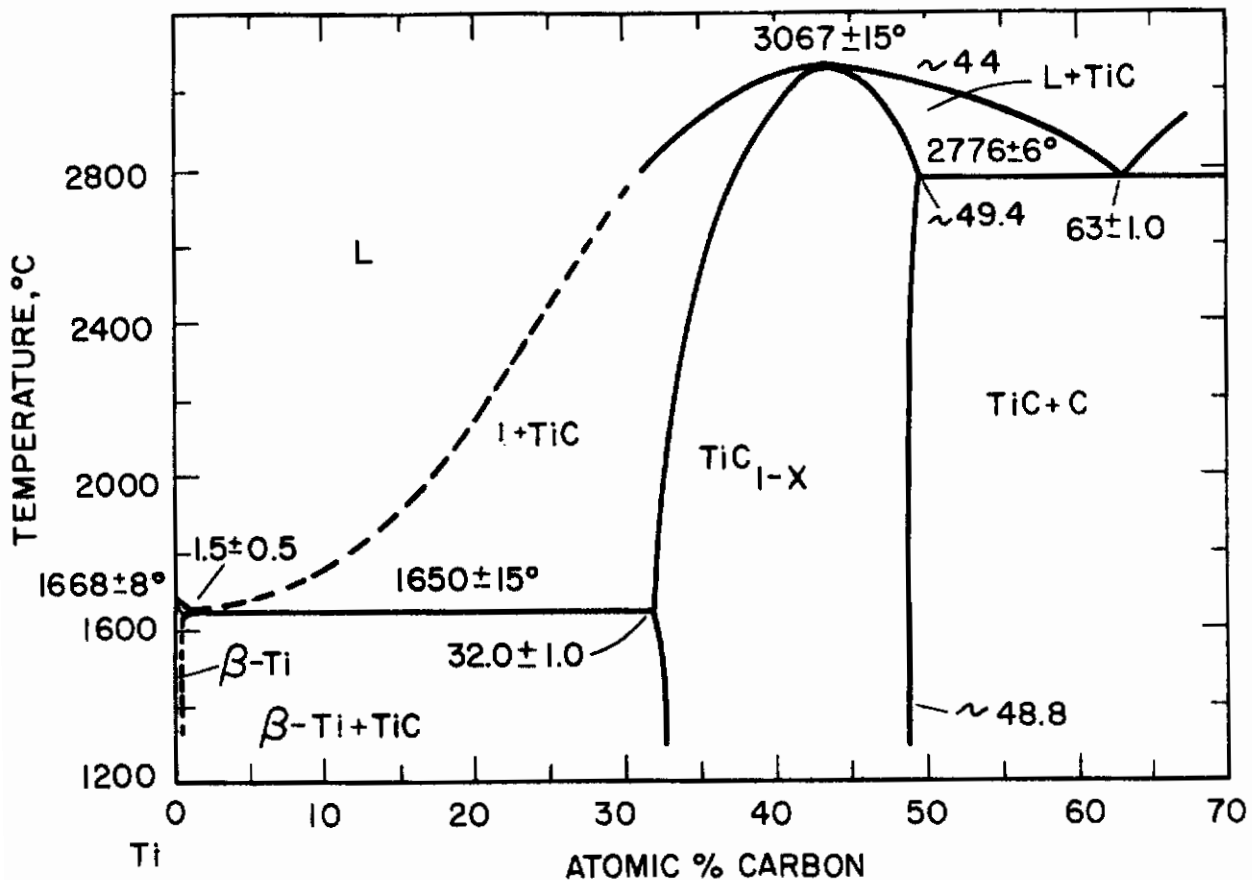


Figure 18. Constitution Diagram Titanium-Carbon.
 (E. Rudy, D. P. Harmon, and C.E. Brukl, 1965)

Hafnium monocarbide, with a face-centered cubic, (B1)-type, of unit cell, extends at 2300°C from approximately 34 At.% C ($a = 4.608 \text{ \AA}$) to 49.5 At.% C ($a = 4.640 \text{ \AA}$)^(31, 32). The lower-carbon boundary at 1500°C⁽²⁷⁾ lies at 37.5 At.% C. The hexagonal close-packed α - (low temperature) modifications of hafnium is stabilized to higher temperatures by incorporation of carbon-atoms into interstitial lattice sites⁽³⁴⁾, and decomposes in a peritectic reaction at 2360°C into monocarbide and melt⁽³¹⁾. The carbon solubility in the b.c.c. β -hafnium is below one atomic percent⁽³¹⁾. The β -hafnium phase forms a eutectic equilibrium with α -Hf (2180°, 1.5 At.% C); the carbon-rich eutectic is located at 3180°C and 65 ± 1 At.% C^(31, 32).

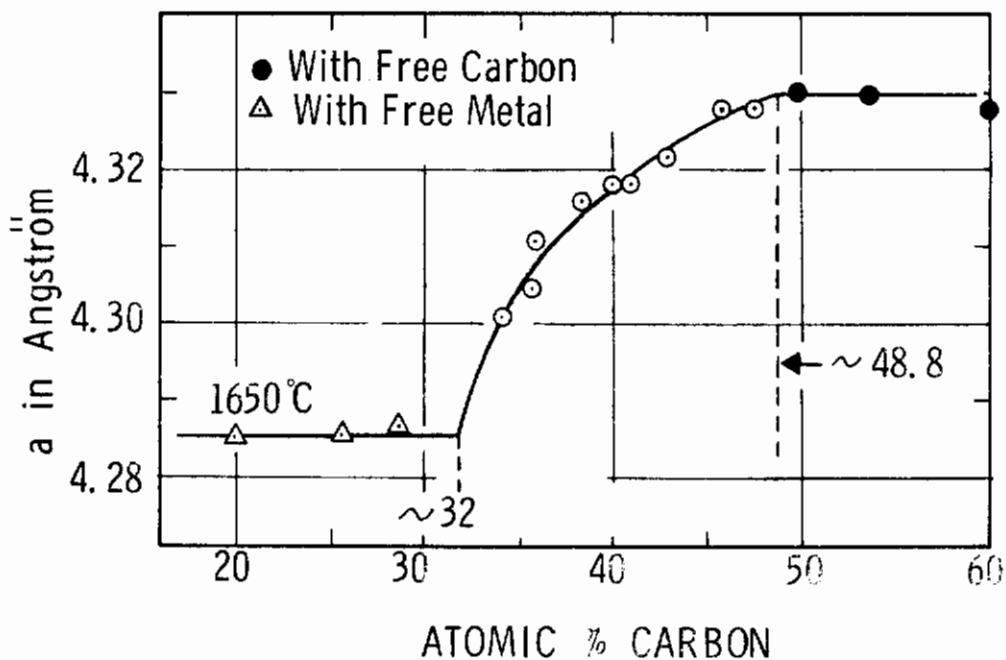


Figure 19. TiC_{1-x} : Variation of the Lattice Parameters with the $^{1-x}$ Carbon Concentration.

4. Titanium-Boron

In the binary titanium-boron system (Figure 22), two stable intermediate phases, both exhibiting narrow ranges of homogeneity, are formed.

The orthorhombic (B-27-type) monoboride⁽³⁸⁾ occurs at compositions close to stoichiometry and melts incongruently at $2190 + 25^\circ C$ ⁽³⁹⁾. Titanium diboride, with a simple hexagonal C32-type of structure^(40, 41), melts with a sharp maximum at 3225° at the stoichiometric composition⁽³⁹⁾. Previous claims for the existence of a tetragonal Ti_2B ^(42, 43), a face-centered cubic (B1) monoboride TiB ^(40, 41, 44, 45), and boron-rich phases Ti_2B_5 (W_2B_5 -type⁽⁴²⁾) and $TiB_{\sim 1.0}$ ⁽⁴⁷⁾, could not be confirmed in more recent investigations^(39, 46) (Table 27).

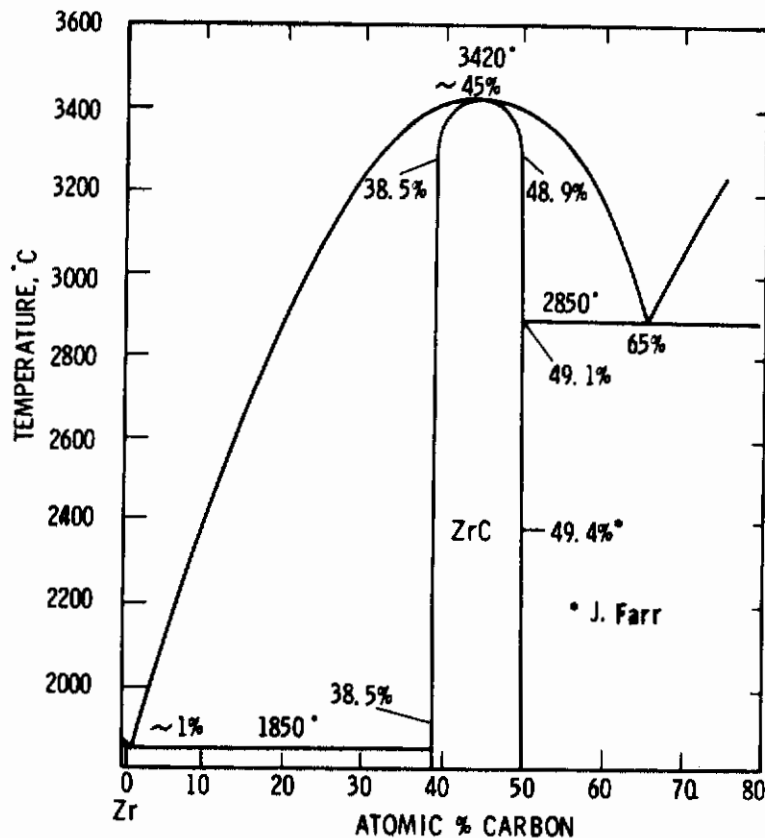


Figure 20. Constitution Diagram Zirconium-Carbon.

(R.V. Sara, C.E. Lowell, and R.T. Doloff, 1963)

The solid solubility of boron in α - and β -titanium is less than one atomic percent^(43, 47-50), and the α - β -transformation temperature remains nearly unaffected by the addition of boron⁽³⁹⁾. TiB and β -Ti form a eutectic equilibrium at 1450°C and 7 At.% B⁽³⁹⁾; a eutectic also is formed between the diboride and boron (Figure 22).

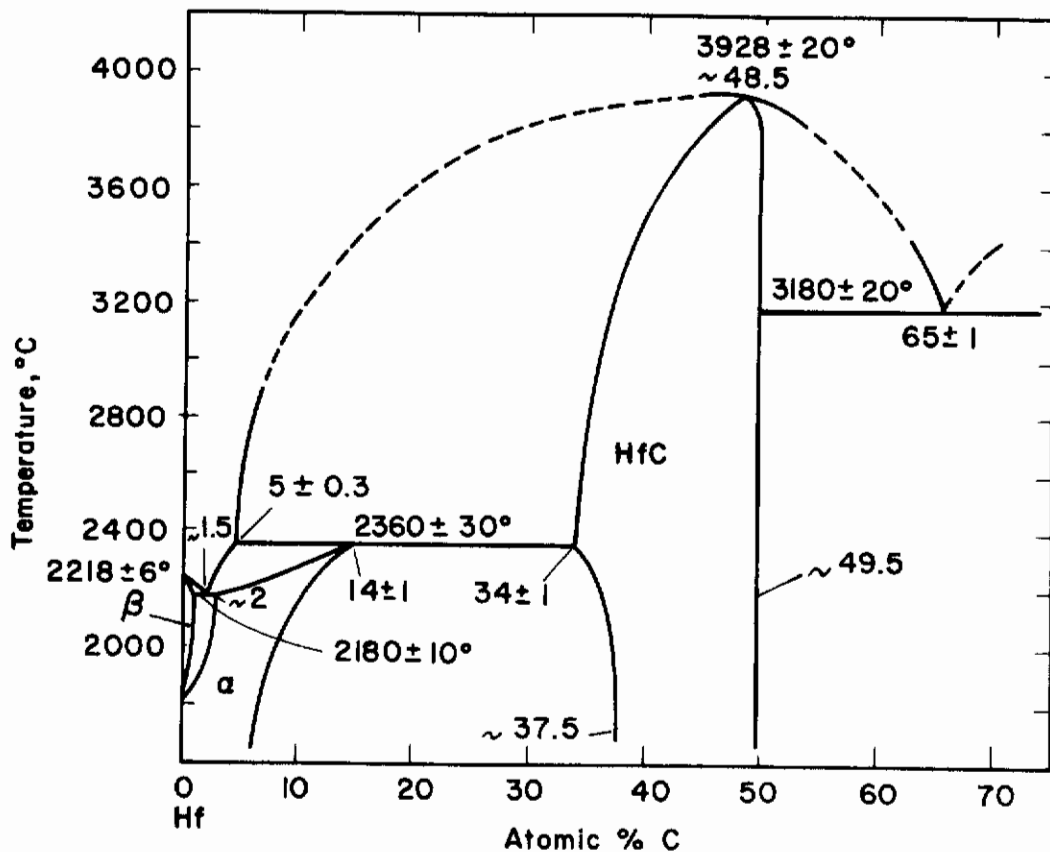


Figure 21. Constitution Diagram Hafnium-Carbon.

(E. Rudy, 1965)

5. Zirconium-Boron (Figure 23)

Two intermediate phases, an extremely high melting diboride^(13, 51-53), and a dodecaboride, which is stable only at temperatures above 1710°C, occur in the system (Figure 23).

Zirconium diboride, with a simple hexagonal, C32-Type, of structure^(41, 54, 55), melts congruently at 3245°C at the stoichiometric composition⁽⁵⁷⁾.

Table 27. Structure and Lattice Parameters of Titanium Borides

Phase	Structure	Lattice Parameters, Å	
		Literature Values	This Investigation
Ti ₂ B*	Tetragonal	a = 6.11 (42, 44) b = 4.56 a = 6.10 or a = 5.24 c = 4.53 or c = 7.602 ⁽⁴³⁾	Not confirmed
TiB**	F.C.C. B3 ⁽¹³⁾ , B1	a = 4.21 (40) a = 4.24 (42) a = 4.26 (43)	Not confirmed
TiB	Orthorhomb. B27-Type(FeB)	a = 6.12 b = 3.06 (38) c = 4.56	a = 6.10 ± 0.03 b = 3.06 ± 0.01 c = 4.56 ± 0.01
TiB ₂	Hexag. C32- Type	a = 3.02 (40) c = 3.21 a = 3.028 (18, 30, 31) c = 3.228	a = 3.032 c = 3.225
Ti ₂ B ₅	Hexag. B8 ₅ -Type (W ₂ B ₅) ^h	a = 2.98 (41, 42) b = 13.98	Not confirmed
TiB _{~10}	n.d.	(47)	Not confirmed

* Previous observations probably refer to TiB (B27)

** Probably (O, N, C)-stabilized impurity phases

ZrB₁₂ has a face-centered cubic, D2_f (UB₁₂)-type of structure with a = 7.408 Å. The phase is stable at high temperatures only⁽⁵⁶⁾, and decomposes in a comparatively rapid solid state (eutectoid) reaction below 1710°C into diboride and boron⁽⁵⁷⁾. F.W. Glaser and B. Post⁽⁵³⁾ as well as W. Schedler⁽⁵⁸⁾ observed maximum melting of the dodecaboride at approximately 2680°C; however, more recent investigations in this laboratory⁽⁵⁷⁾ indicate the phase to decompose peritectically at temperatures around 2250°C.

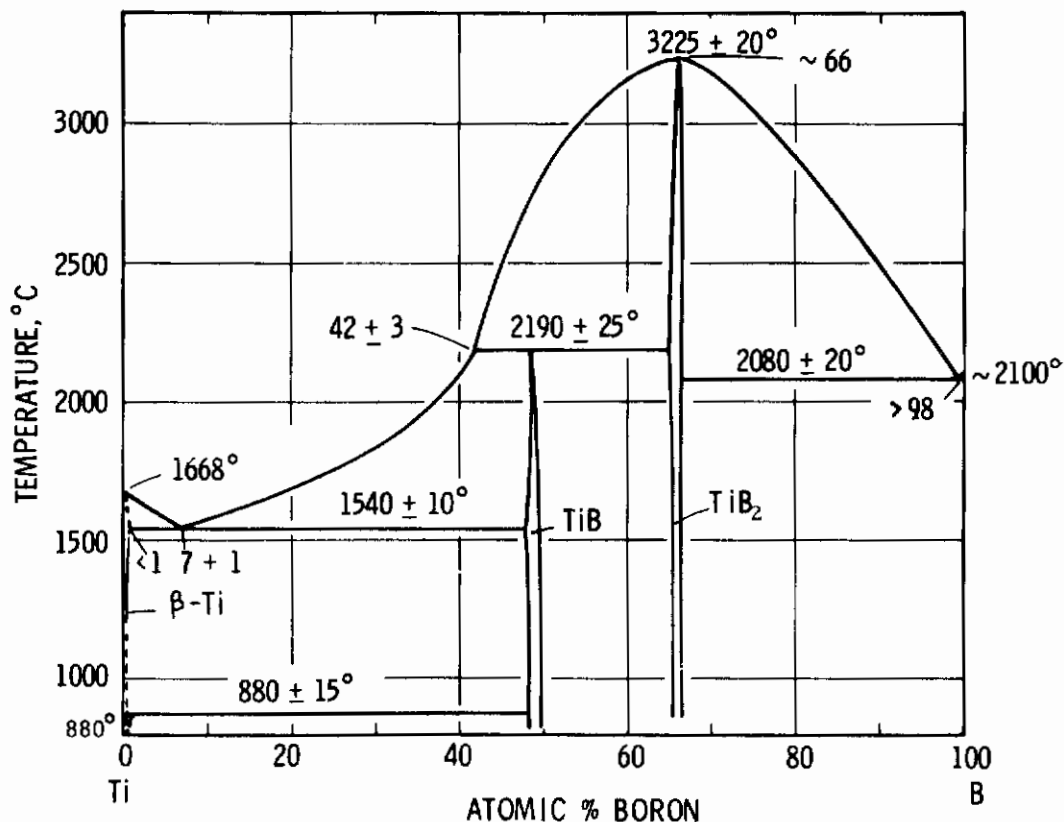


Figure 22. Constitution Diagram Titanium-Boron.

(E. Rudy and St. Windisch, 1966)

A previously claimed, face-centered cubic, monoboride with a $\sim 4.65 \text{ \AA}$ (42, 53, 56, 58), has been identified as oxygen (nitrogen-carbon)-stabilized impurity phases (46, 54, 59). Similarly, previously observed high boron solubilities in zirconium (58) are probably associated with nitrogen or oxygen contamination of the alloys. The boron solubility in zirconium is less than two atomic percent (54, 57, 60), and the α - β -reaction temperature, observed in excess diboride-containing alloys (880°C), is only slightly higher than the transformation temperature in pure zirconium ($T_{\alpha \rightarrow \beta} = 865^\circ$ (61), 872° (57)). ZrB₂ and β -Zr form a eutectic at 12 At.% and 1660°C; the boron-rich eutectic, formed between ZrB₁₂ and boron, is located at $\sim 98\%$ and a temperature of $\sim 2000^\circ\text{C}$ (57).

Lattice parameter and structure data of zirconium borides are summarized in Table 28.

Table 28. Structure and Lattice Parameters of Zirconium Borides

Phase	Structure	Lattice Parameters, Å	
		Literature Data	This Investigation
ZrB*	fcc., B1-type	a = 4.65 ± 0.03 (53)	Not confirmed
ZrB ₂	hex., C32-type (AlB ₂)	a = 3.169 (54) c = 3.530 (54) a = 3.170 (41, 62) c = 3.533 (41, 62) a = 3.168 ± 0.002 (55) c = 3.528 ± 0.002 (55) a = 3.167 (59) c = 3.530 (59)	a = 3.167 ± 0.002 Å c = 3.530 ± 0.001 Å
ZrB ₁₂	fcc, D2 _f -type	a = 7.408 (56) a = 7.408 (59)	a = 7.408 Å

*Probably Zr (N, O, C) Solid Solution

6. Hafnium-Boron

Two intermediate phases, a very refractory diboride, and an incongruently melting monoboride, occur in the alloy system (Figure 24). Both phases form at the stoichiometric composition, and their homogeneity ranges are small.

Hafnium diboride, isomorphous with the other diborides of the group IV, V, and VI refractory transition metal diborides, has a hexagonal, C32-type, of crystal structure, with a = 3.141 Å, and c = 3.470 Å⁽⁶³⁾ (Table 29). Reported melting temperatures for this phase include: ~3100°C^(22, 52) 3240°C⁽⁶³⁾, 3060°C⁽⁶⁴⁾; maximum melting at 3380 ± 20°C at the stoichiometric composition was determined in this laboratory⁽⁶⁵⁾.

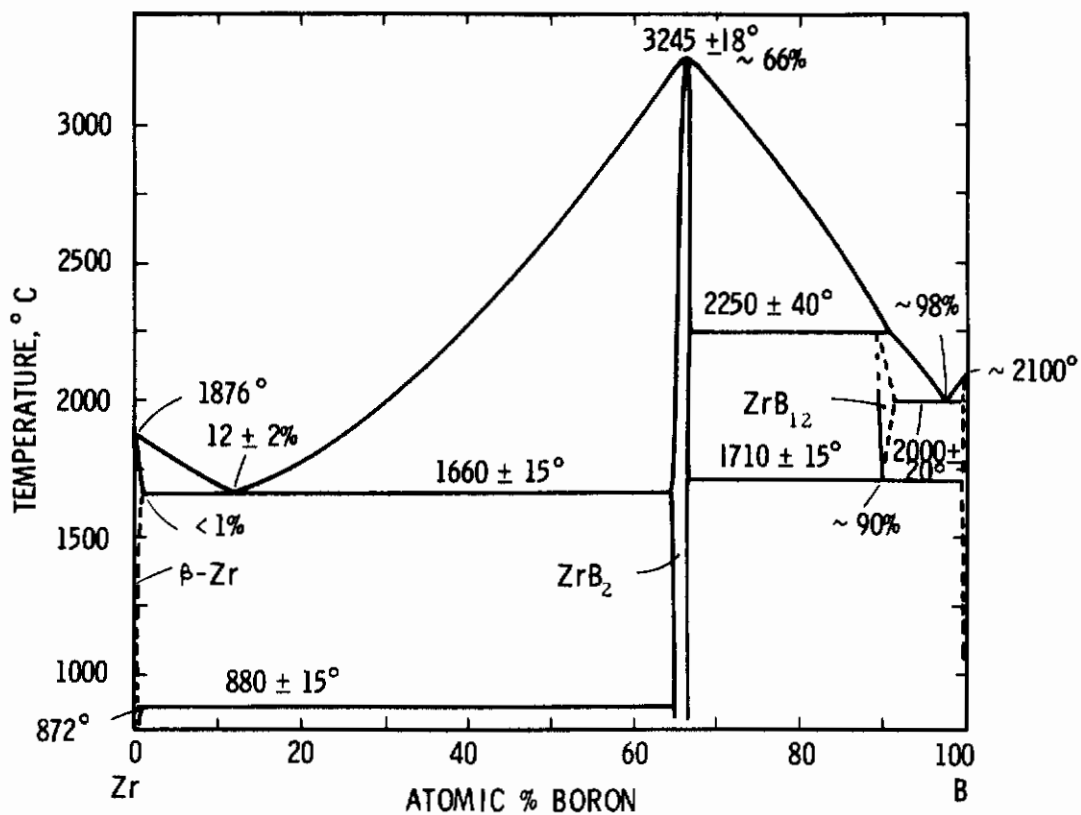


Figure 23. Constitution Diagram Zirconium-Boron.
(E. Rudy and St. Windisch, 1966).

Table 29. Structure and Lattice Parameters of Hafnium Borides

Phase	Structure	Lattice Parameters, Å	
		Literature Values	This Investigation
HfB*	Cubic, B1	4.62 (63)	Not confirmed
HfB	Orthorhombic B27-type(FeB)	a = 6.517 Å b = 3.218 Å (59, 66) c = 4.919 Å	a = 6.517 Å b = 3.218 Å c = 4.920 Å
HfB ₂	Hexag. C32-type (AlB ₂)	a = 3.141 Å c = 3.470 Å (63)	a = 3.142 Å c = 3.477 Å (Hf _{0.96} Zr _{0.04} B ₂)

*Probably Impurity Phases Hf (N, O, B, C).

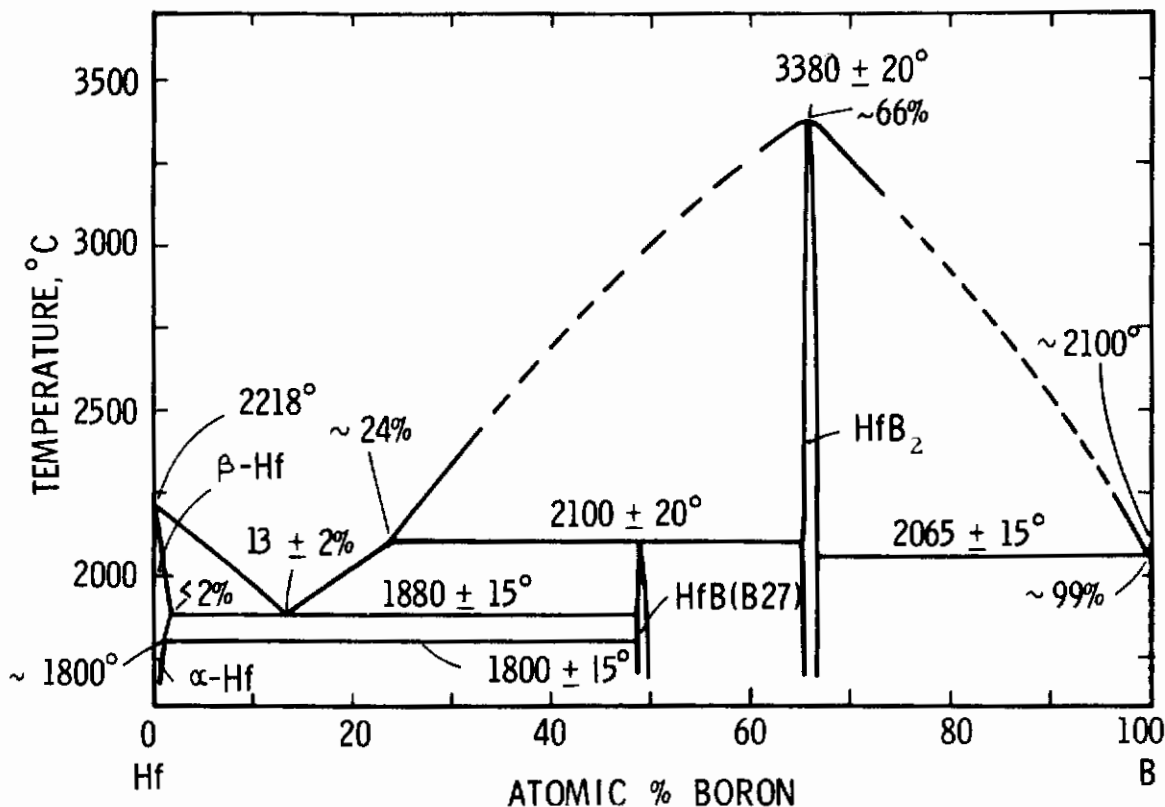


Figure 24. Constitution Diagram Hafnium - Boron.
(E. Rudy and St. Windisch, 1966)

Hafnium monoboride has an orthorhombic, B27-type, of structure, with $a = 6.517 \text{ \AA}$, $b = 3.218 \text{ \AA}$, and $c = 4.919 \text{ \AA}$ ⁽⁵⁹⁾ (Table 29). The phase decomposes in a peritectic reaction at 2100°C into diboride and melt, and also seems to become unstable with respect to mixtures of α -Hf and HfB₂ at temperatures below 1250°C⁽⁶⁵⁾.

A previously claimed face-centered cubic monoboride⁽⁶³⁾ was attributed as being the result of interstitial contamination (O, N, C) of the alloys⁽⁵⁹⁾. The boron solubility in β -hafnium at 1880°C, the eutectic temperature between β -Hf and HfB, is less than two atomic percent, and the α - β -transformation in hafnium remains nearly unaffected by boron additions⁽⁶⁵⁾.

On the boron-rich side, a eutectic equilibrium at $\sim 2100^{\circ}\text{C}$ is formed; the eutectic point is located very close to pure boron (Figure 24).

7. Boron-Carbon

Considerable controversies still exist about the phase relations⁽⁶⁷⁻⁷⁴⁾, as well as the number of phases⁽⁷⁵⁻⁸⁰⁾ existing in the boron-carbon system. The diagram, which seems to have the best experimental foundation is due to R. P. Elliott⁽⁷³⁾ (Figure 25). With the exception of the low temperature homogeneity range for boron carbide, it is very similar to the diagram proposed earlier by R. T. Dolloff⁽⁷²⁾ (Figure 26). While the above

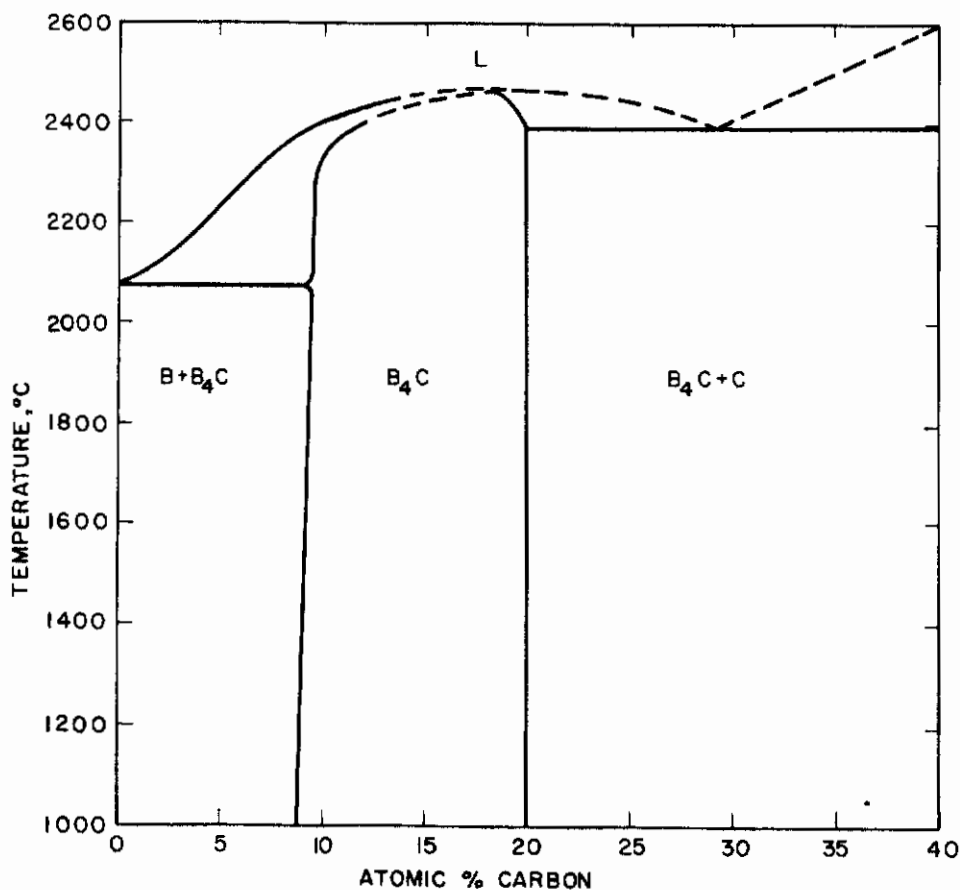


Figure 25. Phase Diagram Boron-Carbon.

(R.P. Elliott, 1961).

investigations as well as other results from previous work^(67, 78, 79, 81) suggest the existence of a single intermediate phase only, based on differences in physical properties, G. V. Samsonov, et al.⁽⁶⁹⁾ concluded, that $B_{12}C_3$ and $B_{13}C_2$ exist as distinct phases. He also indicates the probable occurrence of a third compound B_1C in the boron-rich region of the system⁽⁷¹⁾.

The possibility for the occurrence of multiple stoichiometries within the same structural framework, where more than one interstitial opening is available, has been discussed in detail by J. Economy, et al.⁽⁸²⁾ on the example of boron-carbon (P, As, O, S, Si) phases. The rhombohedral structure of α -boron, containing the boron atoms in icosahedral groupings at the vertices of the unit cell, allows for three interstitial sites along the three-fold axis of the unit cell, with the center site(lb) not being crystallographically

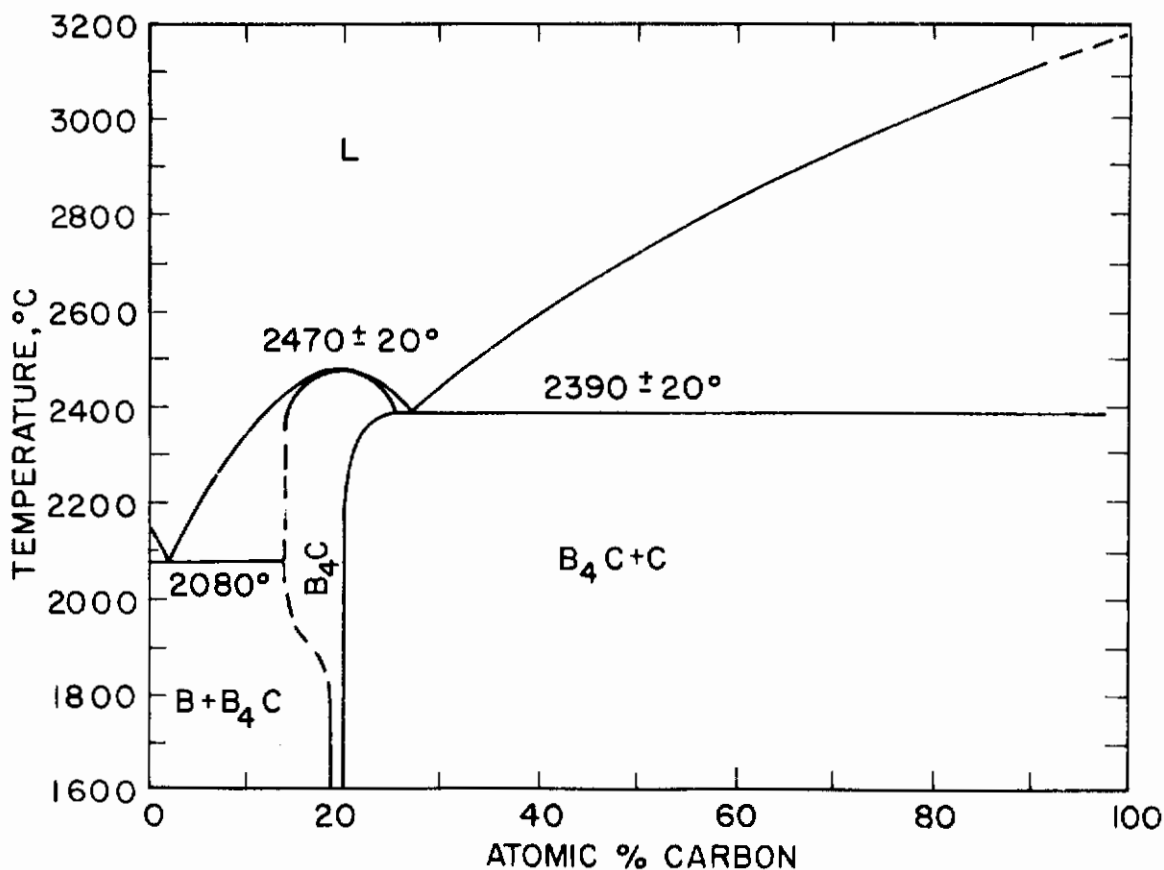
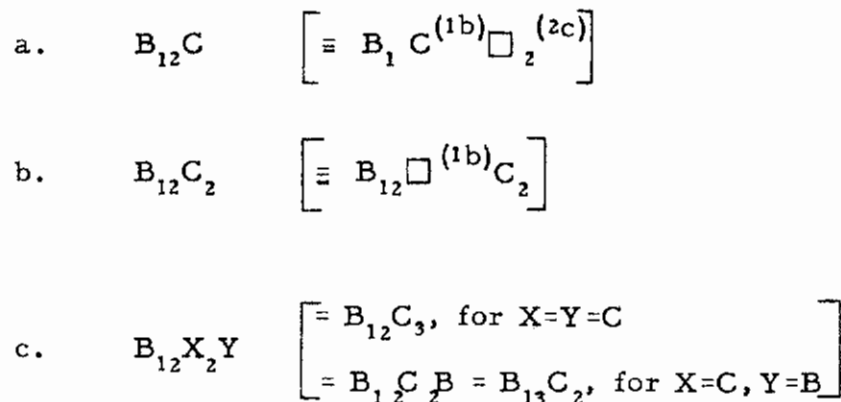


Figure 26. Phase Diagram Boron-Carbon.
(R. T. Doloff, 1960)

Contrails

equivalent to the (identical two) outer sites (2c). Hence, by selected filling of these interstitial lattice sites, and without considering substitutions in the boron frame lattice, three types of stoichiometries could be derived:



\square = Vacant site

Although this classification cannot be regarded as more than an expression for the inequality of the available lattice sites, it does indicate the possibility for a bifurcation of the phase as a result of the rapid change of the distribution equilibria, and hence the positional free energies, with temperature⁽⁸⁴⁾. Since the larger boron atoms may substitute for carbon in the (1b) portion, the free energy differences between the interstitial lattice sites, which in turn are responsible for the relative occupation density, cannot be very large. Thus, one would suspect, that ordering on the two interstitial sublattice systems would occur at comparatively lower temperatures. Phase-separation reactions necessarily are diffusion-controlled nucleation and growth processes; it is therefore possible, that differences in the thermal histories of the specimens studied by the various investigators, may to a part be made responsible for the observed differences. Apparently more work, especially detailed studies of the temperature-dependence of sublattice partition equilibria, will be required for a final clarification of the problem.

B. TERNARY SYSTEMS

1. Titanium-Boron-Carbon

According to H.M. Greenhouse, et al.⁽⁴⁷⁾, mixtures of B_4C and TiC react at high temperatures to form TiB_2 and free graphite; the existence of the equilibrium TiB_2-C was also verified in work by F.W. Glaser⁽⁴⁴⁾. According to W.J. Engel⁽⁸⁵⁾ and C. G. Goetzel⁽⁸⁶⁾, titanium diboride is stable in the presence of boron carbide, and the existence of a eutectic (30 mole % TiB_2 , 1900°C) between these phases was claimed by K.I. Portnoi, et.al.⁽⁸⁷⁾. The existence of a eutectic-type pseudobinary section $TiC-TiB_2$, seems to be well established from the work by G.A. Geach and F.O. Jones⁽⁸⁸⁾, and by G. V. Samsonov⁽⁸⁹⁾. Complete solid solution formation between TiB and TiC ,⁽⁸⁹⁾ as well as the high solubility of TiB_2 in TiC (20 mole %) claimed by G.V. Samsonov,⁽⁸⁹⁾ were not confirmed in later investigations by H. Nowotny, et al.⁽⁹⁰⁾ (Figure 27).

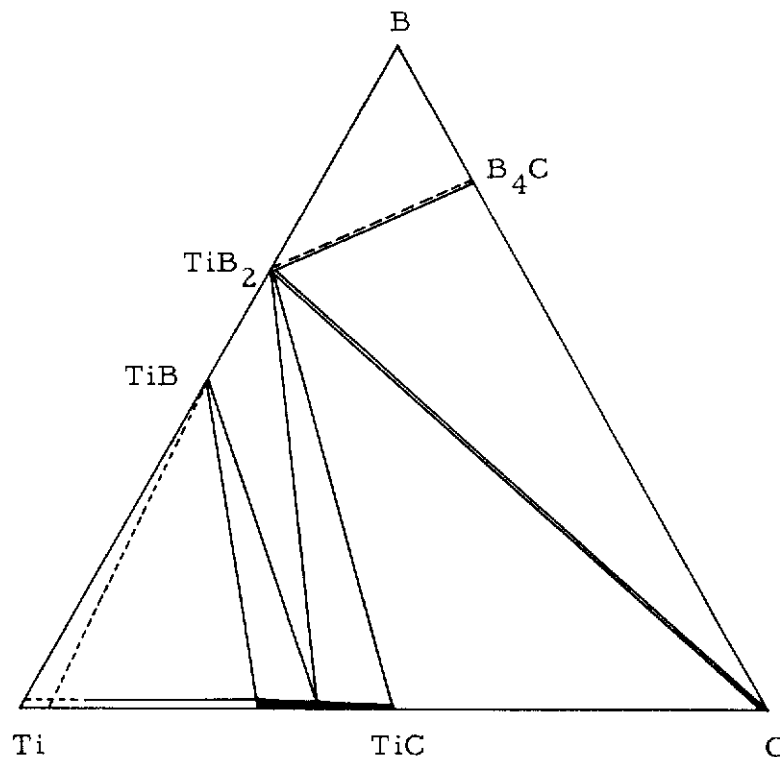


Figure 27. Section of the Phase Diagram Ti-B-C at 1500°C.
(H. Nowotny, F. Benesovsky, C. Brukl, and O. Schob, 1961)

2. Zirconium-Boron-Carbon

The existence of the equilibrium pairs ZrB_2 - B_4C , and ZrB_2 -C has been established by the work of F. W. Glaser⁽⁴⁴⁾, and by L. Brewer and H. Haroldsen⁽⁹¹⁾; ZrB and ZrB_{12} were said to be unstable in the presence of carbon⁽⁴⁴⁾, however, based on extended investigations, G. V. Samsonov⁽⁸⁹⁾ concludes, that the monoboride and the monocarbide form a continuous series of solid solutions. An investigation of a system reaction by H. Nowotny, et al.⁽¹⁾ (Figure 28) shows the equilibria ZrB_2 - B_4C , ZrB_2 -C and ZrB_2 - ZrC , and only very restricted mutual solubilities of the phases; ZrB_{12} does not appear at the chosen equilibrium temperature. Based on metallographic work, the latter authors further conclude, that ZrB_2 forms eutectic-type, pseudobinary equilibria with ZrC , B_4C , and graphite.

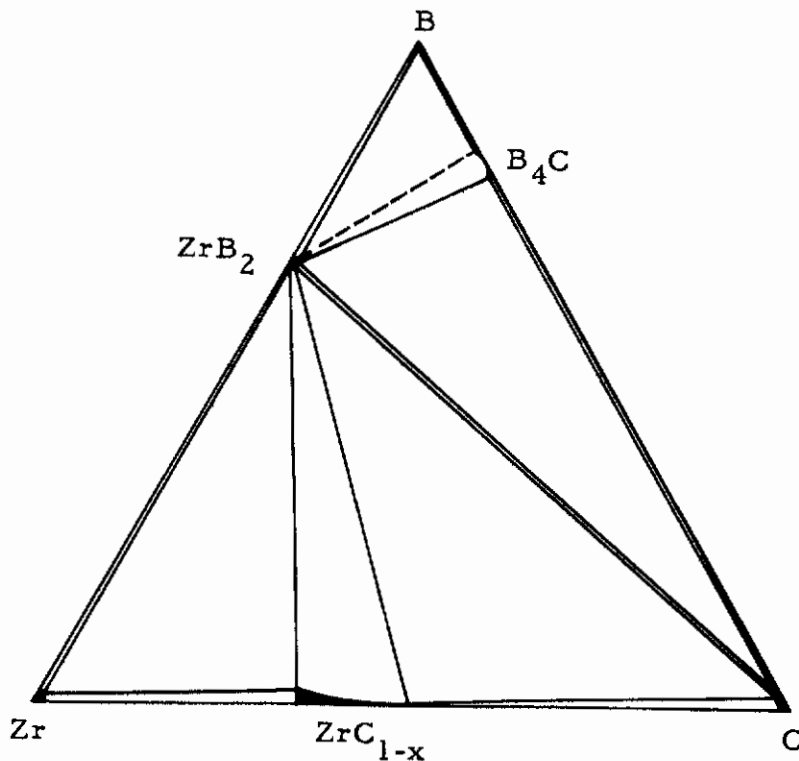


Figure 28. Section of the Phase Diagram Zr-B-C at 1400°C.

(H. Nowotny, E. Rudy, and F. Benesovsky, 1961)

3. Hafnium-Boron-Carbon

An isothermal section of the system at 1500°C was determined by H. Nowotny and co-workers⁽¹⁾ (Figure 29). According to these investigations, the diboride forms two-phase equilibria with the monocarbide, graphite, and B_4C , and the monocarbide dissolves up to ~10 mole % HfB. While, at lower temperatures, hafnium monoboride forms an equilibrium with the monocarbide at high temperatures, the metal-rich portion of the system is dominated by the diboride and monocarbide phases.

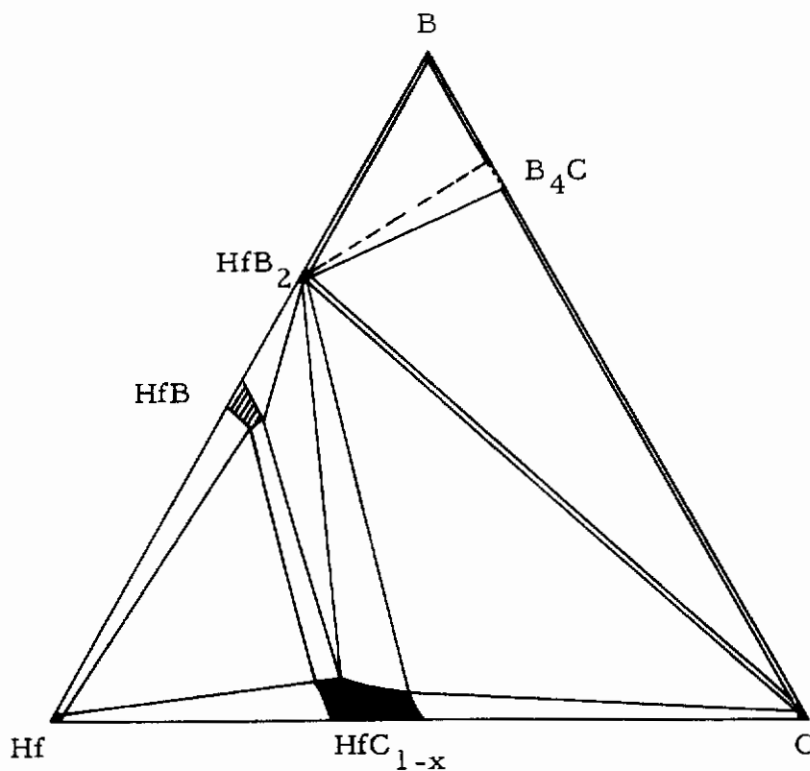


Figure 29. Section of the Phase Diagram Hf-B-C at 1500°C.

(H. Nowotny, E. Rudy, and F. Benesovsky, 1961)

III. EXPERIMENTAL PROGRAM

A. STARTING MATERIALS

The elemental powders, as well as prealloyed monocarbides and diborides served as the starting materials for the preparation of the experimental alloy material.

1. Titanium was purchased in powder form from Var-Lac-Oid Chemical Company. It had the following impurities (contents in ppm): C-1300, H-1500, N-50, Fe-500, and O-200. Lattice parameters of $a = 2.94_9 \text{ \AA}$, $c = 4.68_8 \text{ \AA}$, which were obtained from a Debye-Scherrer pattern with CuK_α radiation, are in reasonable agreement with literature data ($a = 2.950 \text{ \AA}$; $c = 4.6833 \text{ \AA}$)⁽⁹²⁾.

2. Hafnium sponge and hafnium metal powder ($<120\mu$) were purchased from Wah Chang Corporation, Albany, Oregon. The analysis of the powder was as follows (contents in ppm): Al-20, C-210, Nb-680 (<1000)^{*}, Cr- <20 , Cu-40, Fe-265, H-55, Mo-40, N-200 (<300), O-810 (<1000), Si- <40 (10), Ta- <200 (400), Ti-20, W-235, sum of all other impurities- <100 . The hafnium powder, which also contained 4.1 atomic percent zirconium, had lattice parameters of $a = 3.19_6 \text{ \AA}$; $c = 5.05_7 \text{ \AA}$; these values are in close agreement with literature data of $a = 3.194$ to $a = 3.199 \text{ \AA}$, and $c = 5.0510$ to $c = 5.062 \text{ \AA}$ ⁽⁹²⁾.

The hafnium sponge had the following impurities (contents in ppm): Al-94, Cu- <40 , Fe-185, Cl-100, Mg-450, N-30, O-680, Si- <40 , Ti-250, W- <7 . The zirconium content of the sponge was 4 atomic percent. Data from a DTA-analysis of this starting material, which yielded apparent α - β -transformation temperatures of 1770°C and 1800°C for the arc molten metal powder and the sponge hafnium, respectively, are compatible with the values to be expected from the combined interstitial impurity contents⁽⁹³⁾.

*The bracketed figures refer to data obtained from a control analysis performed by the staff of the Quality Control Laboratory at Aerojet-General Corporation.

Contrails

3. Zirconium and zirconium dihydride were purchased as powders from Wah Chang Corporation, Albany, Oregon. The impurity contents in zirconium were as follows (contents in ppm): C-40, Fe-315, Hf-67, O-839, Ta-<400, sum of all other impurities-<460. A comparative DTA-analysis, carried out between crystal-bar zirconium and the above raw material, yielded identical α - β -transformation temperatures of $872 \pm 15^\circ\text{C}$ (literature value: 865° ⁽⁶¹⁾). The lattice parameters were measured $a = 3.232 \text{ \AA}$, and $c = 5.149 \text{ \AA}$.

The analysis supplied for zirconium dihydride was (contents in ppm, unless stated otherwise): H-2.1 Wt.%, C-320, Cu-125, Fe-1800, Hf-137, Mg-255, N-116, O-1300, Si-157, Ta-<200, sum of others-<405.

4. The titanium monocarbide powder (Var-Lac-Oid Chemical Company), with a particle size of $<80\mu$, had an analyzed carbon content of 19.50 Wt.% (49.40 At.%), of which 0.20 Wt.% (0.5 At.%) were present elemental graphite. The following analysis, which largely was confirmed by a semi-quantitative spectrographic analysis carried out in this laboratory, was submitted by the supplier (impurity contents in weight percent): Fe-0.05, Si-0.01, Ca-0.01, Na-0.005, O-0.15. The lattice parameter of the as-received powder was $a = 4.323 \text{ \AA}$.

5. Zirconium monocarbide was purchased as $<44\mu$ powder from Wah Chang Corporation, Albany, Oregon. The carbide had a total carbon content of 11.54 Wt.% and a lattice parameter of $a = 4.698 \text{ \AA}$ were measured for the as-received powder. The impurity contents were as follows (in ppm): Nb-<100, Hf-40, N-1100, O-1040, Ta-<200, sum of all others-<400.

6. Titanium diboride was prepared by direct combination of the elements at high temperatures. In order to circumvent difficulties arising from the violent reaction in the formation of the diboride, a master alloy containing 85 atomic percent boron was prepared first. This intermediate product was then comminuted, the necessary amount of zirconium powder admixed, and again reacted for 2 hours at 1800° to 2000°C under a high purity helium atmosphere. After cooling under vacuum, and discarding of the zones

adjacent to the tantalum container, the reaction lumps were crushed and comminuted in carbide-lined ball mill jars to a particle size smaller than 60μ . Cobalt traces, which were picked up during grinding, were removed by an acid-leach in an 8N mixture of hydrochloric and sulfuric acid.

The chemical analysis of the diboride gave a boron content of 65.3 ± 0.3 At.%; the powder also contained 0.088 Wt.% carbon. Roentgenographically, only the diboride was detected ($a = 3.032 \text{ \AA}$, $c = 3.224 \text{ \AA}$), while metallographic inspection also revealed the presence of small amounts of excess monoboride.

7. Zirconium diboride was prepared in the same way as titanium diboride. The acid-leached and vacuum-dried powder had a total boron content of 65.2 atomic percent, and contained also 0.11 Wt.% carbon. A semiquantitative spectrographic analysis showed the following impurity concentrations (in ppm): Fe-<300, Si-100, Mg-<100, Ca-<100, Co-not detected, Cu + Ni + Mn-<100, Cr-not detected, Mo-<100, Ti-200, V, W, and Ta-not detected. Roentgenographically, the product was single phased ($a = 3.167 \text{ \AA}$, $c = 3.530 \text{ \AA}$), but a metallographic inspection showed the presence of small amounts of excess metal phase.

8. The preparation of hafnium diboride was analogously to the procedures described for titanium diboride. The chemical analysis of the diboride, which contained metallographically detectable quantities of monoboride, gave an average boron content of 65.0 ± 0.3 atomic percent. Carbon was present in a quantity of less than 0.020 Wt.%, and the sum of oxygen, nitrogen, and hydrogen was below 200 ppm. A semiquantitative spectrographic analysis showed the following additional impurities to be present (in ppm): Fe-<200, Si-<200, Mg-<100, Ca-<500, Co + Ni + Mn + Cr + Mo-<100, Ti-300; V, W, Ta, and Nb were below the detectable limit. The lattice parameters, obtained from a Debye-Scherrer pattern with Cu-K $_{\alpha}$ radiation, were $a = 3.142 \text{ \AA}$, and $c = 3.477 \text{ \AA}$.

9. The spectrographic grade graphite powder (Union Carbide Corporation, Carbon Products Division) had the following analysis (contents

in ppm): Sum of metallic impurities (Al + Cu + Mg + Si + Fe), and sulfur - <100, ash - <500 ppm, volatile matter - 100 ppm. No second phase impurities were detected in strongly overexposed X-ray powder diffraction patterns, and the unit cell dimensions measured, $a = 2.463 \text{ \AA}$, and $c = 6.729 \text{ \AA}$, compare reasonably well with literature values of $a = 2.461 \text{ \AA}$, and $c = 6.708 \text{ \AA}$ ⁽⁹²⁾.

10. Boron powder with a purity of better than 99.55% was purchased from United Mineral and Chemical Corporation, New York. Major impurities were 0.25 Wt.% iron and 0.1 Wt.% carbon.

B. ALLOY PREPARATION AND HEAT TREATMENT

The majority of the specimens for the X-ray, DTA, melting point, and metallographic investigations were prepared by short-duration hot-pressing ⁽⁸⁴⁾ of the well-blended ingredient mixtures in graphite dies. After hot-pressing, the surface reaction zones were removed by grinding and the samples subjected to the further homogenization treatments.

Selected alloys from the very metal-rich region ($C + B < 15 \text{ At.}\%$) in each system, specifically intended for melting point and DTA-studies, were electron-beam-(Heraeus gun ES 2/4) or arc-melted prior to the runs.

The lower-temperature homogenization treatments were carried out in a tungsten-mesh element furnace (R. Brew Company) under a vacuum of better than 5×10^{-5} Torr. Equilibrations above 1600°C were either run under a high purity helium atmosphere in the above furnace, or were carried out in the Pirani melting point furnace ⁽⁸⁴⁾. The main equilibration treatments for the three borocarbide systems are summarized in Table 30. Additional treatments, carried out on selected specimens to study the temperature dependence of certain equilibria, are not included, but will be referred to later in the text. Wherever necessary, rapid quenching conditions were achieved by dropping the sample, after equilibration at the desired temperature in the Pirani furnace, directly into a preheated ($\sim 300^\circ\text{C}$) tin bath.

Table 30. Solid State Homogenization Treatments for Ti-B-C, Zr-B-C, and Hf-B-C Alloys

Alloys from the Concentration Range	Annealing Conditions		
	Temperature °C	Duration hrs.	Atmosphere
Ti-B-C	1400	68	Vac, 2×10^{-5} Torr
TiB ₂ -TiC _{1-x} -C-B	1750	12	1.05 atm. He
Zr-B-C	1400°	92	Vac, 2×10^{-5} Torr
ZrB ₂ -ZrC _{1-x} -C-B	1750°	12	1.05 atm. He
ZrB ₂ -B ₄ C-B (rapid quenched)	1900°	12	2 atm. He
Hf-B-C	1400°	92	Vac, 2×10^{-5} Torr
HfB ₂ -HfC _{1-x} -C-B	1750°	12	1.0 atm. He
HfC +5 At.% B	2000°	2	1.05 atm. He
Hf-Hf _{0.8} C _{0.2} -Hf _{0.8} B _{0.2}	melted + 1750°	1-3 hrs	Vac, 2×10^{-5} Torr

A total of approximately 200 alloys were prepared for each alloy system and evaluated. About one-third of the alloy specimens were analyzed for their boron and carbon contents after the runs, and check analyses for oxygen and nitrogen were performed on the specimens in the various stages of preparation, in order to assure the integrity of the experimental alloy material. In general, the latter impurities were present in concentrations less than 250 ppm. It was assumed, that these low impurity contents will have no measurable effect upon the observed phase relationships, and hence were disregarded in the experimental interpretation of the results.

With the exception of the melting point alloys, which were located close to the extremely high melting hafnium monocarbide phase and showed boron losses of up to 2 atomic percent during melting, the

concentration stability of the alloys usually was better than one atomic percent with regard to the weighed-in compositions.

C. MELTING TEMPERATURES

The melting temperatures of the alloys were determined with the previously described Pirani-technique^(84, 94). In this method, a small sample bar with a black body hole of ~ 0.6 mm diameter, drilled or pressed into the center of the specimen; is heated resistively between two water-cooled copper electrodes to the temperature of the phase change. The temperature is measured pyrooptically with a disappearing filament-type pyrometer through a quartz window in the chamber wall of the furnace. Pyrometer calibration, and the relations between black body hole geometry and apparent hole emissivities, have been described in a previous report⁽⁸⁴⁾. The temperature correction chart, which was computed from these data, is shown in Figure 30. For the measurements on Me-B-C alloys, the temperature correction for graphite-free specimens were based on an average emissivity coefficient of $\epsilon = 0.985$. The temperature figures for samples containing more than 20 volume percent elemental carbon were corrected according to an apparent emissivity of $\epsilon = 0.995$.

With the exception of metal-rich alloys, (<20 At. B-element) which also were run under vacuum, the majority of the melting point runs were carried out under a high purity helium atmosphere of 2.5 atmospheres pressure, in order to reduce concentration shifts due to preferential vaporization of the alloy components. The precision of the temperature measurements, in terms of the mean deviation in the individual measurements, was usually better than $\pm 10^\circ\text{C}$ for isothermally or nearly-isothermally melting alloys. Larger scatters were encountered in extremely two-phased melting alloys, and incipient melting in alloys located close to one of the boundary phases usually was difficult to observe; however, since the temperatures for the reaction isotherms were derived from the measurements on alloys located closely to the invariant points, these data have no influence on the accuracy of the finally accepted data.

Where interaction with the container was negligible (metal-rich alloys) or immaterial (alloys from the concentration region $\text{MeB}_2\text{-MeC-C}$), independent melting temperature results were obtained from differential-thermoanalytical studies.

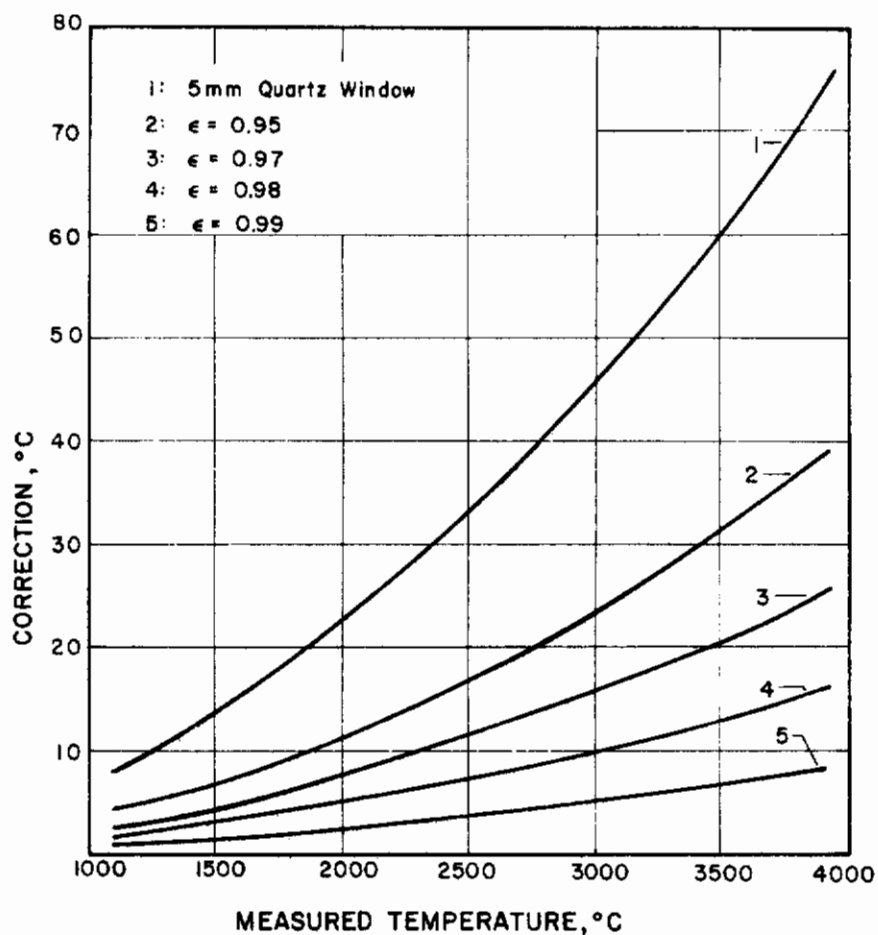


Figure 30. Temperature Correction Chart for the Pirani-Furnace.

The temperature figures, as noted in the figures, refer to the precision of the measurements, and do not include the errors in the pyrometer calibrations. The overall temperature uncertainties can be computed from the relation

$$\bar{\sigma} = \pm \sqrt{\sigma_m^2 + \sigma_c^2}$$

where $\bar{\sigma}$ denotes the overall temperature uncertainty, and σ_m and σ_c stand for the errors in the measurements and the pyrometer calibration, respectively. Representative values for σ_c are $\pm 10^\circ\text{C}$ at 2300°C , $\pm 17^\circ\text{C}$ at 3000°C , and $\pm 30^\circ\text{C}$ (estimated) at 4000°C .

D. DIFFERENTIAL THERMAL ANALYSIS^(84, 95)

DTA-techniques were extensively employed in the course of the investigations of all three systems. They proved to be very useful and for the elucidation of the phase-reaction occurring in the hafnium-corner of the Hf-B-C system and the study of the ternary decomposition of the ZrB_{12} phase; for the determination of the eutectic temperatures in the boron corner of all three systems, differential thermal analysis proved to be a valuable supplemental technique, since the poor electrical conductivity of the specimens usually prevented accurate measurements to be made in the Pirani furnace.

From all container materials tried, graphite ultimately proved to be the best choice, and was exclusively used in the measurements. The maximum temperatures applicable in the experiments are determined by the eutectic temperatures $\text{MeB}_2 + \text{MeC} + \text{graphite}$. Hence, the temperatures to which DTA-investigations could be carried out without serious interaction problems, were limited to approximately 2400°C for the Ti-B-C and Zr-B-C system, and to 2500°C for the Hf-B-C alloys.

Altogether, 47 DTA specimens were prepared in the three alloy systems (Figures 31, 32, and 33), and the results, obtained in multiple runs on each sample, correlated with the data obtained by the other techniques. After the runs, the specimens were sectioned and analyzed by X-ray diffraction and by inspection under the microscope.

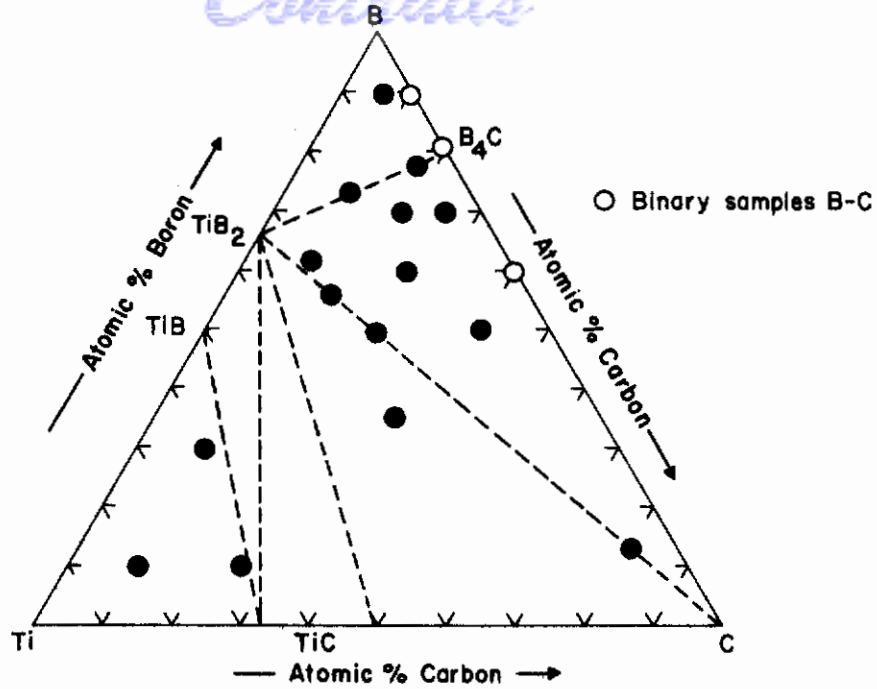


Figure 31. Ti-B-C: Location of Samples Investigated by Differential Thermal Analysis.

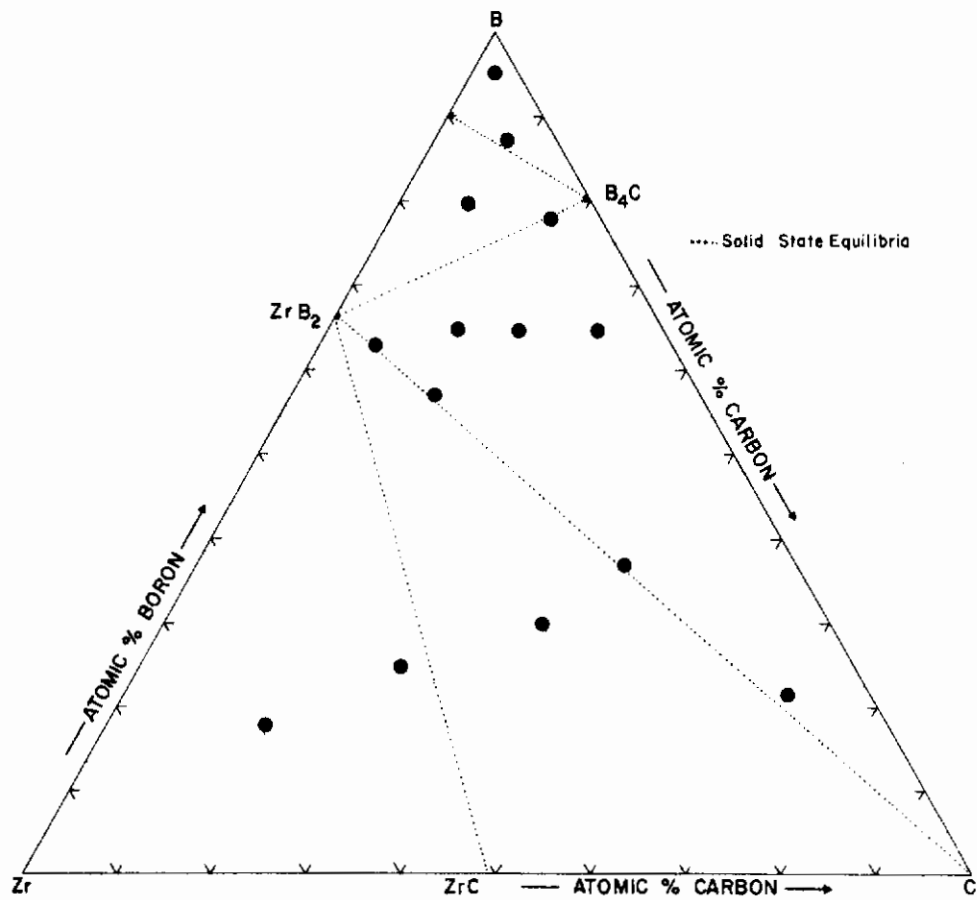


Figure 32. Zr-B-C: Location of Specimens Investigated by Differential Thermal Analysis.

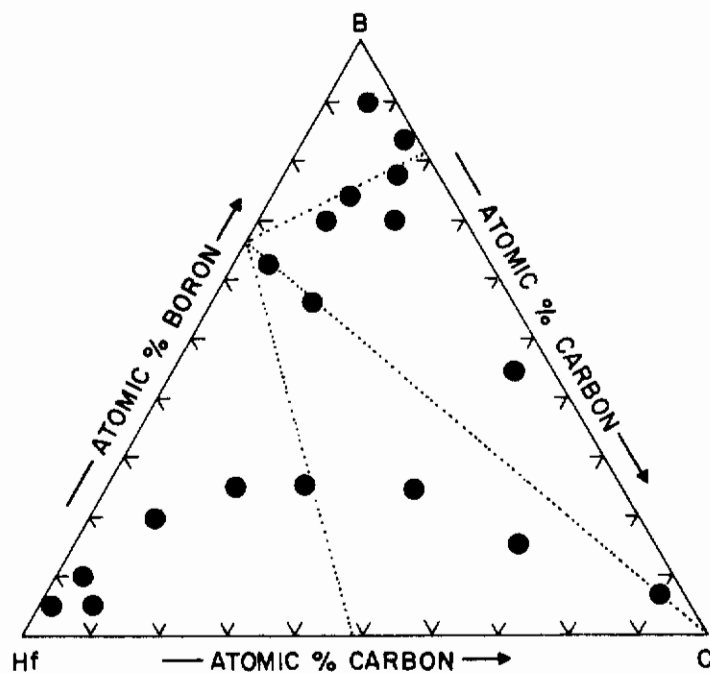


Figure 33. Hf-B-C: Location of Specimens Investigated by Differential Thermal Analysis.

E. METALLOGRAPHY

The specimens were mounted in a combination of diallyl-phthalate and lucite-coated copper powder such, that an electrically conductive path (for electroetching) was provided from the back of the mount to the sample surface. After coarse grinding on silicon carbide paper with grit sizes varying between 120 and 600, the samples were mechano-chemically polished. Polishing as well as etching procedures varied with the phases present in the alloys (Table 30). Excess metal-containing alloys from all three systems were electro-etched in 10% aqueous oxalic acid solution. The anodic oxidation provided excellent phase contrast. The metal phases usually appeared as light blue, whereas the monoborides assumed a brown color. The diboride phases remained unaffected by the anodization treatment. Usually, no etching was required for excess graphite, B_4C , or boron-containing alloys; however, in order to reveal the substructures present in certain phase components,

addition of 5% chromic acid-solution to the polishing agents proved to be advantageous. The microscopic examinations were made, and the exposures taken, on a Zeiss Ultraphot II metallograph, using contrast process Ortho film by Kodak.

Table 31. Etching Procedures for Group IV Metal-Boron-Carbon Alloys.

a. Ti-B-C Alloys

Alloys from the Concentration Range	Etchant and Procedure
Ti-Ti _{0.7} C _{0.3} -Ti _{0.5} C _{0.2} B _{0.3} -Ti _{0.7} B _{0.3}	10% oxalic acid, electroetch
Ti _{0.7} C _{0.3} -Ti _{0.5} C _{0.2} B _{0.3} -C _{0.7} B _{0.3}	1% Aqua Regia + Hf, dip-etch
Ti _{0.7} B _{0.3} -Ti _{0.2} B _{0.3} C _{0.5} -Ti _{0.2} B _{0.5} C _{0.3} -Ti _{0.5} B _{0.5}	Pre-polish and etch with Murakami's, followed by dip-etching in 1% Aqua Regia + Hf
Other	Polish and etch: Slurry of Linde "A" alumina in 5% chromic acid solution.
b. Zr-B-C Alloys	
Zr-Zr _{0.6} C _{0.4} -Zr _{0.40} B _{0.50}	10% oxalic acid, electroetch
Zr _{0.6} C _{0.4} -Zr _{0.4} B _{0.6} -Zr _{0.3} B _{0.7} -Zr _{0.2} C _{0.8}	10% Aqua Regia + Hf, dip-etch
Other	Polish and etch: Slurry of Linde "A" alumina in 5% chromic acid solution.
c. Hf-B-C	
Hf-Hf _{0.7} C _{0.3} -Hf _{0.4} B _{0.3} C _{0.3} -Hf _{0.3} B _{0.7}	10% oxalic acid, electroetch
Hf _{0.7} C _{0.3} -Hf _{0.4} B _{0.3} C _{0.3} -Hf _{0.4} C _{0.}	10% Aqua Regia + Hf, dip-etch
Other	As polished.

F. X-RAY ANALYSIS

X-ray powder patterns with Cu-K_α radiation were prepared from all alloys prepared in the course of the experimental investigations. Powders from specimens, containing excess metal phase, received a stress-annealing treatment at the respective temperatures prior to the exposures, in order to obtain sharp patterns. Excessive back-ground fogging due to fluorescent radiation from titanium-containing alloys was eliminated by using a cover film.

The exposures were made on a 57.4 mm dia powder camera on a Siemens Kristalloflex II unit, and the Bragg angles were measured on a Siemens-Kirem coincidence scale with precision micrometer attachment.

G. CHEMICAL ANALYSIS

Samples were analyzed for free and combined carbon, boron, as well as oxygen and nitrogen contaminants.

Total carbon was determined using the standard combustion technique. Down to carbon contents of 0.1 Wt.% the analyses were carried out in a Leco carbon analyzer; for still lower carbon concentrations, the gas analysis was performed conductometrically. Free carbon was determined in the usual manner by determining the quantity of the graphite residue left after the powdered sample had been dissolved in a mixture of nitric and hydrofluoric acid.

The procedure followed for the boron analysis was in brief as follows: the powdered alloy samples were fused at 1000°C in pre-dried sodium carbonate and the resulting melt-cake dissolved in water. Excess carbonate was precipitated with barium hydroxide and, together with other metal hydroxide precipitates, removed by filtration. The filtrate was then acidified to a pH-value of 5.3 and, after addition of mannitol, titrated differentially with N/10 NaOH between pH 5.3 and 8.5. The consistency of the data obtained by this method varied somewhat with the nature of the phases present in the alloys, but generally was within the limits of ± 0.5 atomic percent boron.

Oxygen and nitrogen were hot-extracted in a gas-fusion analyzer, using a platinum bath. As indicated in Section III-B, the concentrations of these latter impurities did in neither case exceed 250 ppm and hence were disregarded in the final analysis of the experimental data.

IV. RESULTS

A. TITANIUM-BORON-CARBON

1. The Titanium Phase

While the pure metal phase melts at 1668°C, an alloy Ti(94)-B(3)-C(3) atomic percent already collapsed at 1510°C (Table 32). Metallographically, the alloy was three-phased, containing primary crystallized β -Ti (transformed) and monoboride in a matrix of β -Ti + TiB + TiC eutectic. A DTA-run performed on a sample Ti(80)-B(10)-C(10) At.% yielded an apparent α - β -transformation of 890°C, which is higher than that of the pure metal (880°C), but lies between those of the corresponding reaction isotherms in the binary edge systems Ti-B ($T_{tr} \approx 880^\circ\text{C}$), and TiC ($T_{tr} \sim 930^\circ\text{C}$).

2. Phase Equilibria in the Metal-Rich Portion of the System

Melting in the alloys with a total semimetal content of more than 15 atomic percent becomes increasingly heterogeneous. After cooling, the alloys were three-phased, consisting of metal, monocarbide, and monoboride (Figures 34 through 37). The lattice parameters measured for the monoboride ($a = 6.12 \text{ \AA}$; $b = 3.07 \text{ \AA}$; $c = 4.56 \text{ \AA}$) and for the titanium phase ($a = 2.952 \text{ \AA}$; $c = 4.692 \text{ \AA}$), are nearly the same as obtained for the binary phases. Depending upon the quenching conditions, parameters varying between 4.308 and 4.310 \AA were obtained for the monocarbide in three-phased alloys, thus indicating a certain amount of boron substitution in the semimetal sublattice. An average parameter of $a = 4.305 \text{ \AA}$, obtained for the monocarbide phase in the alloys heat-treated at 1400°C (Figure 38), is closer to that of the carbon-deficient binary phase ($a_{\text{TiC}_{1-x}} = 4.304 \text{ \AA}$ at 1490°C; $a_{\text{TiC}_{1-x}} = 4.286 \text{ \AA}$ at 1650°C).

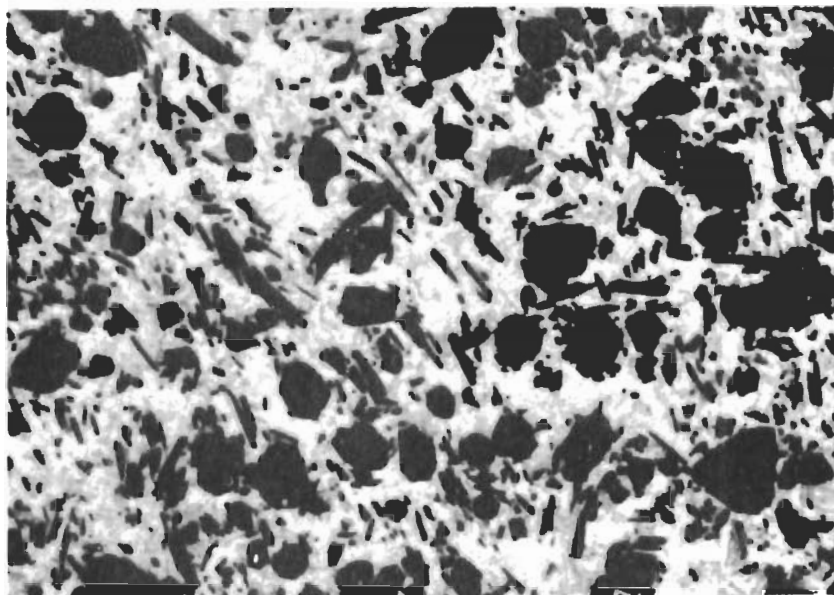


Figure 34. Ti-B-C (84-10-6 At.%), Cooled from 1550°C. X950
Monocarbide (Dark Equiaxed Grains) and Monoboride in
a Matrix of Transformed β -Ti (Light).

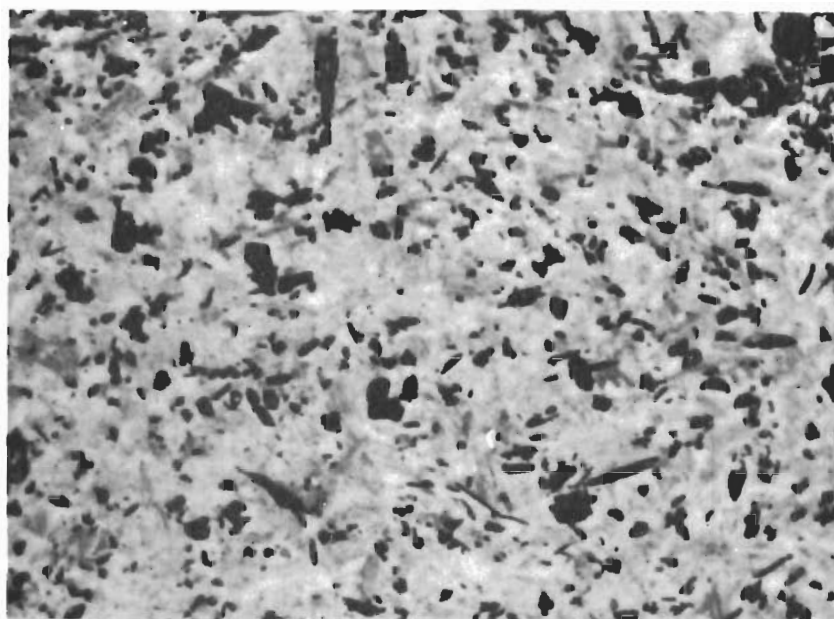


Figure 35. Ti-B-C (90-6-4 At.%), Cooled at Approximately X1000
15°C per Second from 1515°C.
Traces of Primary Monocarbide in a Partially Annealed
Eutectic Matrix.

Table 32. Melting Temperatures and Phase Evaluation of Titanium-Boron-Carbon Alloys

Composition At. %				Observed Melting Temperatures, °C			Phases Present After Melting		
No	Ti	B	C	Incipient	Collapse	Melting	Phases	X-ray Lattice Parameters	Metallography
1	94	3	3	1510°	1510° ↓	sharp	$\alpha + \gamma + \rho$	n.d.	β (prim.) + eutectic
2	85	5	10	1512°	1590° ↓	heterogeneous	$\alpha + \gamma + \rho$	n.d.	ρ (prim.) + eutectic
3	84	10	6	1510°	1550° ↓	sl. heterog.	$\alpha + \gamma + \rho$	n.d.	ρ (prim.) + eutectic
4	75	10	15	1515°	1705° ↓	heterogeneous	$\alpha + \gamma + \rho$	a = 2.952 c = 4.692	ρ (prim.) + bivar. eutec
5	63	10	27	2160°	2333° ↓	very heterog	$\rho + \text{trace } \delta$	ρ : a = 4.311	$\rho + \delta + \text{trace } \beta$
6	73	20	7	1518°	1580° ↓	heterogeneous	$\alpha + \gamma + \rho$	a = 6.12 γ : b = 3.072 c = 4.56	$\rho + \gamma$ (prim) + eutectic
7	64	29	7	1530°	1600° ↓	heterogeneous	$\alpha + \gamma + \rho$	a = 6.11 γ : b = 3.07 c = 4.56	$\beta + \rho + \gamma$
8	59	20	21	2240°	2460° ↓	very heterog	$\rho + \delta + \text{trace } \alpha$	ρ : a = 4.308	$\rho + \delta + \text{trace } \beta$
9	55	15	30	2600°	2642° ↓	very heterog	$\rho + \delta$	ρ : a = 4.321	ρ (prim.) + eutectic
10	55	30	15	2170°	2518° ↓	very heterog	$\rho + \gamma + \delta + \text{trace } \alpha$	ρ : a = 4.310	$\rho + \gamma + \delta + \beta$
11	54	35	10	2190°	2415° ↓	very heterog	$\rho + \gamma + \text{little } \delta$	ρ : a = 4.311	$\rho + \delta + \text{traces } \gamma + \beta$
12	52	42	6	2200°	2260°	very heterog	$\rho + \gamma + \delta + \text{trace } \alpha$	n.d.	$\rho + \gamma + \text{traces } \alpha + \delta$
13	51	47	2	2170°	2210° ↓	heterogeneous	$\gamma + \delta + \text{trace } \rho$	n.d.	$\gamma + \text{traces } \delta + \rho + \beta$
14	48	50	2	2180°	2191° ↓	heterogeneous	$\gamma + \delta + \text{trace } \rho$	n.d.	$\gamma + \text{traces } \delta + \rho$
15	43	47	10	2630°	2661°	very heterog	$\rho + \delta$	ρ : a = 4.318	$\rho + \delta$
16	47	15	38	2622°	2661° ↓	heterogeneous	$\rho + \delta$	ρ : a = 4.329	ρ (prim) + eutectic
17	63	3	31	1535°	2373° ↓	very heterog	$\rho + \text{trace } \alpha$	ρ : a = 4.309	$\rho + \text{traces } \beta \text{ and } \rho$
18	62	3	35	2795°	2800° ↓	very heterog	ρ	ρ : a = 4.319	ρ with precipitations

Table 32. (Continued)

Composition At. %			Observed Melting Temperature, °C			Phases Present After Melting		Metallography	
			Incipient	Collapse	Melting	X-ray Phases	Lattice Parameters Å		
No	Ti	B	C						
19	57	3	40	2640°	2860° ↓	very heterog.	ρ	ρ: a = 4.326	ρ
20	52	3	45	2630°	2992° ↓	very heterog.	ρ	ρ: a = 4.330	ρ with precipitations
21	44	26	30	2620°	2622° ↓	sharp	ρ + δ	ρ: a = 4.328	ρ (prim.) + eutectic
22	44	29	27	2620°	2620° ↓	sharp	ρ + δ	n.d.	ρ + δ eutectic.
23	50	25	25	2617°	2629° ↓	fairly sharp	ρ + δ	n.d.	ρ (prim.) + eutectic
24	42	23	25	2620°	2620° ↓	sharp	ρ + δ	a = 3.022 δ: c = 3.223	δ (prim.) + eutectic
25	40	40	20	2618°	2660°	slightly heterog	ρ + δ	ρ: a = 4.329	δ (prim.) + annealed eutec.
26	38	50	12	2648°	2745° ↓	heterogeneous	ρ + δ	a = 3.024 δ: c = 3.223	n.d.
27	35	60	5	2667	3002° ↓	very heterog.	ρ + δ	a = 3.024 δ: c = 3.223	δ (prim.) + traces eutec.
28	35	40	25	2430°	2543°	very heterog	ρ + δ trace K	a = 3.028 δ: c = 3.224	ρ + δ + traces K
29	34	31	35	2398°	2476° ↓	heterogeneous	ρ + δ + K	n.d.	n.d.
30	33	21	46	2432°	2517° ↓	heterogeneous	ρ + δ + K	ρ: a = 4.322	Bivar. ρ + K(prim) + eutec.
31	36	10	54	2460°	2620° ↓	very heterog	ρ + δ + K	ρ: a = 4.328	ρ + K (prim) + eutectic
32	25	15	60	2470°	2838° ↓	very heterog	ρ + δ + K	a = 2.464 K: c = 6.720	n.d.
33	25	30	45	2424°	2625° ↓	heterogeneous	ρ + δ + K	ρ: a = 4.329	K (prim) + eutectic
34	25	40	35	2400°	2424° ↓	fairly sharp	δ + K + trace ρ	n.d.	eutectic + trace prim. K
35	15	30	55	2636°	2852° ↓	very heterog.	δ + K	K: a = 2.464 c = 6.714	K (prim) + eutectic
36	19	36	65	2517°	2605° ↓	heterogeneous	δ + K	a = 3.022 δ: c = 3.223	n.d.
37	22	43	35	2498°	2520° ↓	fairly sharp	δ + K	n.d.	traces K (prim) + eutec.

Table 32 (Continued)

No	Composition At. %			Observed Melting Temperature, °C Incipient	Collapse	Melting	Phases Present After Melting		Metallography
	Ti	B	C				X-ray	Lattice Parameters λ	
38	23	45	32	2507°	↓	sharp	$\delta + \kappa$	n. d.	$\delta + \kappa$ eutectic
39	23	47	30	2514°	↓	sharp	$\delta + \kappa$	n. d.	trace δ (prim) + eutec.
40	25	50	25	2512°	↓	sl. heterog.	$\delta + \kappa$	n. d.	δ (prim) + eutectic
41	27	53	20	2507°	↓	heterogeneous	$\delta + \kappa$	a = 3.022 c = 3.224	δ (prim) + eutectic
42	29	59	12	2522°	↓	very heterog.	$\delta + \kappa$	n. d.	δ (prim) + eutectic
43	30	60	10	2545°	↓	very heterog.	$\delta + \text{trace } \kappa$	a = 3.023 c = 3.223	n. d.
44	31	63	6	(2900°)		very heterog	δ	a = 3.024 c = 3.223	$\delta + \kappa$
45	20	63	17	2270°	↓	very heterog	$\delta + \omega + \kappa$	a = 3.024 c = 3.223	δ (prim) + eutectic
46	8	64	28	2240°	↓	sharp	$\delta + \omega + \kappa$	n. d.	traces (prim) + eutec.
47	17	55	28	2257°		heterogeneous	$\delta + \omega + \kappa$	n. d.	$\delta + \omega + \kappa$
48	10	55	35	2265°		heterogeneous	$\delta + \omega$	n. d.	$\delta + \omega + \kappa$
49	8	46	46	2293°		heterogeneous	$\delta + \omega + \kappa$	n. d.	$\delta + \omega + \kappa$
50	24	70	6	2317°	↓	very heterog.	$\delta + \omega$	a = 3.028 c = 3.225	δ (prim) + eutectic
51	15	80	5	2043°	↓	very heterog	$\delta + \omega + \epsilon$ (?)	n. d.	δ (prim) + $\delta + \omega + \epsilon$
52	48	32	20	2512°	↓	heterogeneous	$\rho + \delta$	$\rho: a = 4.322$	δ (prim) + eutectic
53	30	35	35	2406°		sl. heterog.	$\rho + \delta + \kappa$	n. d.	traces $\kappa + \rho$ (prim) + eutec.

Legend to Table ↓ Quenched

α
 β
 γ
 δ
 ϵ
 ρ

κ
 ω
 ρ
 TiB_2
 B
 TiC
 C
 B_4C

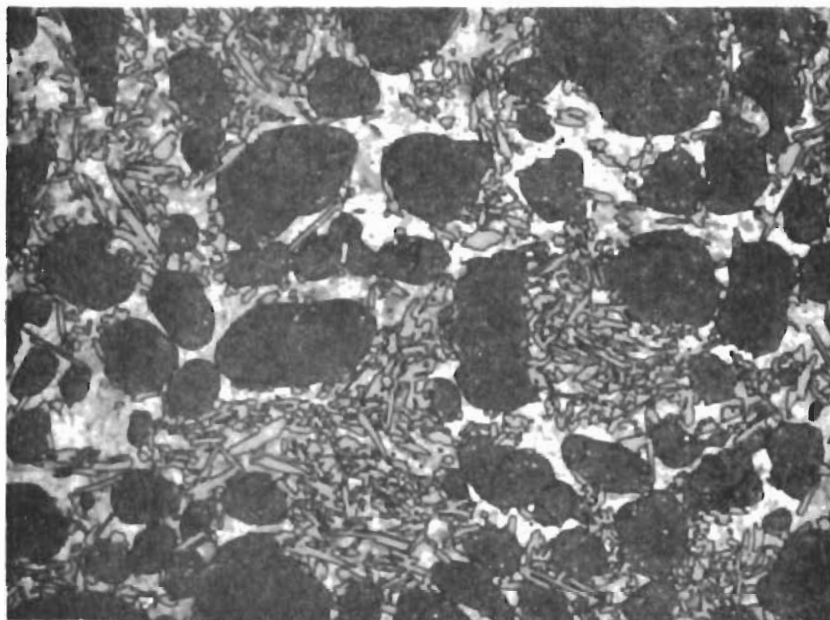


Figure 36. Ti-B-C (75-10-15 At.%), Cooled at Approximately 10°C per Second from 1710°C. X1000

Primary Monocarbide (Strongly Etched, Dark Crystals);
Monoboride, and Transformed β -Ti (Light).

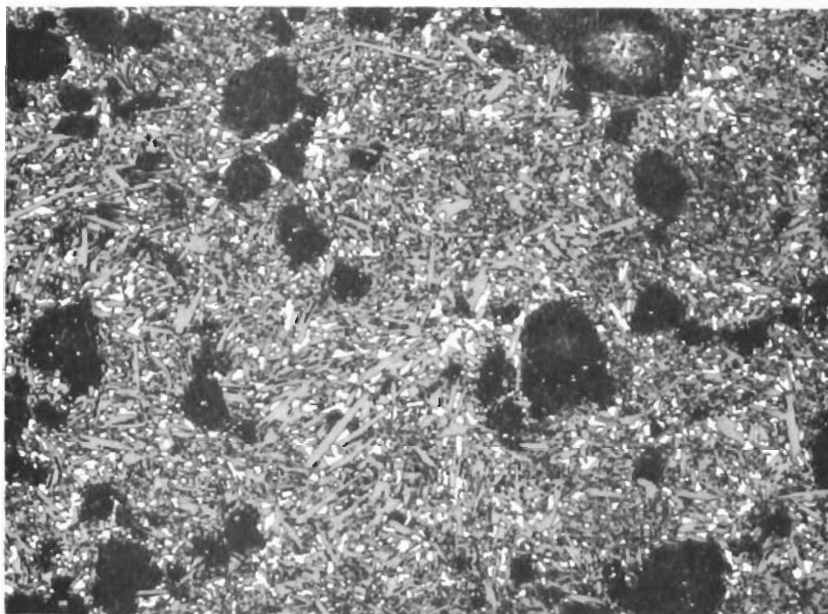


Figure 37. Ti-B-C (64-29-7 At.%), Cooled at $\sim 20^\circ\text{C}$ per Second from 1600°C. X700

Primary Monocarbide (Dark, Heavily Etched), Monoboride
(Small, Elongated Crystals), and Excess Titanium (Light).

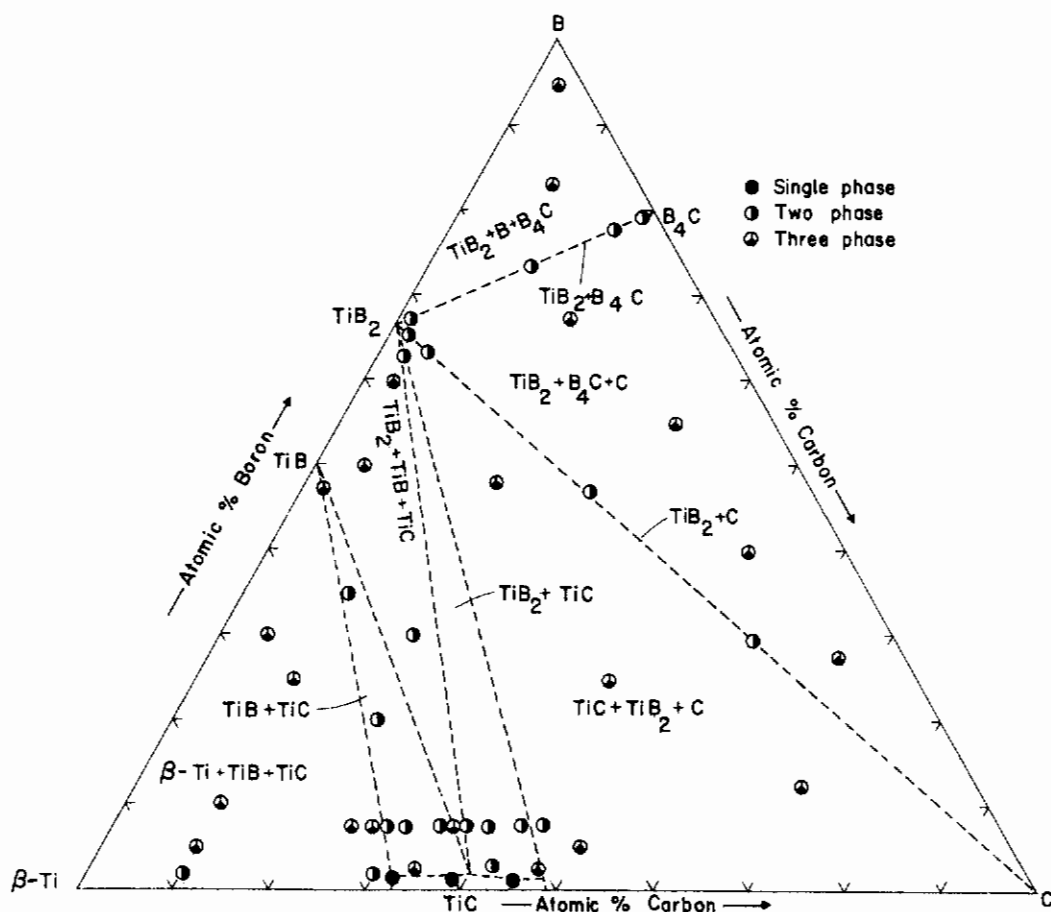


Figure 38. Ti-B-C: Location and Qualitative Phase Evaluation of the Alloy Series Equilibrated at 1400°C.

Metallographically, an alloy Ti-B-C (66-3-31 At.%) quenched from 1800°C is still three-phased, containing eutectic and excess monoboride at the grain boundaries of the primary crystallized monocarbide (Figure 39). An alloy Ti-B-C (62-3-35 At.%) is single-phased after quenching from 2700°C (Figure 40), but shows significant monoboride precipitation after re-equilibration and slow cooling from 1800°C (Figure 41).

Alloys located along the section $TiB-TiC_{1-x}$ generally were three-phased after quenching from temperatures in excess of 2160°C, containing a non-equilibrium mixture consisting of TiB_2 , TiB , TiC , and Ti

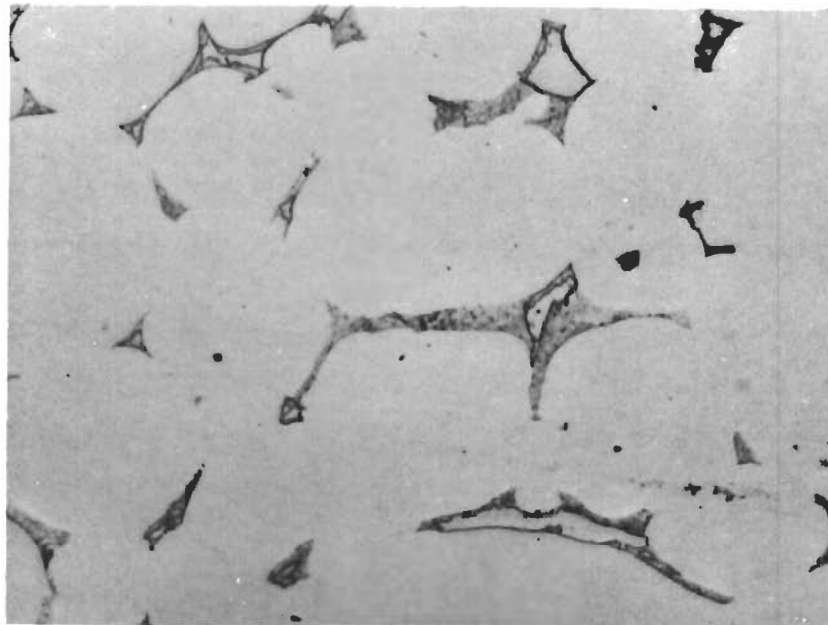


Figure 39. Ti-B-C (66-3-31 At.%), Quenched from 1900°C. X720
Primary Monocarbide with Excess Monoboride and
Ti + TiB + TiC Eutectic at the Grain Boundaries.

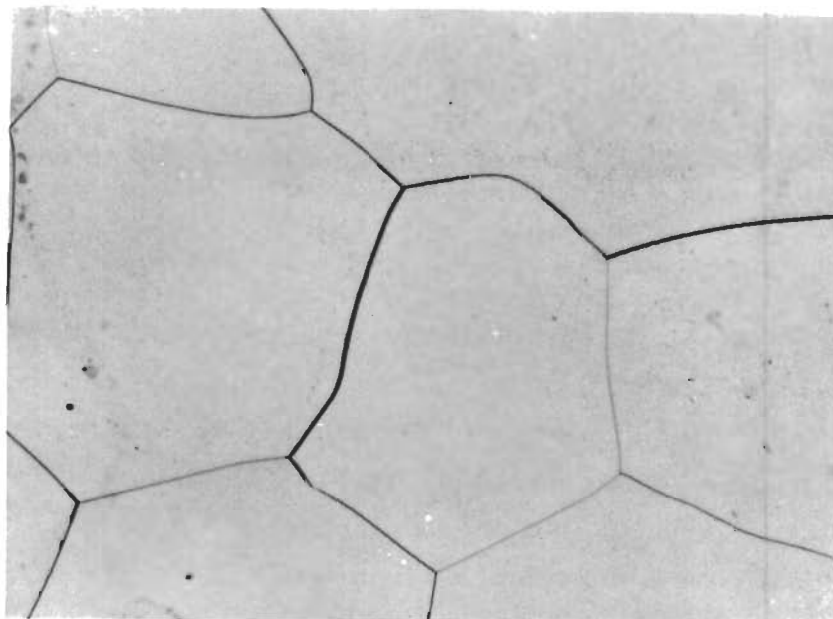


Figure 40. Ti-B-C (62-3-35 At.%), Quenched from 2700°C. X220
Single Phase Monocarbide Solution.

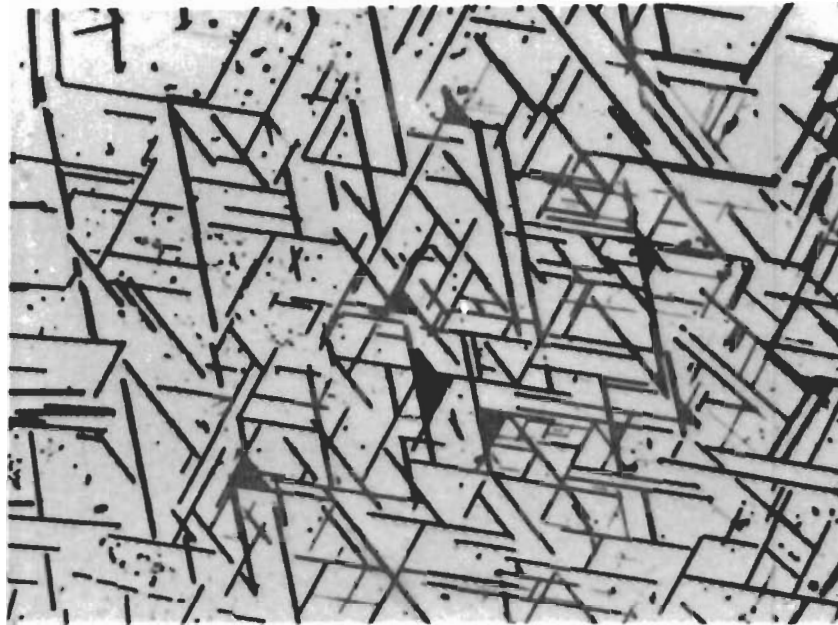


Figure 41. Ti-B-C (62-3-35 At.%), Sample from Figure 40 X1000
Re-equilibrated for 10 Minutes at 1800°C, and
Slowly Cooled.

Monocarbide Solution with Localized Precipitations of TiB.

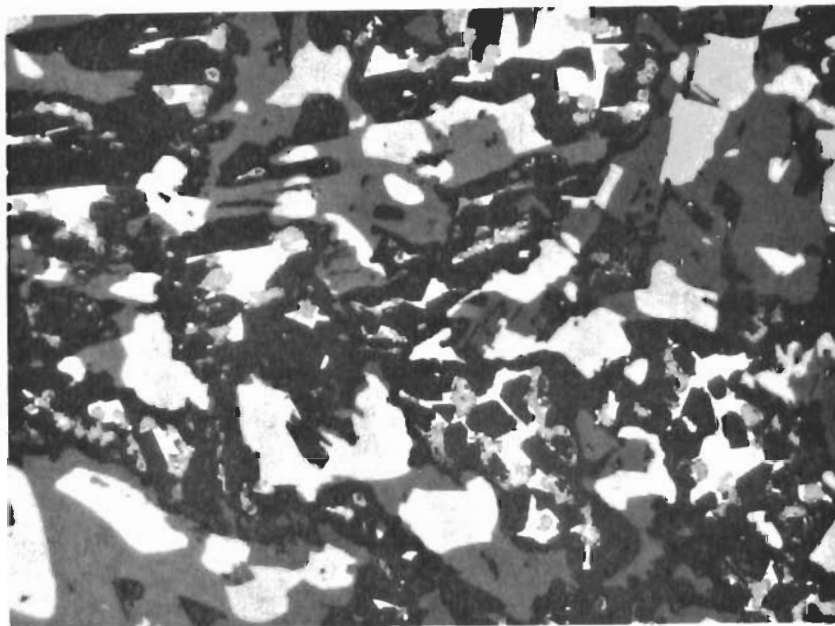


Figure 42. Ti-B-C (51-47-2 At.%), Cooled with Approximately X600
5°C per Second from 2210°C.

Four-Phase Non-Equilibrium Mixture - Ti + TiB₂ + TiC + TiB.

(Table 32, Figures 42 and 43); the equilibration reaction proceeds to completion, and the alloys ultimately become two-phased TiB + TiC-ss, if either slow cooling rates ($< 1^{\circ}\text{C}\cdot\text{sec}^{-1}$) are employed, or if these alloys are re-annealed at lower temperatures (Figure 44). Based on the incipient melting data obtained by DTA as well as by Pirani-techniques, the class II reaction isotherm



was placed at a temperature of 2160°C .

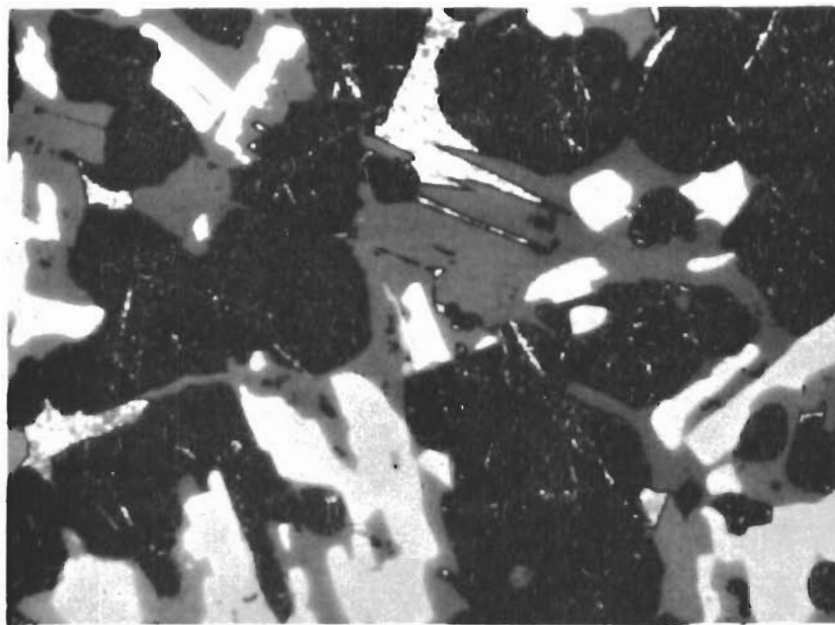


Figure 43. Ti-B-C (55-30-15 At.%), Cooled with
Approximately 10°C per Second from 2300°C .

X1000

Four-Phase Reaction Mixture $\text{L}(\text{Ti}) + \text{TiB}_2 \rightarrow \text{TiC} + \text{TiB}$

3. The Pseudobinary Section Diboride-Monocarbide

With the exception of alloys containing less than 2 atomic percent boron, 1400°C homogenized alloys located along the section TiB_2 - TiC_{1-x} ($0 < x < 28$) are two-phased monoboride + diboride (Figure 38). The two-phase equilibrium pertains up to the melting range, as after quenching from the molten state, the X-ray patterns revealed the presence of only these phases. Melting of the alloys with diboride contents of approximately 40 atomic percent occurred isothermally at 2620°C (Table 32, Figure 45). The eutectic

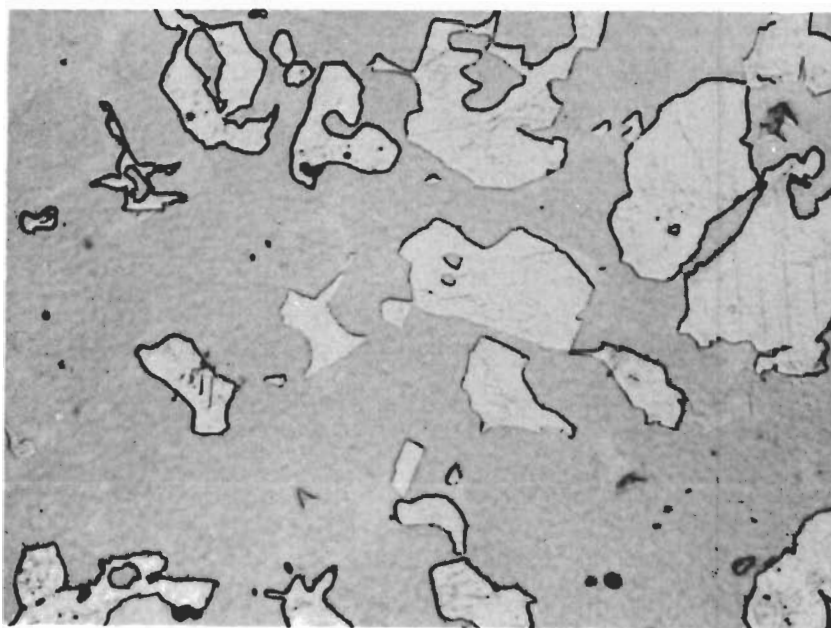


Figure 44. Ti-B-C (62-12-26 At.%), Melted Re-Equilibrated X750 for 20 Minutes at 2100°C, and Quenched. As Polished.

X-ray: TiC -ss + TiB .

composition was bracketed to within 57 ± 2 mole % TiC_{1-x} by metallographical inspection of alloys which were rapidly quenched from the molten state (Figure 46 through 51). In either instance, cooling rates in excess of 50°C per second proved to be necessary, in order to prevent partial annealing of the eutectic (Figures 52 and 53.) The monocarbide dissolves temperature-dependently

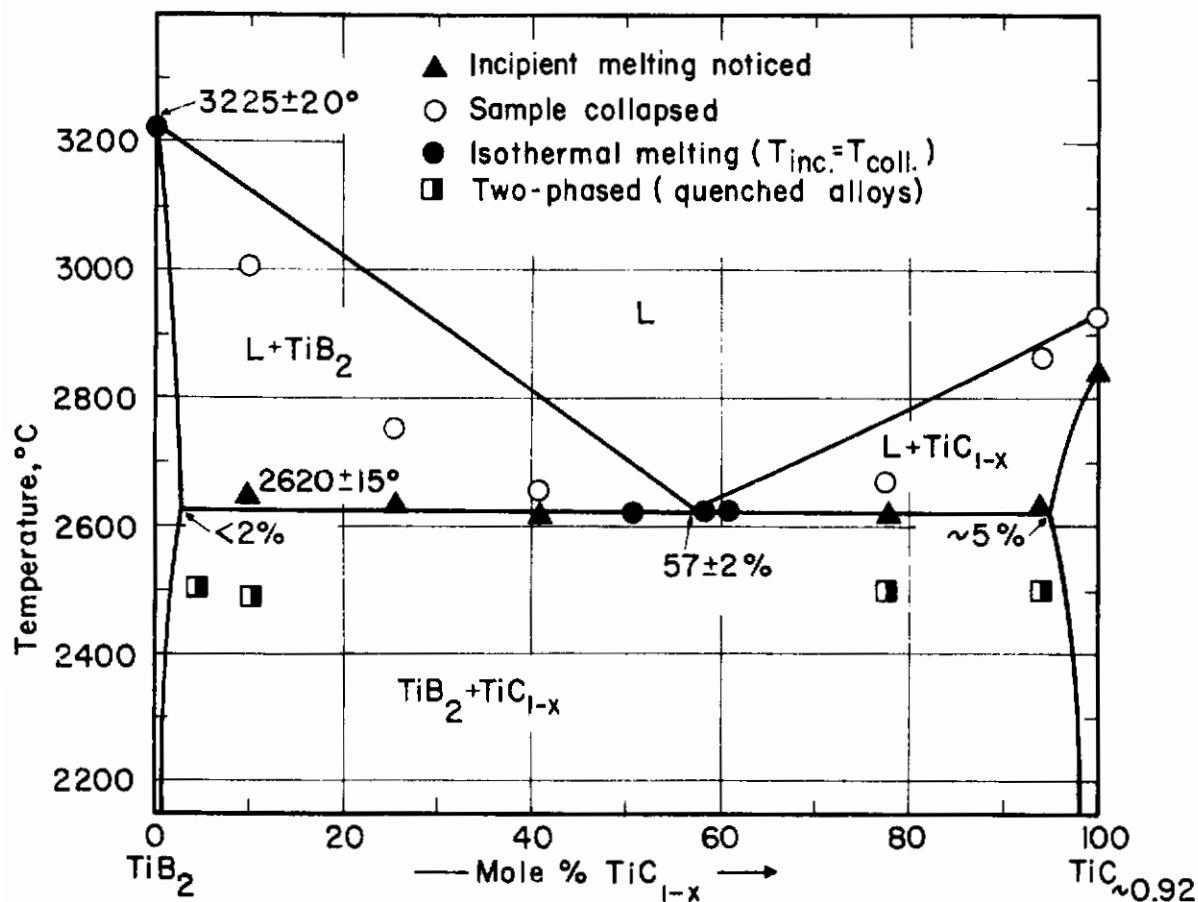


Figure 45. Ti-B-C: Pseudobinary Section TiB_2 - $TiC_{0.92}$.

to a maximum of approximately 5 atomic percent boron. Although less pronounced than in Hf-B-C system, the solubility seems to be larger in the carbon-deficient carbide, i.e. solid solution formation occurs by substitution for carbon, but also by filling of carbon vacancies with boron atoms in the substoichiometric carbide. Precipitation of boride from the monocarbide occurs considerably faster from the carbon-richer compositions, and cooling rates in excess of 40°C are usually required, in order to prevent dissolution reactions [Figures 54, 55, 56(a) through 56(c)].

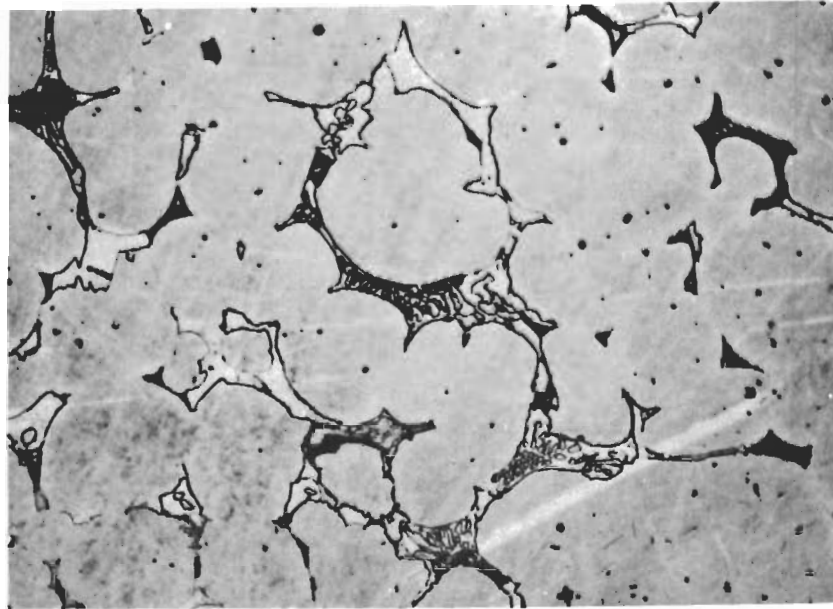


Figure 46. Ti-B-C (63-10-27 At.%), Quenched from 2580°C. X550
Primary Monocarbide with Bivariantly Solidified
Ti + TiB₂ + TiC Mixture at the Grain Boundaries.

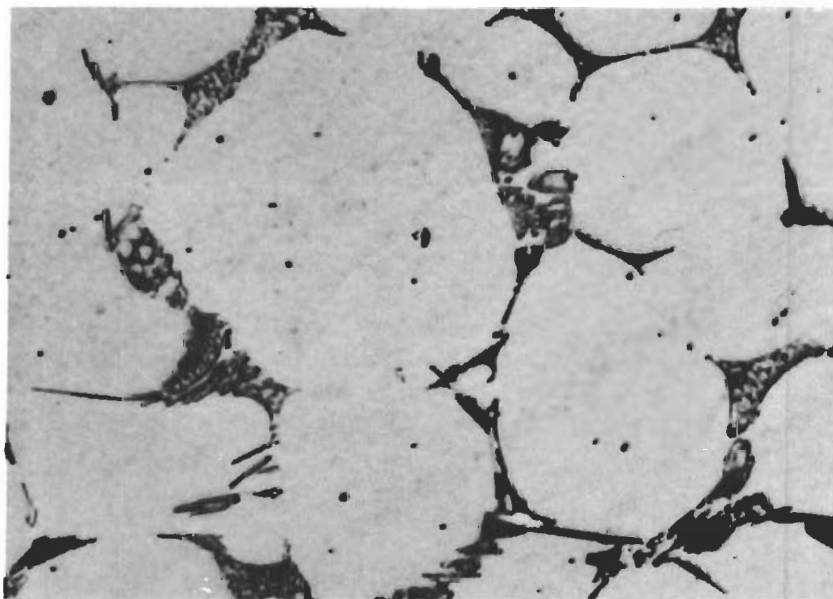


Figure 47. Ti-B-C (55-10-35 At.%), Rapidly Quenched
from 2640°C. X1000
Primary Monocarbide, with TiB₂ + TiC Eutectic at
the Grain Boundaries.

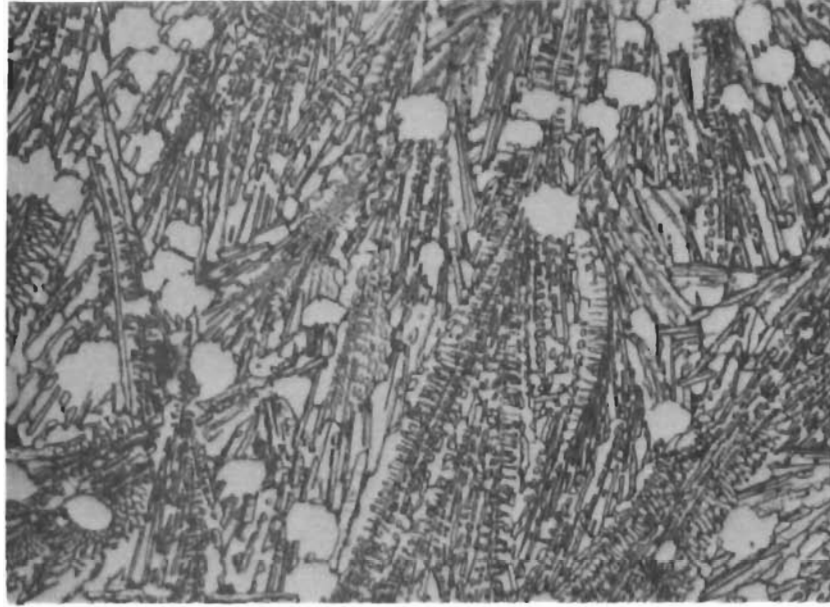


Figure 48. Ti-B-C (44-26-30 At.%), Quenched from 2622°C. X600
Small Amounts of Primary Monocarbide in a Matrix of
TiC + TiB₂ Eutectic.

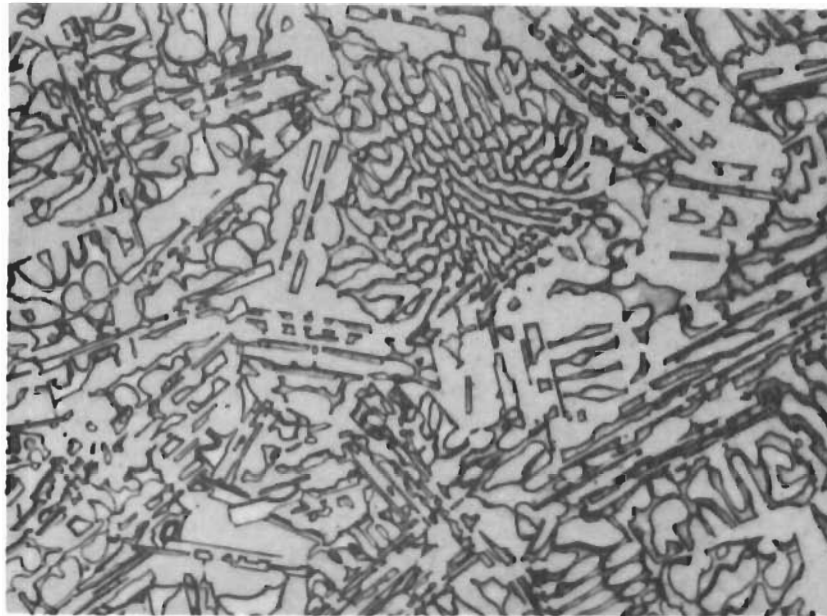


Figure 49. Ti-B-C (44-29-27 At.%), Cooled with
Approximately 80°C per Second from 2620°C. X750
TiB₂ + TiC Eutectic.

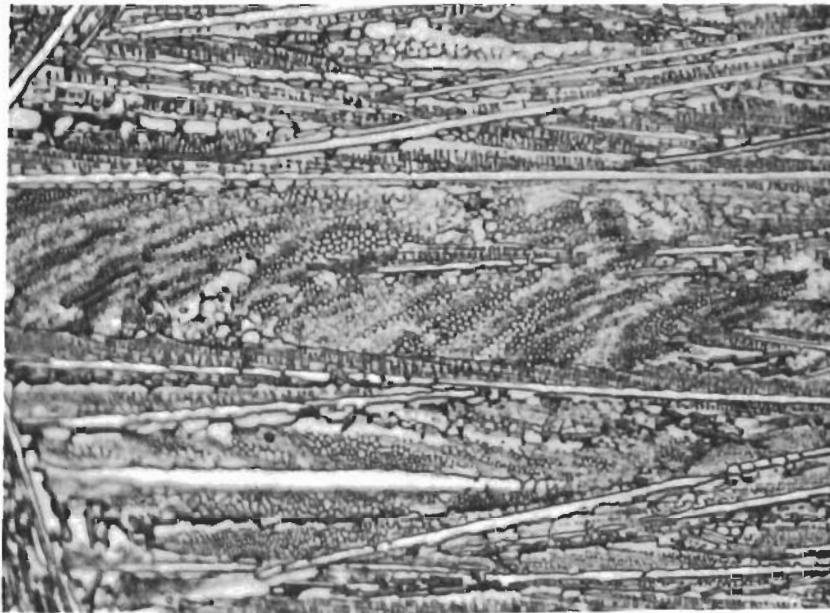


Figure 50. Ti-B-C (42-33-25 At.%), Quenched from 2620°C. X700
Traces of Primary Diboride in a Matrix of $TiB_2 + TiC$ Eutectic.

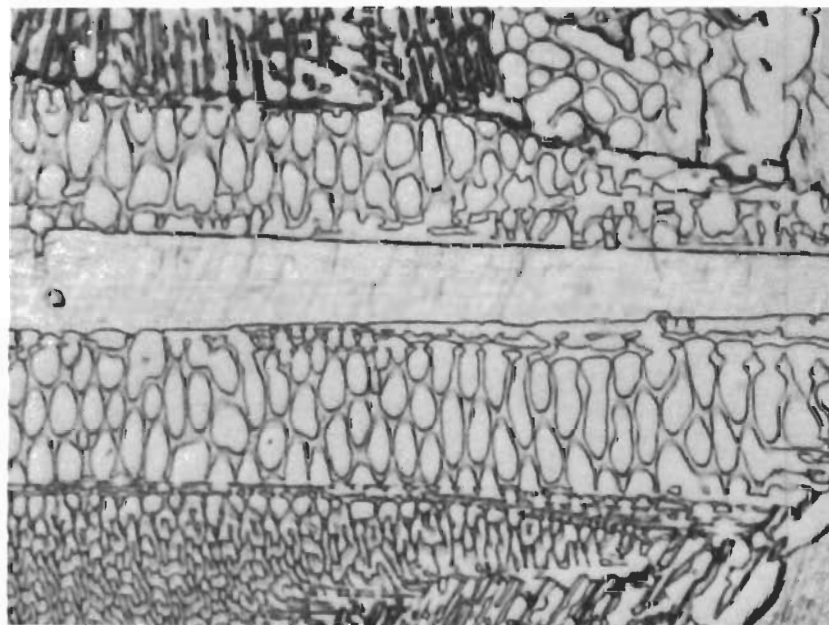


Figure 51. Enlarged View of the Sample from Figure X2000
Primary Diboride Crystal in Surrounding Matrix of $TiB_2 + TiC$ Eutectic.

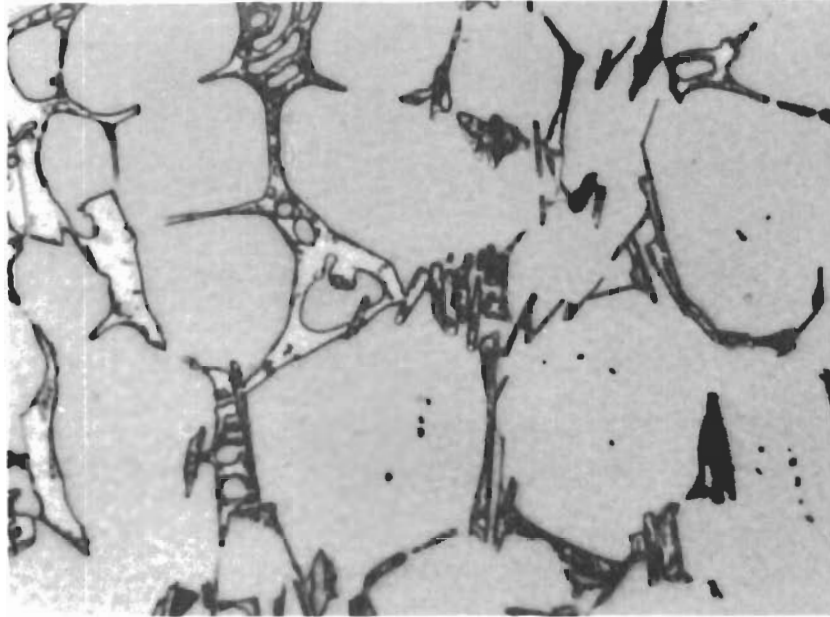


Figure 52. Ti-B-C (55-10-35 At.%), Cooled with
Approximately 50°C from 2645°C.

X1000

Primary Monocarbide + Partially Annealed $TiB_2 + TiC$
Eutectic at the Grain Boundaries.

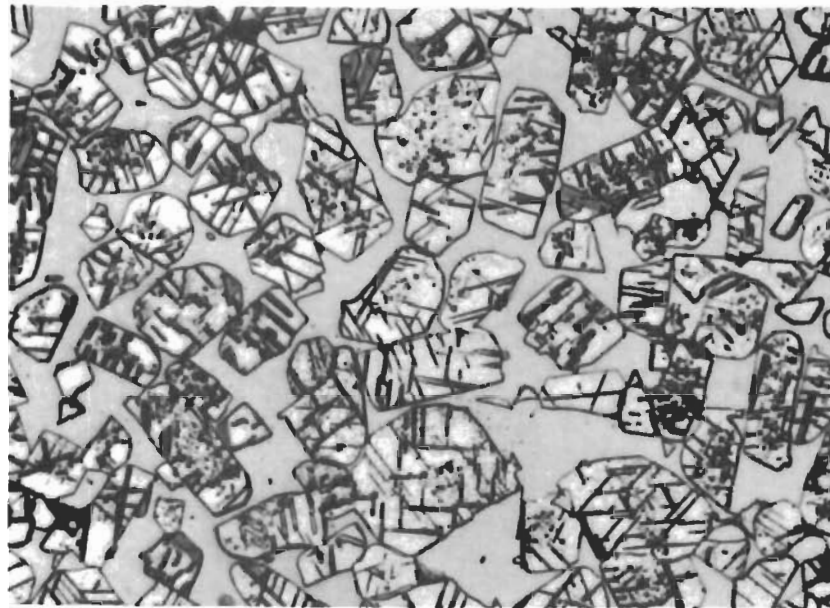


Figure 53. Ti-B-C (44-29-27 At.%), Cooled with
Approximately 2°C per Second from 2620°C.

X750

Annealed Eutectic $TiB_2 + TiC$. Note Localized Diboride
Precipitations in TiB_2 .

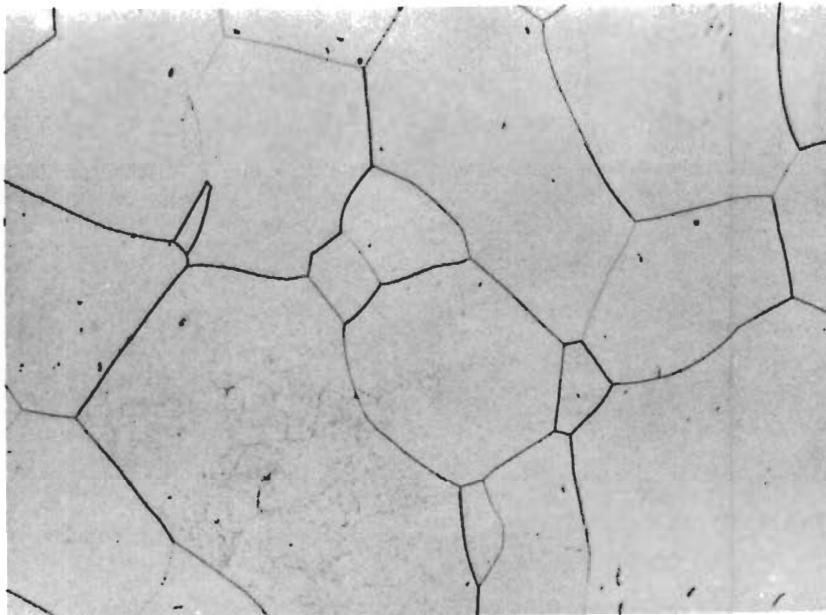


Figure 54. Ti-B-C (57-3-40 At.%), Quenched from 2800°C. X150
Single Phase Monocarbide Solution. $a_{\text{Ti(C,B)}_{1-x}} = 4.326 \text{ \AA}$.

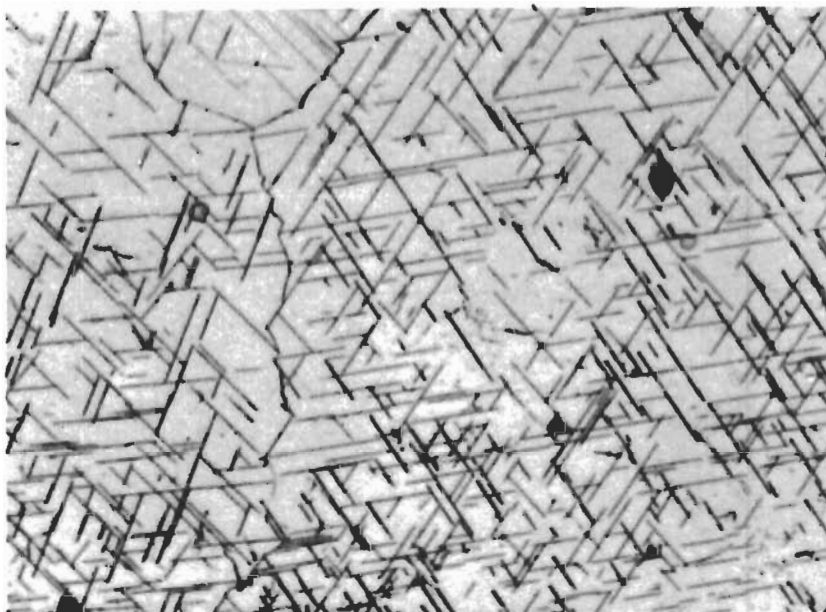


Figure 55. Ti-B-C (57-3-40 At.%), Cooled with Approximately 20°C per Second from 2600°C. X1000
Monocarbide with Precipitation of TiB_2
 $a_{\text{Ti(C,B)}_{1-x}} = 4.323 \text{ \AA}$

Contrails

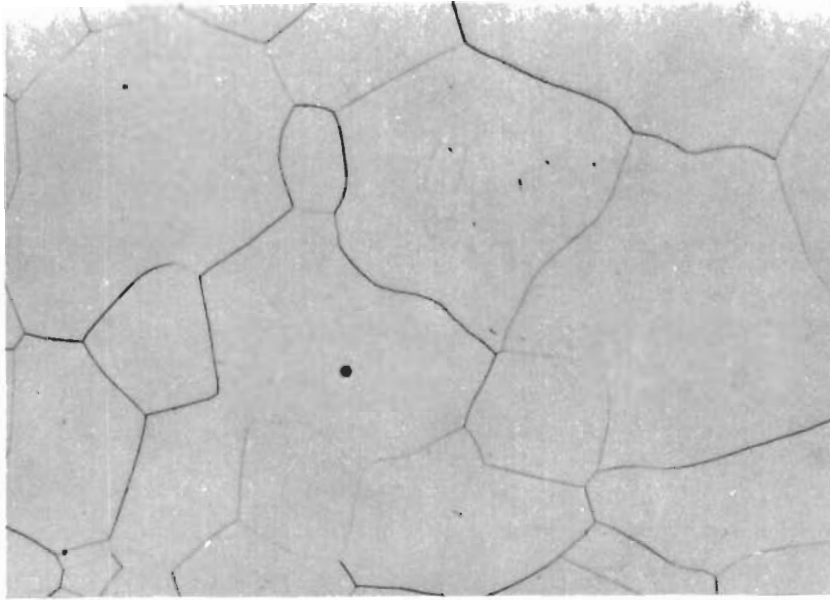


Figure 56(a). Quenched Single Phase $Ti (C,B)_{1-x}$.

X240

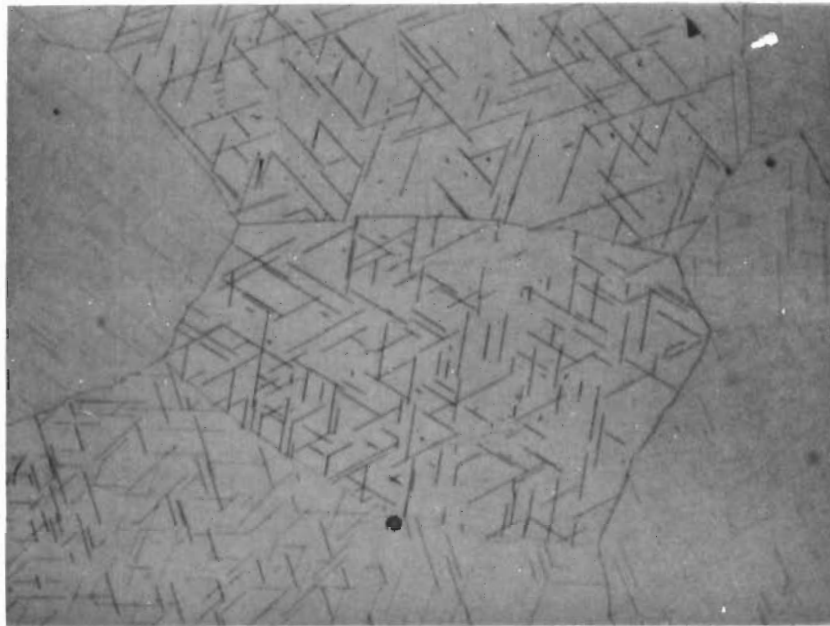


Figure 56(b). Cooled with Approximately $50^{\circ}C$ per Second.
Initiation of Localized Diboride Precipitations.

X600

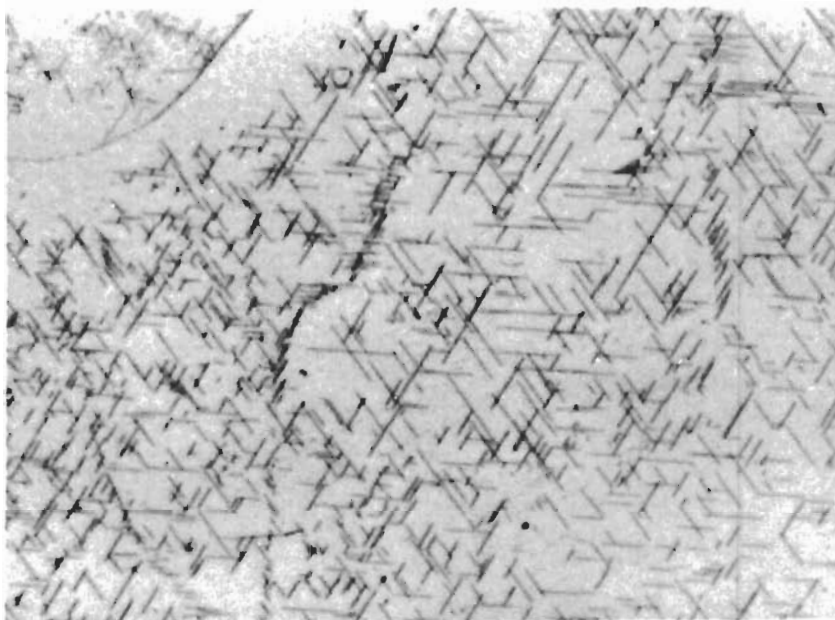


Figure 56(c). Cooled with Approximately 30°C per Second. X1000
TiB₂ Precipitations in the Monocarbide.

Figures 56(a) through 56(c): Alloy: Ti-B-C (52-3-45 At.%).
Diboride Precipitation from Slightly Understoichiometric Titanium
Monocarbide.

The solubility in the diboride phase must be below 2 atomic percent; all alloys located in the vicinity of the diboride were either two- or three-phased, and the lattice parameter changes (Table 32) with respect to the pure binary phase were only nominal.

4. The Pseudobinary Section Diboride-Graphite

Melting point alloys, as well as solid state equilibrated samples located along the concentration line diboride-graphite were two-phased, containing diboride and graphite (Figures 38 and 57).

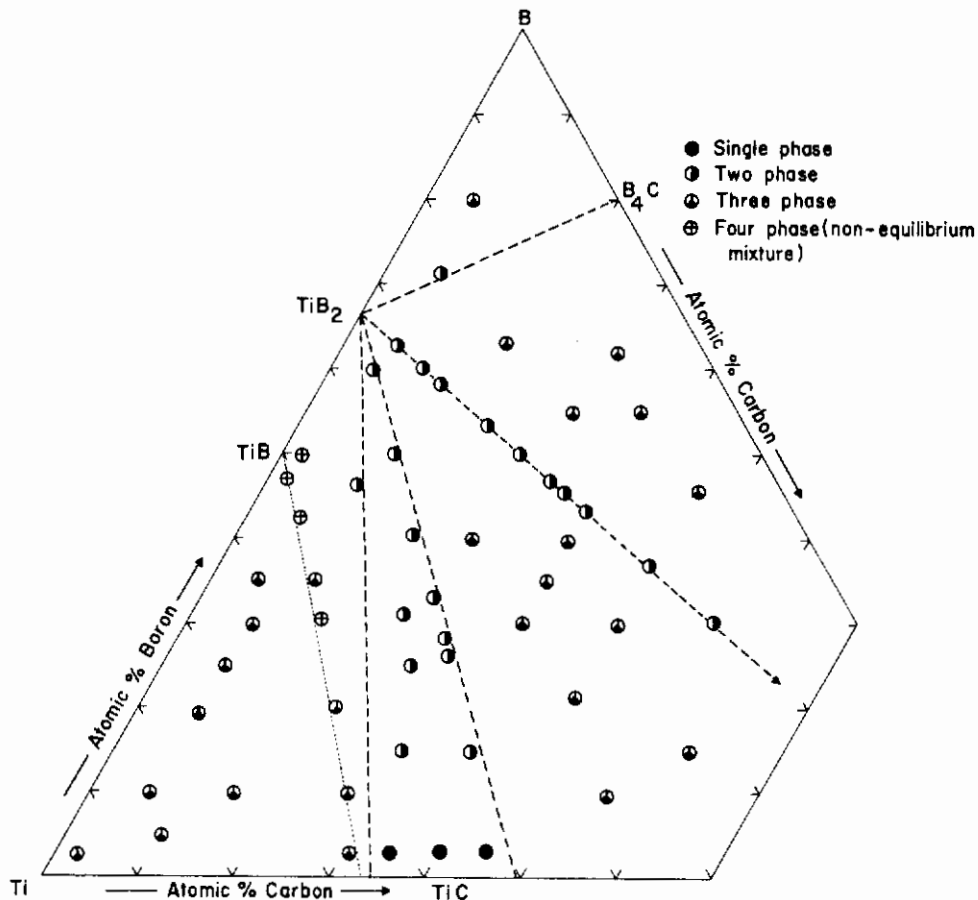


Figure 57. Ti-B-C: Location of Melting Point Samples, and Qualitative Phase Evaluation after Melting.

Incipient melting at small (< 10 At.%) and high (> 50 At.%) carbon concentrations was difficult to observe, and generally noted only at temperatures in excess of the eutectic line (Figure 58). Nevertheless, heterogeneity at the eutectic temperature in a sample with a carbon content of 5 atomic percent was established by differential thermal analysis, i.e. the maximum carbon exchange in the diboride must therefore be lower. Alloys with carbon contents of 30 and 32 atomic percent melted sharp (Figure 58), indicating that the eutectic point must be located in this composition region.

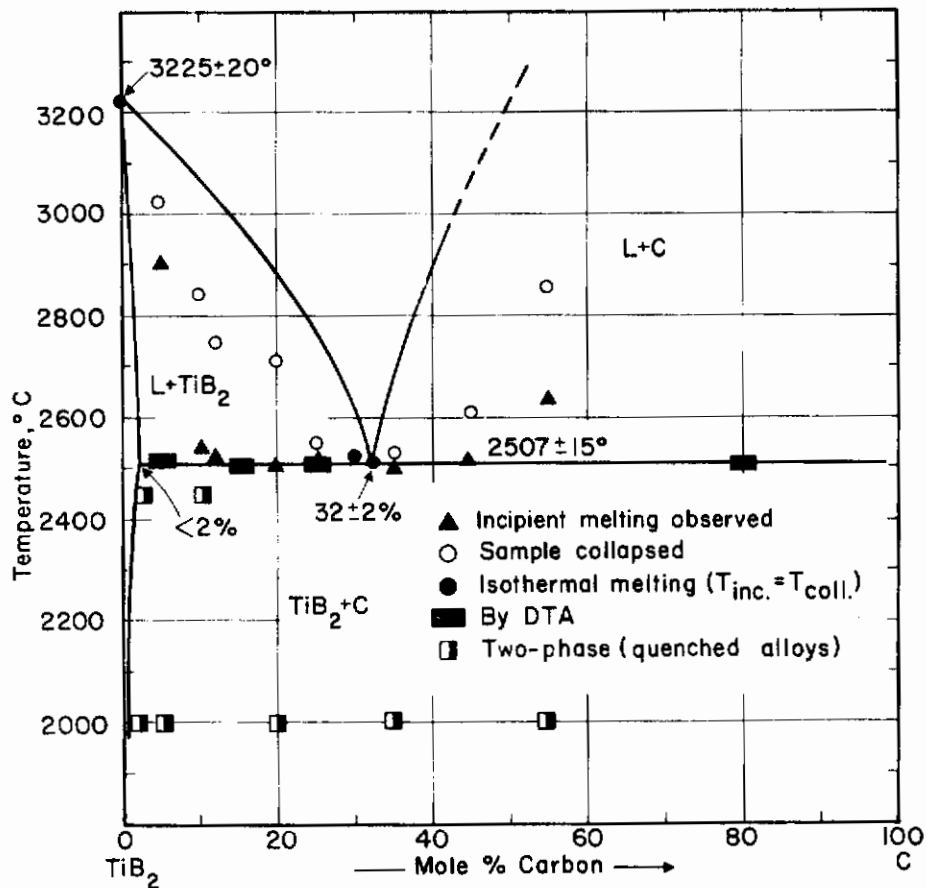


Figure 58. Pseudobinary Section TiB₂-C:

Melting Temperatures and Qualitative Phase Evaluation of Solid State Equilibrated and Quenched Alloys.

Metallographically, the alloys with carbon concentration up to 30 atomic percent contained primary crystallized diboride (Figures 59 through 61). A purely eutectic structure was exhibited by the alloy with a carbon content of 32 atomic percent (Figure 62). Carbon-richer alloys showed, besides eutectic, primary crystallized graphite (Figures 63 and 64).

5. The Pseudobinary Section Diboride-Boron Carbide

An alloy Ti-B-C (24-70-6 At.%), located along the section TiB₂-B₄C showed incipient melting at 2317°C (Table 32), and melted through

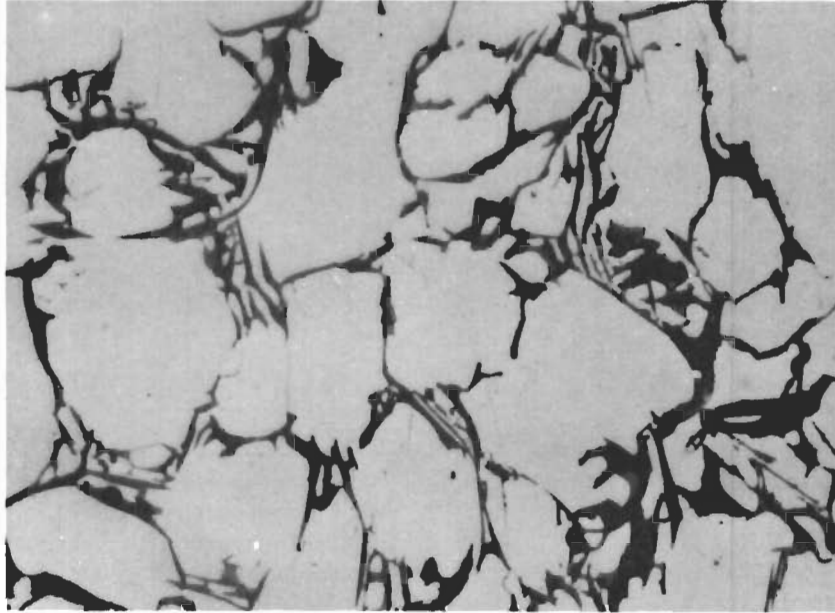


Figure 59. Ti-B-C (28-57-15 At.%), Cooled with 8°C per Second from 2550°C. X650

Primary Diboride in a Matrix of Partly Annealed $TiB_2 + C$ Eutectic.

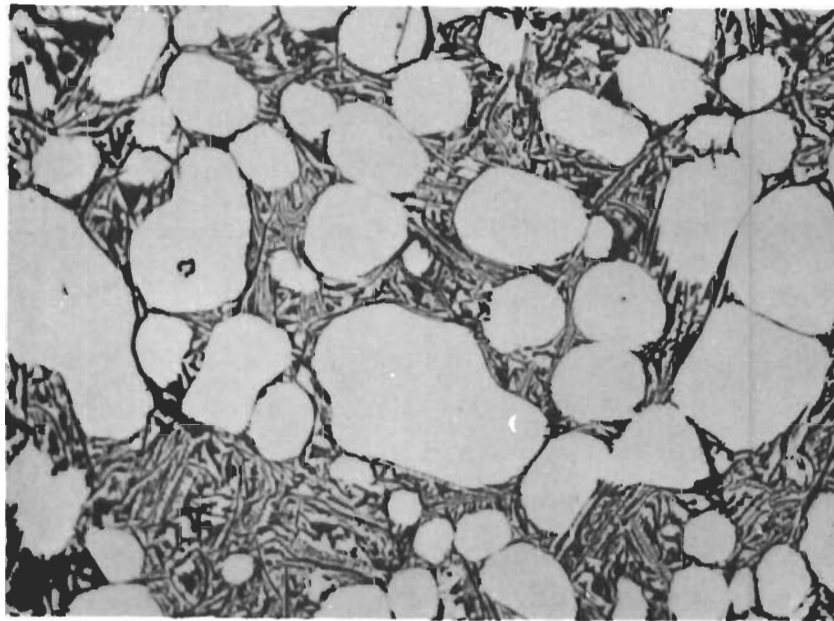


Figure 60. Ti-B-C (25-50-25 At.%), Quenched from 2545°C. X500

Primary TiB_2 and $TiB_2 + C$ Eutectic.



Figure 61. Ti-B-C (23-47-30 At.%), Quenched from 2514°C. X340
Traces of Primary Diboride in a Matrix of $TiB_2 + C$ Eutectic.

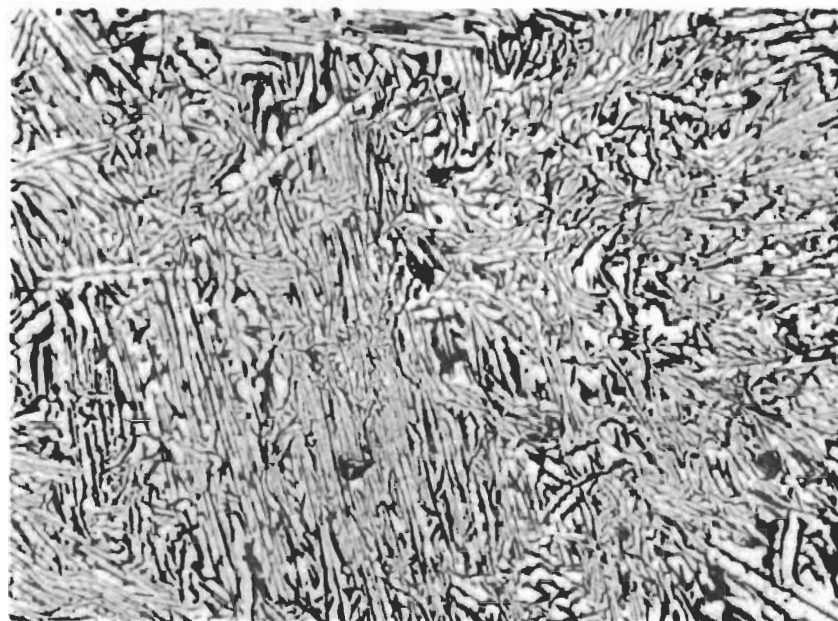


Figure 62. Ti-B-C (23-45-32 At.%), Quenched from 2507°C. X375
 $TiB_2 + C$ Eutectic.

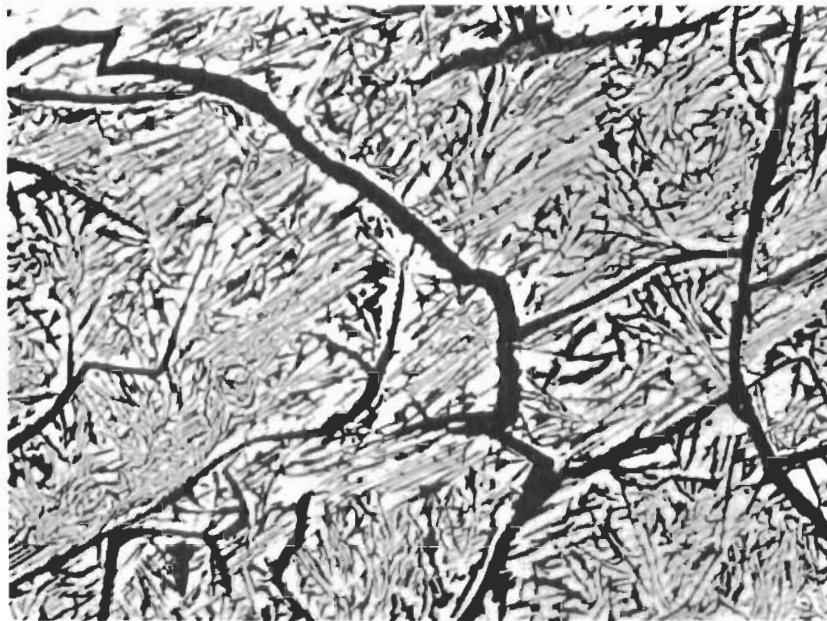


Figure 63. Ti-B-C (19-36-45 At.%), Quenched from 2517°C. X300
Primary Crystallized Graphite and TiB₂ + C Eutectic.



Figure 64. Ti-B-C (15-30-55 At.%), Cooled with Approximately 20°C per Second from 2640°C. X1000
Primary Graphite (Dark) in a Matrix of TiB₂ + C Eutectic.

at a temperature of 2850°C. While two-phased melting was still fairly pronounced in an alloy Ti(18)-B(73)-C(8) At.%, whose incipient melting temperature was determined by differential thermal analysis (Figure 65), the alloy with a boron carbide content of 86 atomic percent melted fairly sharp. Metallographically, the alloy contained small amounts of primary diboride in a eutectic matrix. The presence of large pores as well as excessive breakout of structure components during pregrinding resulted in poor metallographic specimens. The microstructures were therefore examined visually only.

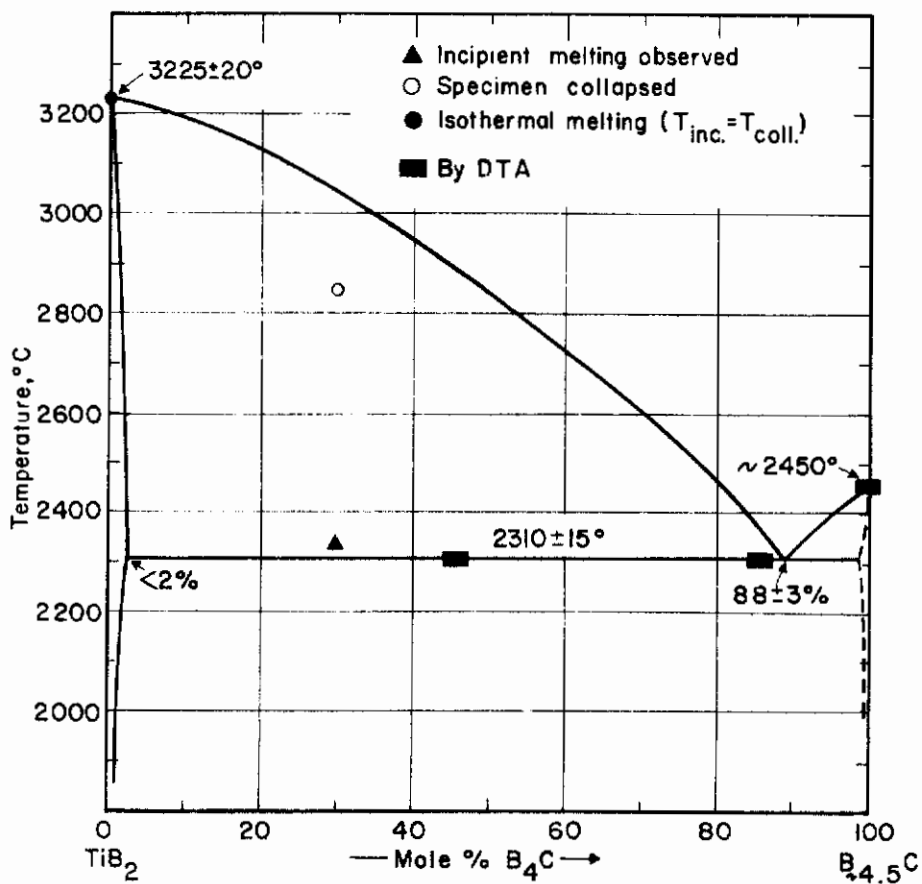


Figure 65. Pseudobinary Section TiB₂-B₄C.

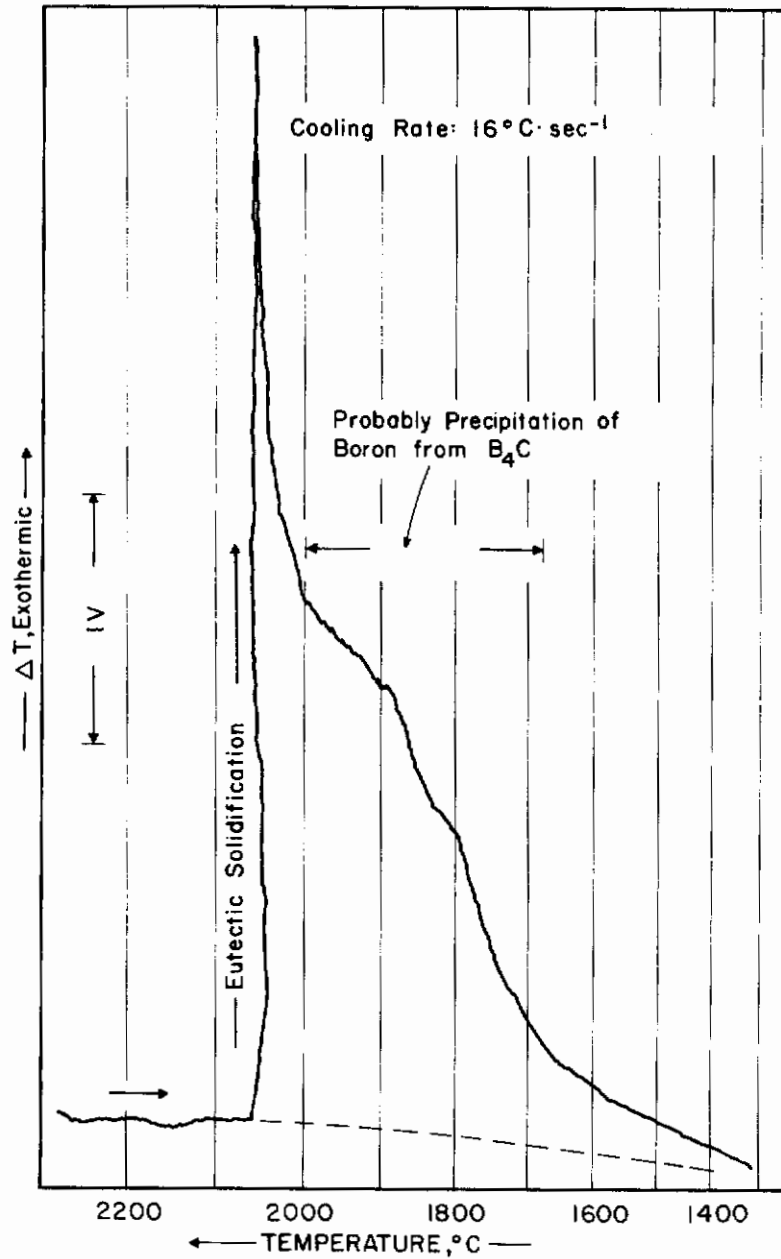


Figure 66. DTA-Thermogram (Cooling) of a Boron-Carbon Alloy with 10 Atomic Percent Carbon.

6. Ternary Equilibria in the Composition Region TiC-TiB₂-B-C

Incipient melting in an alloy located in the boron-corner of the system was noticed at 2016°C. This temperature is lower than the eutectic temperatures of the surrounding binary or pseudobinary sections [TiB₂ + B: 2080°C, TiB₂ + B₄C: 2310°C, B₄C + B: 2080°C^(72, 73), Figure 66]. Metallographically, an alloy Ti-B-C (4-90-6 At.%) which was cooled with approximately 10°C per second from 2040°C, consisted of approximately 80 of a eutectic-type structure, the primary constituents being B₄C and TiB₂. The microstructures however, were of comparatively poor quality and hence the photographs were not taken up into the report.

In three-phase alloys TiB₂ + B₄C + C incipient melting consistently was observed at temperatures in the vicinity of 2240°C (Table 32, Figures 67 and 68). Microscopically, an alloy Ti-B-C (20-63-17 At.%) cooled from 2300°C, contained primary crystallized TiB₂ in a matrix of B₄C and carbon (Figure 69). Although recrystallization, but especially, segregation of the diboride and graphite grains to the boron carbide grain boundaries, could not be fully prevented, the microstructure of a sample Ti-B-C (8-64-28 At.%, Figure 70) indicates, that the ternary eutectic must be located close to this composition. In concurrence with previous work by R. P. Elliott⁽⁷³⁾ and R. T. Dolloff⁽⁷²⁾, we found the binary eutectic reaction isotherm L + B₄C + C to occur in the vicinity of 2400°C. It is especially noteworthy, that strong supercooling of the boron-carbon melts consistently was observed in the DTA-runs (Figure 71).

In three-phase alloys TiB₂ + TiC + C incipient melting was found to occur at 2400°C (Table 32, Figure 72). Melting was nearly isothermal in the alloys located close to the pseudobinary TiB₂ + C eutectic compositions, and, characteristically, the low viscosity eutectic melt would fill the observation hole of the melting point specimens, as soon as the eutectic temperatures were reached [Figure 73 (a) and 73 (b)].

Metallographically, an alloy Ti-B-C (25-40-35 At.%) after quenching from 2420°C, is almost purely eutectic [Figure 74(a)]. Alloys

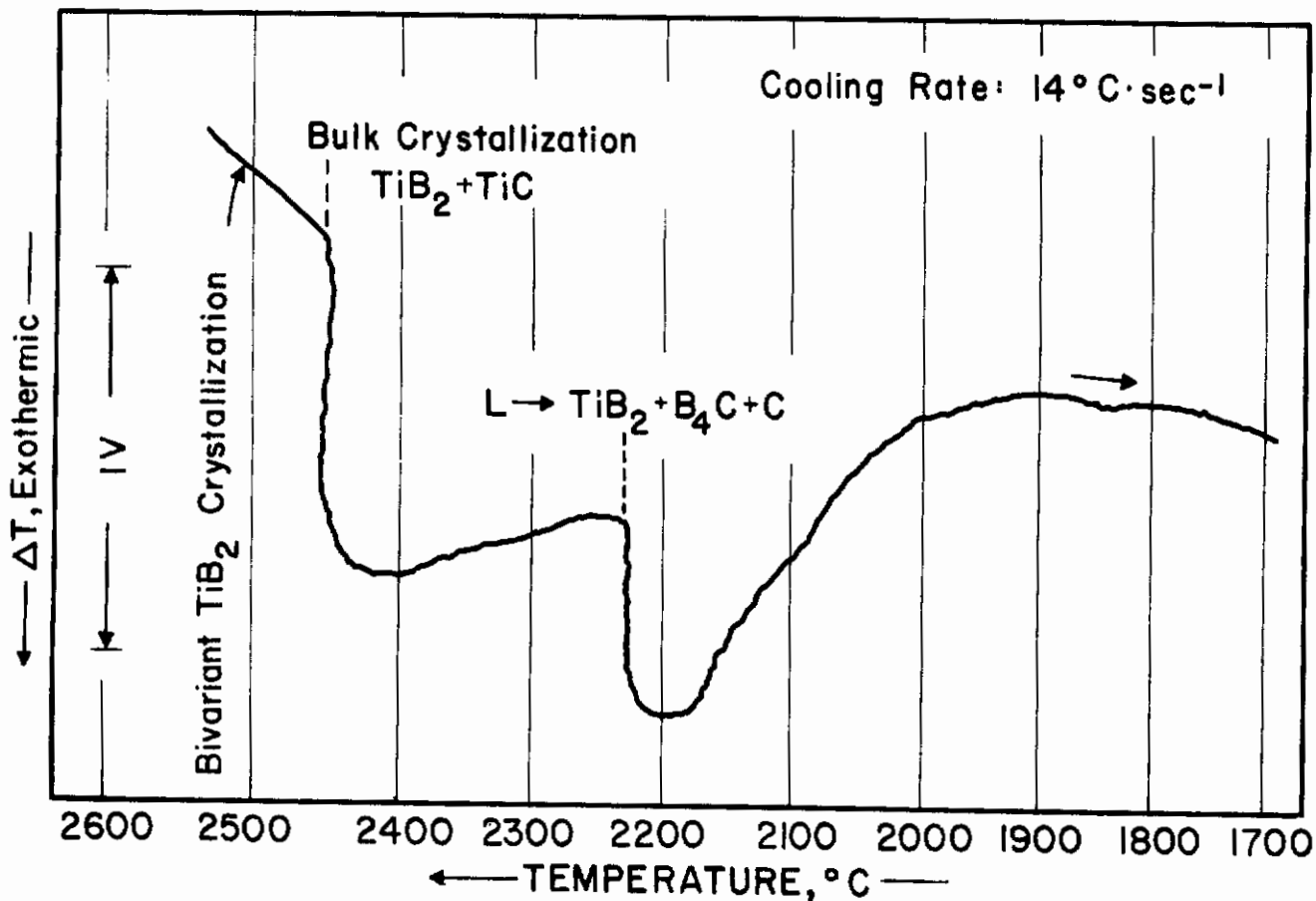


Figure 67. DTA-Thermogram (Cooling) of a Ti-B-C (28-62-10 At.%) Alloy Located Close to the Pseudobinary Section $\text{TiB}_2 + \text{C}$.

located closer to the boundary system Ti-C, or the pseudobinary section TiB_2 -C, contain either the monocarbide and/or graphite [Figures 74(b) and 75], or diboride and graphite (Figure 76), as primary crystallizing species.

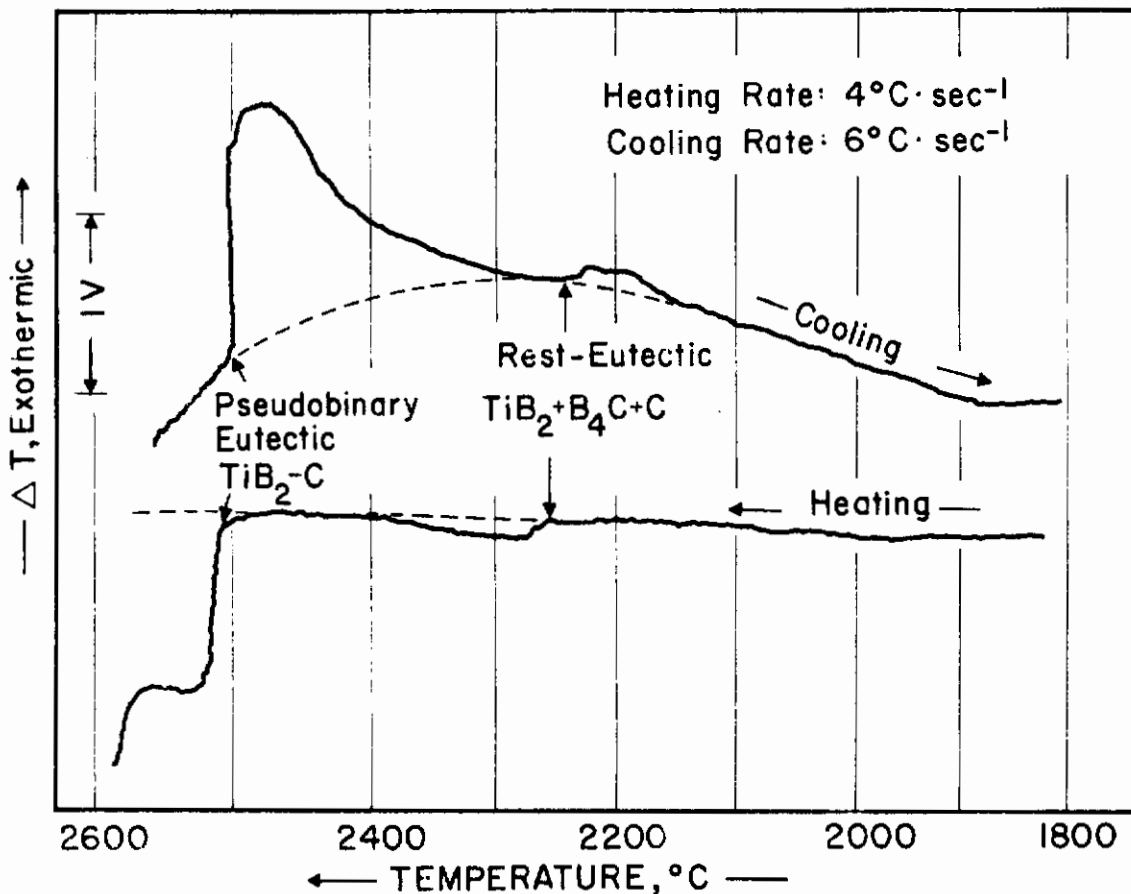


Figure 68. DTA-Thermogram of a Ti-B-C (27-58-15 At.%) Alloy Containing Small Amounts of Excess B_4C .

7. Assembly of the Phase Diagram

The results gained in the course of the experimental work have been combined in the phase diagram shown in Figure 1. Although the Pirani-technique does not allow a precise determination of the liquidus temperatures of the alloys, a fairly close estimate can be made from the observed melting behavior of the alloys. Independent liquidus data for the temperature range below 2500°C were also obtained by differential-thermo-analytical techniques and were incorporated in the diagram.

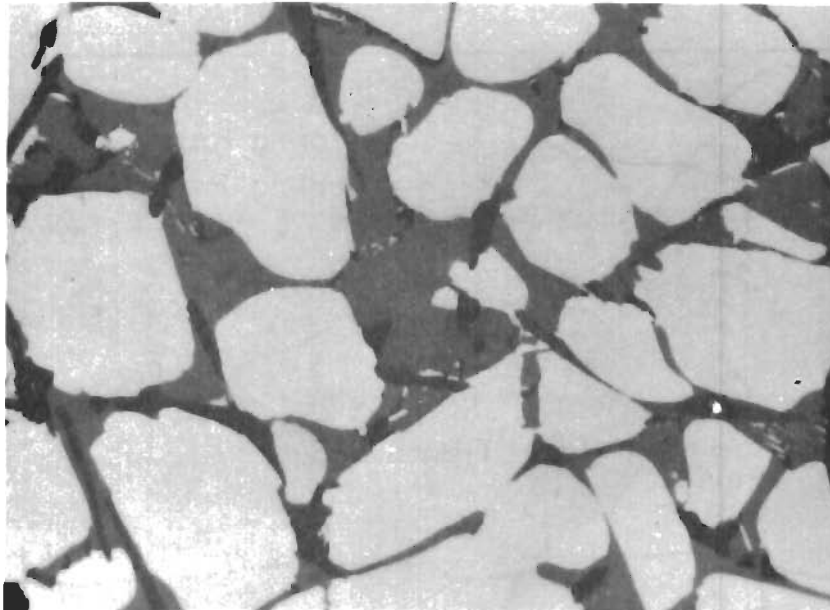


Figure 69. Ti-B-C (20-63-17 At.%), Cooled with Approximately 15°C per Second from 2300°C.

X750

Primary TiB (Bright, Large Grains), B₄C (Grey), and Graphite (Black, Elongated Staples).

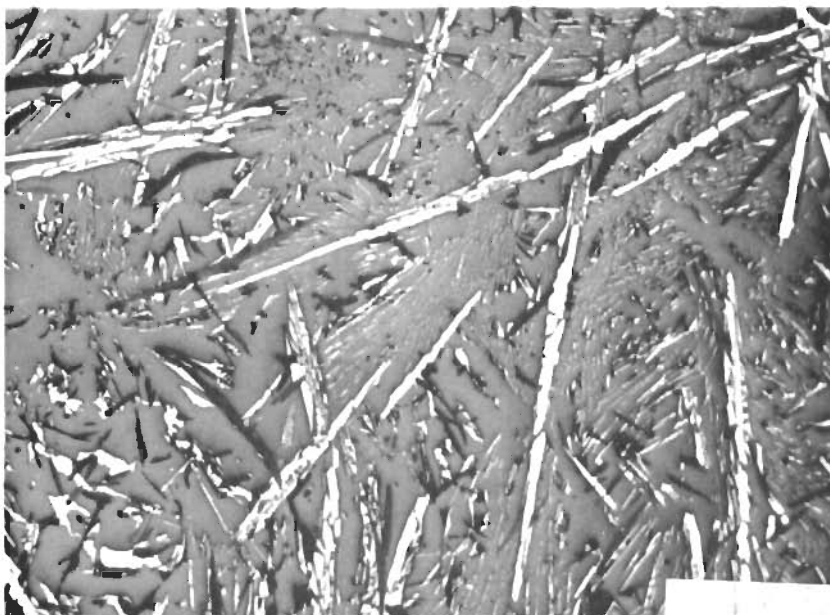


Figure 70. Ti-B-C (8-64-28 At.%), Quenched from 2246°C

X180

Traces of Primary TiB₂ in an Eutectic Matrix
TiB₂ + B₄C + C.

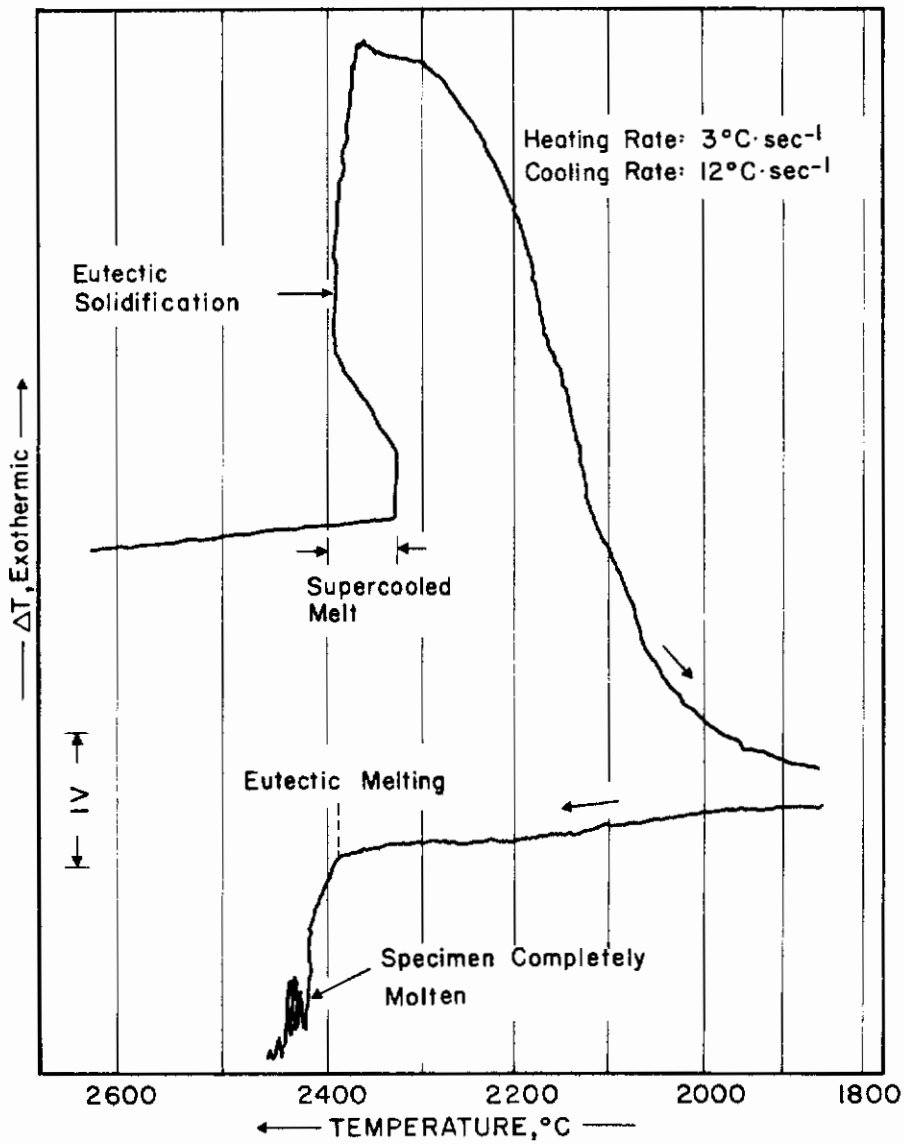


Figure 71. DTA-Thermograms of a Boron-Carbon Alloy with 30 Atomic Percent Carbon.

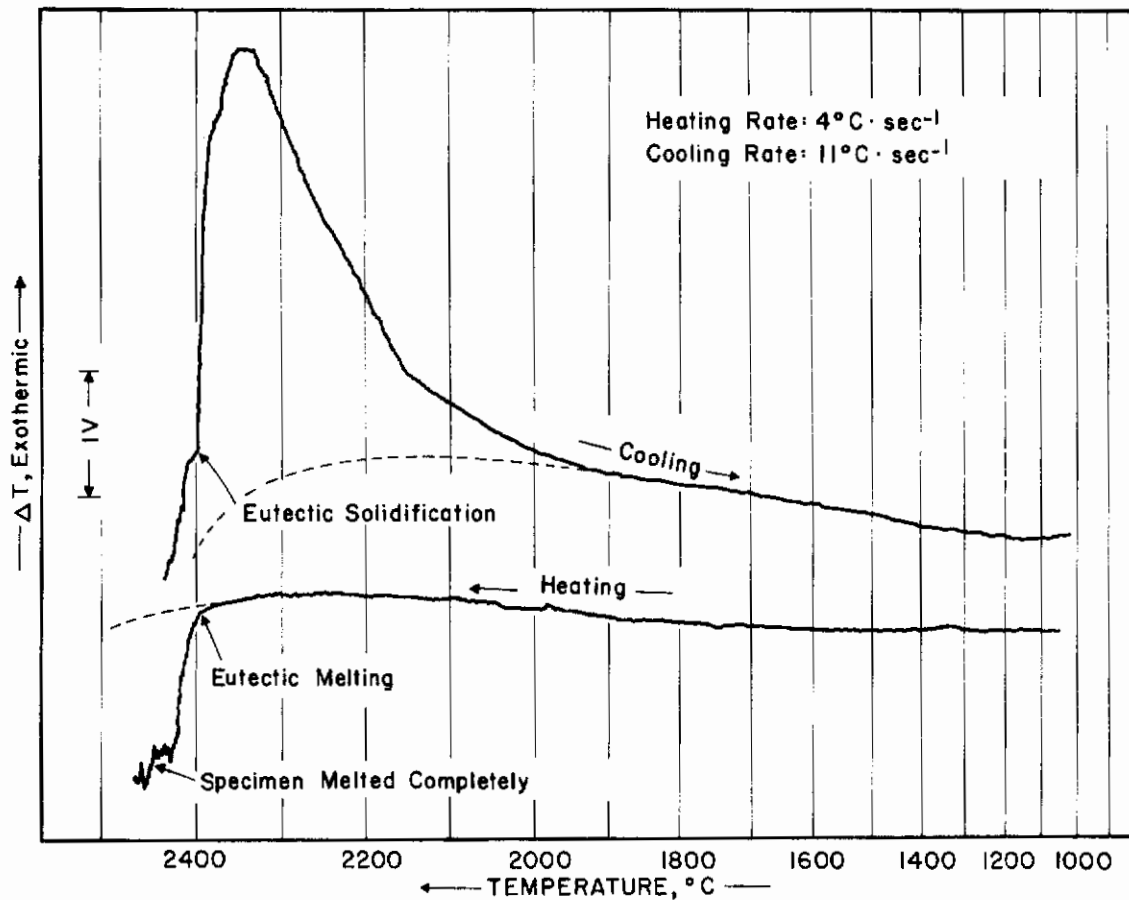


Figure 72. DTA-Thermogram of a Ti-B-C (30-35-35 At.%) Alloy, Showing Liquification and Solidification of the $TiB_2 + TiC + C$ Eutectic at 2400°C.

Although care was taken to present the phase diagram data as clearly as possible in the assembly drawing of Figure 1, three-dimensional drawings are inherently complex and difficult to visualize. Hence, in order to facilitate consultation of the phase diagram data, and also to show more clearly the temperature sequence of reactions occurring in the alloy system, a series of isothermal sections have been prepared from the smoothed experimental data. They are presented in Figures 77(a) through 77(i).

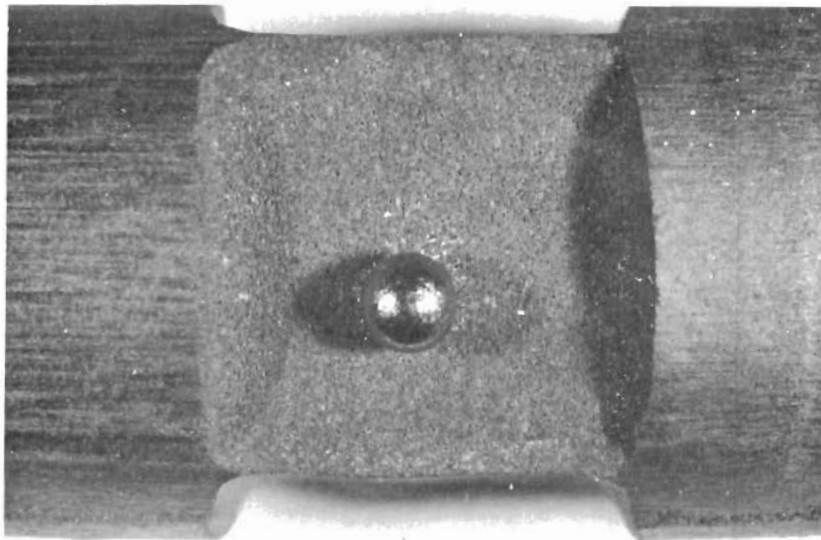


Figure 73(a) Pirani-Melting Point Specimen of a Ti-B-C
(34-25-40 At.%) After Reaching 2400°C.

X8

Note Eutectic Melt Exuding from the Black-Body Hole
in the Specimen.

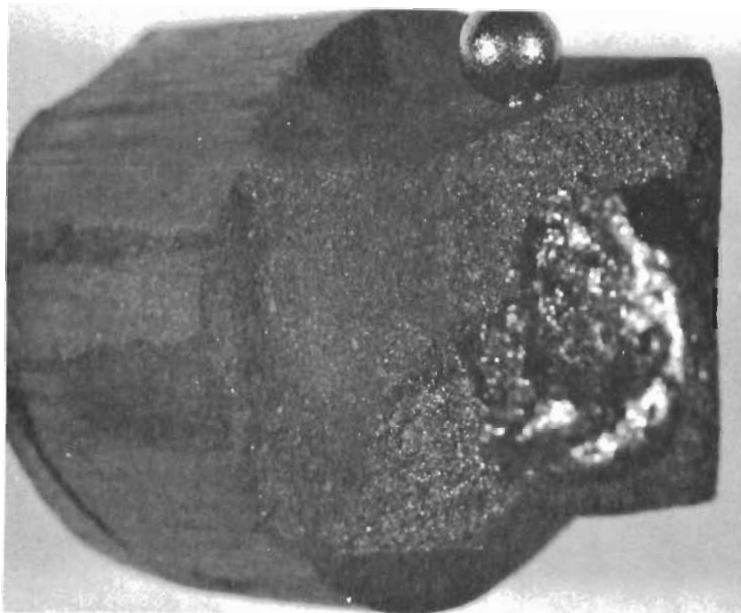


Figure 73(b) Sample from Figure 73, After Sectioning.

Note Melt-Cavity in the Interior.

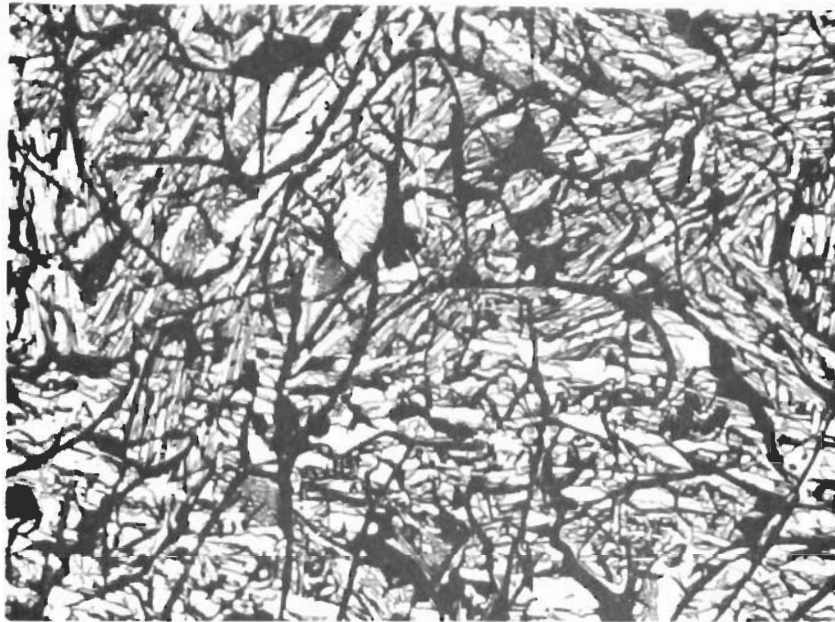


Figure 74 (a). Ti-B-C (25-40-35 At.%), Quenched from 2424°C. X160

Small Amounts of Primary Graphite, and $TiB_2 + TiC + C$ Eutectic.



Figure 74 (b). Ti-B-C (33-21-46 At.%), Quenched from 2517°C. X1000

Bivariantly Crystallized $TiC + C$, in a Matrix of Ternary Eutectic $TiB_2 + TiC + C$.

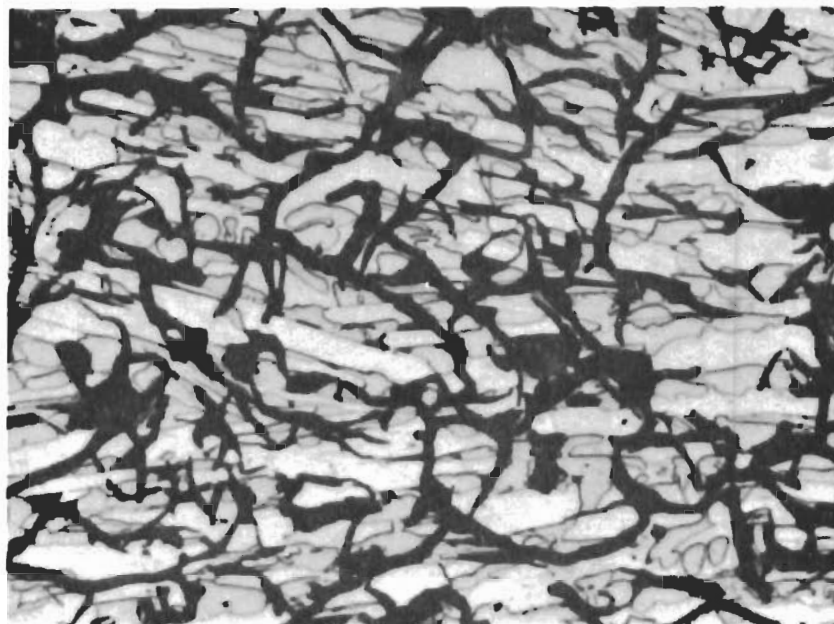


Figure 75. Ti-B-C (25-30-45), Rapidly Cooled from 2550°C. X625

Primary Graphite (Dark, Veinlet Shaped Crystals), in a
Partially Divorced and $\text{TiB}_2 + \text{TiC} + \text{C}$
Eutectic Matrix.



Figure 76. Ti-B-C (25-40-35), Cooled at Approximately 10°C per Second from 2430°C. X200

Primary Diboride (Light, Elongated Crystals) and
Graphite (Dark) in a $\text{TiB}_2 + \text{TiC} + \text{C}$ Eutectic Matrix.

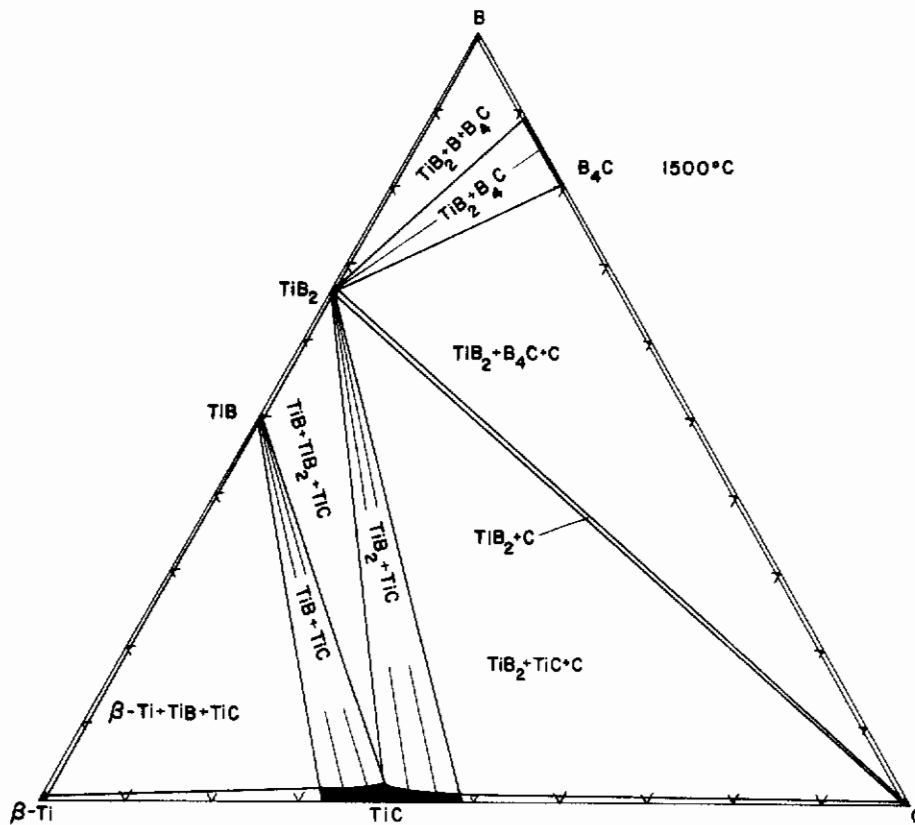


Figure 77(a). Isothermal Section at 1500°C.

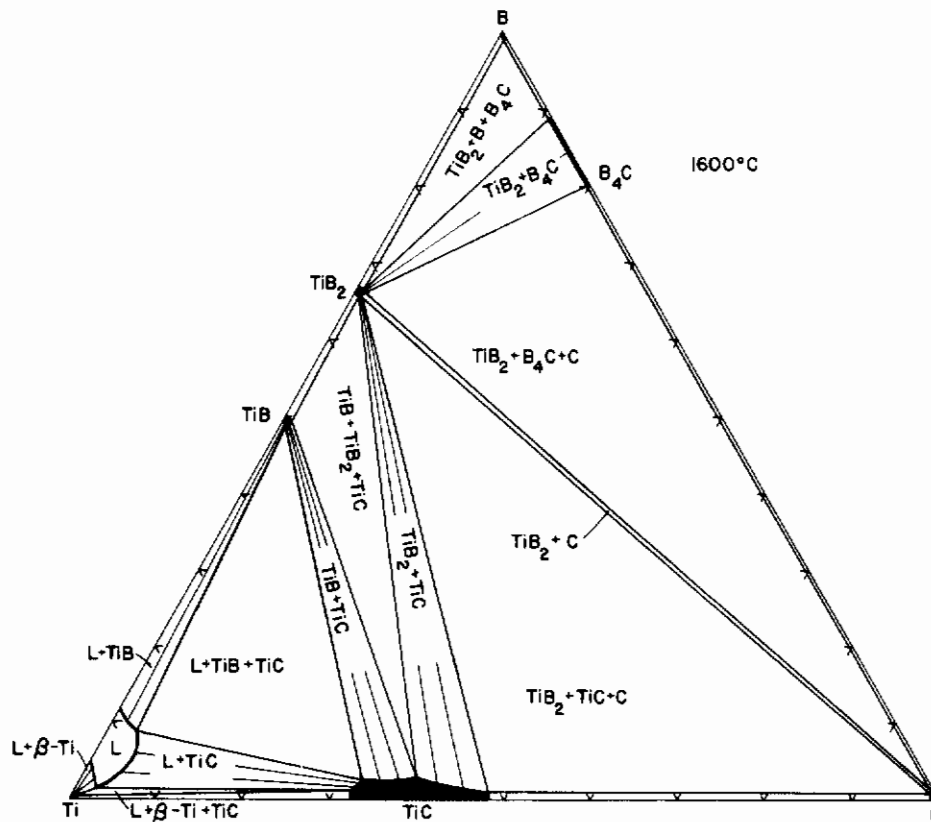


Figure 77(b) Isothermal Section at 1600°C.

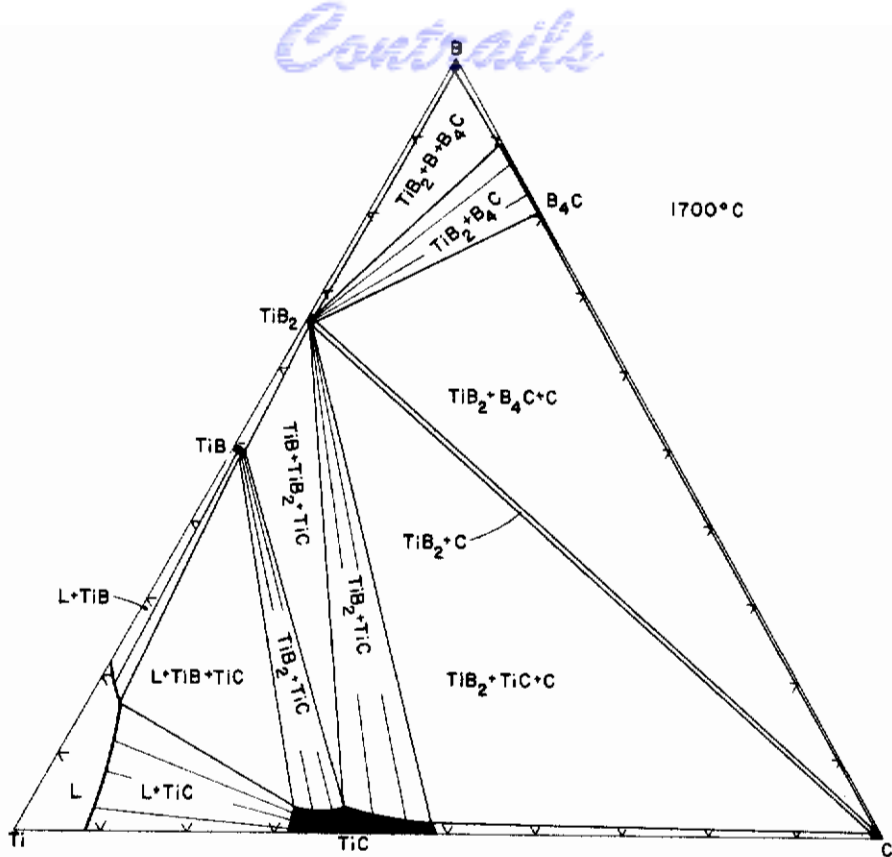


Figure 77(c) Isothermal Section at 1700°C.

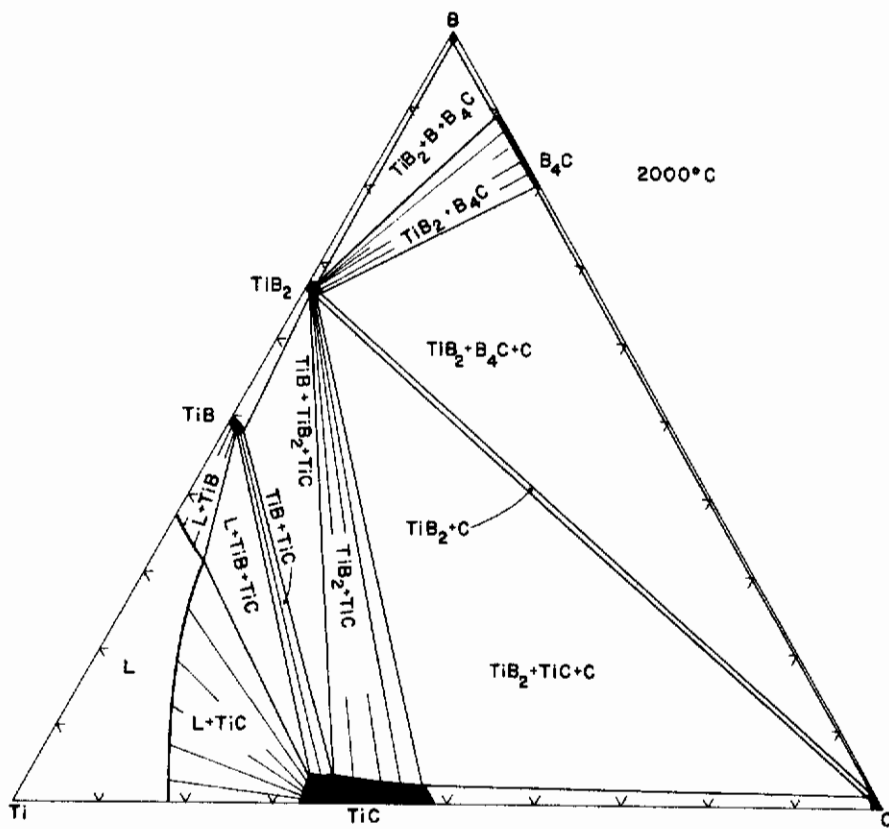


Figure 77(d) Isothermal Section at 2000°C.

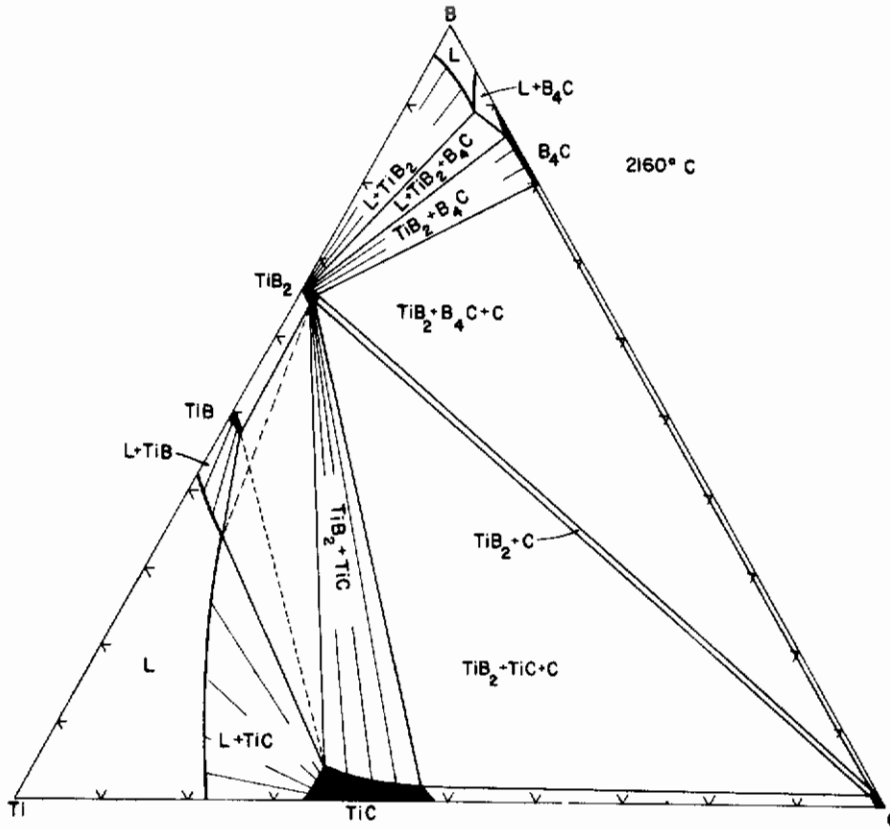


Figure 77(e). Isothermal Section at 2160°C.

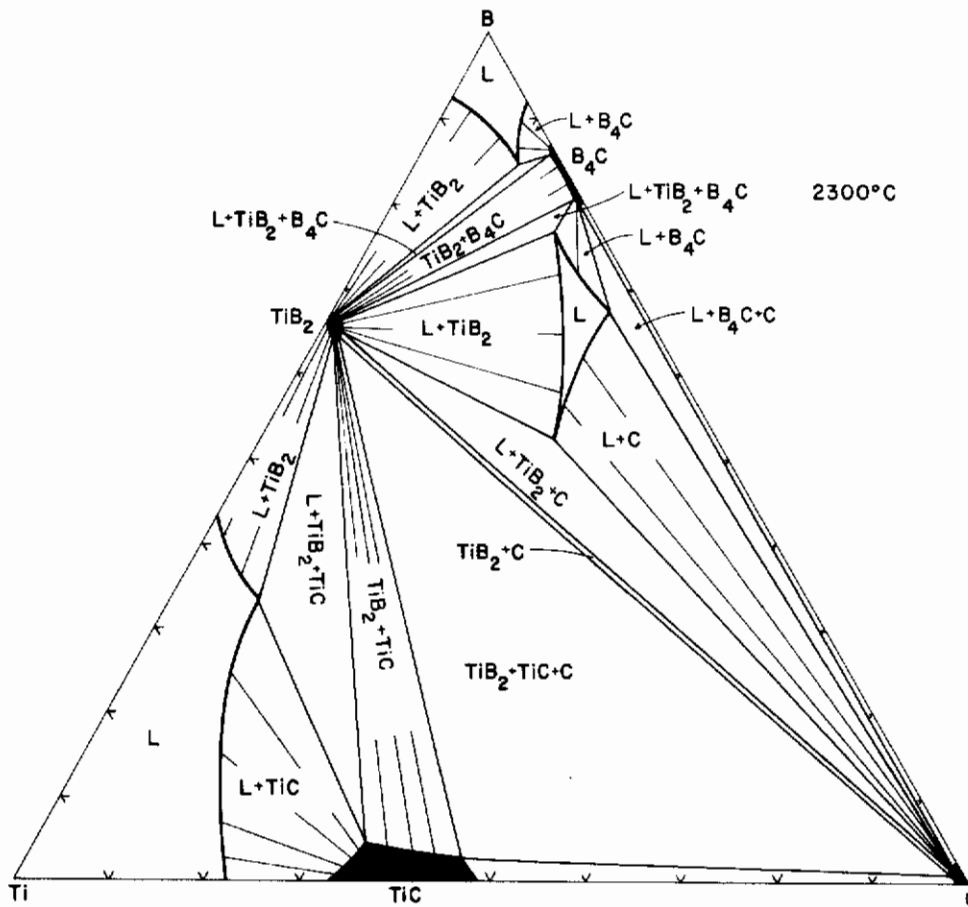


Figure 77(f). Isothermal Section at 2300°C.

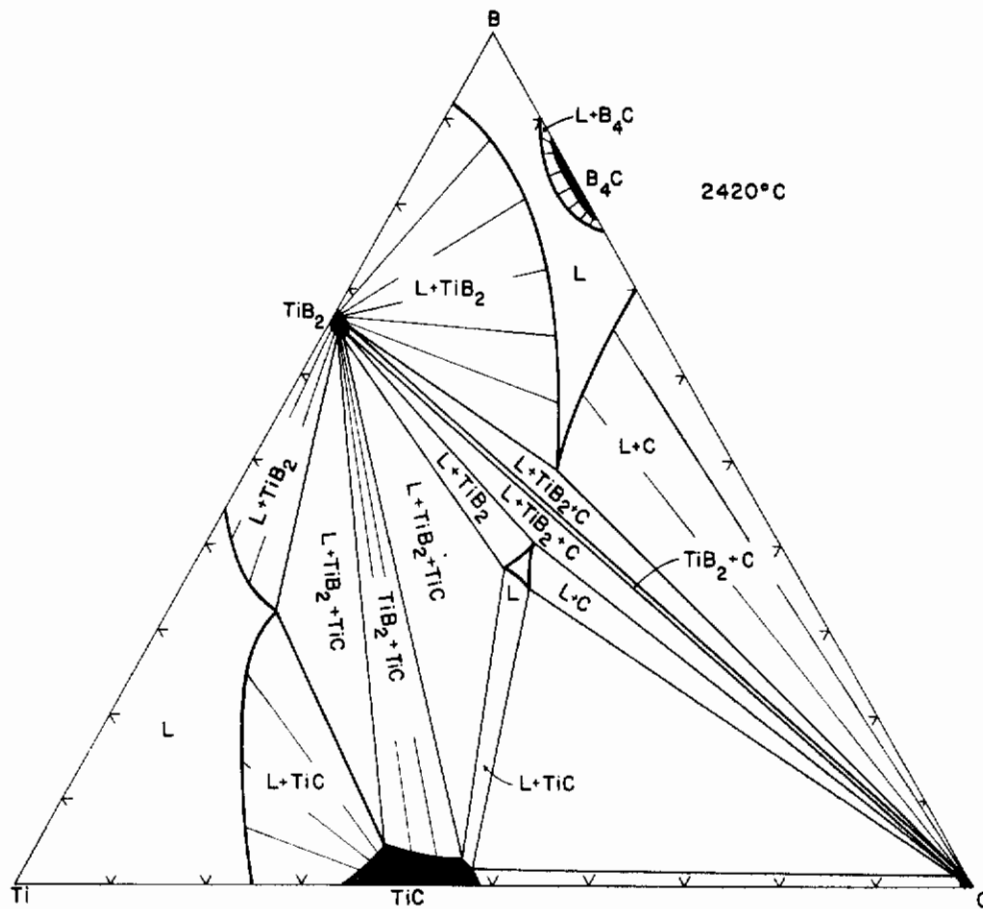


Figure 77(g). Isothermal Section at 2420°C.

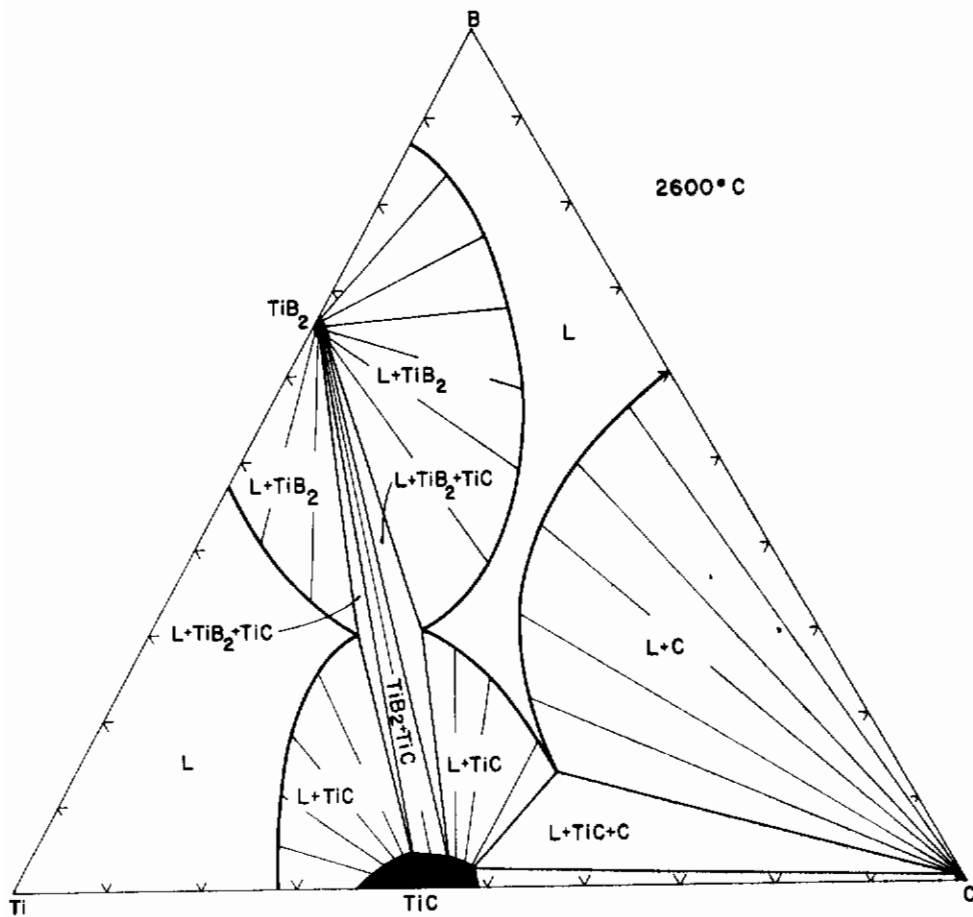


Figure 77(h). Isothermal Section at 2600°C.

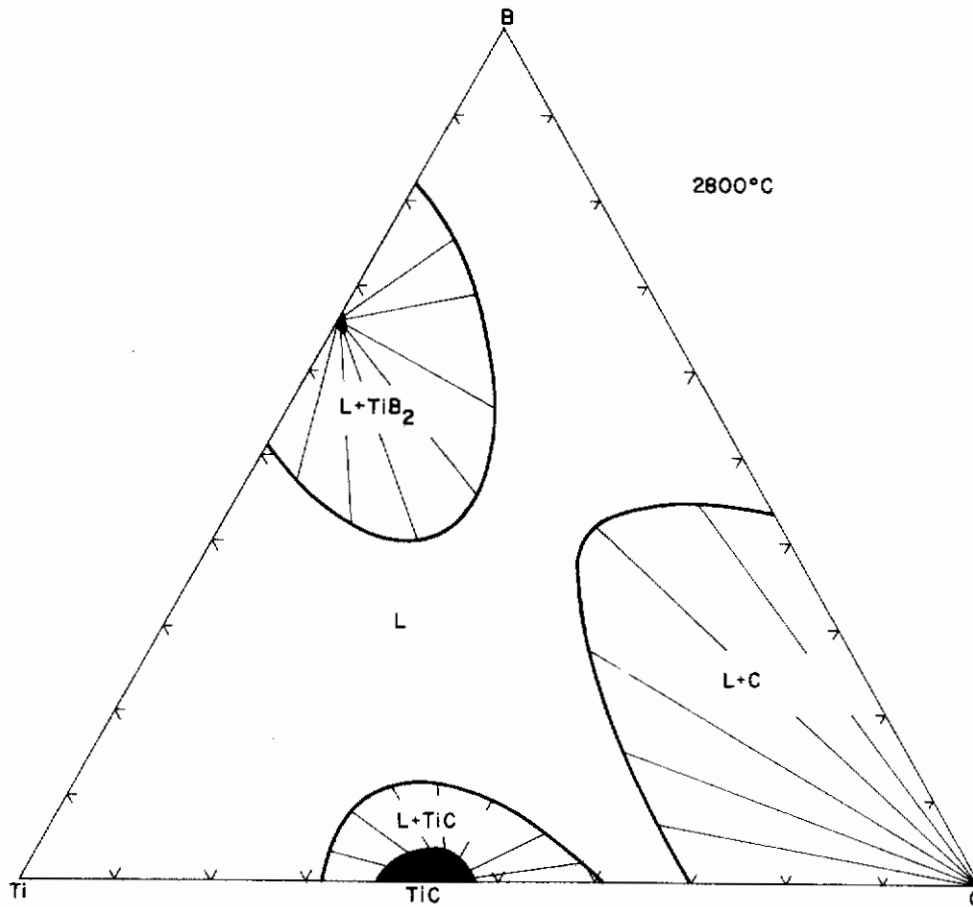


Figure 77(i) Isothermal Section at 2800°C.

Vertical sections (isopleths) are often useful in determining the temperature behavior of specific alloy compositions, or of alloys located along given concentration lines; three such section, covering in essence all the important equilibria in the system, have been prepared from the temperature sections, and are illustrated in Figures 3, 4, and 5.

Finally, the compositions of the melts participating in nonvariant equilibria ($p = \text{const}$), as well as the concentration lines for bivariant solidification (melting troughs), have been combined to yield the diagram shown in Figure 78.

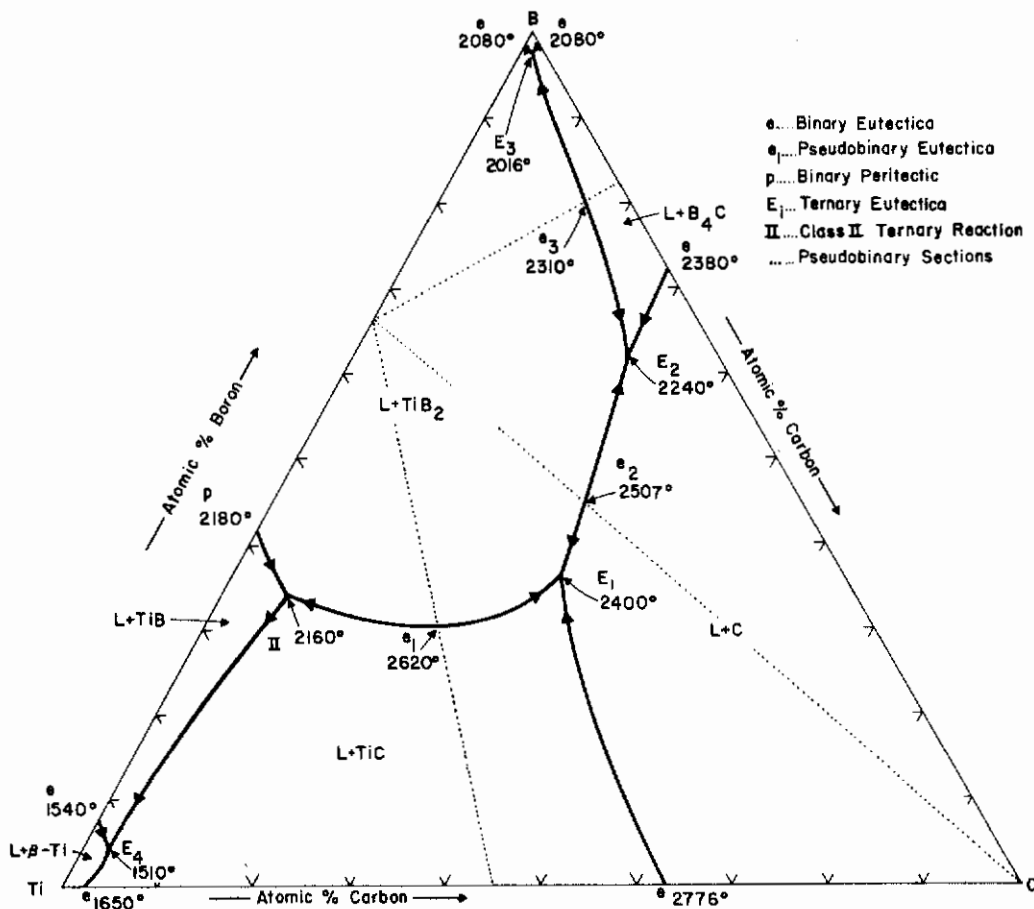


Figure 78. Ti-B-C: Melting Troughs and Compositions of the Melts Participating in Nonvariant ($p = \text{const}$) Equilibria.

B. ZIRCONIUM-BORON-CARBON

1. The Zirconium Phase

A study of the α - β -transformation reaction in zirconium in ternary alloys revealed practically no change with respect to the value of $872 \pm 15^\circ\text{C}$, obtained from a DTA-run on crystal-bar zirconium* (Figure 79).

*The specimen used for the DTA experiments was machined from a zirconium crystal bar obtained from Wah Chang Corporation, Albany, Oregon.

As a mean value of eight runs, a temperature of $880 \pm 15^\circ\text{C}$ was obtained in three-phased specimens $\text{Zr} + \text{ZrB}_2 + \text{ZrC}$ (Figure 80). Although, in view of the error limits in the measurements, a firm conclusion certainly cannot be drawn, the data suggest a peritectic-type of decomposition of the α -modification initiating at the binary Zr-B system, and extending to the edge binary Zr-C . As to be expected from the solubility data in the two boundary systems, the ternary solid solubility at the ternary eutectic temperature $\beta\text{-Zr} + \text{ZrB}_2 + \text{ZrC}$ in β -zirconium is below 1 atomic percent B-metal.

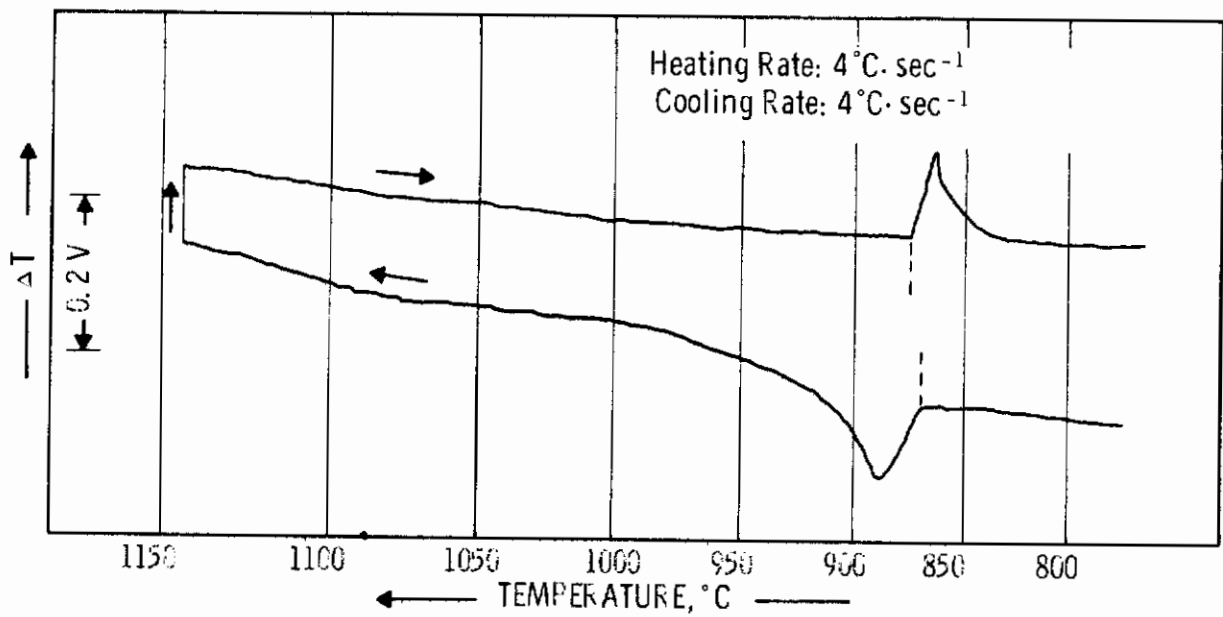


Figure 79. α - β (hcp — bcc) Transformation in Crystal Bar Zirconium.

2. Phase Equilibria in the Metal-Rich Portion of the System

Samples located within the concentration region $\text{Zr} + \text{ZrB}_2 + \text{ZrC}$, and which were equilibrated at 1400°C (Figure 81), or were melted (Table 33), contained only the above three phases. In the average, lattice parameters of $a = 3.238 \text{ \AA}$, and $c = 5.160 \text{ \AA}$ were measured for the zirconium phase

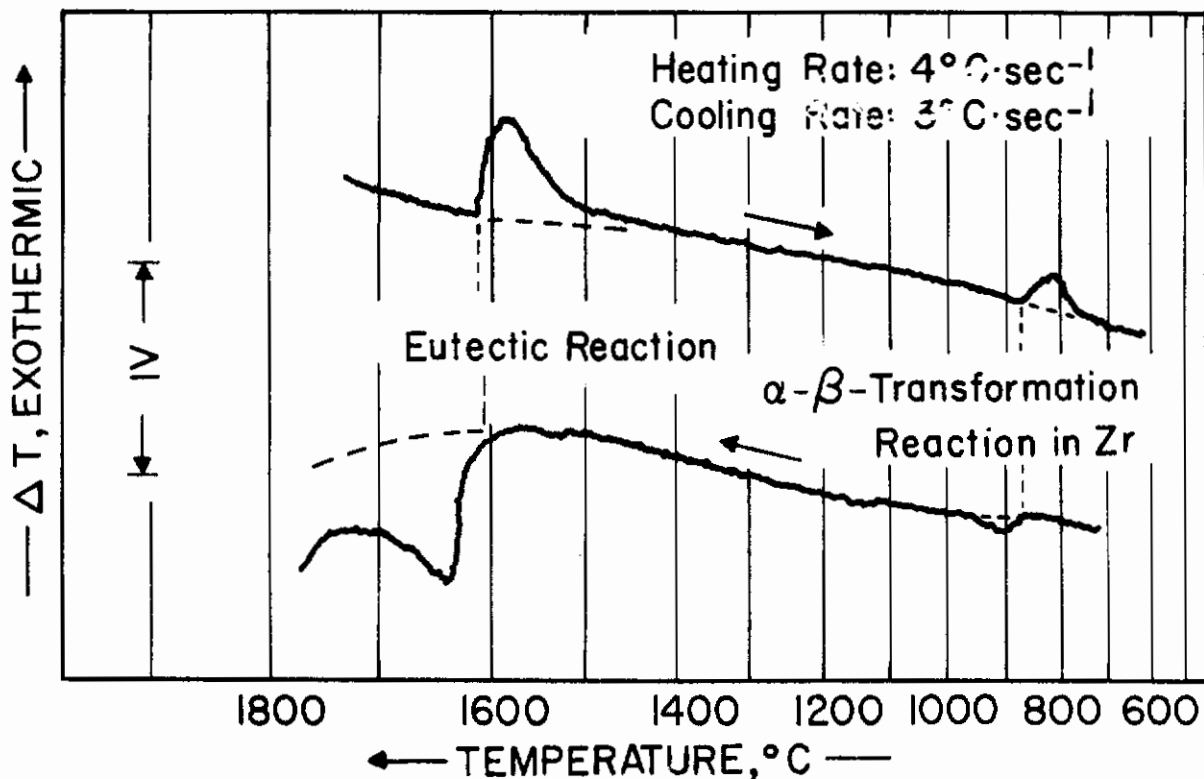


Figure 80. DTA-Thermogram of a Zr-B-C (65-18-17 At.%) Alloy.

and $a = 4.702 \text{ \AA}$, $c = 3.532 \text{ \AA}$ for zirconium diboride in an alloy series equilibrated and quenched from 1600°C. From these parameters, a significant semimetal exchange seems only to be indicated for the monocarbide phase.

From the melting point measurements (Table 33) as well as the differential-thermoanalytical studies (Figure 80), a temperature of 1615°C was derived for the eutectic reaction isotherm $L \rightarrow \beta\text{-Zr} + \text{ZrB}_2 + \text{ZrC}$. Although isothermal melting in the alloy Zr-B-C (88-10-2 At.%) indicated the approximate composition of the ternary eutectic point, the precise location by a metallographic analysis of the microstructures initially presented difficulties. The annealing reactions are very rapid (Figures 82 through 86), and the

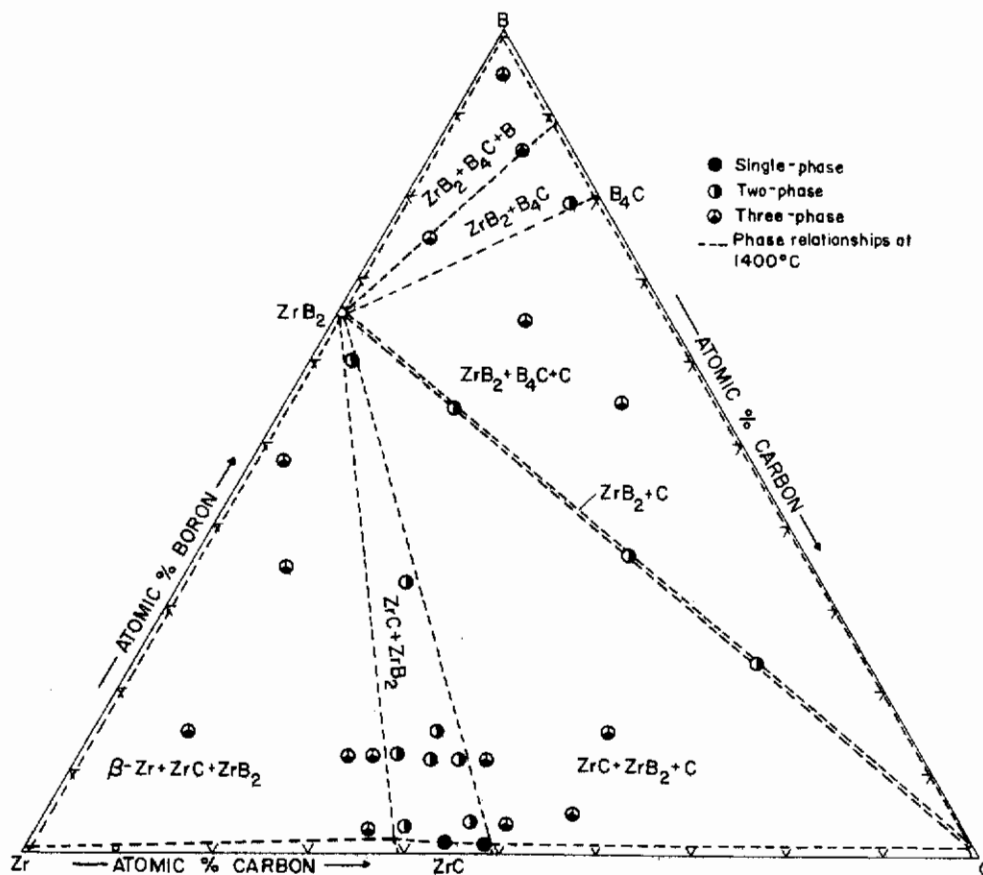


Figure 81. Zr-B-C: Location and Qualitative Phase Evaluation of the Alloys Equilibrated at 1400°C.

clustering tendency of the diboride resulted in poorly interpretable microstructures (Figures 83 and 84). Rapid quenching ($>150^{\circ}\text{C}$ per second) proved to be essential, in order to retain the structures in the as-crystallized state (Figures 87 through 89). The metal-rich eutectic trough, extending from the ternary eutectic to higher semimetal contents, proceeds close to the Zr-B edge binary, since carbon contents in excess of three atomic percent result in the presence of increasing amounts of primary crystallized monocarbide phase (Figures 90 through 93).

Table 33. Melting Temperatures and Phase Evaluation of Zirconium-Boron-Carbon Alloys

No.	Composition		Observed Melting Temperature, °C	Incipient Collapse	Phases Present After Melting			Lattice Parameters \bar{A}	Metallography
	Zr	B			C	Melting	Phase		
1	90	6	4	1740°	heterogeneous	a + δ + ρ	n. d.	β (prim) + ρ + δ	
2	85	5	10	1790° ↓	heterogeneous	a + δ + ρ	n. d.	ρ (prim) + eutectic.	
3	88	10	2	1615° ↓	sharp	a + δ + ρ	a = 3.240 a:c = 5.162	β + ρ + δ eutectic	
4	83	10	7	1660° ↓	heterogeneous	a + δ + ρ	n. d.	ρ (prim) + eutectic	
5	80	15	5	1650° ↓	sl. heterog	a + δ + ρ	a = 3.237 a:c = 5.159	ρ (prim) + bivar. eutec.	
6	70	10	20	1796° ↓	heterogeneous	a + δ + ρ	ρ :a = 4.702	ρ (prim) + bivar. eutec.	
7	70	20	10	1672° ↓	sl. heterog	a + δ + ρ	δ :a = 3.168 δ :c = 3.532	n. d.	
8	70	25	5	1676°	sl. heterog.	a + δ + ρ	ρ :a = 4.703	ρ + δ (prim) + β	
9	60	25	15	2077° ↓	very heterog	a + δ + ρ	ρ :a = 4.700	n. d.	
10	60	15	25	2030°	very heterog	a + δ + ρ	ρ :a = 4.704	n. d.	
11	60	8	32	2852° ↓	very heterog	a + δ + ρ	ρ :a = 4.704	ρ + little β + δ	
12	61	3	36	2898° ↓	very heterog	ρ	ρ :a = 4.696	ρ	
13	57	3	40	3385° ↓	very heterog	ρ	ρ :a = 4.700	ρ	
14	53	3	44	3388° ↓	very heterog	ρ	ρ :a = 4.703	ρ	
15	50	3	47	3265° ↓	very heterog	ρ	ρ :a = 4.703	ρ	
16	52	16	32	2900° ↓	heterogeneous	δ + ρ	ρ :a = 4.705	ρ (prim) + eutectic	
17	45	23	32	2842° ↓	sl. heterog.	δ + ρ	ρ :a = 4.699	ρ (prim) + eutectic	
18	50	30	20	2740°	very heterog.	δ + ρ	ρ :a = 4.705	δ + ρ + trace β	
19	46	30	23	2839° ↓	heterogeneous	δ + ρ	ρ :a = 4.704	ρ (prim) + eutectic	
20	43	30	27	2830° ↓	fairly sharp	δ + ρ	δ :a = 3.170 δ :c = 3.533	little (prim) ρ + eutec δ + ρ	

Table 33. (Continued)

No	Composition At. %			Observed Melting Temperature, °C	Incipient Collapse	Melting	Phases Present After Melting		
	X-ray						Lattice Parameters \bar{a}	Metallography	
	Zr	B	C						
21	42	37	21	2830° ↓	2830°	sharp	δ + ρ	δ: a = 3.169 c = 3.533	eutectic-type structure
22	41	42	17	2835° ↓	2835°	sharp	δ + ρ	δ: a = 3.169 c = 3.532	traces δ (prim) + eutec.
23	41	45	14	2918° ↓	2820°	sharp	δ + ρ	ρ: a = 4.703	δ (prim) + eutec.
24	47	46	7	2578° ↓	1642°	very heterog	α + δ + ρ	ρ: a = 4.704	n.d.
25	36	55	9	2908° ↓	2843°	heterogeneous	δ + ρ	δ: a = 3.171 c = 3.533	δ (prim) + eutec-type struct.
26	34	65	1	3120° ↓	1760°	very heterog	δ	a = 3.170 c = 3.533	δ
27	32	66	2	3200° ↓	2890°	very heterog	δ	a = 3.170 c = 3.532	δ + traces second phase
28	30	68	2	2873° ↓	2360°	very heterog	δ	a = 3.171 c = 3.533	δ + trace ω
29	32	15	18	2647° ↓	2397°	very heterog	δ + ρ + κ	a = 3.169 c = 3.532	n.d.
30	35	41	24	2682° ↓	2384°	very heterog	δ + ρ + κ	n.d.	n.d.
31	31	42	27	2418° ↓	2371°	heterogeneous	δ + ρ + κ	n.d.	ρ + δ (prim) + eutectic
32	26	43	31	2390° ↓	2368°	fairly sharp	δ + ρ + κ	n.d.	traces ρ + δ (prim) + eutec.
33	33	36	31	2478° ↓	2364°	heterogeneous	δ + ρ + κ	n.d.	n.d.
34	28	35	37	2395° ↓	2385°	fairly sharp	δ + ρ + κ	n.d.	ρ + C(prim) + eutectic
35	33	30	37	2437° ↓	2374°	heterogeneous	δ + ρ + κ	ρ: a = 4.701	ρ(prim) + κ (sec) + eutec.
36	35	20	45	2490° ↓	2385°	very heterog	δ + ρ + κ	ρ: a = 4.700	ρ + κ (prim) + eutectic
37	35	10	55	2590° ↓	2413°	very heterog	δ + ρ + κ	ρ: a = 4.702	ρ + κ (prim) + eutectic
38	13	27	60	3135° ↓	2510°	very heterog.	δ + κ	a = 2.466 c = 6.723	κ (prim) + eutectic.

Table 33. (Continued)

No	Composition At. %			Observed Melting Temperature, °C	Phases Present After Melting			Metallography	
	Zr	B	C		Melting	X-ray			Lattice Parameters Å
						Phase			
39	17	33	50	2387°	2662° ↓	very heterog	δ + κ	δ: a = 3.170 c = 3.533	n. d.
40	20	40	40	2390°	2408° ↓	fairly sharp	δ + κ	n. d.	κ (prim) + eutectic
41	22	43	35	2390°	2390° ↓	sharp	δ + κ	n. d.	κ (prim) + eutectic
42	23	47	30	2402°	2425° ↓	heterogeneous	δ + κ	n. d.	δ + κ eutectic
43	25	50	25	2398°	2440° ↓	heterogeneous	δ + κ	δ: a = 3.168 c = 3.531	δ (prim) + eutectic
44	26	54	20	2415°	2445° ↓	heterogeneous	δ + κ	n. d.	n. d.
45	30	58	12	2466°	2645° ↓	very heterog	δ + κ	n. d.	n. d.
46	30	60	10	2433°	2550° ↓	very heterog	δ + trace	n. d.	n. d.
47	32	63	5	2475°	2955° ↓	very heterog	δ + trace	n. d.	n. d.
48	10	40	50	2308°	2686° ↓	very heterog	δ + κ + trace ω	a = 2.466 c = 6.720	κ (prim) + δ + ω
49	10	50	40	2190°	2461°	very heterog	δ + κ + ω	n. d.	κ (prim) + δ (sec) + eutec.
50	10	60	30	2200°	2322° ↓	very heterog	δ + κ + ω	n. d.	n. d.
51	23	71	6	2233°	2522° ↓	very heterog	δ + ω	δ: a = 3.168 c = 3.531	δ (prim) + eutectic
52	17	78	5	2193°	2305° ↓	very heterog	δ + ω + trace γ	n. d.	δ (prim) + γ + eutectic
53	15	75	10	2220°	2325°	heterogeneous	δ + ω	n. d.	δ (prim) + eutectic

Legend to Table

↓ Quenched
 α..... α-Zr-ss
 β..... β-Zr-ss
 δ..... ZrB₂

γ..... ZrB₁₂
 ε..... B
 ω B₄C

κ.....C
 ρ.....ZrC



Figure 82. Zr-B-C (94-3-3 At.%), Cooled with Approximately 20°C per Second from 1700°C.

X 700

β -Zr (Transformed, Dark Stained Matrix) + ZrB_2 (light) and ZrC (Grey).

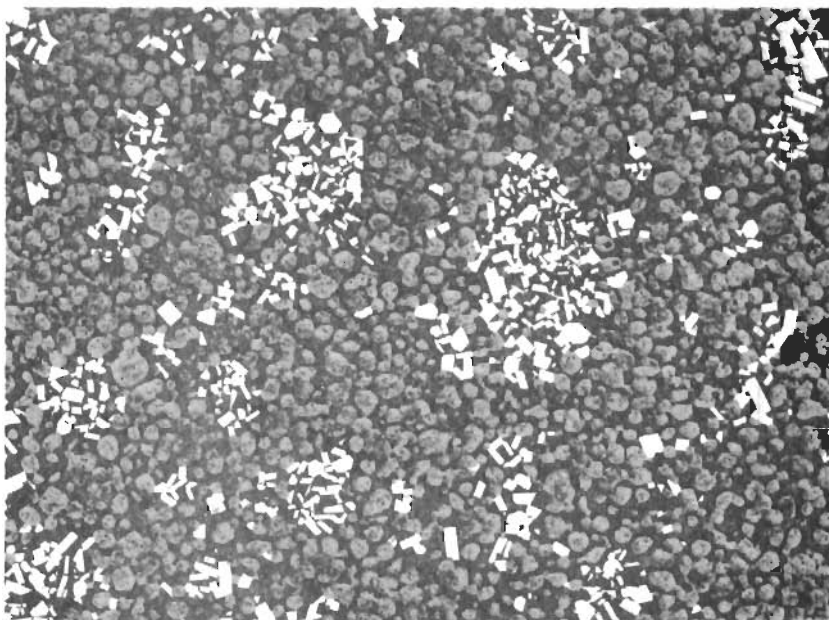


Figure 83. Zr-B-C (65-18-17 At.%), Cooled at Approximately 10°C per Second from 1800°C.

X275

Diboride Clusters (Light Crystals) and Monocarbide (Grey), in a Matrix of Zirconium (Stained Dark by Anodization).

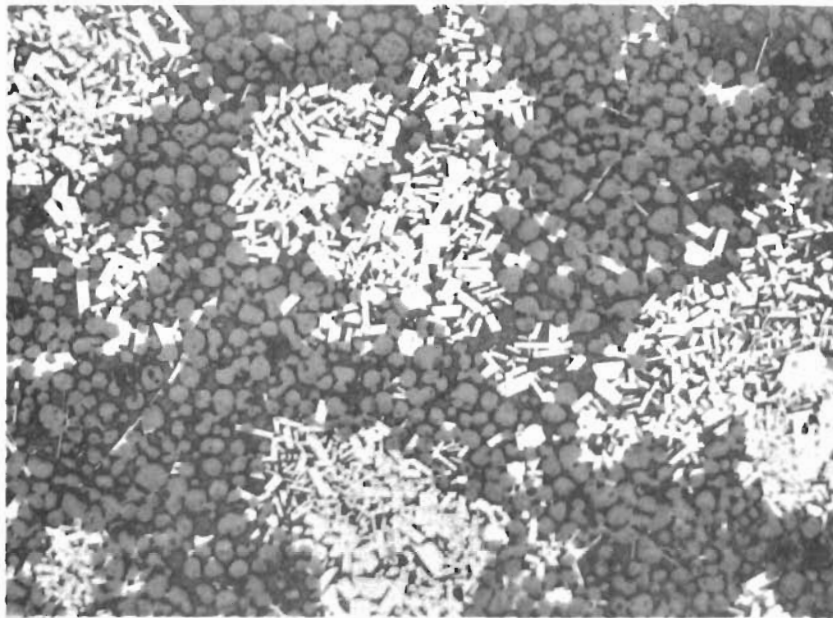


Figure 84. Zr-B-C (60-25-15 At.%), Cooled at Approximately 30°C per Second from 2050°C.

X300

Clustering of Diboride (Light) in a Three-Phased Alloy $ZrB_2 + ZrC + Zr$.

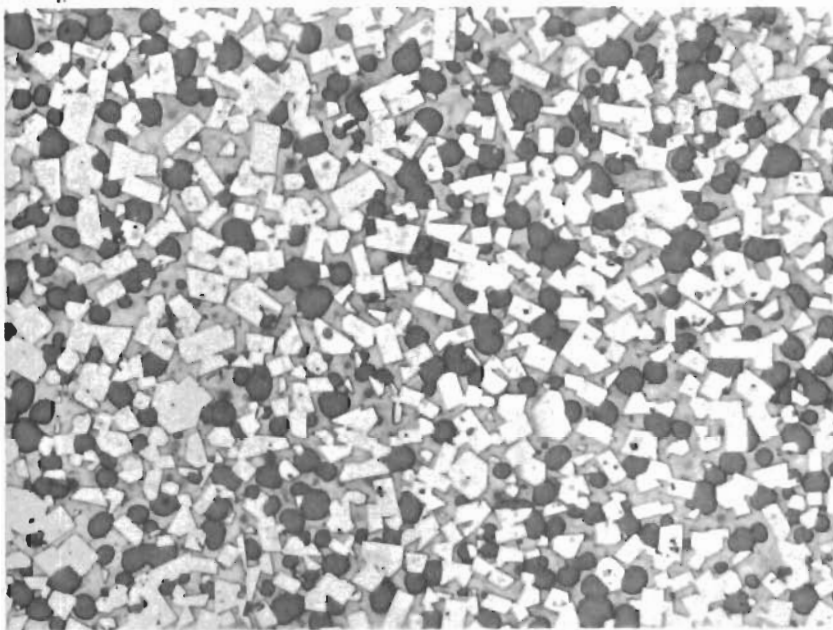


Figure 85. Zr-B-C (45-47-8 At.%), Cooled with Approximately 30°C per Second from 1800°C.

X400

Diboride (Light, Angular Crystals) and Round Monocarbide Grains in a Zirconium Matrix.

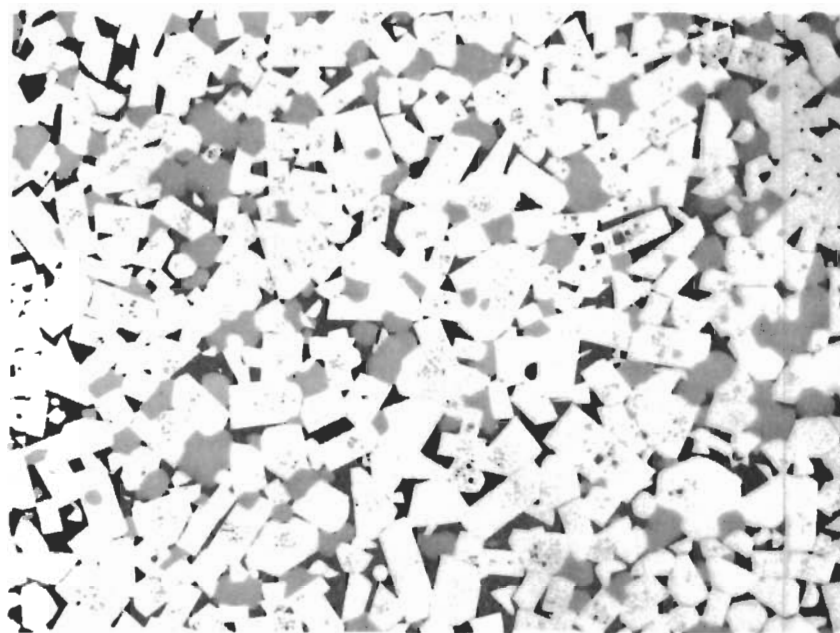


Figure 86. Zr-B-C (37-58-5 At.%), Cooled at Approximately 40°C per Second from 2800°C.

X450

Diboride (Light, Angular Grains) and Small Amounts of Monocarbide (Grey) and Zirconium (Dark).

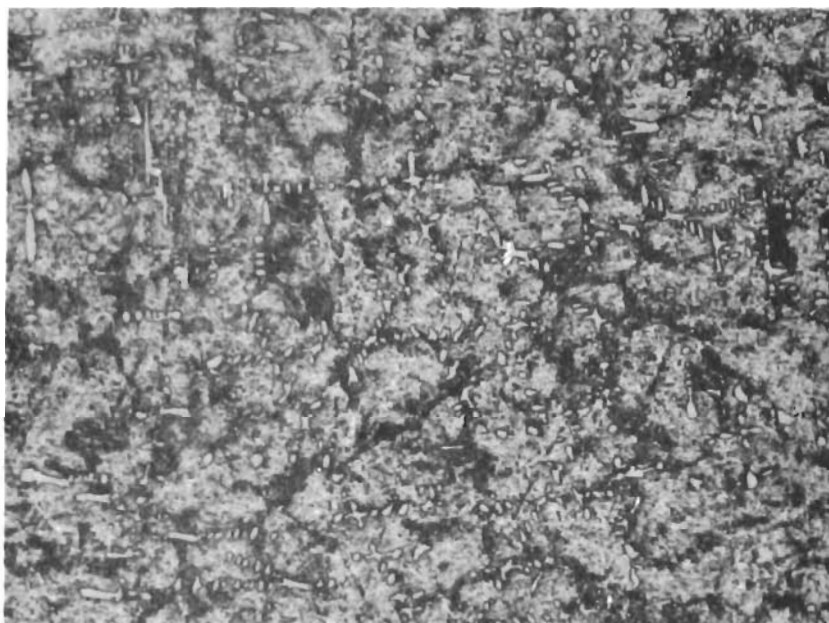


Figure 87. Zr-B-C (90-6-4 At.%), Quenched from 1750°C.

X600

Traces of Primary Monocarbide, Secondary Crystallized β -Zirconium (Transformed), and Ternary Eutectic β -Zr + ZrB₂ + ZrC.

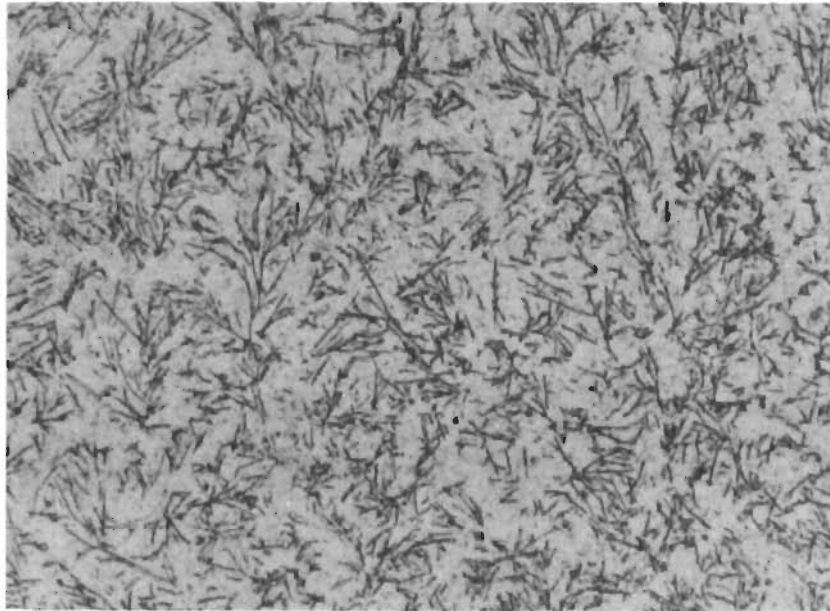


Figure 88. Zr-B-C (90-8-2 At.%), Quenched from 1700°C. X800
Small Amounts of Primary Zirconium and Ternary Eutectic.

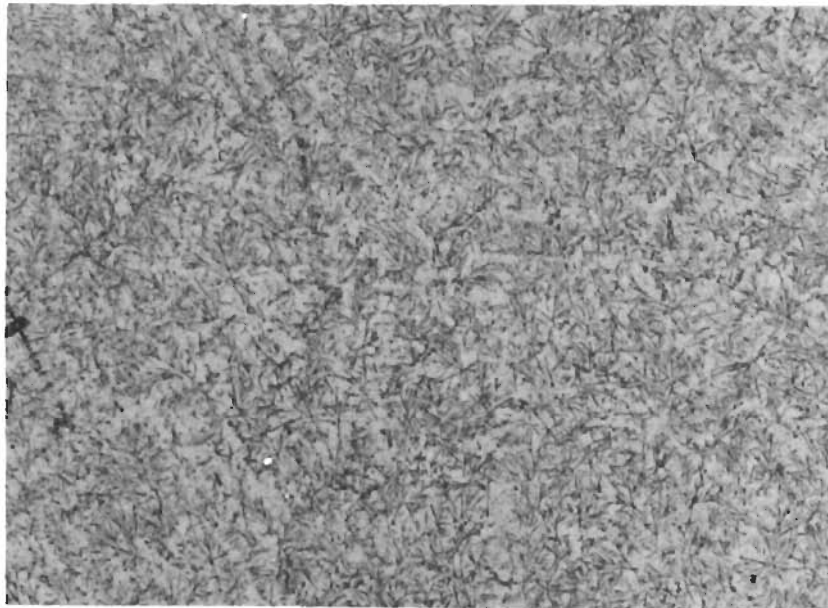


Figure 89. Zr-B-C (88-10-2 At.%), Quenched from 1615°C. X300
 $ZrB_2 + \beta\text{-Zr} + ZrC$ Ternary Eutectic.

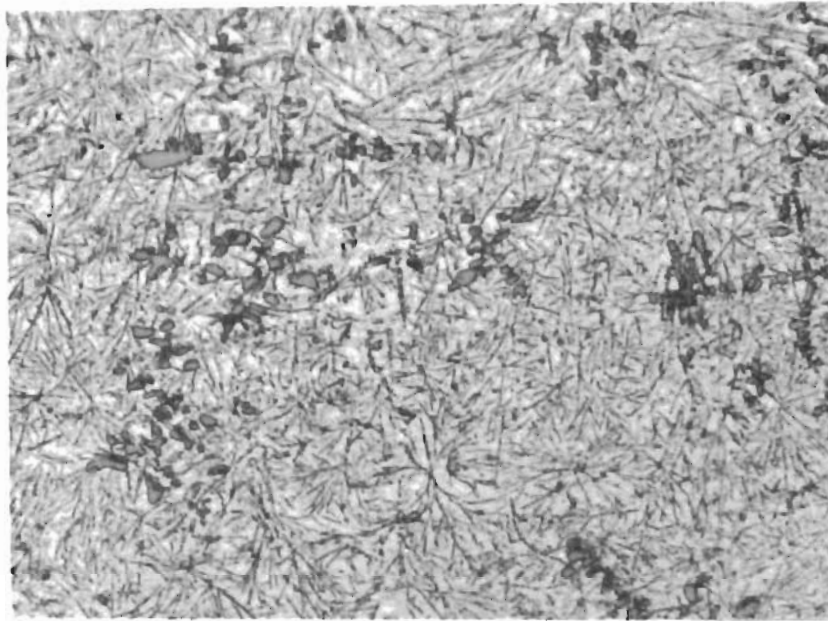


Figure 90. Zr-B-C (80-15-5 At.%), Quenched from 1650°C. X800
Small Amounts of Primary Carbide in a Eutectic Matrix.

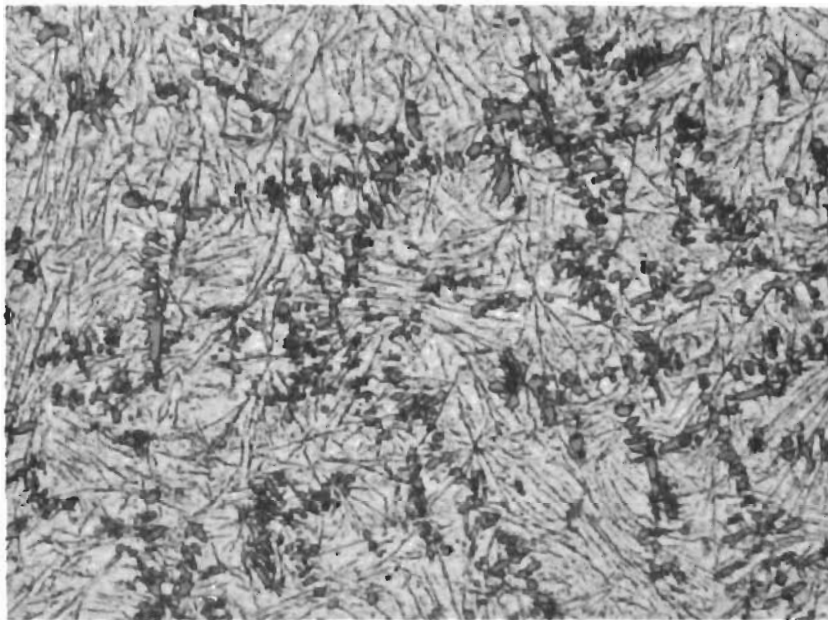


Figure 91. Zr-B-C (73-20-7), Quenched from 1700°C. X800
Primary Monocarbide and Eutectic.

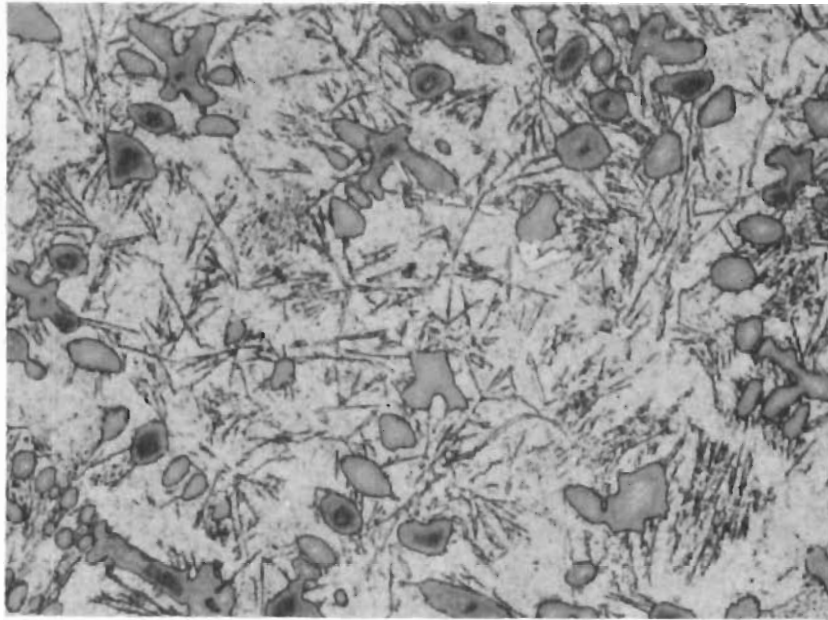


Figure 92. Zr-B-C (83-10-7 At.%), Quenched from 1690°C. X800
Primary Monocarbide, and β -Zr + ZrB + ZrC Eutectic.



Figure 93. Zr-B-C (70-10-20 At.%), Quenched from 1800°C. X400
Increased Amounts of Primary Monocarbide, and Ternary Eutectic.

3. The Pseudobinary Section Diboride-Monocarbide

Solid state-equilibrated, as well as melted, alloys located within the concentration field diboride-monocarbide were two-phased $Zr(C,B)_{1-x} + ZrB_2$. From the observed melting temperatures (Figure 94) and the metallographic analysis of the melted and quenched specimens (Figures 95 through 100), the pseudobinary eutectic point was located at 42 ± 2 mole percent $ZrC_{0.88}$.

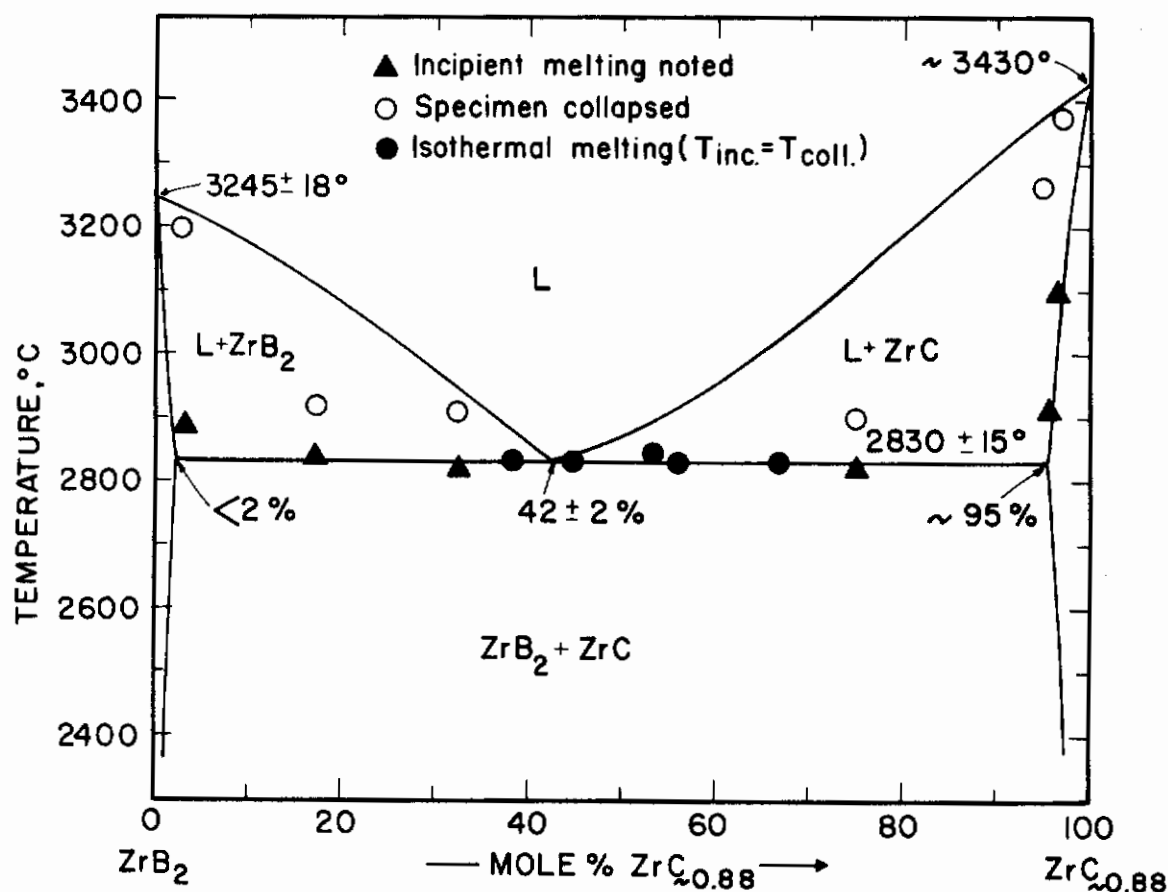


Figure 94. Melting Temperatures Along the Pseudobinary Section ZrB_2 - ZrC .

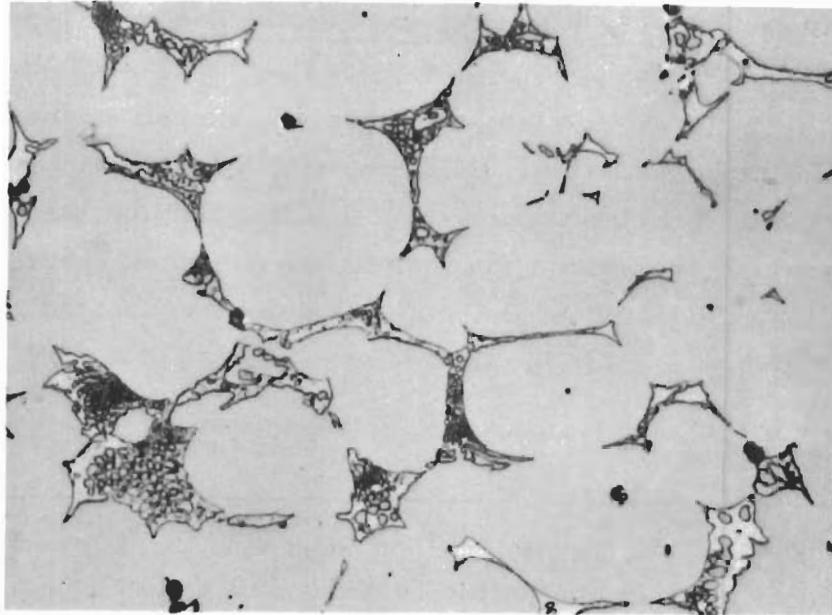


Figure 95. Zr-B-C (49-12-39 At.%), Quenched from 3080°C. X600

Primary Carbide with Pseudobinary $ZrB_2 + ZrC$ Eutectic at the Grain Boundaries.

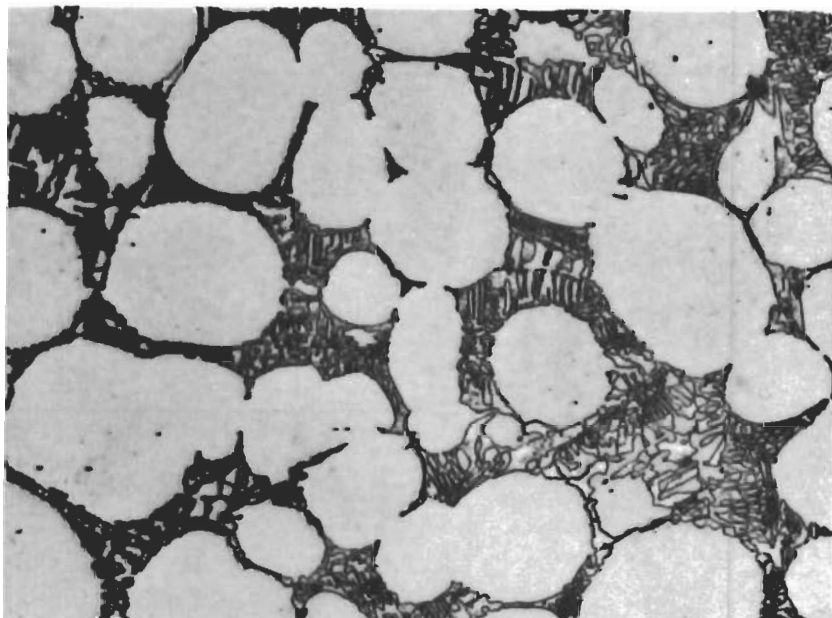


Figure 96. Zr-B-C (45-23-32 At.%), Quenched from 2842°C. X500

Primary Monocarbide in a Pseudobinary Eutectic Matrix.

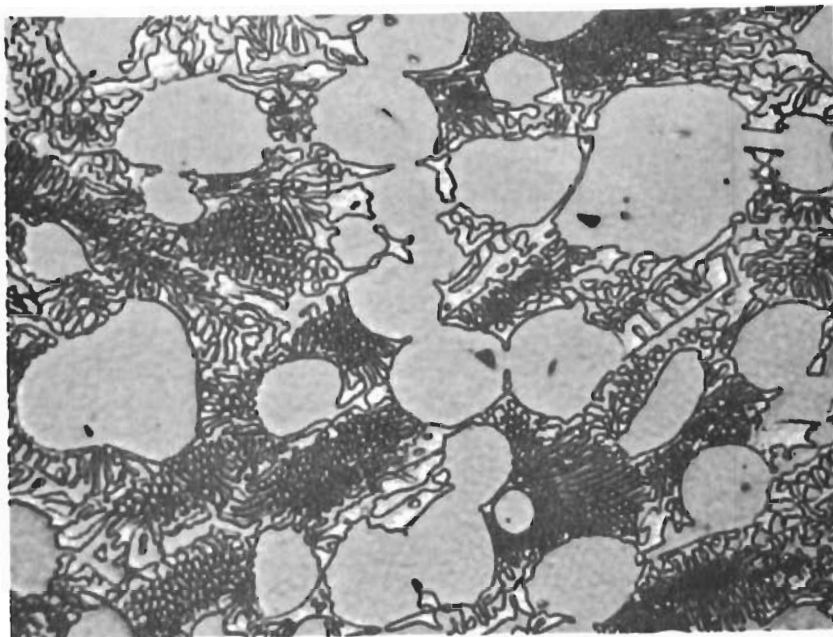


Figure 97. Zr-B-C (43-30-27 At.%), Quenched from 2830°C. X1000
Primary Monocarbide and Eutectic.

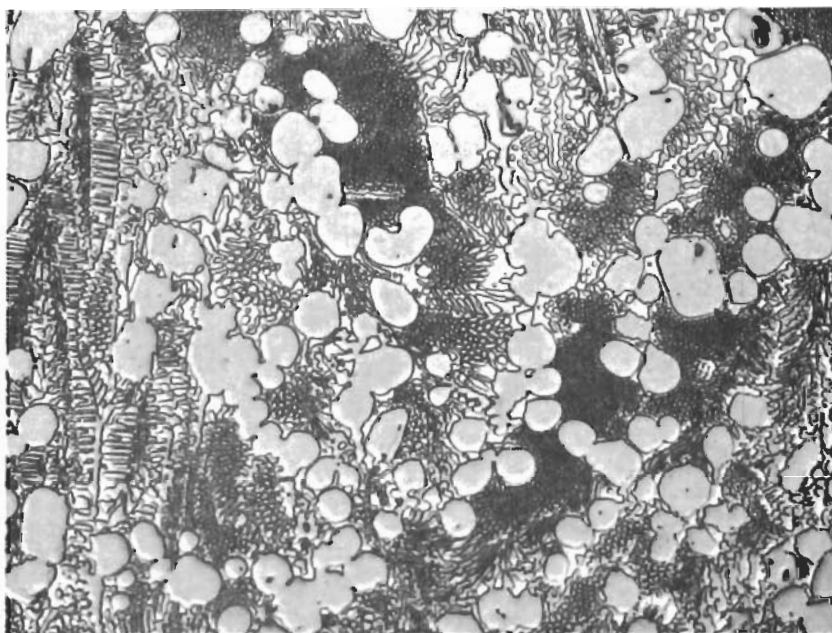


Figure 98. Zr-B-C (50-30-20 At.%), Quenched from 2740°C. X600
Primary Monocarbide in Bivariantly Solidified Eutectic.
Note: The specimen contains small amounts of excess Zirconium.

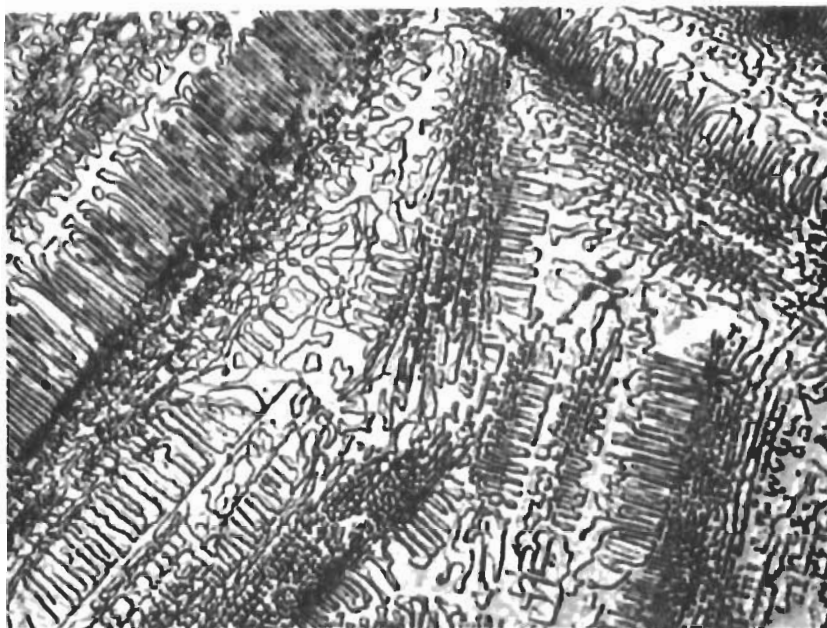


Figure 99. Zr-B-C (42-37-21 At.%), Quenched from 2830°C. X1000
Pseudobinary Eutectic ZrC + ZrB₂.

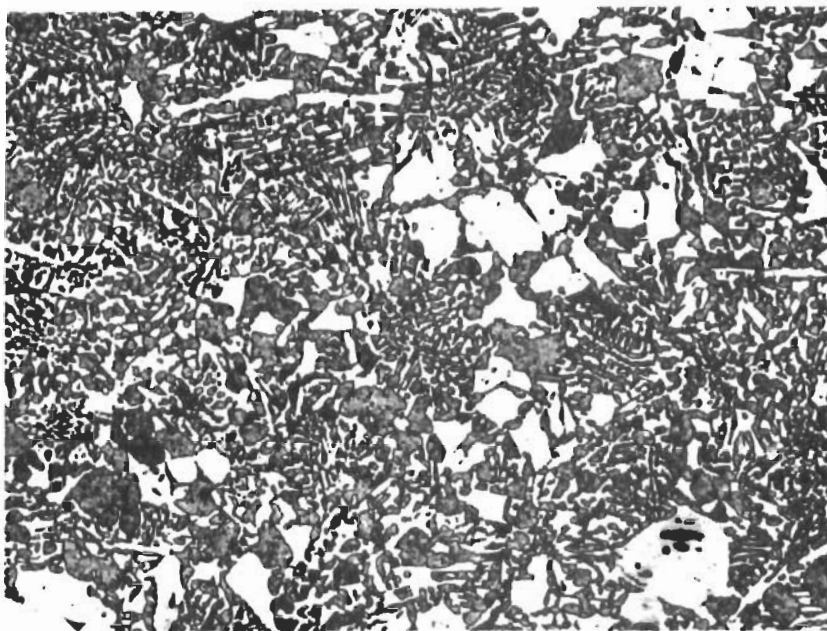


Figure 100. Zr-B-C (41-42-17 At.%), Cooled at Approximately 80°C per Second from 2835°C. X250
Primary ZrB₂ in a Partially Recrystallized Pseudobinary Eutectic Matrix ZrB₂ + ZrC.

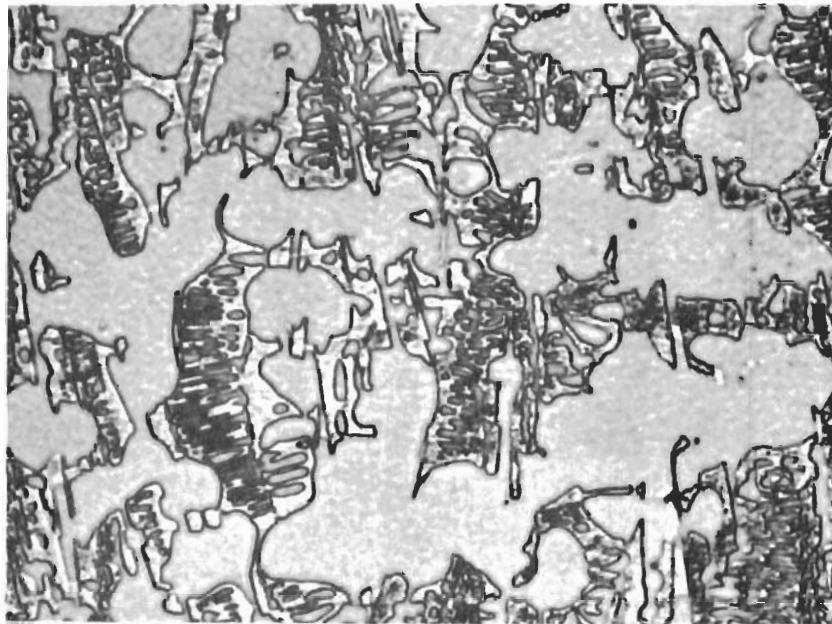


Figure 101. Zr-B-C (45-23-32 At.%), Cooled at Approximately 30°C per Second from 2840°C.

X1000

Primary ZrC in Partially Annealed $ZrB_2 + ZrC$ Eutectic.

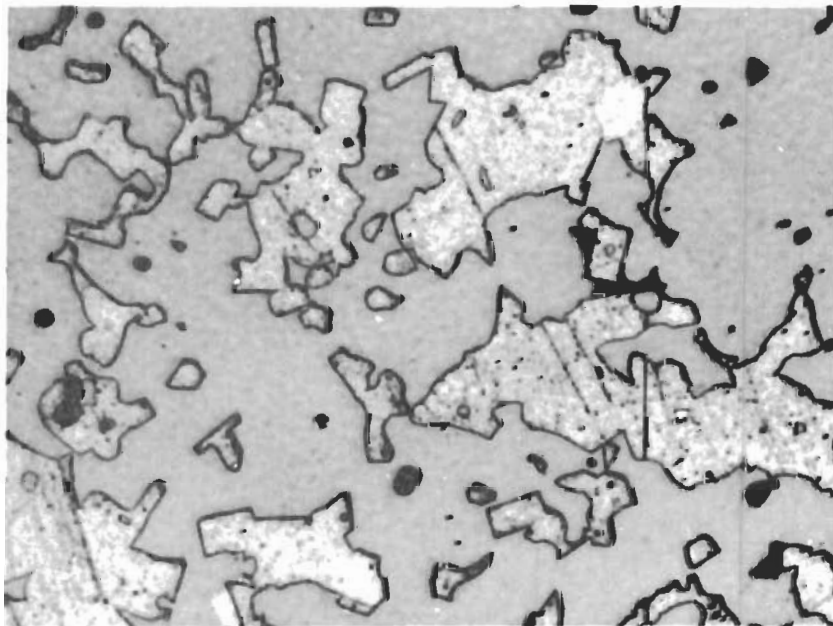


Figure 102. Zr-B-C (45-23-32 At.%), Cooled at Approximately 5°C per Second from 2840°C.

X1000

Primary ZrC and ZrB_2 . $ZrB_2 + ZrC$ Eutectic Completely Recrystallized.

Similar to the findings in the Ti-B-C system, discussed in the previous section, recrystallization of the eutectic structure at temperatures close to the eutectic line occurs extremely fast, and partially or complete annealed structures result, if cooling rates lower than approximately 30°C are employed (Figures 101 and 102).

An alloy series, located at 5 atomic percent boron across the homogeneity range of the binary monocarbide phase, was single phased after quenching from temperatures varying between 2900° and 3400°C (Figures 103 and 104). An alloy Zr-B-C (60-8-32 At.%), rapidly cooled from

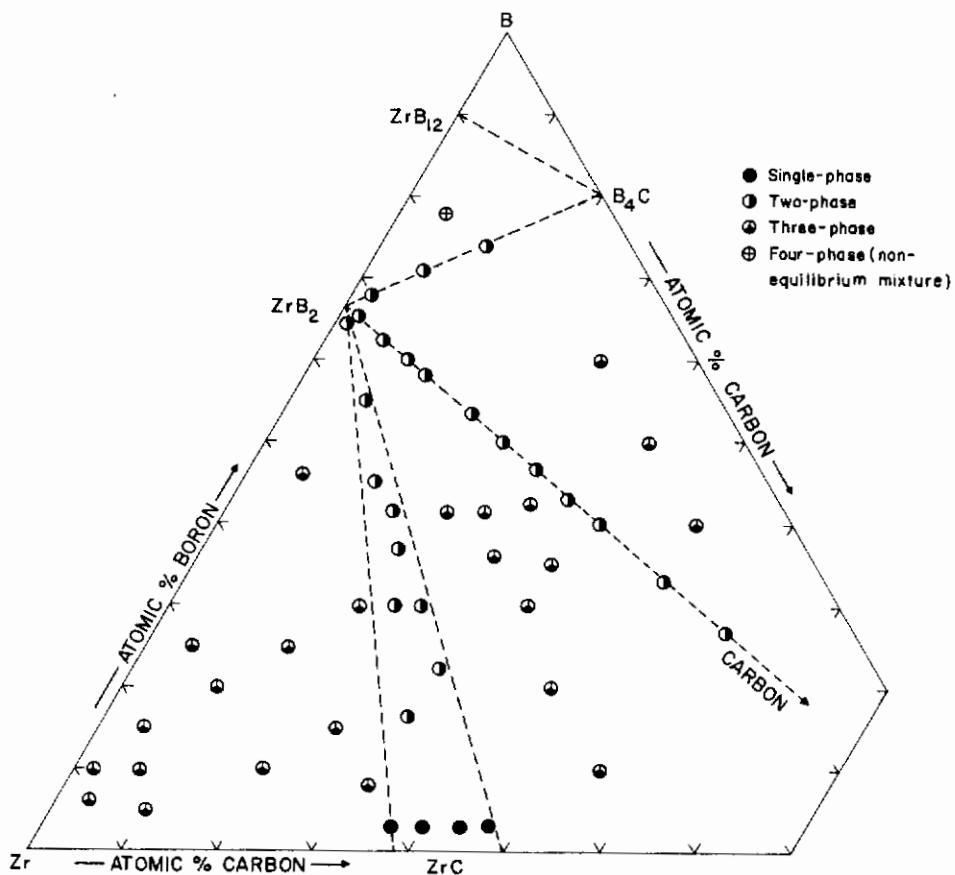


Figure 103. Zr-B-C: Location of Melting Point Samples, and Qualitative Phase Evaluation After Melting.

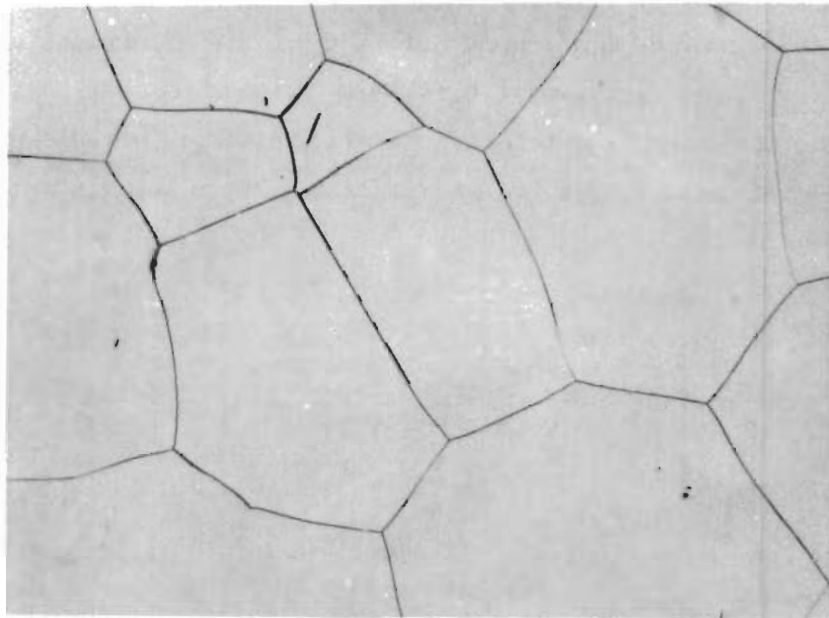


Figure 104. Zr-B-C (57-3-40 At.%), Quenched from 3385°C. X500
Single Phase Zirconium Monocarbide Solution.

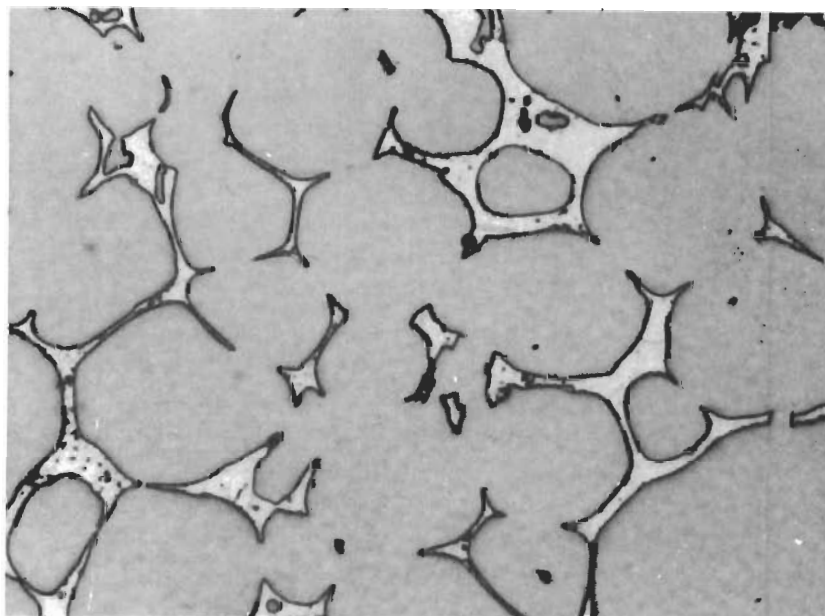


Figure 105. Zr-B-C (60-8-32 At.%), Cooled at Approximately 20°C per Second from 2850°C. X500
Monocarbide with Excess Metal and Traces of Diboride at the Grain Boundaries.

2850°C, was three-phased, but contained only minute quantities of diboride (Figure 105). The same alloy, after re-equilibration at 1600°C, shows considerable precipitation of diboride within the monocarbide grains (Figure 106). Compared to Ti-B-C alloys, boride precipitation from the zirconium monocarbide phase was slow.

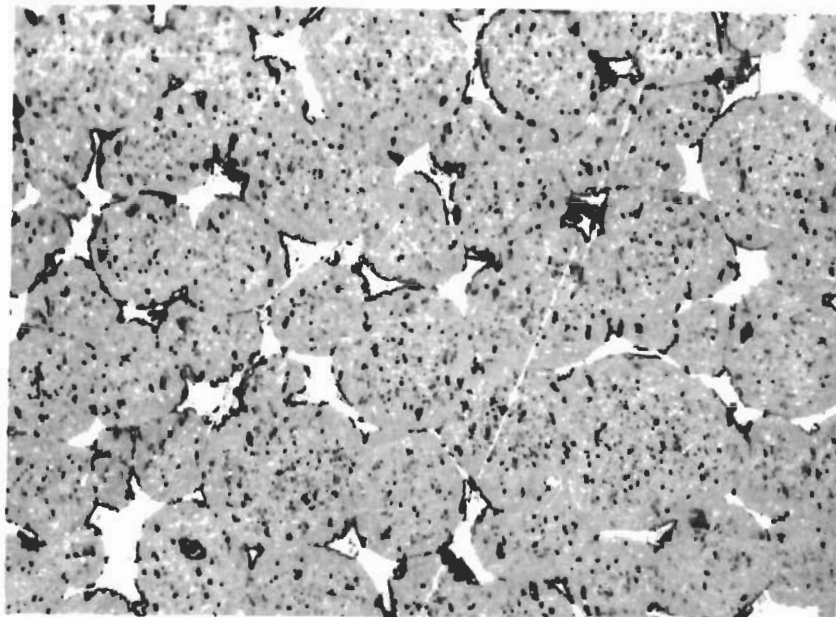


Figure 106. Zr-B-C (60-8-32 At.%), Sample from Figure 105 X550
Re-equilibrated for 15 Minutes at 1700°C, and
Cooled to Room Temperature.

4. The Pseudobinary Section Zirconium Diboride-Graphite

X-ray patterns prepared from molten, as well as solid state-equilibrated, alloys located along the concentration line diboride-graphite (Figures 81 and 94, Table 33) showed only the presence of these two phases. The lattice parameter changes with respect to the pure compounds were small, thus indicating only very nominal mutual solid solubilities.

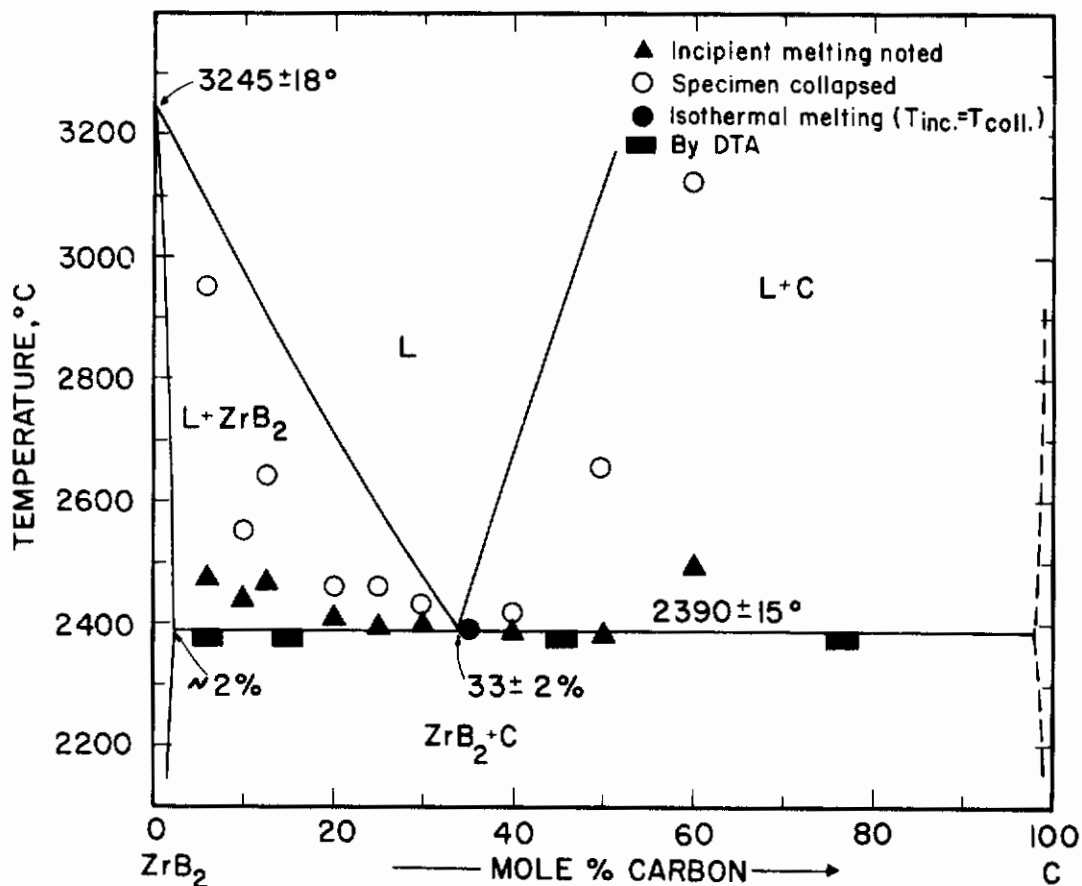


Figure 107. Melting Temperatures of Pseudobinary $ZrB_2 + C$ Alloys.

Melting of graphite-containing diboride alloys was extremely heterogeneous up to carbon concentrations of 20 mole percent, and incipient melting was difficult to note. Nevertheless, heterogeneity, i.e. eutectic melting definitely could be discerned in a DTA-run on an alloy containing 6 mole percent graphite (Figure 107). In general, the data obtained by differential-thermoanalytical techniques, of which a reproduction of a typical recorder trace is shown in Figure 108, were in excellent agreement with the values determined by the Pirani-method (Figure 107 and Table 33). Alloys in the concentration range from 30 to 40 mole percent carbon melted fairly isothermal, indicating that the eutectic must be located somewhere between these compositions. The concentration of the pseudobinary eutectic finally was bracketed to between $33 \pm 2\%$ by metallographic examination of the molten and quenched alloys (Figures 109 through 111).

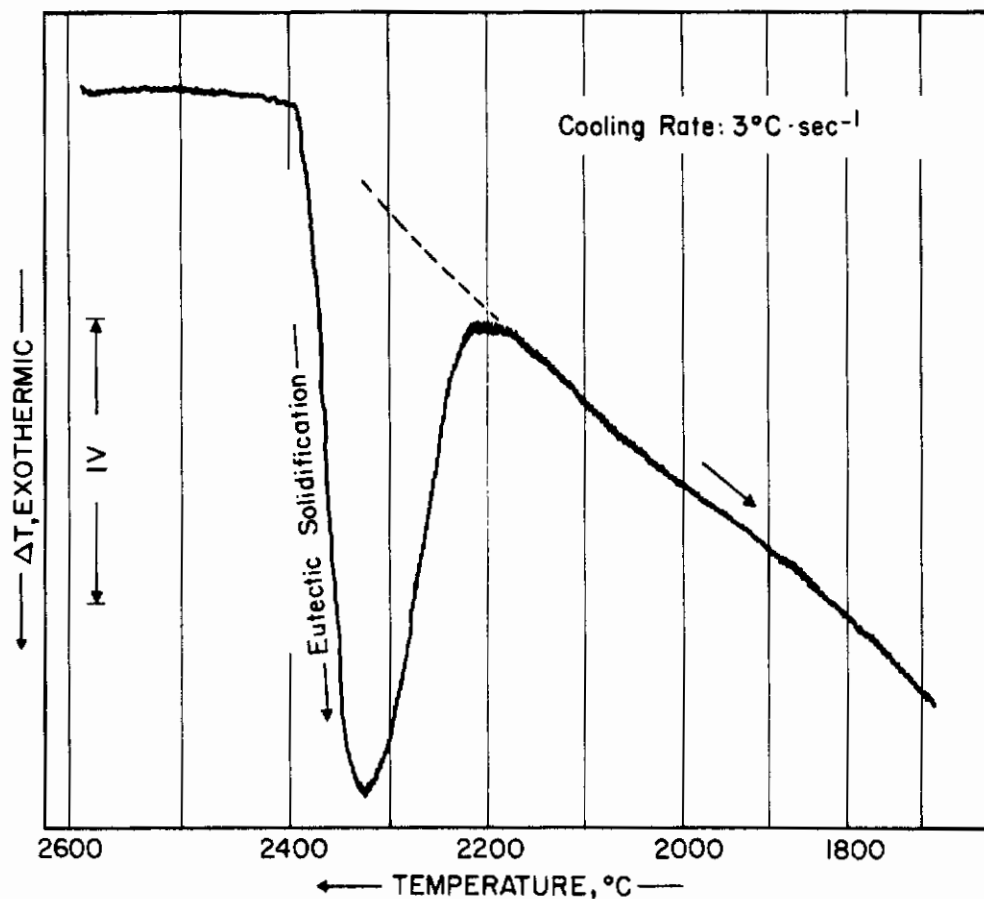


Figure 108. Pseudobinary Eutectic Solidification at 2390°C in a Zr-B-C (31-63-6 At.%) Alloy.

5. The Pseudobinary Section Diboride-Boron Carbide

Incipient melting in two-phased alloys $ZrB_2 + B_4C$ was noted at 2193° and 2220°C in two melting point specimens (Table 33 and Figure 112). Although specimens richer in boron carbide were initially prepared, their electrical conductivity was too low to allow measurements to be carried out in the Pirani furnace. An additional datum point on a high- B_4C alloy, which is in close agreement with the aforementioned melting point data, was obtained by differential thermal analysis (Figure 113). The eutectic

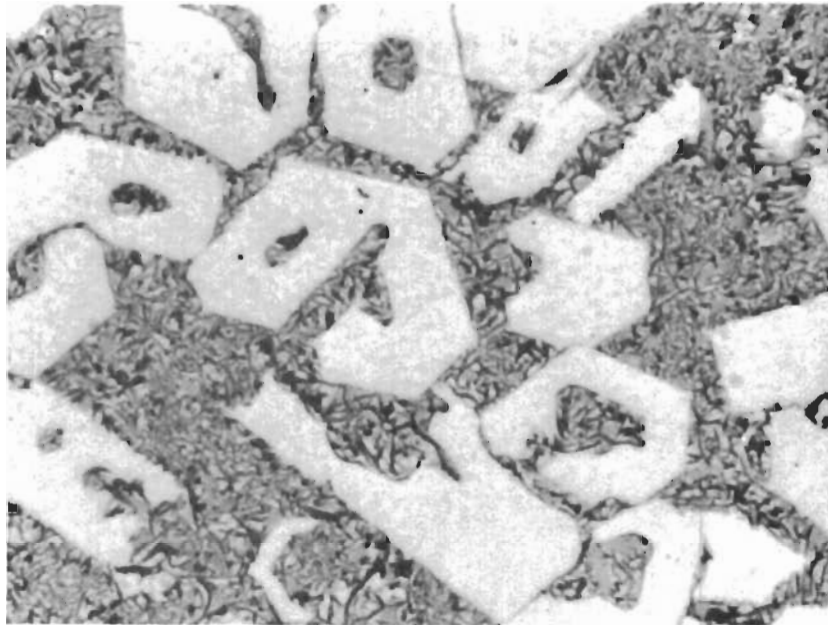


Figure 109. Zr-B-C (26-54-20 At.%), Quenched from 2445°C. X625.

Primary ZrB_2 and $ZrB_2 + C$ Eutectic.

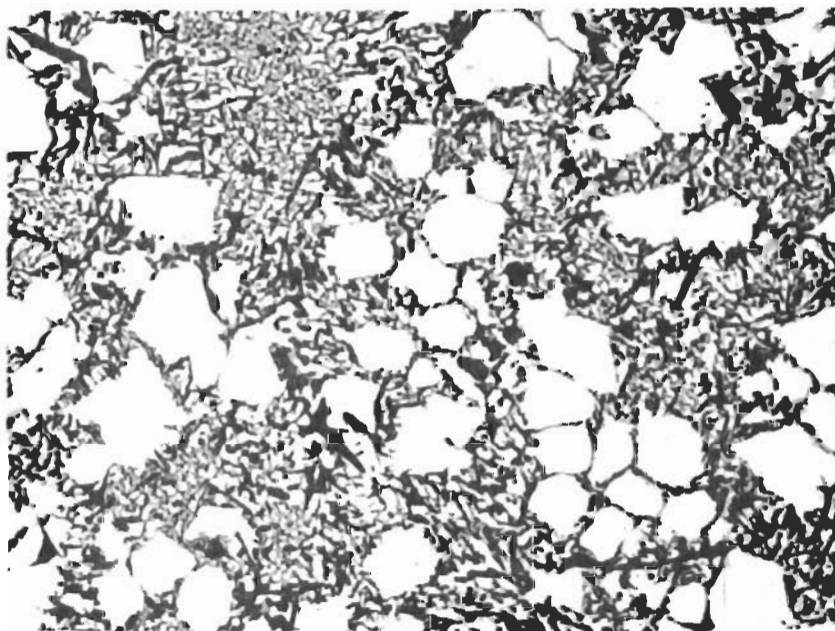


Figure 110. Zr-B-C (23-47-30 At.%), Quenched from 2425°C. X400

Primary Diboride and Eutectic.

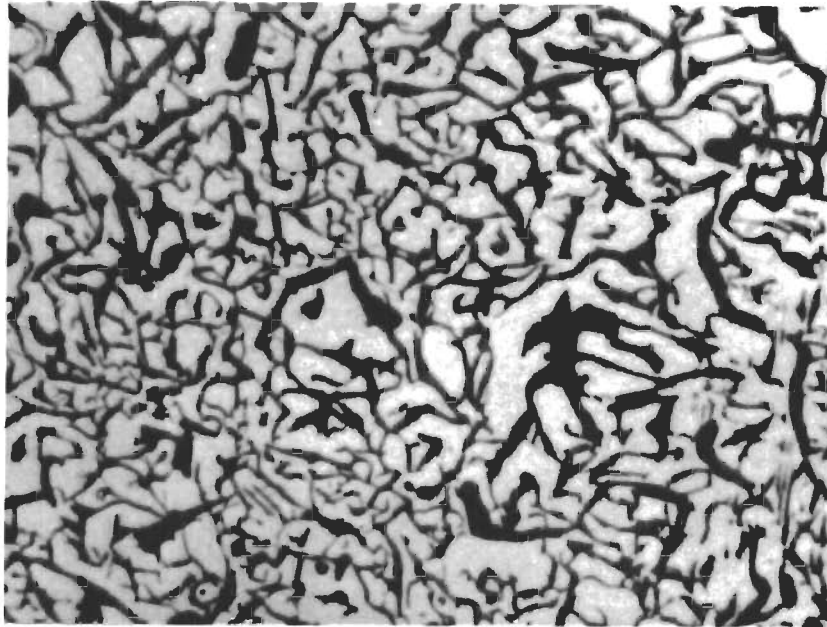


Figure 111. Zr-B-C (22-43-35 At.%), Quenched from 2390°C. X1000
Trace of Primary Graphite in a Matrix of Pseudobinary Eutectic $ZrB_2 + C$.

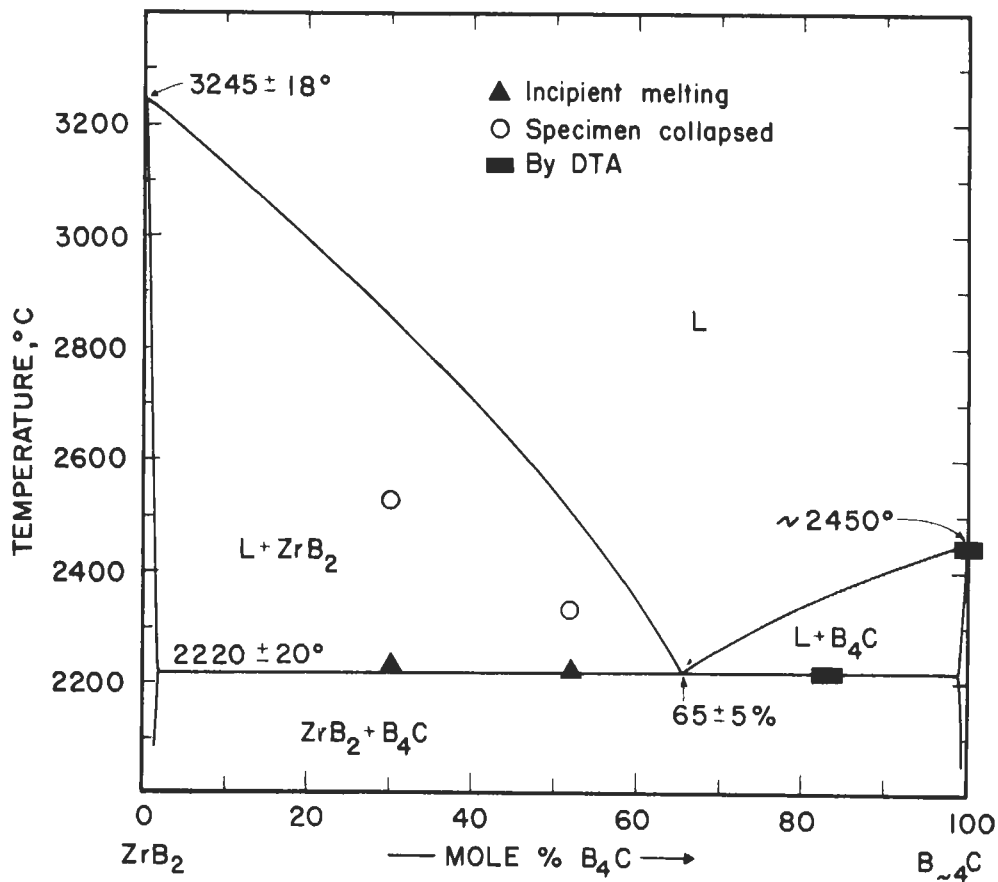


Figure 112. Melting Temperatures of Pseudobinary $ZrB_2 + B_4C$ Alloys.

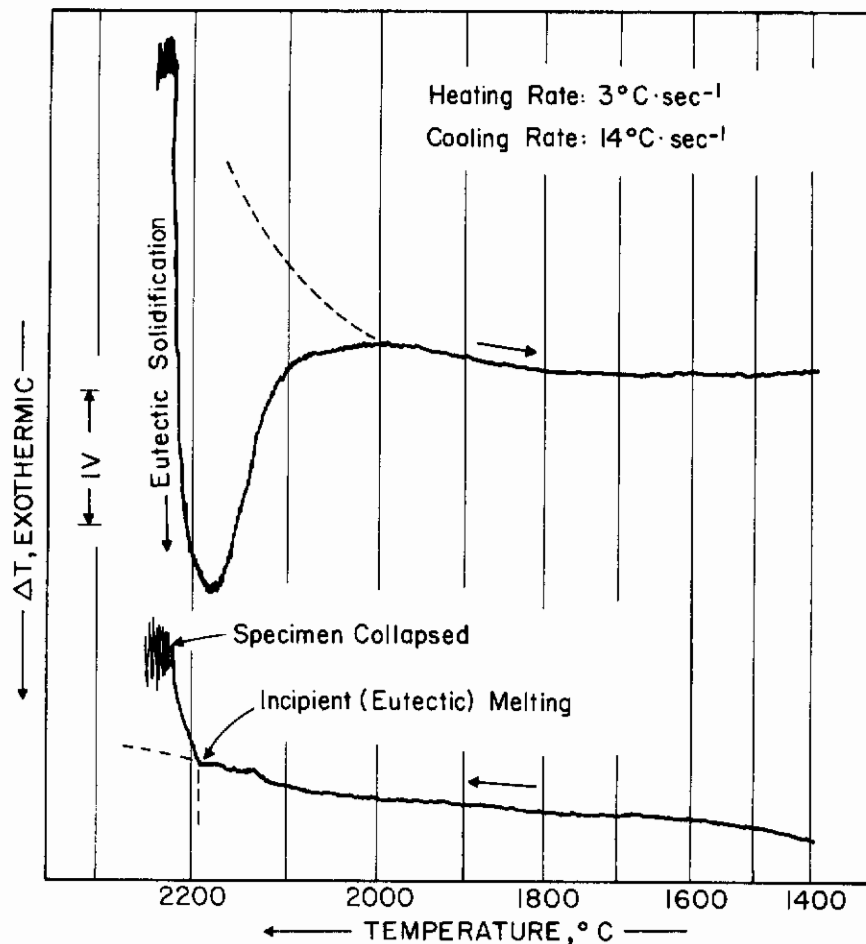


Figure 113. DTA-Thermogram of a Zr-B-C (5-78-17 At. %), Alloy, Showing Pseudobinary Eutectic Melting (Heating) and Solidification (Cooling) Along the Section $\text{ZrB}-\text{B}_4\text{C}$.

composition was located at approximately 65 mole percent B_4C primarily by metallographic inspection of a series of arc molten alloys located along the pseudobinary concentration line (Figure 114 through 117). As evidenced by the micrographs shown in Figures 116 and 118a, the eutectic structure consists of fibrillous zirconium diboride, embedded in a continuous matrix of B_4C . Eutectic colonies, differing in their orientation, usually are separated by a characteristic zone of diboride-free boron carbide (Figure 118 b).

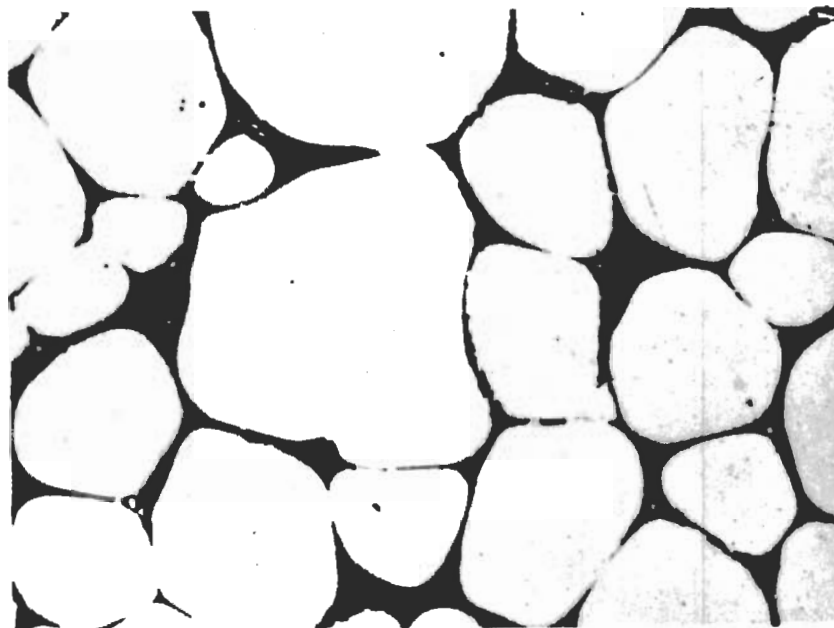


Figure 114. Zr-B-C (28-69-3 At.%), Arc-Melted and Quenched. X600
Primary Diboride and Smaller Amounts of $ZrB_2 + B_4C$
Eutectic.

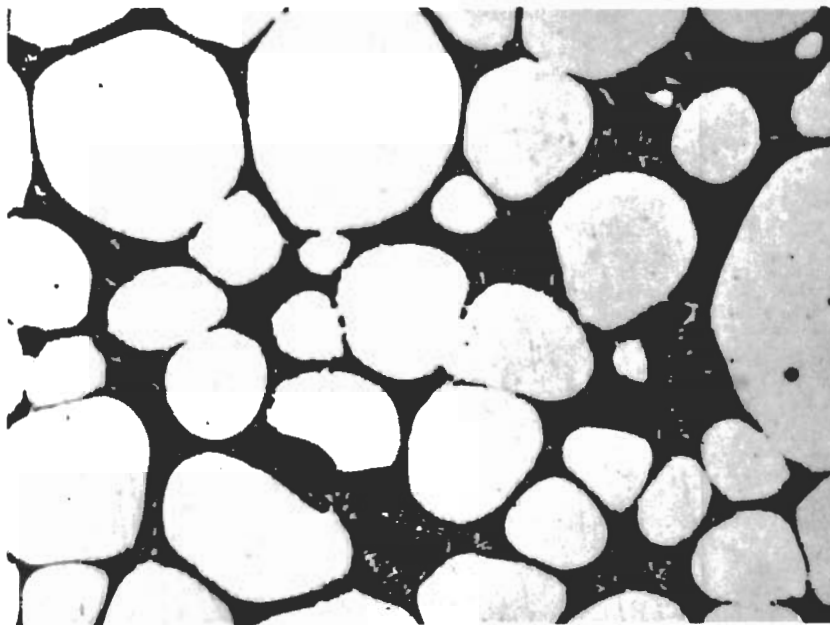


Figure 115. Zr-B-C (23-71-6 At.%), Arc-Melted and Quenched. X600
Primary Diboride in a Eutectic Matrix.

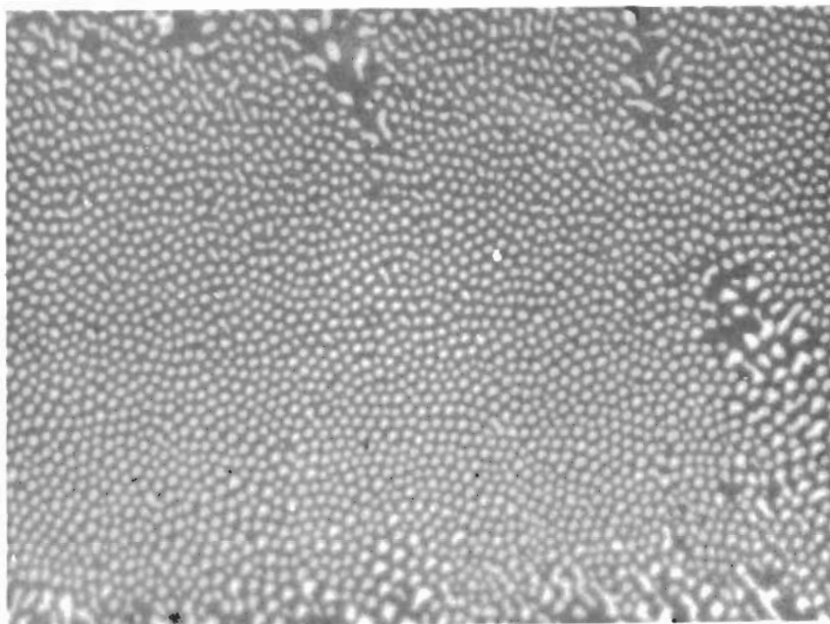


Figure 116. Zr-B-C (9-78-13 At.%), Cooled at Approximately 20°C per Second from 2220°C. X1000

ZrB₂ + B₄C Pseudobinary Eutectic.

Note the fibrillous diboride in a matrix of boron carbide.

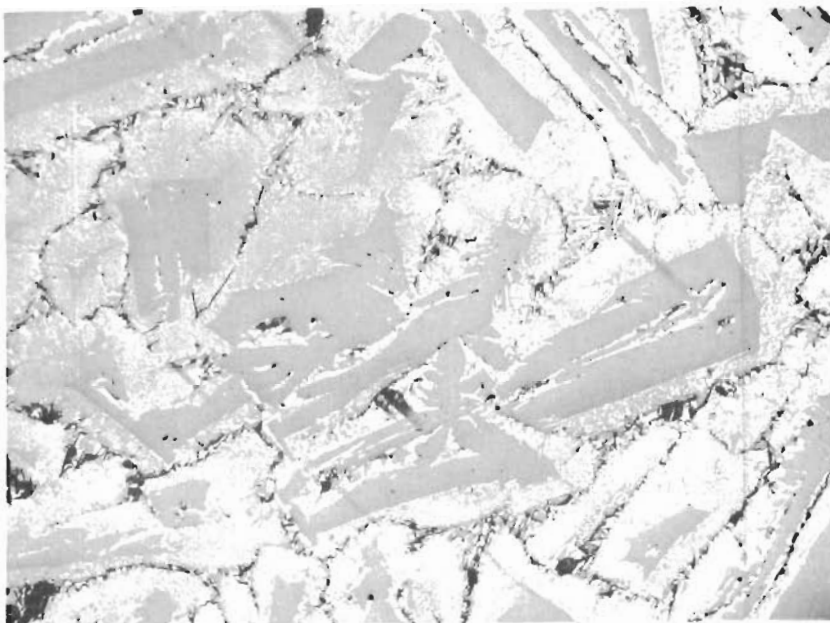


Figure 117. Zr-B-C (5-78-17 At.%), Arc-Melted and Quenched. X100
Primary B₄C in a ZrB₂ + B₄C Eutectic Matrix.

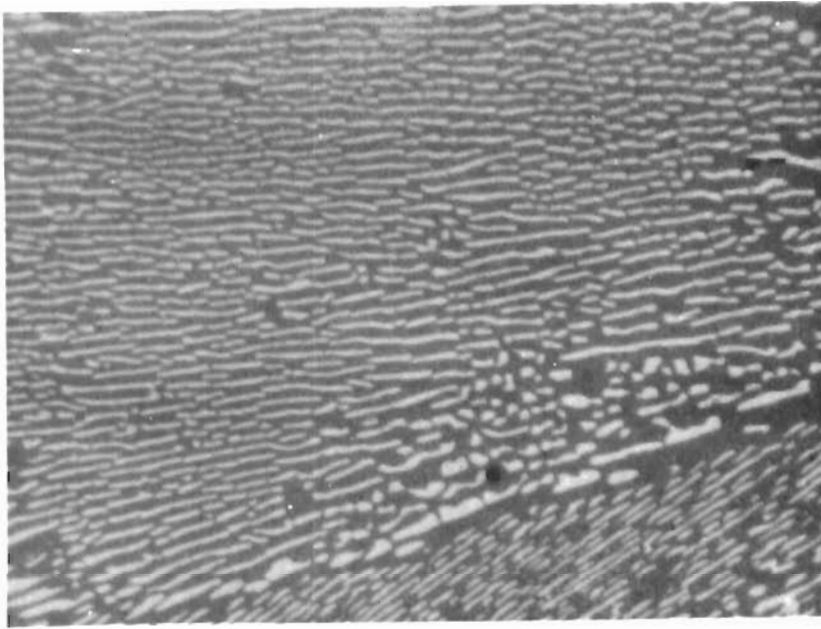


Figure 118(a) X1000

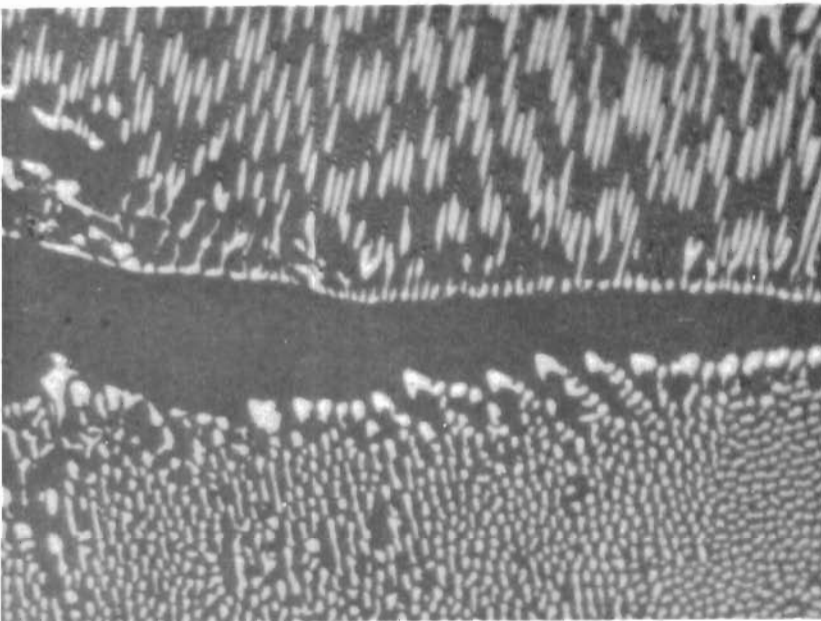


Figure 118(b) X800

'Grain Boundary' Between
Two Eutectic Colonies of
Different Orientation.

Figure 118(a) and (b). Sample from Figure 116.
Details of the Eutectic Structure $ZrB_2 + B_4C$.

6. Ternary Equilibria in the Composition Region ZrC-ZrB₂-B₄C-C.

Three alloys (No. 34, 35, and 36 in Table 33), located in the concentration region ZrB₂ + B₄C, melted extremely two-phased. The incipient melting temperatures noted were higher than the average ternary eutectic temperature of 2165°C, derived from DTA-runs on three alloys from this concentration region. Metallographically, an alloy Zr-B-C (10-50-40) contained primary crystallized graphite in a matrix of secondary ZrB₂ and ternary eutectic ZrB₂ + B₄C + C (Figure 119). Although rapid agglomeration of the staple-like graphite crystals present in structure resulted in uneven phase distributions, the microstructure of the melted and rapidly cooled alloy Zr-B-C (12-66-24 At.%, Figure 120), may be considered as representative for the ternary eutectic ZrB₂ + B₄C + C.

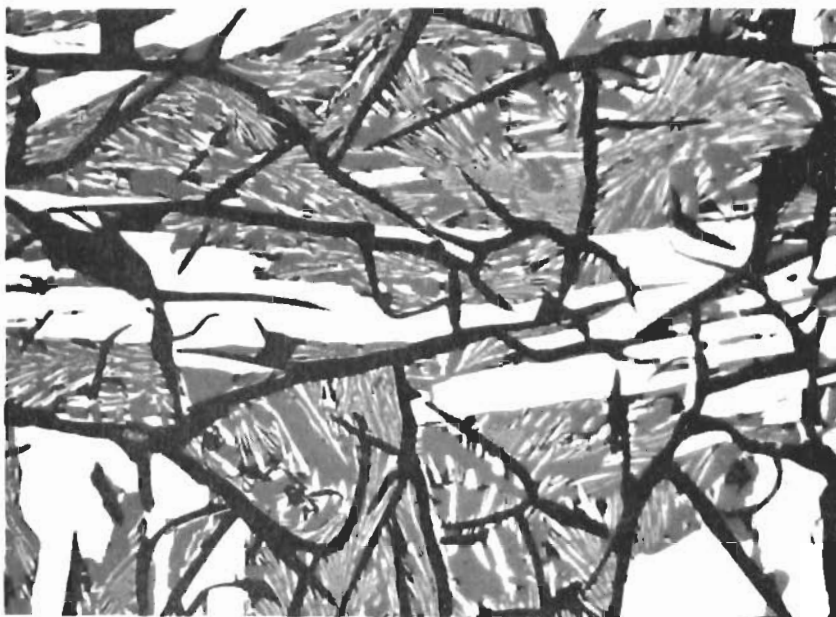


Figure 119. Zr-B-C (10-50-40 At.%), Cooled at Approximately X500 40°C per Second from 2460°C.

Primary Graphite, Secondary Crystallized Diboride (Light, Elongated Crystals), and Ternary Eutectic ZrB₂ + B₄C + C.

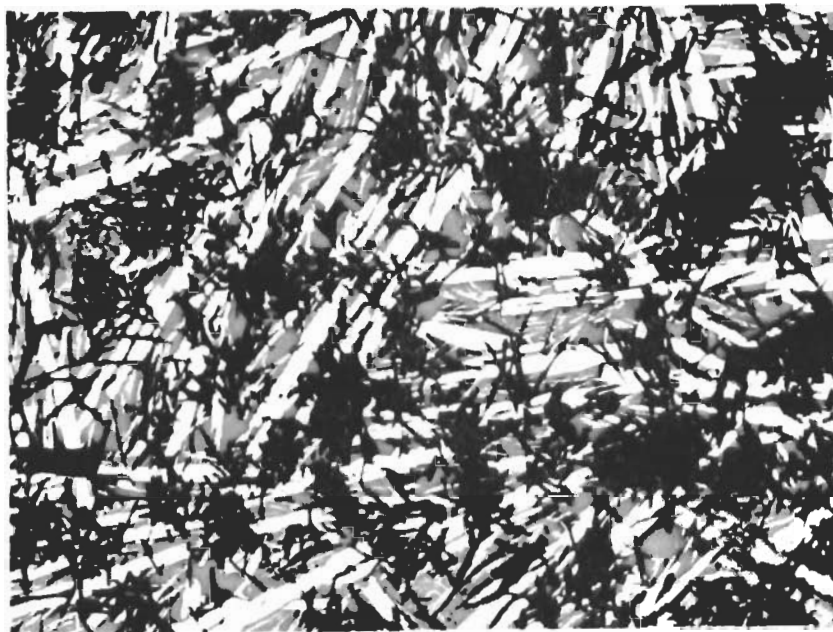


Figure 120. Zr-B-C (12-66-24 At.%), Cooled at Approximately X200
20°C per Second from 2180°C.

Ternary Eutectic $ZrB_2 + B_4C + C$ Graphite Crystals
Agglomerated During Cooling.

Incipient melting in three-phased alloys $ZrB_2 + ZrC + C$ generally was noted in the temperature range from 2360 to 2390°C (Table 33). An alloy Zr-B-C (26-43-31 At.%), located close to the $ZrB_2 + C$ pseudobinary eutectic, melted nearly isothermally at 2368° and the microstructure was almost purely eutectic (Figure 121). An alloy Zr-B-C (28-35-37) already contains significant quantities of primary monocarbide (Figure 122), and a further specimen Zr-B-C (35-20-45), located on the eutectic trough extending to the zirconium-carbon binary, is eutectic-like in appearance (Figure 123). A sample Zr-B-C (48-5-47 At.%) shows monocarbide phase, accompanied with traces of ZrB_2 and C at the grain boundaries (Figure 124).

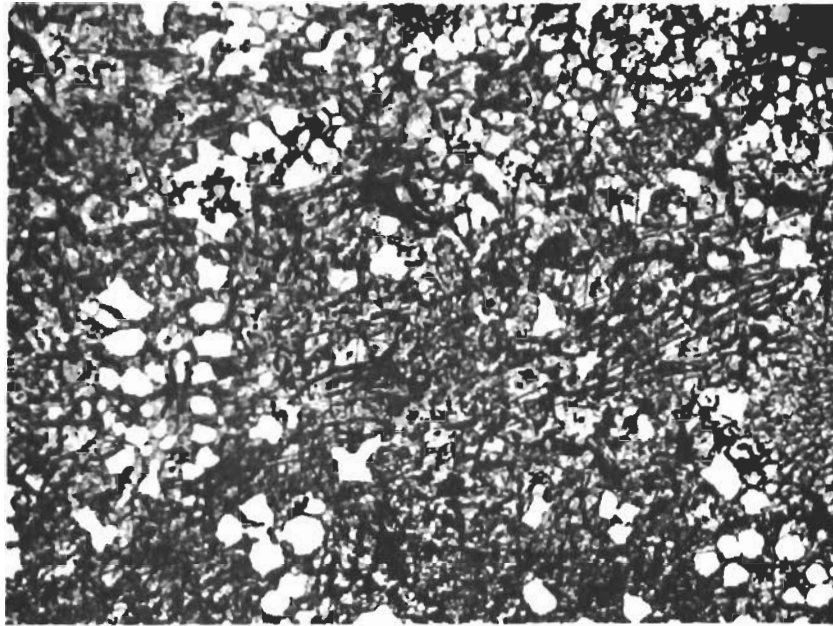


Figure 121. Zr-B-C (26-43-31 At.%), Quenched from 2490°C. X250

Traces of Primary Diboride in a Eutectic Matrix
 $ZrB_2 + ZrC + C$.

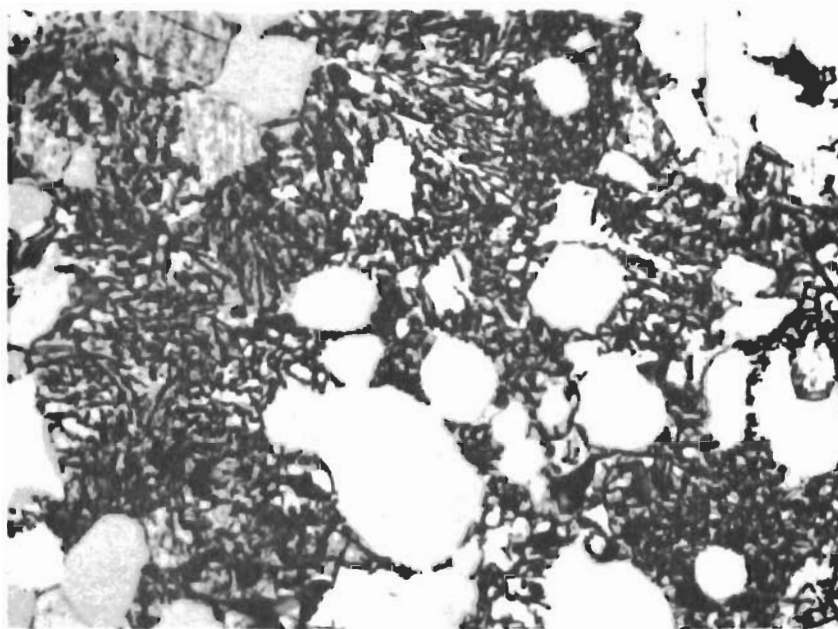


Figure 122. Zr-B-C (28-35-37 At.%), Quenched from 2385°C. X850

Primary Crystallized Monocarbide in a
Eutectic Matrix.

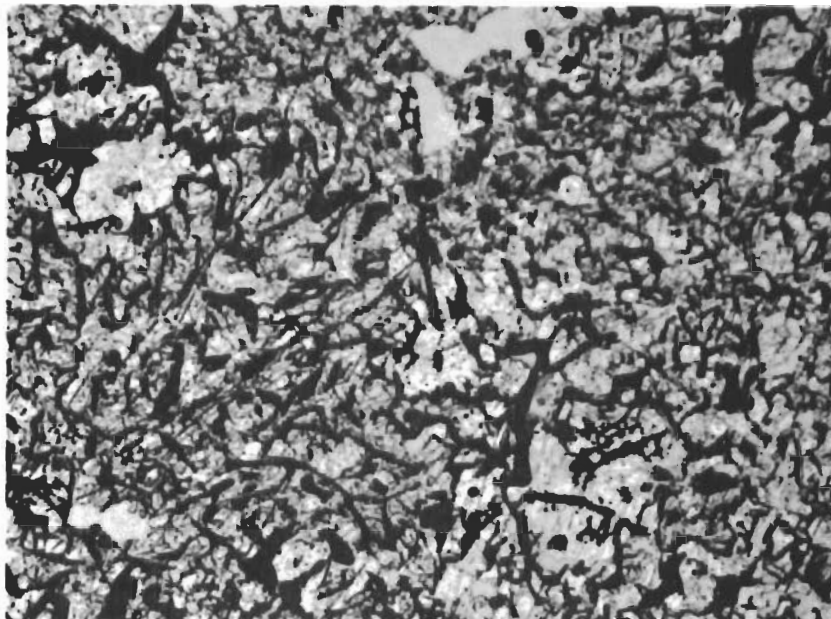


Figure 123. Zr-B-C (35-20-45 At.%), Quenched from 2500°C. X600

Eutectic-Like Structure Formed by Bivariant Solidification
Along the Eutectic Trough $ZrC + C$ — $ZrC + ZrB_4 + B_4C$.

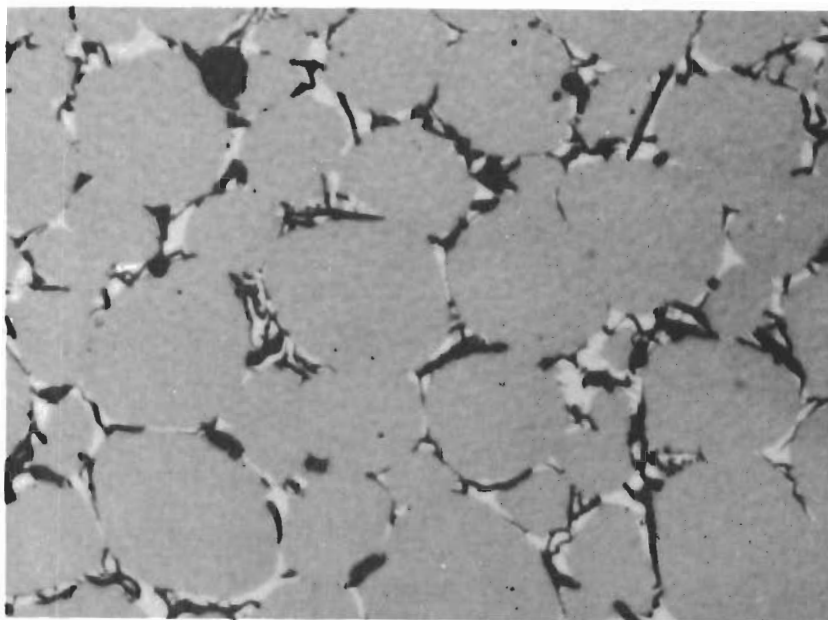


Figure 124. Zr-B-C (48-5-47 At.%), Quenched from 3160°C. X1000

Monocarbide, with Small Amounts of Graphite and Zirconium
Diboride at the Grain Boundaries.

7. Equilibria in the Boron-Corner of the System

While the ZrB_{12} phase was absent in the alloy series heat-treated at 1400° and $1600^\circ C$, the X-ray investigations on alloys, which were equilibrated and then quenched from $1900^\circ C$, revealed the existence of a two-phase equilibrium ZrB_{12} - B_4C (Figure 125). The lattice parameter of $a = 7.408 \text{ \AA}$, measured for the dodecaboride in excess diboride and B_4C -containing alloys, was identical with that of the binary compound. A possible range of homogeneity in the ternary must therefore be small.

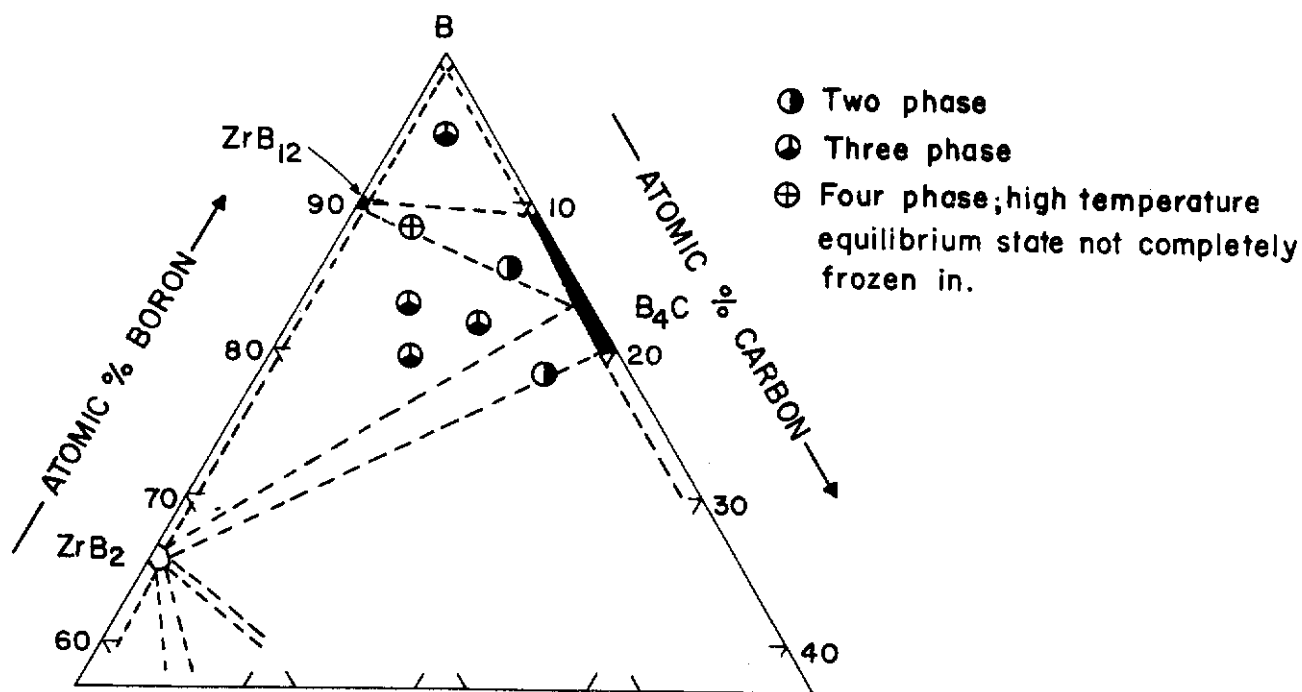
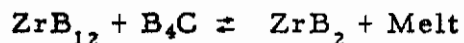


Figure 125. Qualitative Phase Evaluation on Quenched Alloys Located in the Boron Corner of the Zr-B-C System.

----- Phase Relations at $1900^\circ C$.

The isothermal reaction leading to the ternary (lower temperature) decomposition occurs approximately 100°C higher than the binary eutectoid temperature⁽⁵⁷⁾ (Figure 126). The high-temperature decomposition of the dodecaboride, occurring under participation of melt according to a reaction scheme:



at 2160°C, also was determined by differential thermoanalytical means (Figure 127). The microstructure of boron-rich alloy, Zr-B-C (90-5-5 At.%), containing about equal amounts of boron carbide and ZrB_{12} , as well as small amounts of unreacted ZrB_2 , is shown in Figure 128.

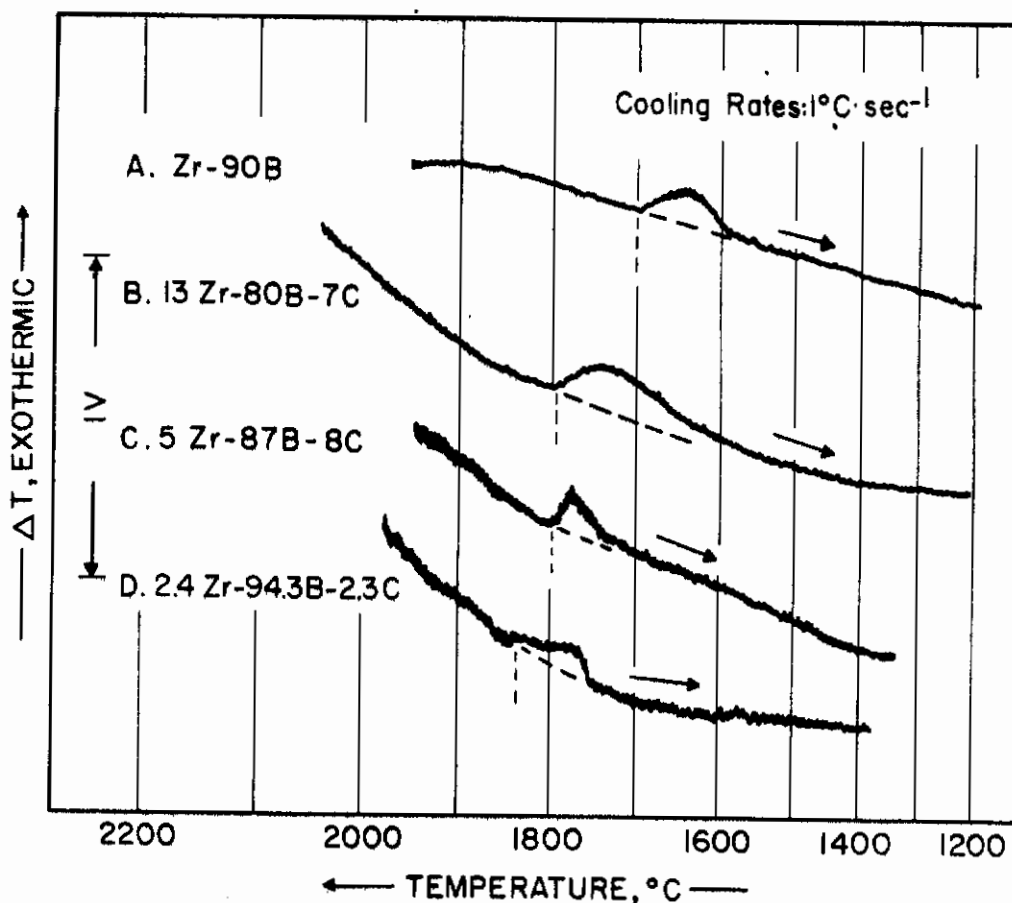


Figure 126. Binary (A) and Ternary (B, C, and D) Decomposition of ZrB_{12} .

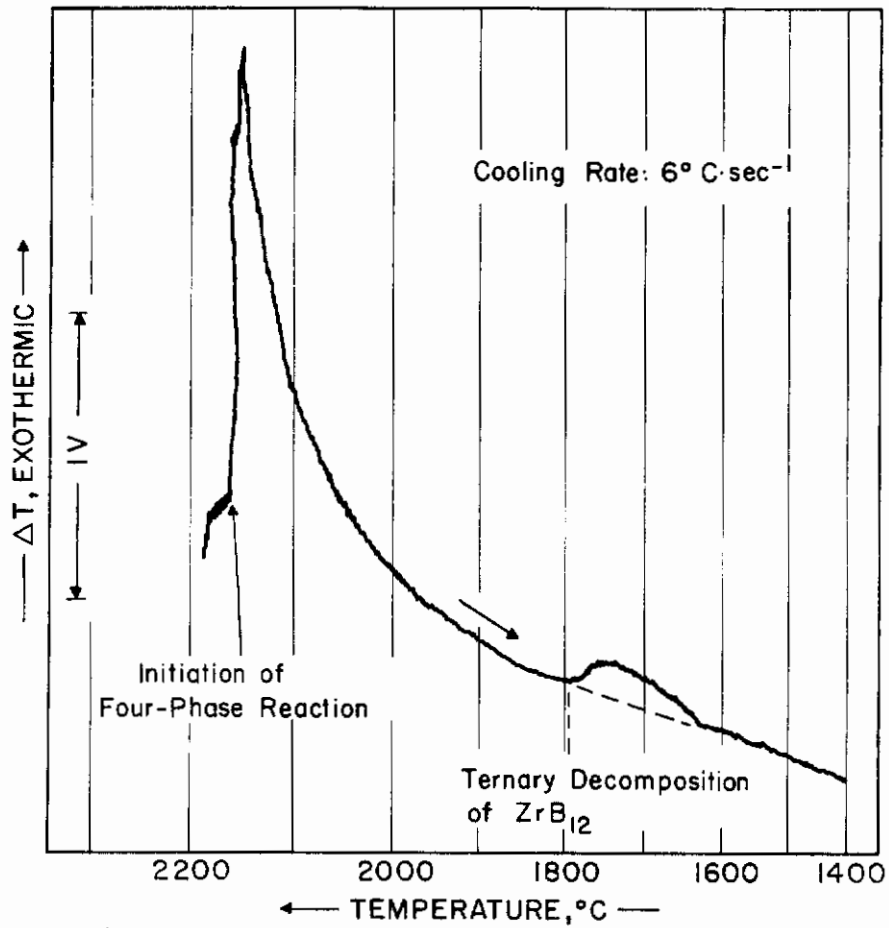
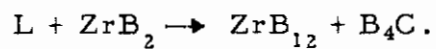


Figure 127. DTA-Thermogram (Cooling) of a Zr-B-C (13-80-7 At.%) Alloy.

Four Phase Reaction at T = ~2160°C:



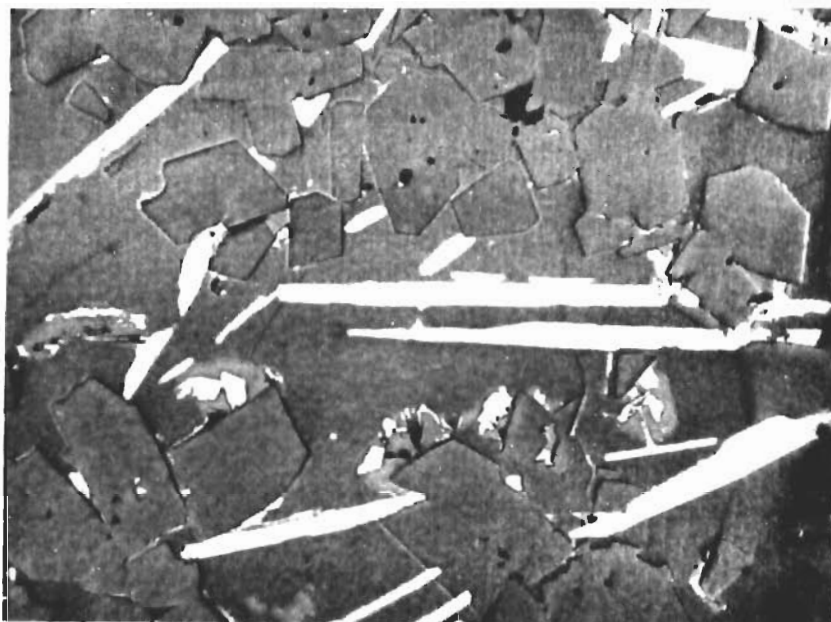


Figure 128. Zr-B-C (90-5-5 At.%), Equilibrated for 10 Minutes X 600 at 2050°C After Melting, and Quenched.

Small Amounts of Unreacted ZrB_2 (White, Long Crystals), in a Matrix Containing About Even Amounts of ZrB_{12} and B_4C .

Genuine Phase Colors: ZrB_{12} - Purple
 B_4C - Grey

8. Assembly of the Phase Diagram

The experimental results presented in the previous sections have been combined to construct the phase diagram shown in Figure 7. For the sake of convenience in the use of the phase diagram data, as well as to depict more clearly the equilibria and the types of reactions occurring in the system, a series of isothermal sections have been prepared and are illustrated in Figures 129(a) through 129(h). The phases entering or emerging from the isothermal phase reactions ($p = \text{const}$) in the boundary systems as well as in the ternary phase field, are summarized in concise form in the Scheil-Schultz reaction diagram presented in Figure 8. Melting troughs and the location of nonvariant melting equilibria are depicted in the drawing shown in Figure 130.

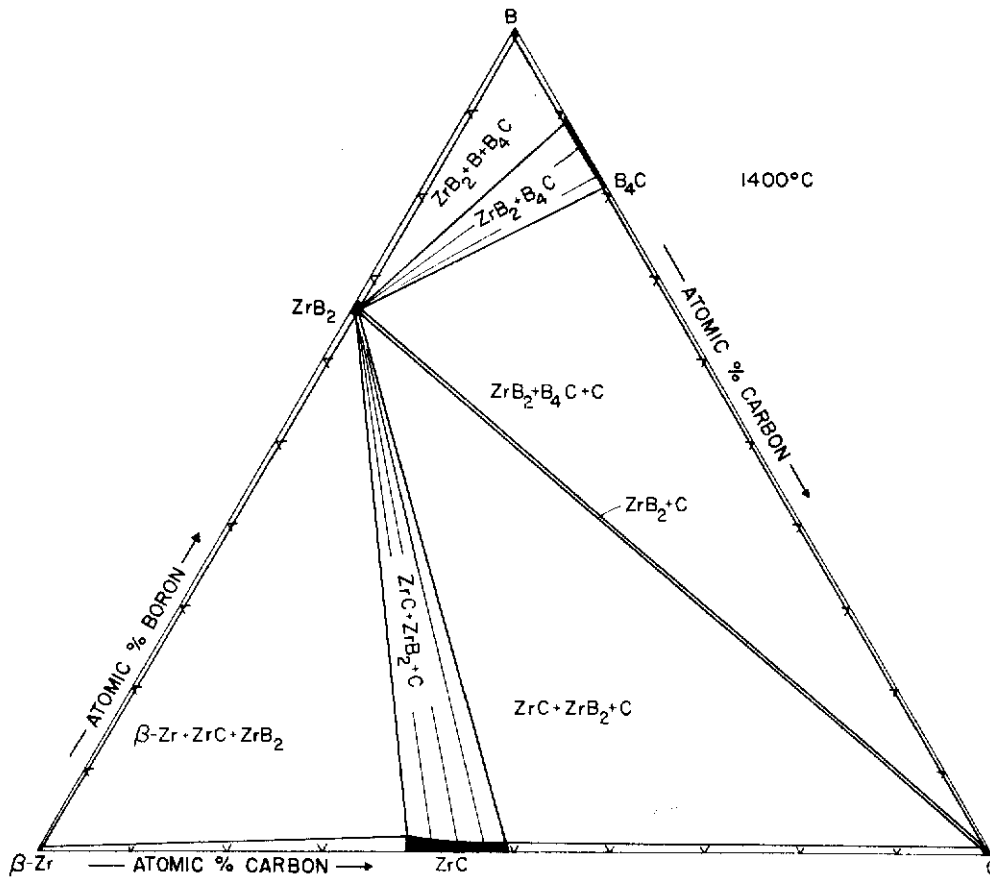


Figure 129(a). Isothermal Section at 1400°C.

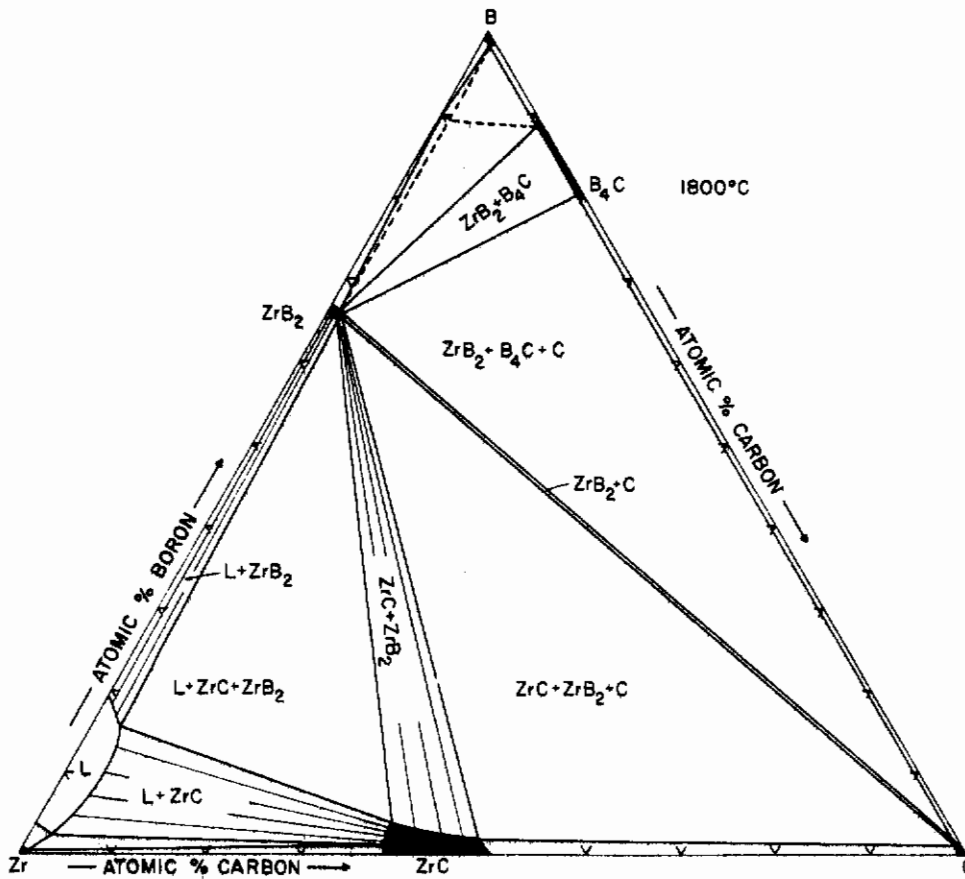


Figure 129(b). Isothermal Section at 1800°C.

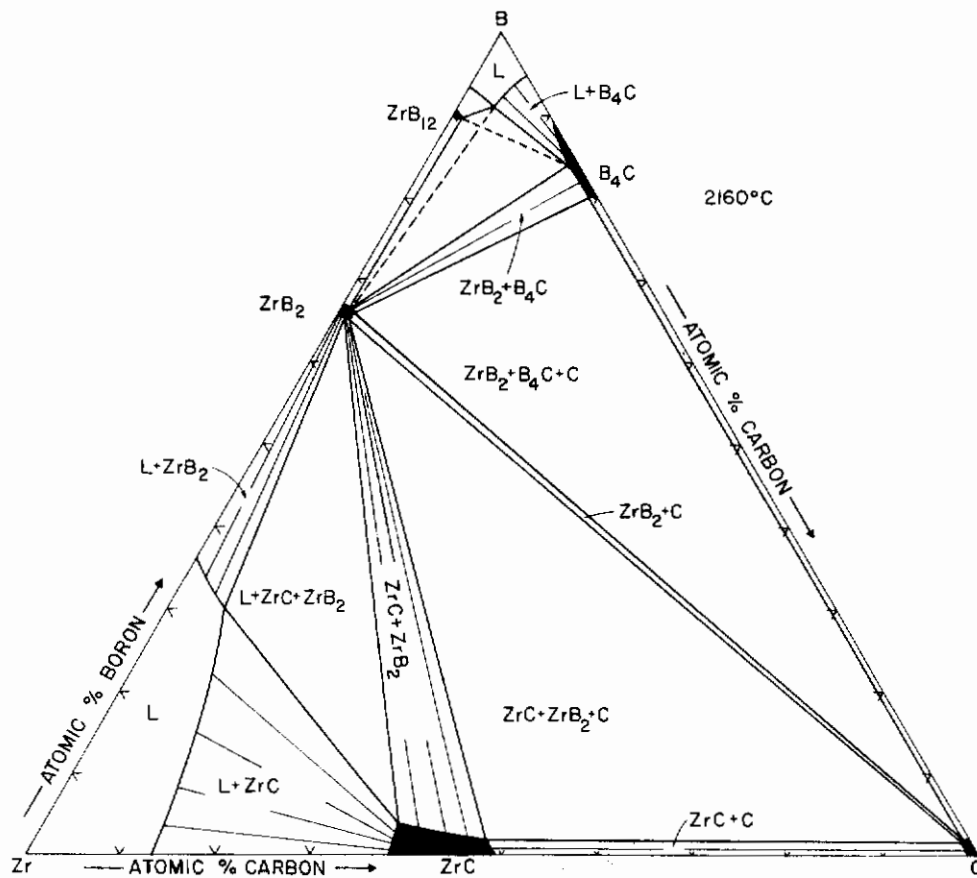


Figure 129(c). Isothermal Section at 2160°C.

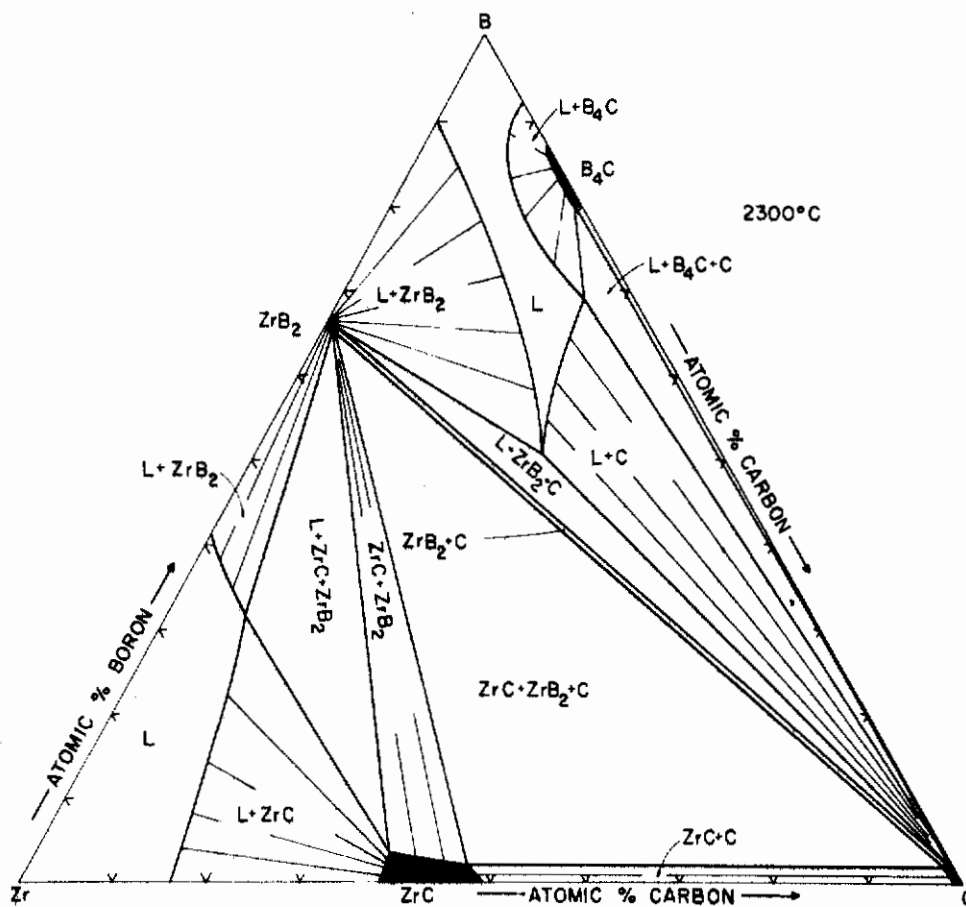


Figure 129(d). Isothermal Section at 2300°C.

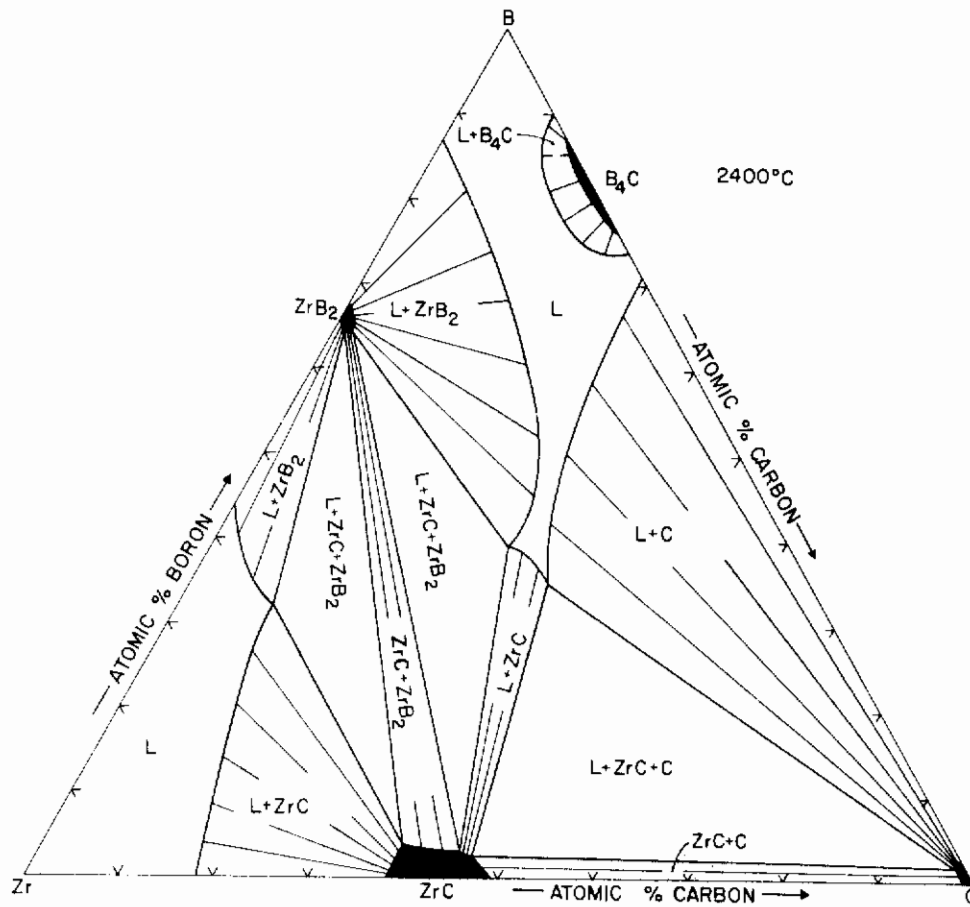


Figure 129(e) Isothermal Section at 2400°C.

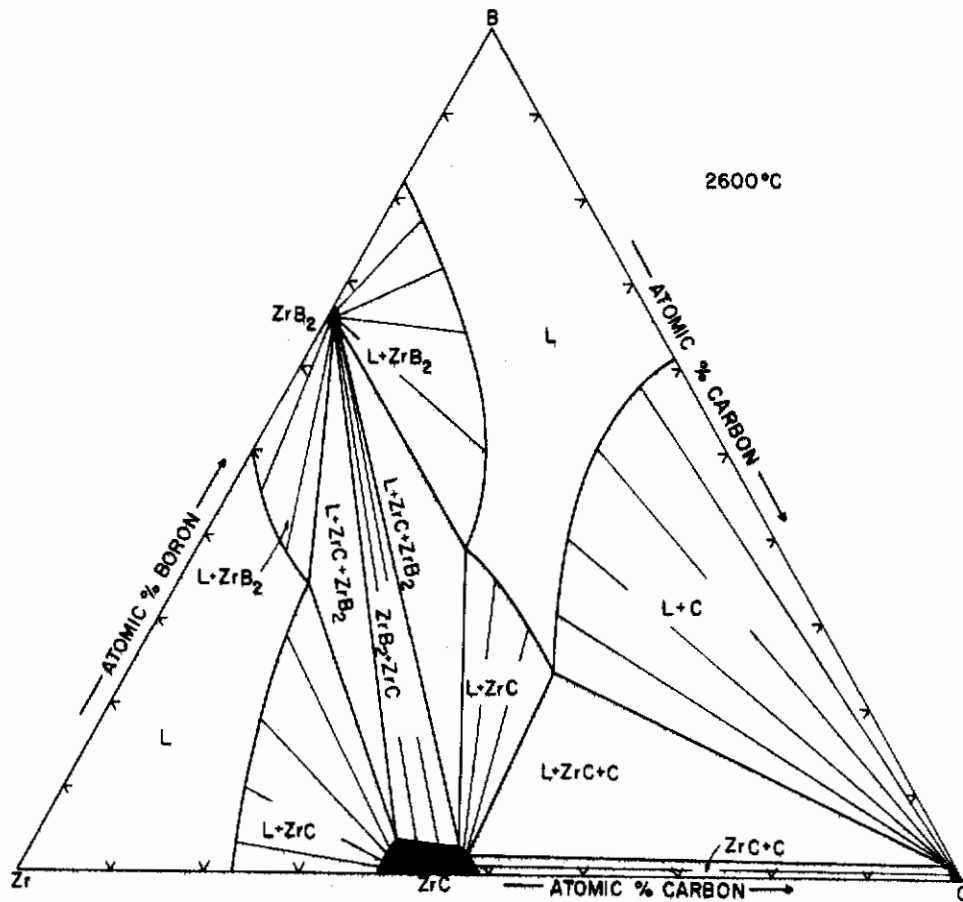


Figure 129(f). Isothermal Section at 2600°C.

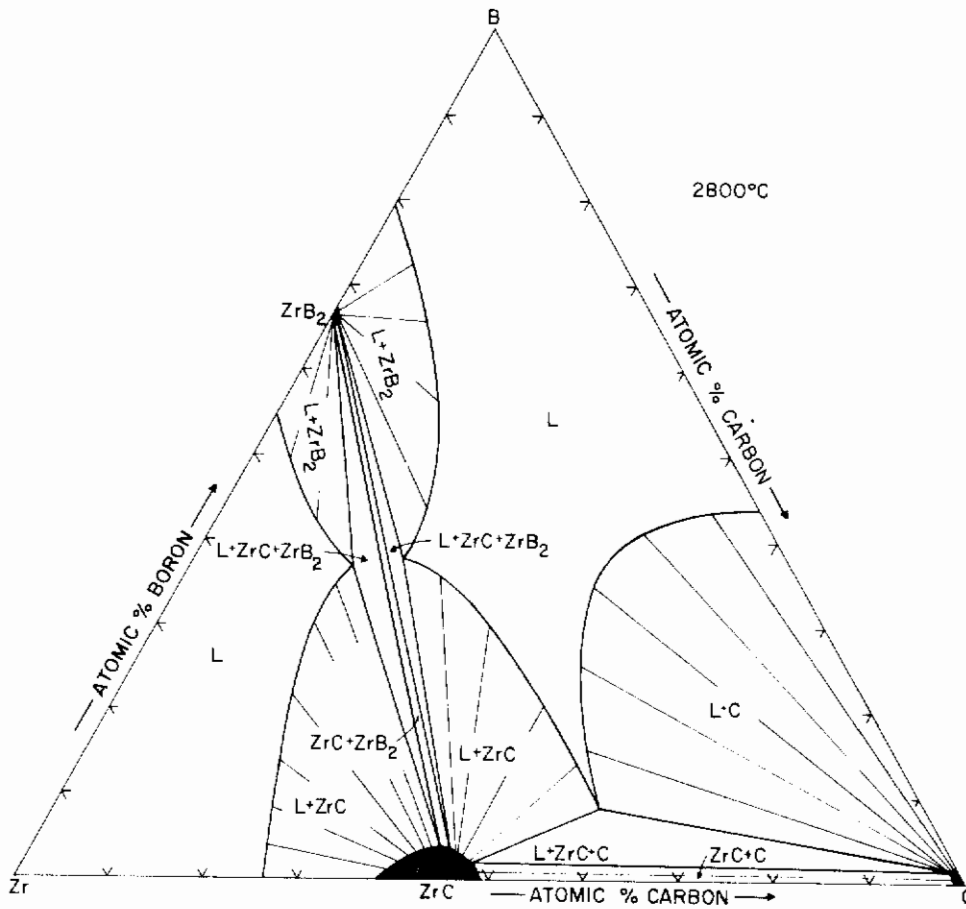


Figure 129(g). Isothermal Section at 2800°C.

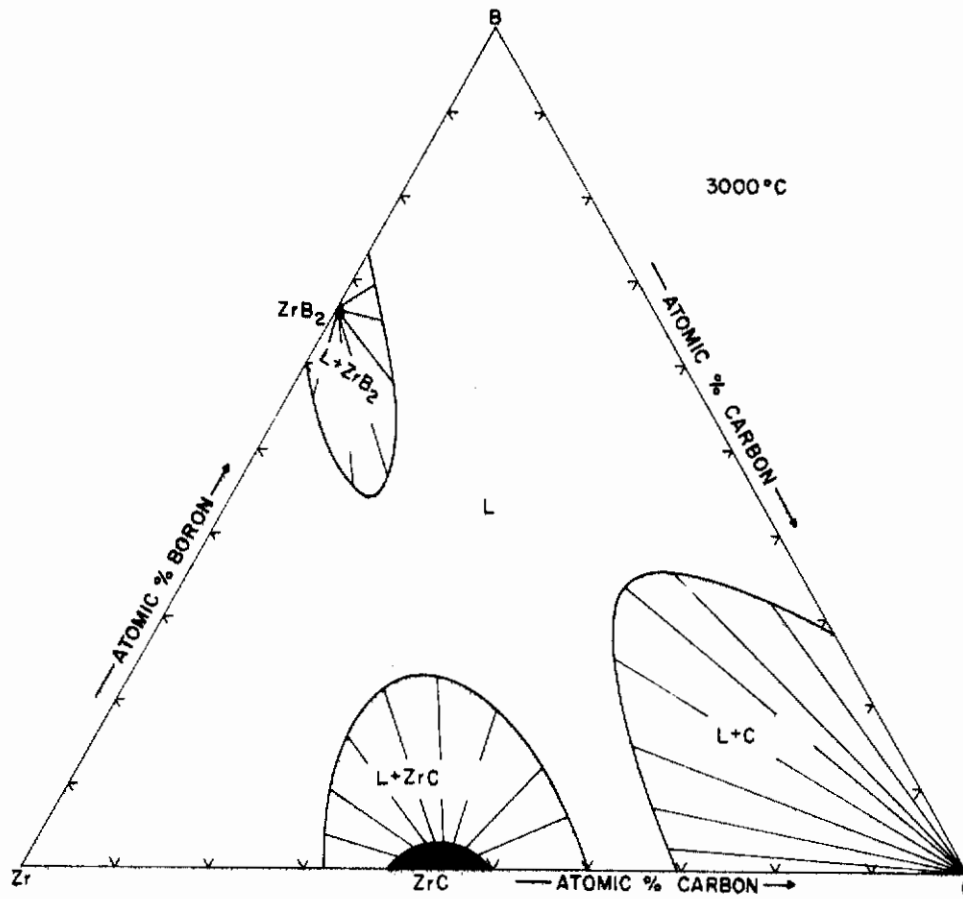


Figure 129(h). Isothermal Section at 3000°C.

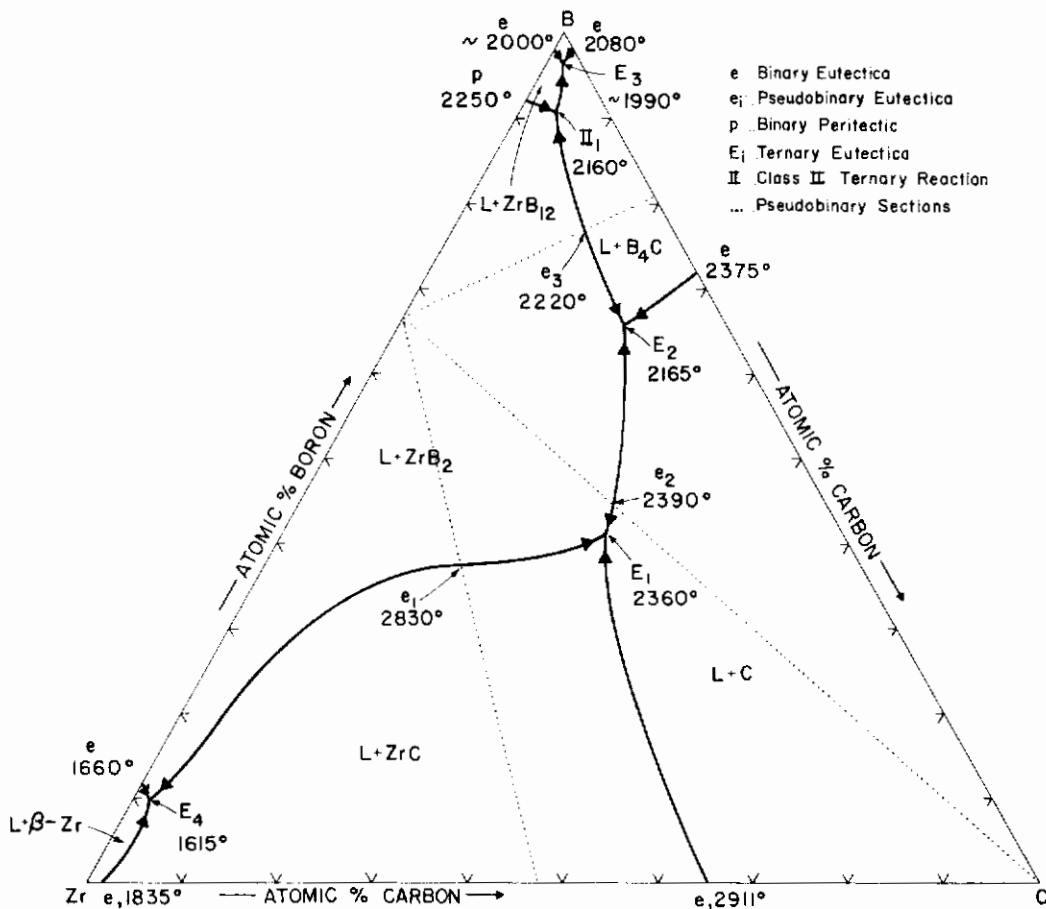


Figure 130. Melting Troughs and Nonvariant Melting Equilibria in the Zr-B-C System.

C. HAFNIUM-BORON-CARBON

1. Equilibria in the Hafnium-Corner of the System

As noted from the binary systems (Figure 21 and 24) addition of boron does not affect to any appreciable extent the α - β -transformation in pure hafnium; on the other hand, the hexagonal close-packed α (low temperature) modification dissolves interstitially up to 14 atomic percent carbon, and is stabilized to temperatures, which are above the melting point of the pure element. It is now of interest to investigate, how the simultaneous presence of boride and carbide phases will affect the phase behavior of α - and β -hafnium. In the alloy series equilibrated at 1400°C (Figure 131), X-ray

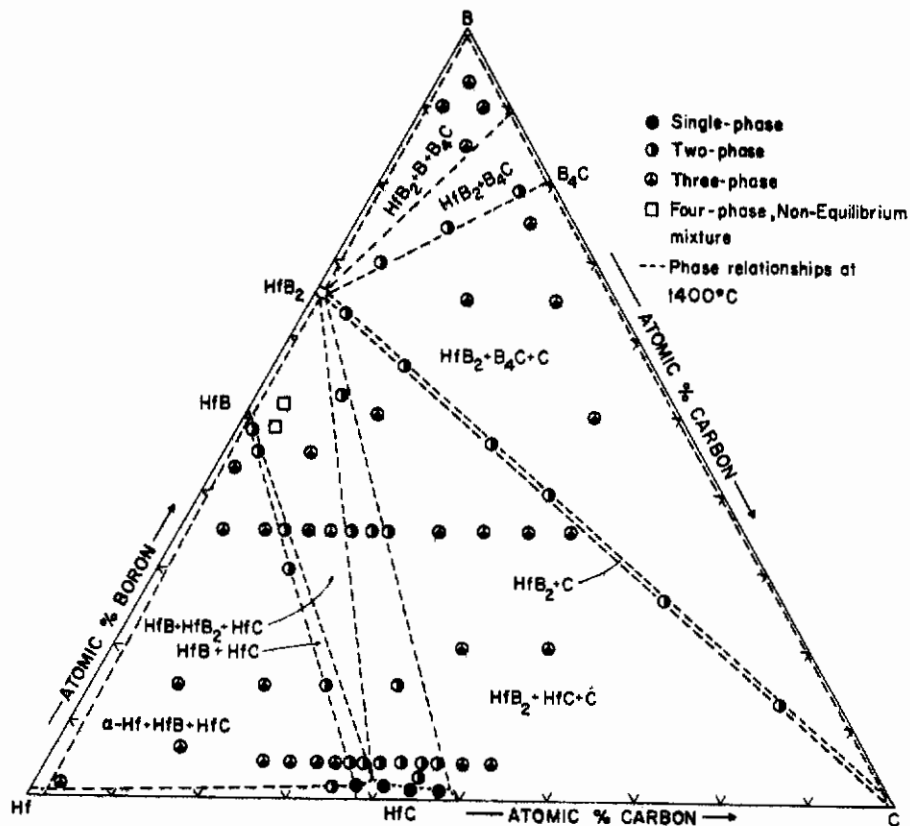


Figure 131. Hf-B-C: Location and Qualitative Phase Evaluation of the Alloy Series Equilibrated at 1400°C.

diffraction studies on the metal-rich alloys showed the patterns of α -Hf, HfB, and HfC. Incipient melting in an alloy Hf-B-C (92-6-2 At.%, Table 34) was noted at 1861°C, but melting in this alloy was extremely two-phased, as evidenced by the high collapsing temperature of 2036°C. Heterogeneity in the melting behavior was less pronounced in the alloy Hf-B-C (88-8-4 At.%), but true isothermal melting was observed in neither of the alloy samples run in the Pirani furnace.

The temperatures at which the samples collapsed, increased rapidly with increasing carbon content of the alloys, indicating, that the eutectic trough in the metal-rich region of the system must run close to the hafnium-boron edge binary.

X-ray analysis of the as-melted and quenched alloys generally revealed the presence of α -Hf and HfB or of α -HfB₂ and HfC solid solution (Table 34) in the alloys quenched from below 2000°C; no, or only small amounts of monoboride, were detected in higher-temperature quenched alloys, which usually consisted of a mixture of hafnium, hafnium monocarbide, and traces of diboride.

In repeated DTA runs on three alloys located in the hafnium-corner, signs for the α - β -hafnium phase reaction could only be observed in the samples containing less than 5 atomic percent carbon (Figure 132). The reaction was absent in the alloy Hf-B-C (88-4-8 At.%), and also was not noticed in another alloy Hf-B-C (70-20-10 At.%, Figure 133). X-ray as well as metallographic analysis showed the reaction isotherm appearing at about 1950°C in the latter sample, to be associated with the replacement of the equilibrium α -Hf + HfB by an equilibrium monocarbide + melt.

The data gained by X-ray and differential-thermo-analytical means were independently confirmed and supplemented by metallographic data on melted, heat-treated, as well as quenched alloys. Melted samples, located at less than 2 atomic percent carbon along the hafnium-boron boundary systems, contain no, or very little, primary carbide phase (Figures 134 through 137). A pure eutectic structure was observed in the alloy containing 12 atomic percent boron (Figure 137).

Table 34. Melting Temperatures and Phase Evaluation of Hafnium-Boron-Carbon Alloys

No	Composition At. %			Observed Melting Temperature, °C	Incipient Temperature, °C	Melting	Phases Present After Melting		Lattice Parameters Å	Metallography
	Hf	B	C				X-ray	Phases		
1	92	6	2	2036°	1861°	very heterog.	a + δ	n.d.	β + a (?) + δ	
2	92	3	5	2312°	1911°	very heterog.	a + δ	a: 3.204 c: 5.075	β + a + trace δ	
3	88	8	4	1985°	1846°	heterogeneous	a + δ	n.d.	β + a + trace δ	
4	85	5	8	2315°	1924°	very heterog	a + γ	a: 3.22 c: 5.13	a + trace γ	
5	86	3	11	2386°	2180°	very heterog	a + γ	a: 3.21 c: 5.10	a + γ	
6	83	5	12	>2400°	2215°	extrem. heterog	a + γ + little δ	γ:a = 4.627	n.d.	
7	80	5	15	<2300°	2205°	extrem. heterog	a + γ	γ:a = 4.624	a + γ	
8	83	10	7	2036°	1945°	very heterog	a + γ + δ	n.d.	a + δ + trace γ	
9	80	10	10	2133°	1970°	very heterog	a + γ + δ	n.d.	γ (prim) + a or β, and δ	
10	86	12	2	1945°	1935°	sl. heterog	a + δ	a: 3.21 c: 5.09	a + β + δ eutectic	
11	83	14	3	1951°	1943°	sl. heterog	a + δ + trace γ	n.d.	traces of (prim) + eutec.	
12	76	20	4	1986°	1943°	heterogeneous	a + δ + γ	a = 6.52 δ:b = 3.22 c = 4.92	a or β + δ	
13	70	15	15	2276°	2115°	very heterog	γ + a + trace δ	n.d.	γ(prim) + a or β + δ	
14	68	27	5	2084°	1963°	heterogeneous	a + γ + ε	n.d.	γ (prim) + ε + a or β	
15	61	33	6	2290°	1973°	very heterog	a + ε + γ	n.d.	a or β + ε + γ	
16	51	47	2	2063°	2012°	very heterog	a + δ + ε + trace γ	n.d.	n.d.	
17	52	40	8	2670°	2031°	very heterog	a + γ + ε	n.d.	a or β + γ + ε	
18	52	35	13	2811°	2087°	very heterog	γ + ε + trace a	n.d.	n.d.	
19	56	30	14	2738°	2064°	very heterog	γ + ε + trace a	γ:a = 4.639	a or β + γ + ε	
20	56	25	19	2968°	2346°	very heterog	γ + ε + trace a	n.d.	n.d.	

Continued

Table 34. (Continued)

No	Composition At. %		Observed Melting Temperature °C	Incipient Collapse	Melting	Phases Present After Melting		Metallography
	Hf	B				X-ray	Lattice Parameters Å	
21	58	20	2412°	2860°	very heterog.	γ + ε + trace α	γ:a = 4.640	n.d.
22	59	14	2733°	2938°	very heterog	γ + trace ε	γ:a = 4.643	γ (prim) + little α and ε
23	55	15	3117°	3321°	very heterog	γ + trace ε	γ:a = 4.644	γ (prim) + traces of ε
24	60	10	3136°	>3500°	very heterog	γ + trace ε	γ:a = 4.644	γ (with precip) + little α + ε
25	60	8	3369°	3687°	very heterog	γ	γ:a = 4.640	γ + traces α
26	56	9	3295°	3790°	very heterog	γ	γ:a = 4.644	γ
27	64	3	3055°	3548°	very heterog	γ	γ:a = 4.623	γ + little α
28	60	3	3125°	3786°	very heterog	γ	γ:a = 4.627	γ
29	55	4	3467°	3843°	very heterog	γ	γ:a = 4.636	γ
30	53	4	3862°	3862°	fairly sharp	γ	γ:a = 4.639	γ
31	50	4	3160°	3732°	very heterog	γ	γ:a = 4.636	γ with precipitations
32	47	4	2960°	3458°	very heterog	γ	γ:a = 4.637	γ with precipitations, + p
33	51	14	3132°	3354°	very heterog	γ + ε	γ:a = 4.639	n.d.
34	50	29	2926°	3118°	very heterog	γ + ε	γ:a = 4.643	γ + ε
35	46	39	2507°	2860°	very heterog	γ + ε	n.d.	n.d.
36	44	48	2435°	2938°	very heterog	γ + ε + trace α	a = 3.143 ε: c = 3.479	α + δ + ε + eutectic
37	34	63	3161°	3368°	very heterog	ε + trace γ	a = 3.143 ε: c = 3.478	ε + traces second phase
38	32	66	3134°	3353°	very heterog	ε	a = 3.144 ε: c = 3.479	ε + traces ρ
39	30	68	2500°	3200°	very heterog	ε + trace sec phase	a = 3.143 ε: c = 3.477	ε + traces ω
40	35	60	3134°	3353°	very heterog	ε + γ	a = 3.142 ε: c = 3.474	n.d.

Table 34. Melting Temperatures and Phase Evaluation of Hafnium-Boron-Carbon Alloys
(Continued)

No	Composition At. % Hf B C			Phases Present After Melting				Metallography	
				Observed Melting Temperatures, °C Incipient Collapse	Melting	Phase	X-ray		Lattice Parameters Å
41	36	55	9	3148°	3193°	heterogeneous	ε + γ	n.d.	n.d.
42	38	49	13	3140°	3145°	sharp	ε + γ	a = 3.145 c = 3.476	ε (prim) + eutectic
43	40	43	17	3142°	3142°	sharp	ε + γ	γ:a = 4.639	ε + γ eutectic
44	41	38	21	3136°	3136°	sharp	ε + γ	γ:a = 4.639	γ (prim) + eutectic
45	45	32	23	3140°	3146°	fairly sharp	ε + γ	n.d.	n.d.
46	44	28	28	3143°	3180°	sl. heterog.	ε + γ	γ:a = 4.640	γ (prim) + eutectic
47				3153°	3311°	heterogeneous	ε + γ	n.d.	n.d.
48	46	20	34	3157°	3348°	heterogeneous	ε + γ	n.d.	γ (prim) + eutectic
49	37	25	38	2522°	2940°	very heterog	ε + γ + ρ	n.d.	n.d.
50	35	35	30	2511°	2893°	very heterog	ε + γ + ρ	n.d.	n.d.
51	30	45	25	2486°	2774°	very heterog	ε + γ + ρ	n.d.	n.d.
52	30	40	30	2480°	2680°	very heterog	ε + γ + ρ	n.d.	γ (prim) + eutectic
53	30	35	35	2493°	2733°	very heterog	ε + γ + ρ	γ:a = 4.639	n.d.
54	31	30	39	2503°	2537°	sl. heterog	ε + γ + ρ	a = 3.142 c = 3.476	γ (prim) + eutectic
55	33	20	47	2507°	2589°	heterogeneous	ε + γ + ρ	n.d.	n.d.
56	33	10	57	2512°	3064°	very heterog.	ε + γ + ρ	n.d.	γ + ρ(prim) + eutectic
57	27	20	53	2505°	2610° ↓	heterogeneous	ε + γ + ρ	n.d.	n.d.
58	25	35	40	2493°	2507° ↓	relat. sharp	ε + γ + ρ	n.d.	little (prim) γ + ρ + eutec.
59	12	24	64	2573°	2923° ↓	very heterog.	ε + ρ	a = 2.468 c = 6.709	n.d.
60	15	30	55	2512°	2784° ↓	very heterog	ε + ρ	n.d.	ρ (prim) + eutectic
61	18	36	46	2514°	2650° ↓	heterogeneous	ε + ρ	n.d.	ρ (prim) + eutectic

Table 34. (Continued)

Composition At. %		Observed Melting Temperatures, °C	Incipient Collapse	Melting	Phases Present After Melting		Lattice Parameters λ	Metallography
No	Hf B				Phase	X-ray		
62	20 40	2515°	2512° ↓	sharp	$\epsilon + \rho$	X-ray	traces ρ (prim) + eutec.	
63	22 44	2517°	2517° ↓	sharp	$\epsilon + \rho$	X-ray	traces ϵ (prim) + eutec.	
64	22 45	2522°	2555° ↓	heterogeneous	$\epsilon + \rho$	X-ray	ϵ (prim) + eutectic	
65	25 50	2517°	2600° ↓	heterogeneous	$\epsilon + \rho$	X-ray	ϵ (prim) + eutectic	
66	29 58	2613°	2745° ↓	very heterog.	$\epsilon + \rho$	X-ray	ϵ (prim) + eutectic	
67	30 64	3090°	3296°	very heterog.	$\epsilon + \rho$	X-ray	n. d.	
68	15 55	2310°	2490°	heterogeneous	$\epsilon + \rho + \text{trace } \omega$	X-ray	eutectic-type structure	
69	10 60	2275°	2305°	heterogeneous	$\epsilon + \rho + \omega$	X-ray	eutectic-type structure	
70	20 73	2354°	2705°	very heterog.	$\epsilon + \omega$	X-ray	ϵ (prim) + eutectic	

Legend to Table :

- ↓ Quenched
- α α -Hf-ss
- β β -Hf-ss
- γ HfC
- δ HfB
- ϵ HfB₂
- κ B
- ω B₄C
- ρ C

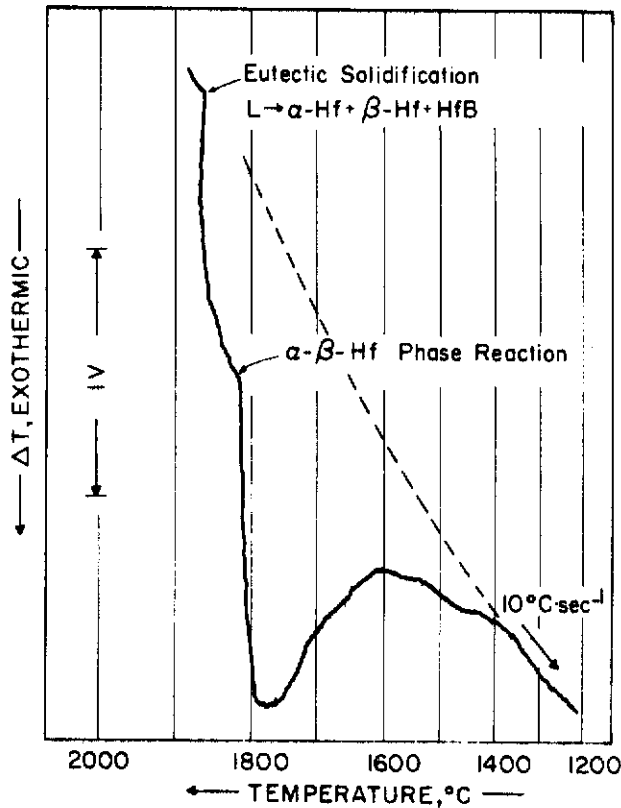


Figure 132. DTA-Thermogram of a Metal-Rich Hf-B-C (86-10-4 At.%) Alloy.

Although the α - and transformed β -hafnium could be clearly distinguished only in alloys with low semimetal contents (Figures 138 through 142), direct and independent evidence for the existence of an equilibrium $\text{HfB} + \alpha\text{-Hf}$ at lower temperatures was gained by a comparison between the microstructures of melted and quenched, and lower-temperature re-equilibrated alloys (Figures 143 through 147).

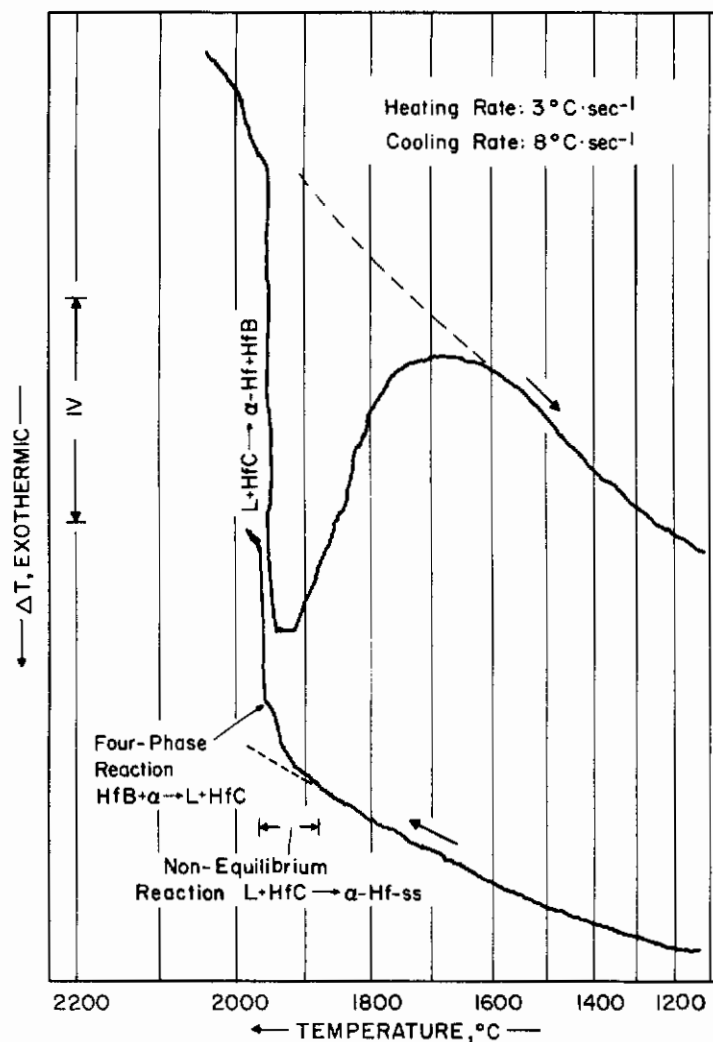


Figure 133. DTA-Thermogram of a Hf-B-C (70-20-10 At.%), Alloy.

Note: The reaction initiating at about 1900°C on the heating cycle is due to non-equilibrium conditions obtained by quenching from the molten state in the preceding run.

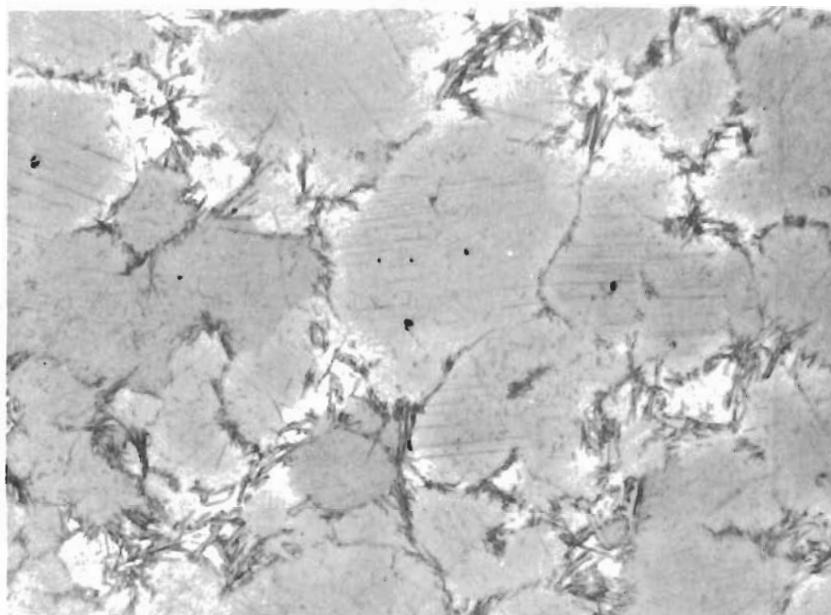


Figure 134. Hf-B-C (95-3-2 At.%), Quenched from 2100°C. X275

Primary β -and/or α -Hf, with Ternary Eutectic at the Grain Boundaries.

X-ray: Hf + HfB

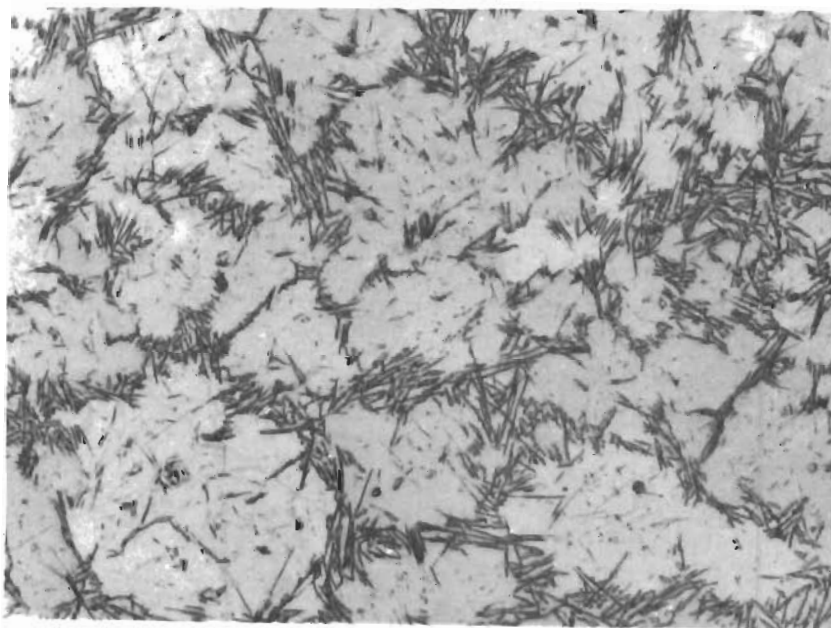


Figure 135. Hf-B-C (92-6-2 At.%), Quenched from 1900°C. X325

Primary α - and β -Hf, and Ternary Eutectic $\alpha+\beta$ + HfB.

X-ray After Cooling: α -Hf + HfB.

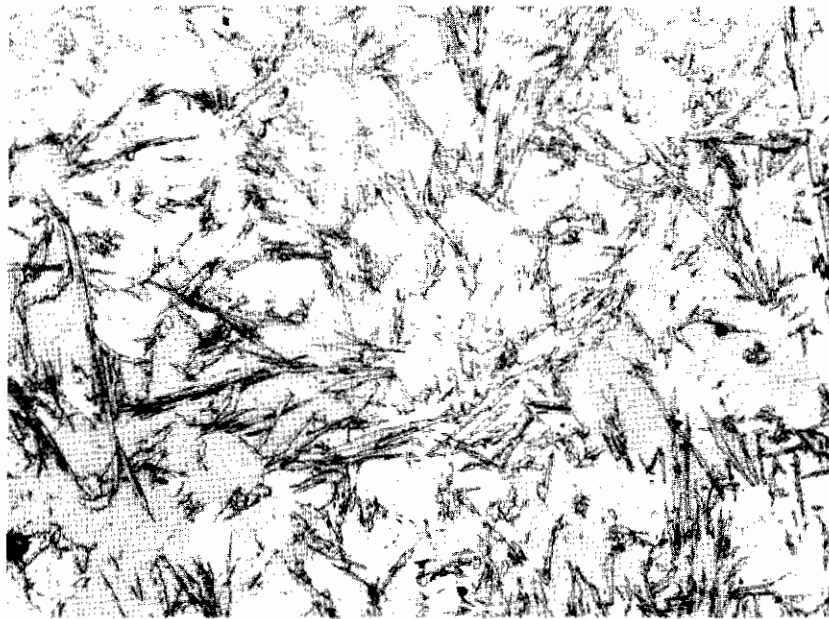


Figure 136. Hf-B-C (88-10-2 At.%), Quenched from 1860°C. X480
Small Amounts of Primary Metal Phase and Ternary
Eutectic $\alpha + \beta + \text{HfB}$

X-ray After Cooling: $\alpha\text{-Hf} + \text{HfB}$



Figure 137. Hf-B-C (86-12-2 At.%), Quenched from 1850°C X520

Ternary Eutectic $\alpha\text{-Hf} + \beta\text{-Hf} + \text{HfB}$

X-ray After Cooling: $\alpha\text{-Hf} + \text{HfB}$

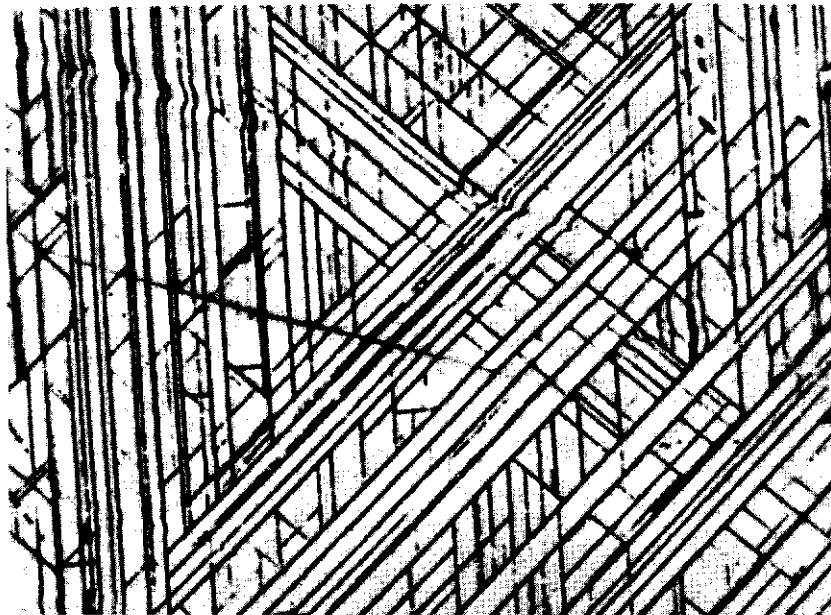


Figure 138. Hf-B-C (95-3-2 At.%), Equilibrated at 1850°C, and Quenched. X1000

β -Hafnium (Transformed).

Note: Average structure contained traces of excess monoboride.

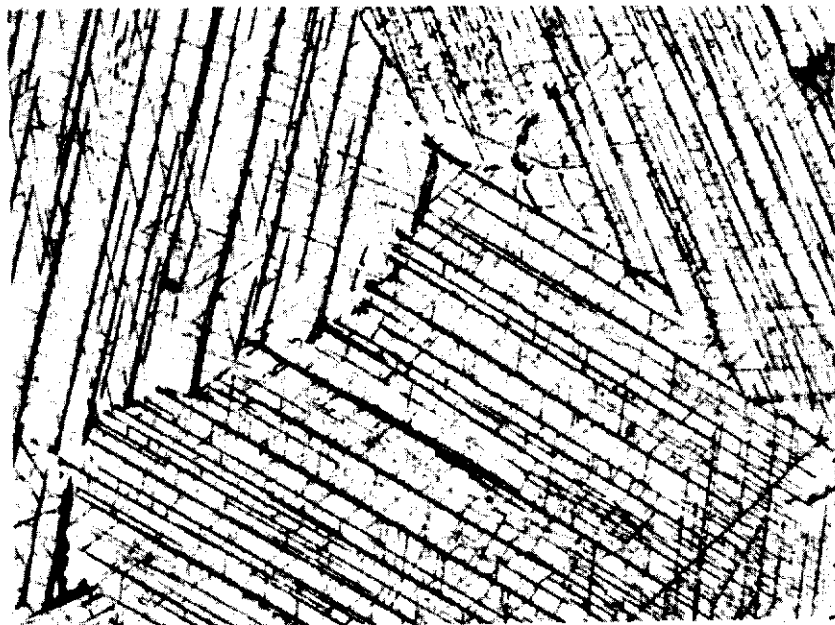


Figure 139. Hf-B-C (92-3-5 At.%), Equilibrated, and Cooled at 1°C per Second from 1850°C. X800

α -Hf-Solid Solution with Oriented Precipitations, and Small Amounts of Excess Monoboride.

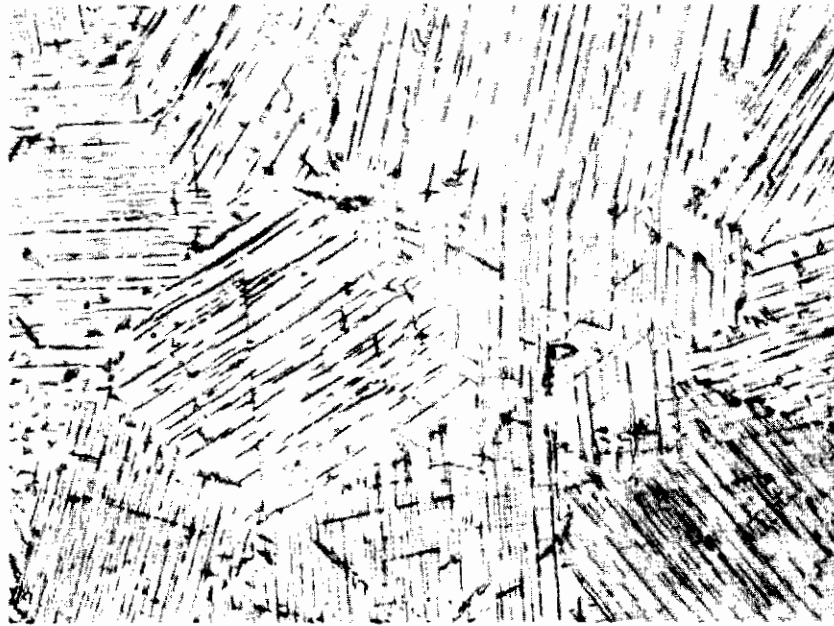


Figure 140. Hf-B-C (87-3-10 At.%), Heat-Treated at 1800°C X700
and Cooled.

α -Hf-Solid Solution with Unidirectional Monocarbide
Precipitations, and Small Amounts of Excess Monoboride.

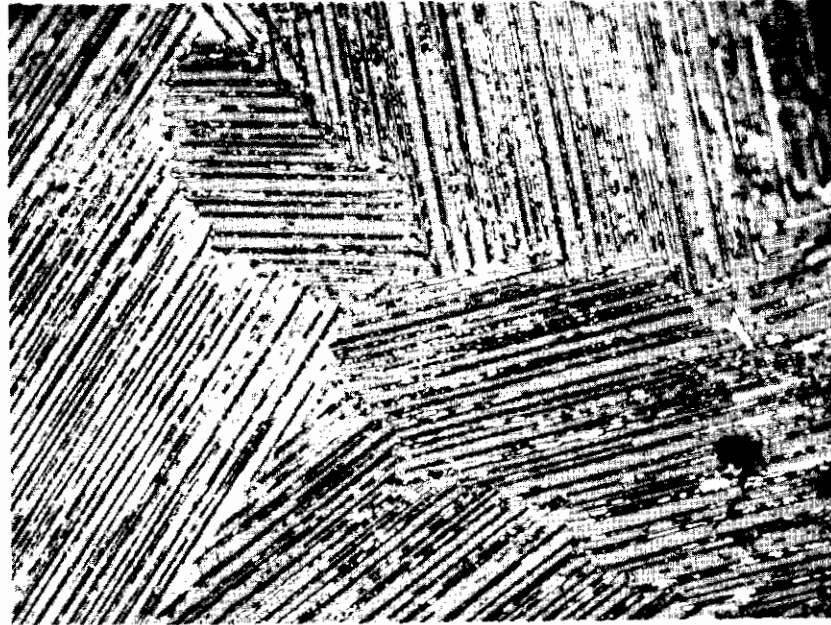


Figure 141. Hf-B-C (85-2-13 At.%), Melted, Re-equilibrated for X700
30 Minutes at 2300°C, and Cooled at $< 1^\circ\text{C}$ per Second.

α -Hf-Solid Solution with Heavy Precipitation of Monocarbide Phase.

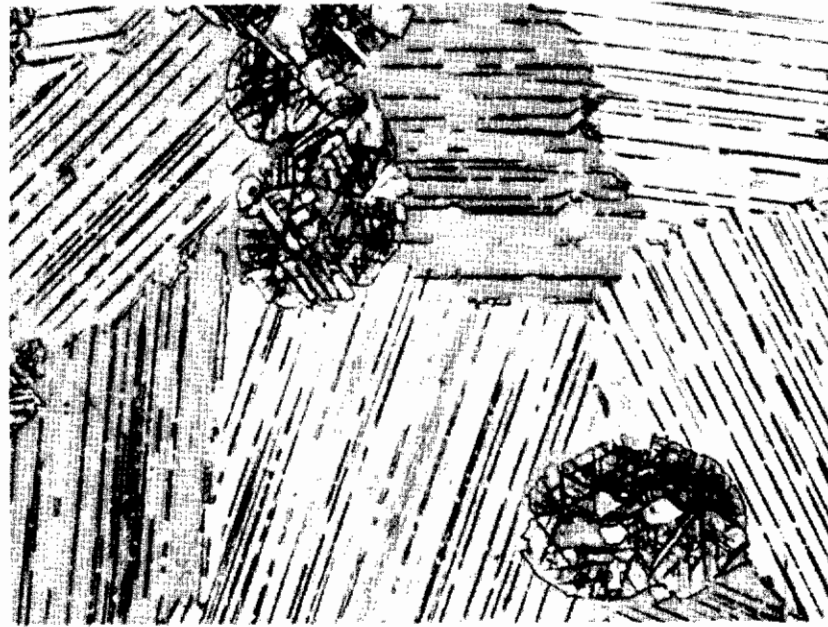


Figure 142. Hf-B-C (82-2-16 At.%), Melted, Re-equilibrated X700
at 2300°C, and Cooled at Approximately 10°C per
Second.

Monocarbide (with α -Hf Precipitations, in a Matrix of α -Hf-
Solid Solution, with localized Monocarbide Precipitates.

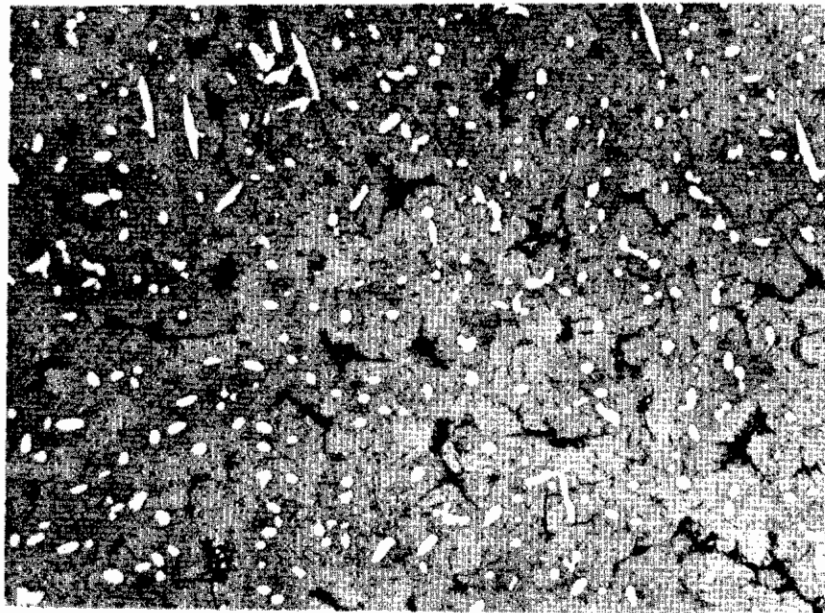


Figure 143. Hf-B-C (91-4-5 At.%), Quenched from 2300°C. X275

Primary Carbide (Light, Isolated Grains), Metal Phase,
and Small Amounts of Ternary Eutectic.

Non-Equilibrium Structure.

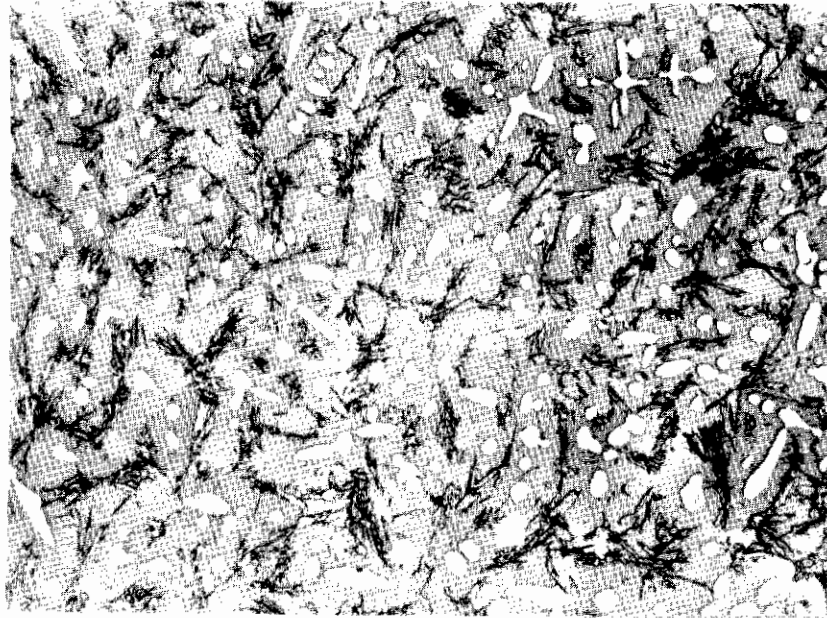


Figure 144. Hf-B-C (83-10-7 At.%), Quenched from 1850°C. X440

Primary Monocarbide (Rounded, Light Grains), Secondary Metal Phase, and Ternary Eutectic.

X-ray After Cooling: α -Hf + HfB + HfC

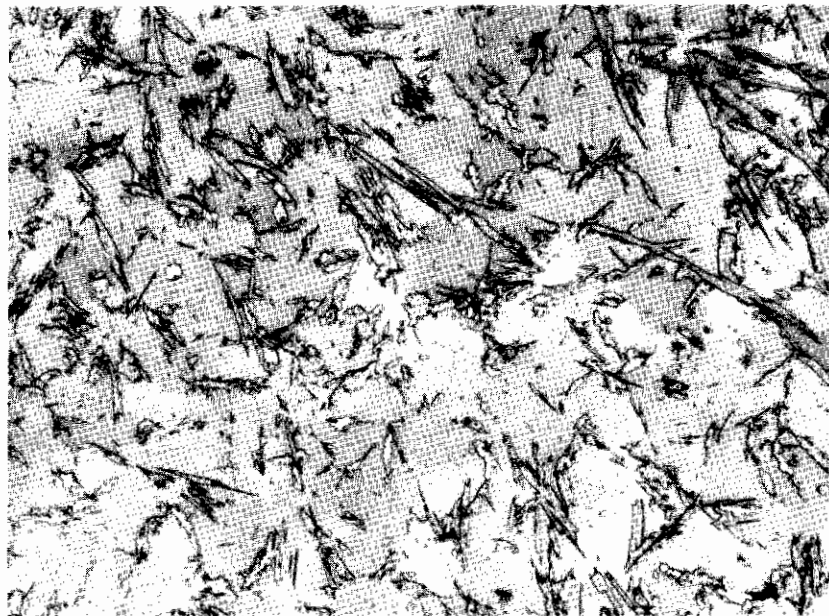


Figure 145. Sample from Figure 144, Equilibrated for 15 Minutes in the Liquidus + Solidus Region (1900°C), and Cooled. X480

Hf + HfB. Note Absence of the Carbide Phase.

X-ray: α -Hf + HfB.

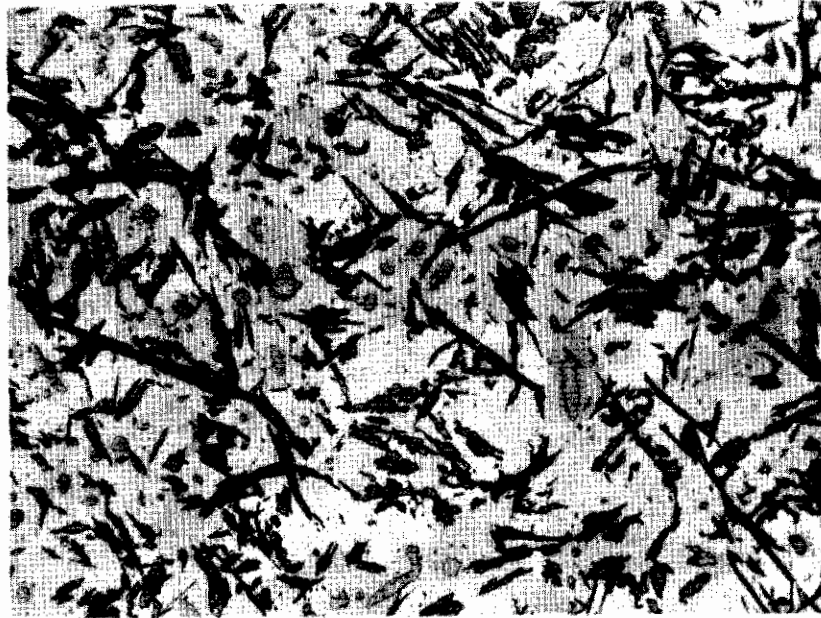


Figure 146. Hf-B-C (83-14-3 At.%), Quenched from 2000°C . X480
Primary Carbide (Rounded Grains) in a Bivariant Eutectic Matrix.

X-ray After Cooling: HfB + Hf + HfC-ss.

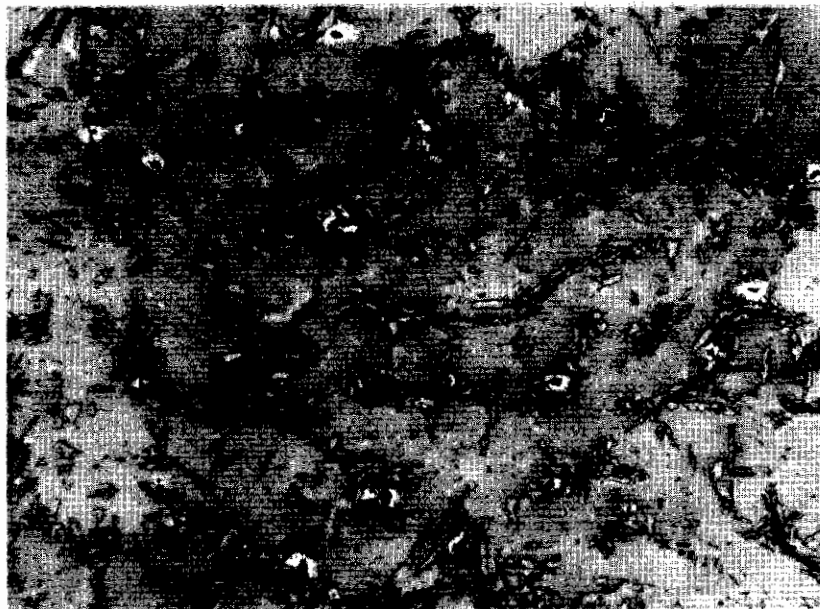


Figure 147. Sample from Figure 146, Re-equilibrated for 20 Minutes at 1820°C, and Quenched. X480

Note Hole Formation Due to Disappearance of the Carbide Phase.

Contrails

A sample Hf-B-C (68-27-5 At.%), contains a three-phase mixture of $\text{HfB}_2 + \text{HfC} + \text{Hf}$ after rapid cooling from 2085°C (Figure 148). The diboride phase disappeared completely (Figure 149), however, upon reannealing of the alloy at temperatures lower than the four-phase reaction plane



at approximately 2050°C (Table 34). In view of the slow formation of the monoboride at subsolidus temperatures⁽⁶⁵⁾, the presence of liquid phase in the equilibration procedures is essential in order to achieve rapid phase conversion.

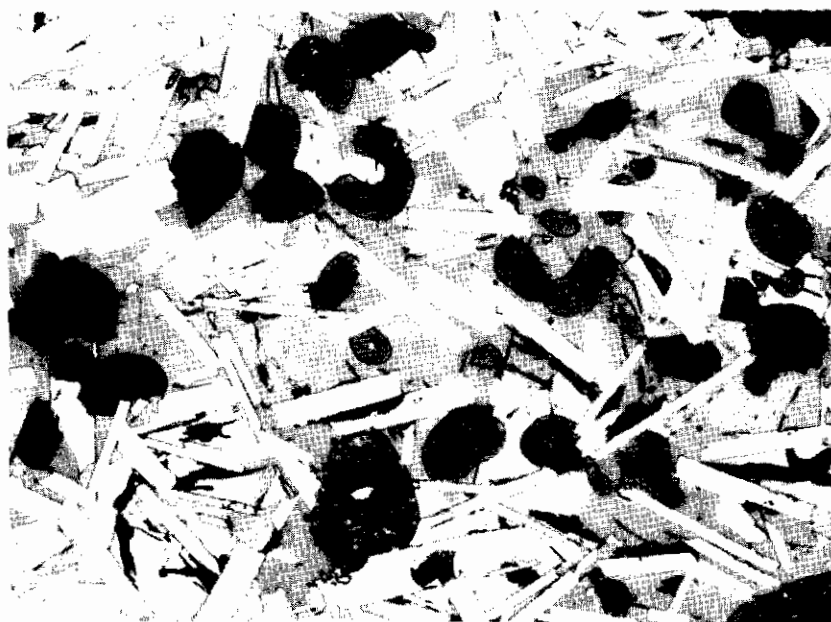


Figure 148. Hf-B-C (68-27-5 At.%), Rapidly Cooled from 2085°C .

X700

Quenched Non-Equilibrium Mixture Monocarbide (Dark, Equiaxed Grains), Hafnium Diboride (Light, Elongated Crystals), and Metal Matrix (Gray).



Figure 149. Sample from Figure 148, Re-equilibrated for 15 Minutes in the Liquidus + Solidus Region (2000°C), and Cooled. X900

Hafnium Monoboride (Grey, Irregular Shaped Grains), Metal Phase (Light), and Small Amounts of Monocarbide (Rounded Grains, with Localized Precipitations).

With the exception of the monocarbide, for which lattice parameters considerably larger than those of the binary, carbon-deficient carbide were measured (Table 34), the lattice parameter changes for the other phases were negligible; hence, only very restricted ternary homogeneity ranges for the boride phases, as well as for the α -hafnium solid solution, are to be assumed. The metallographic findings are in support of the X-ray results.

2. Phase Equilibria in the Concentration Region
HfB-HfB₂-HfC_{1-x}

Solid state-equilibrated alloys located along the concentration line HfB-HfC_{1-x} (0.30 < x < 0.40) were two-phased (Figure 131), consisting of mechanical mixtures of monoboride and monocarbide. An average

lattice parameter of $a = 4.636 \text{ \AA}$ was obtained for the carbon-deficient monocarbide phase in equilibrium with the monoboride at 1400°C .

Melting in the alloys located on the metal-rich side of the concentration line diboride-monocarbide, occurred extremely two-phased. The alloys, which usually were quenched, or rapidly cooled, from temperatures in excess of 2500°C , contained non-equilibrium phase mixtures, consisting of Hf, HfB_2 , HfC, and smaller amounts of hafnium monoboride, formed in the final solidification of the alloys. The existence of the four-phase reaction plane



at temperatures around 2050°C resulted in the formation of characteristic crystallization patterns: In an alloy Hf-B-C (44-48-8 At.%), located on the diboride side of the pseudobinary eutectic HfB_2 -HfC, the primary product of crystallization is HfB_2 (Figure 150). Bivariant solidification of the melt along the eutectic trough e_1 -II₁ (Figure 12) produces a eutectic-type structure diboride + monocarbide. However, as soon as the four-phase temperature-plane is reached, the phase combination $\text{HfB}_1 + \text{HfC}$ -ss becomes unstable with respect to the pair $\text{HfB} + \text{HfC}$ -ss, and the eutectic-type structure diboride + monocarbide is abruptly replaced by the phase combination monoboride + monocarbide (Figure 151 a and b). Crystallization finally is completed at 1850°C , the temperature of the metal-rich ternary eutectic.

With the exception of alloys close to hafnium monocarbide, melted, as well as solid state-equilibrated, specimens located along the concentration field HfB_2 - HfC_{1-x} ($0 < x < 0.33$) contained only these two phases (Figures 131 and 152 through 154).

From the observed melting pattern (Figure 155, Table 34) and the metallographic examination of the melted and quenched alloys (Figure 156 through 162), the pseudobinary eutectic point was located at $3140 \pm 15^\circ$, at a concentration of 34 ± 2 mole % $\text{HfC}_{0.90}$. Annealing of the eutectic structures at temperatures slightly below the eutectic isotherm occurs extremely rapid (Figure 159), and precipitation of hafnium diboride from the monocarbide solution could not be prevented by quenching (compare Figures 156 and 157).

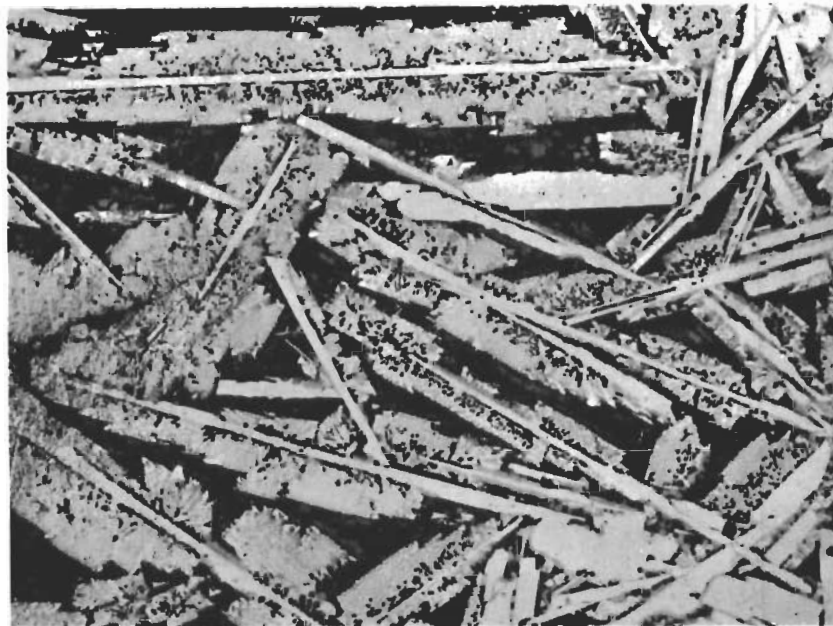


Figure 150. Hf-B-C (44-48-8 At.%), Cooled at Approximately 15°C per Second from 2940°C. X120

Primary HfB_2 (Needle-Shaped, Bright Crystals), Surrounded by Secondary Eutectic $\text{HfB}_2 + \text{HfC}_{1-x}$. The Dark Areas Consists of Ternary Monoboride Formed at Temperatures Below 2050°C, Small Amounts of Monocarbide and Metal Phase. For Structural Details, See Figure 151.

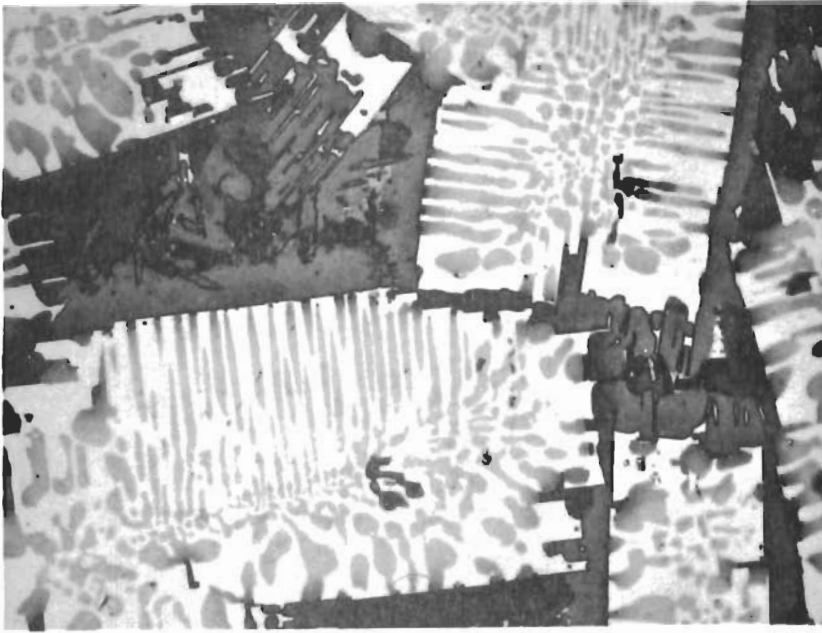


Figure 151(a) X750



Figure 151(b) X150

Figure 151 (a) and (b). Enlarged View of Specimen Shown in Figure 150.

Note the Abrupt Onset of Monoboride Formation in the Zone Adjacent to Eutectic-Type Structure.

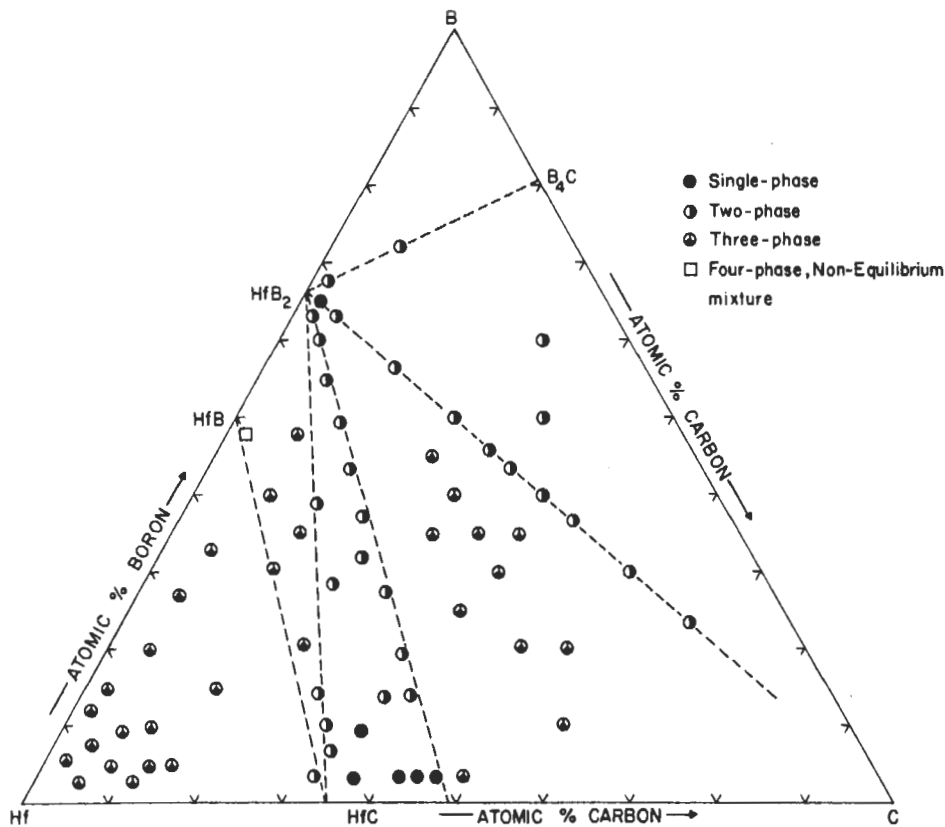


Figure 152. Hf-B-C: Location of Melting Point Samples, and Qualitative (X-ray) Phase Evaluation After Melting.

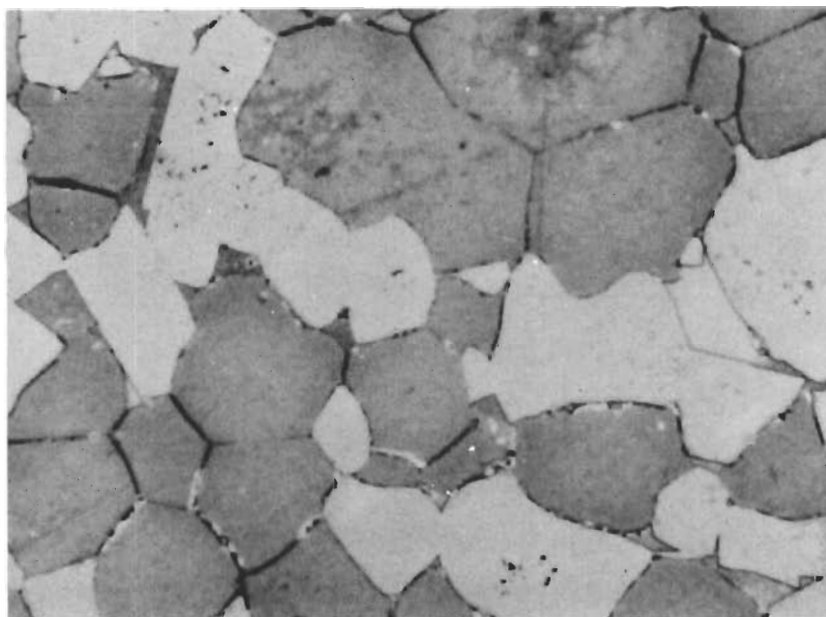


Figure 153. Hf-B-C (53-20-27 At.%), Melted, Re-equilibrated at 2200°C, and Quenched.

X1000

Diboride (Light) and Monocarbide (Grey), with Traces of Metal Phase and Monoboride at the Grain Boundaries.

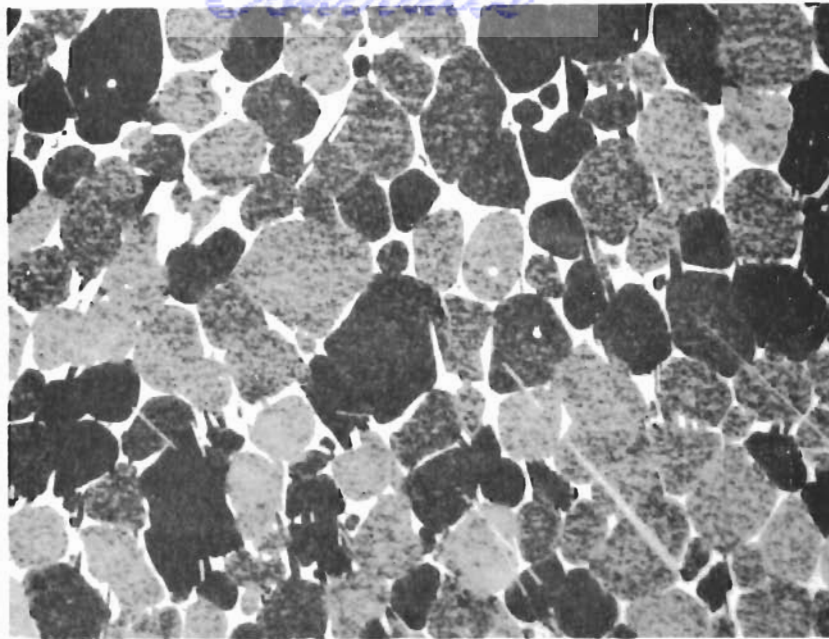


Figure 154. Hf-B-C (51-14-35 At.%), Melted at 3350°C, and X750
 Cooled at Approximately 20°C per Second After
 Re-equilibration at 2800°C.

Monocarbide (Dark, with Heavy Diboride Precipitations),
 with Small Amounts of Diboride (Light) at the Grain Boundaries).

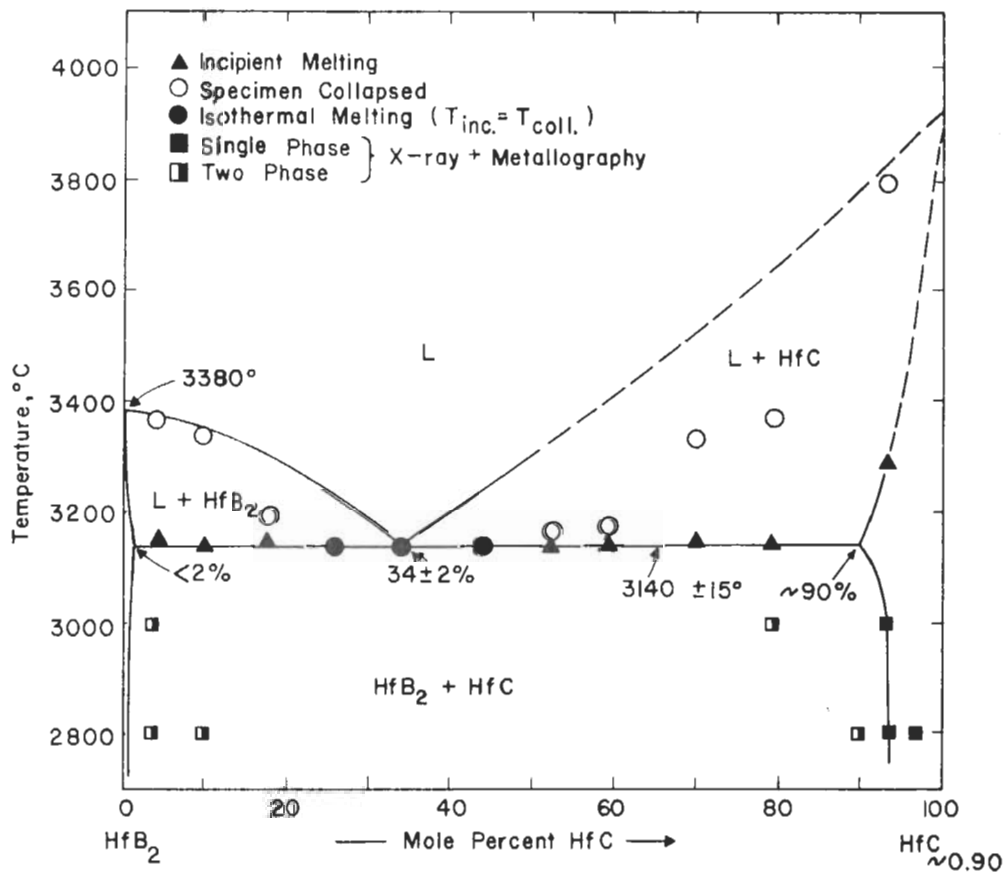


Figure 155. Melting Temperatures of Alloys Located Along
 the Pseudobinary Section HfB₂-HfC_{~0.90}

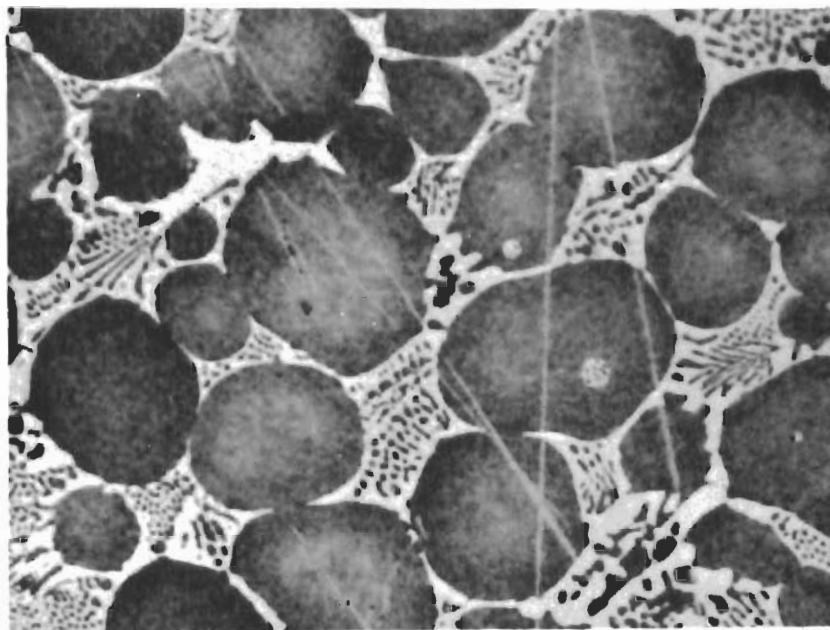


Figure 156. Hf-B-C (46-20-34 At.%), Rapidly Quenched from 3348°C.

X1000

Primary Monocarbide (Dark Grains, with Heavy Diboride Precipitation), in a Matrix of $\text{HfB}_2 + \text{HfC-ss}$ Pseudobinary Eutectic.

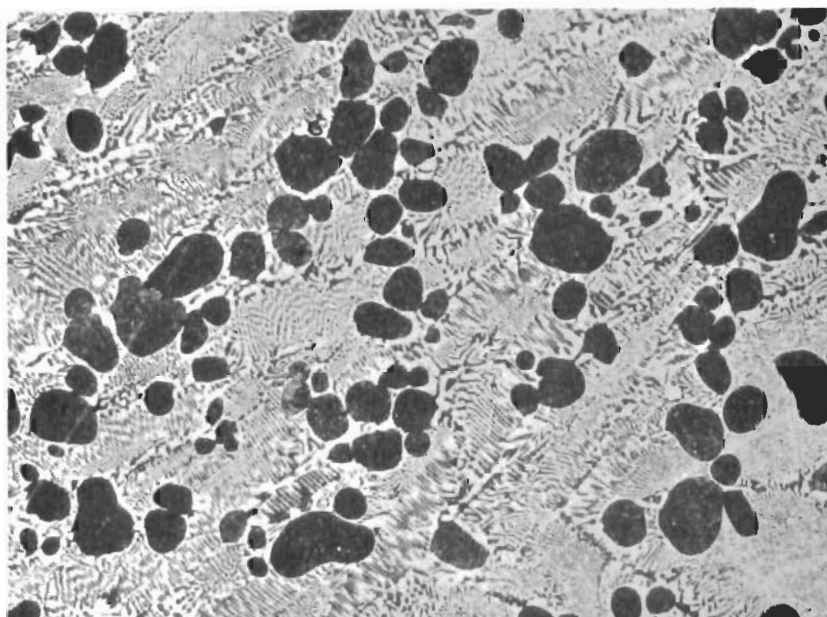


Figure 157. Hf-B-C (41-38-21 At.%), Rapidly Quenched from 3145°C.

X400

Smaller Amounts of Primary Monocarbide (Rounded, Dark Grains), in a Pseudobinary $\text{HfB}_2 + \text{HfC-ss}$ Eutectic Matrix.

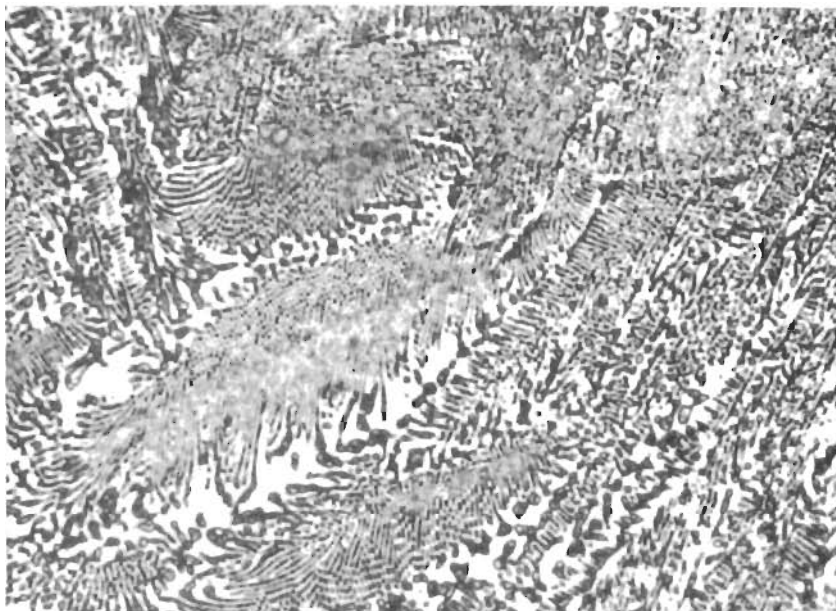


Figure 158. Hf-B-C (40-43-17 At.%), Quenched from 3142°C. X1000
HfB₂ + HfC-ss Pseudobinary Eutectic.

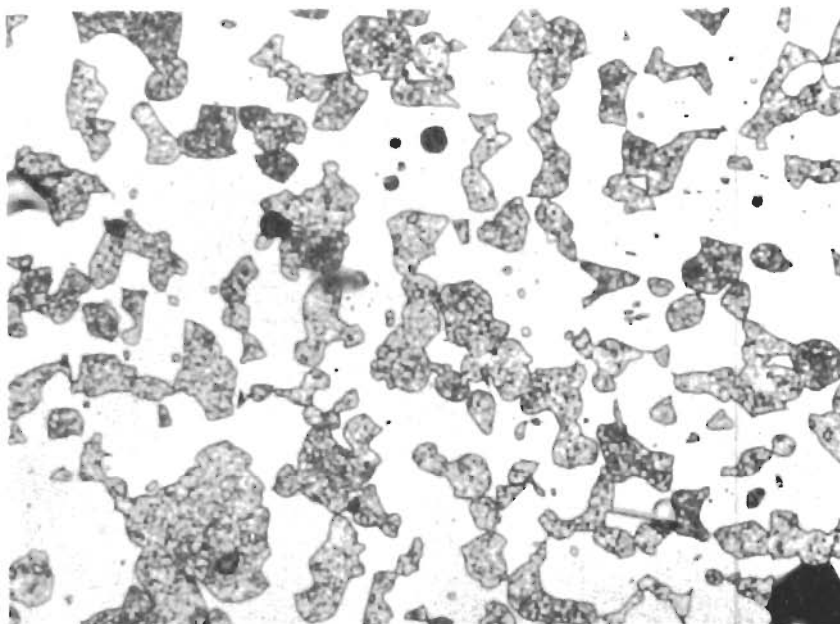


Figure 159. Sample from Figure 158, Equilibrated for 40 Seconds at 3100°C, and Quenched. X1000

Annealed Eutectic Structure. Note Heavy Precipitations in the Monocarbide (Dark) Grains.

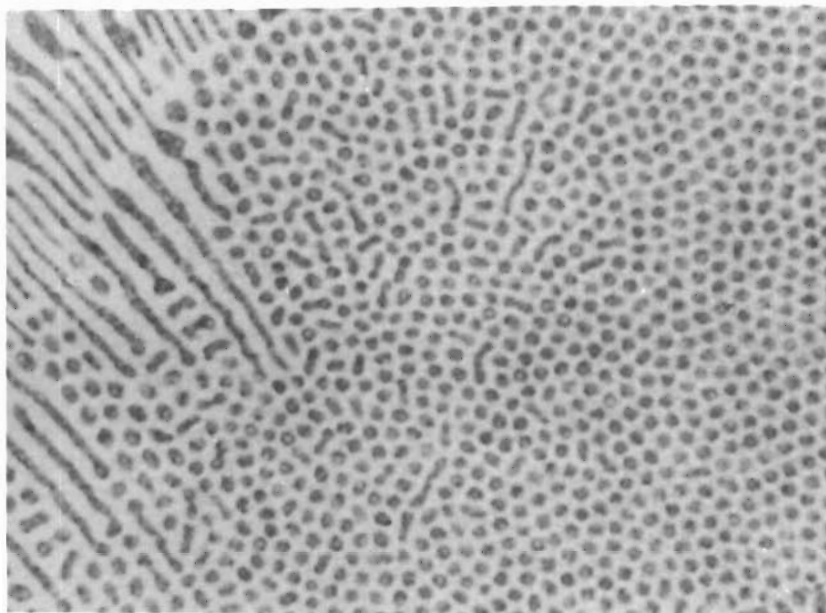


Figure 160. Magnified Portion of Specimen Shown in Figure 158.

X2500

Fine Structure of the Pseudobinary Eutectic $\text{HfB}_2 + \text{HfC}$:
Fibrillous Monocarbide Embedded in a Continuous Matrix
of HfB_2 .

Note the portion of a differently oriented eutectic colony in
the lower right of the micrograph.



Figure 161. Hf-B-C (40-45-15 At.%), Quenched from 3145°C . X1000

Traces of Primary Hafnium Diboride in a Matrix of
Pseudobinary Eutectic $\text{HfB}_2 + \text{HfC}$ -Solid Solution.

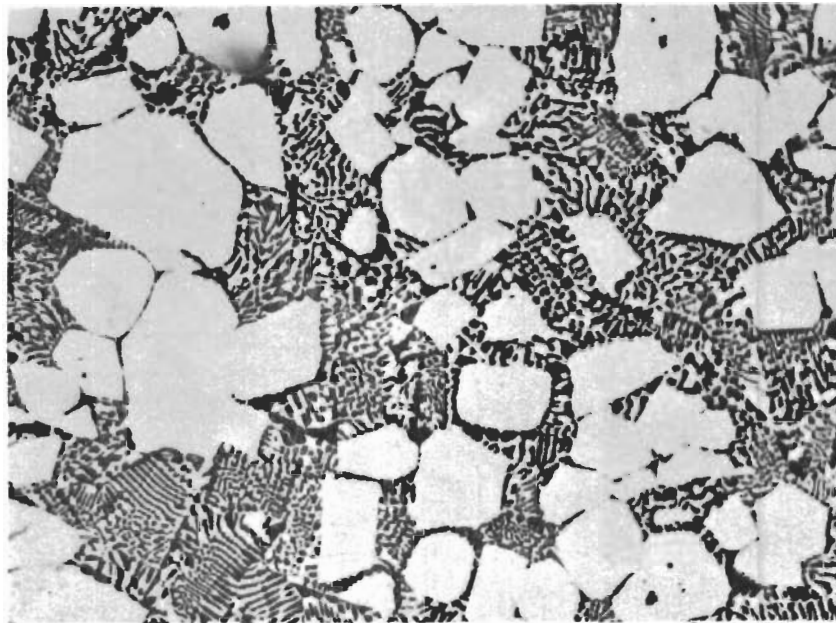


Figure 162. Hf-B-C (38-49-13 At.%), Quenched from 3145°C. X500

Primary Crystallized Hafnium Diboride and Pseudobinary Eutectic $\text{HfB}_2 + \text{HfC-ss}$.

The ternary solid solubility range of hafnium monocarbide was investigated by a series of high temperature-equilibrated, and quenched, alloys. An alloy Hf-B-C (60-8-32 At.%), which was quenched from 3350°C, was three-phased, containing small amounts of excess metal phase and monoboride besides the monocarbide (Figure 163). An alloy series traversing at 4 atomic percent boron the range of the monocarbide defect solid solutions is single-phased after equilibration and quenching from 3200°C (Figures 164 through 166).

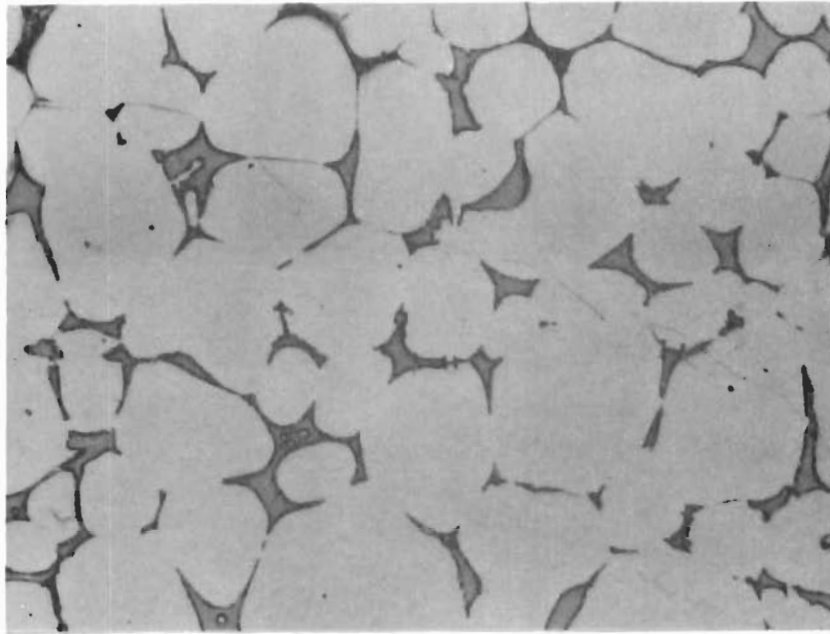


Figure 163. Hf-B-C (60-8-32 At.%), Quenched from 3350°C. X800

Primary Monocarbide, with Metal and Small Amounts of Monoboride at the Grain Boundaries.

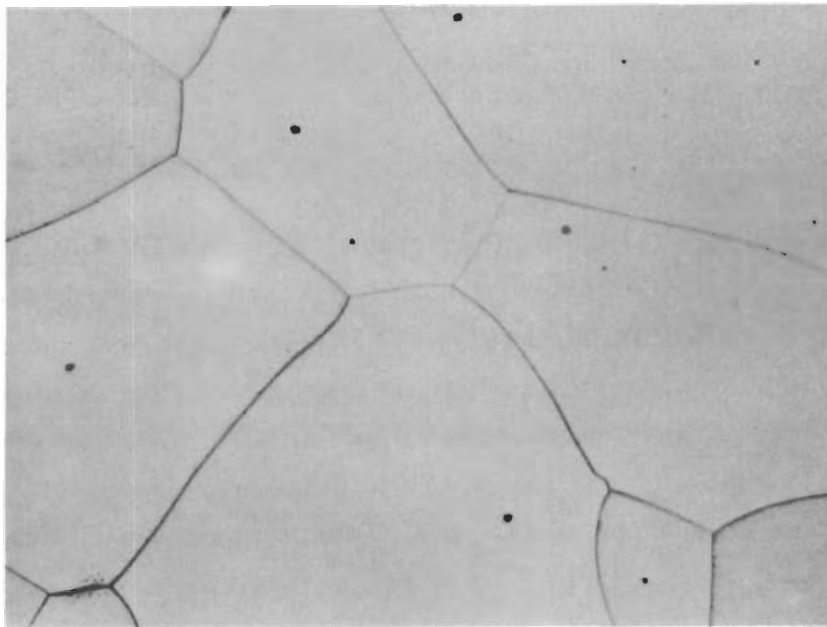


Figure 164. Hf-B-C (55-4-61 At.%), Quenched at Approximately 60°C per Second from 3200°C. X500

Single Phase $\text{Hf}(\text{C}, \text{B})_{1-x}$ Solid Solution.

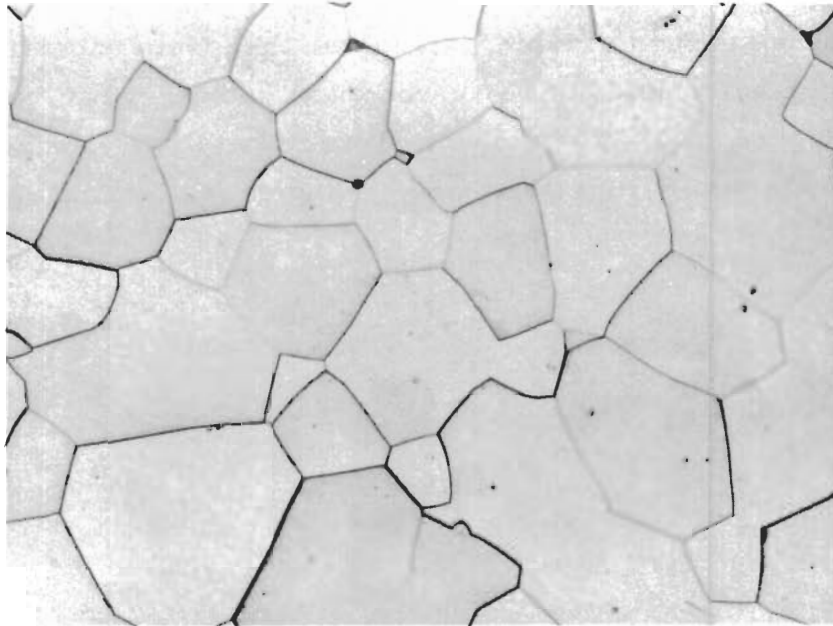


Figure 165. Hf-B-C (53-4-43 At.%), Quenched at Approximately 60°C per Second from 3200°C.

X200

Single Phase $\text{Hf(C,B)}\text{C}_{1-x}$ Solid Solution.

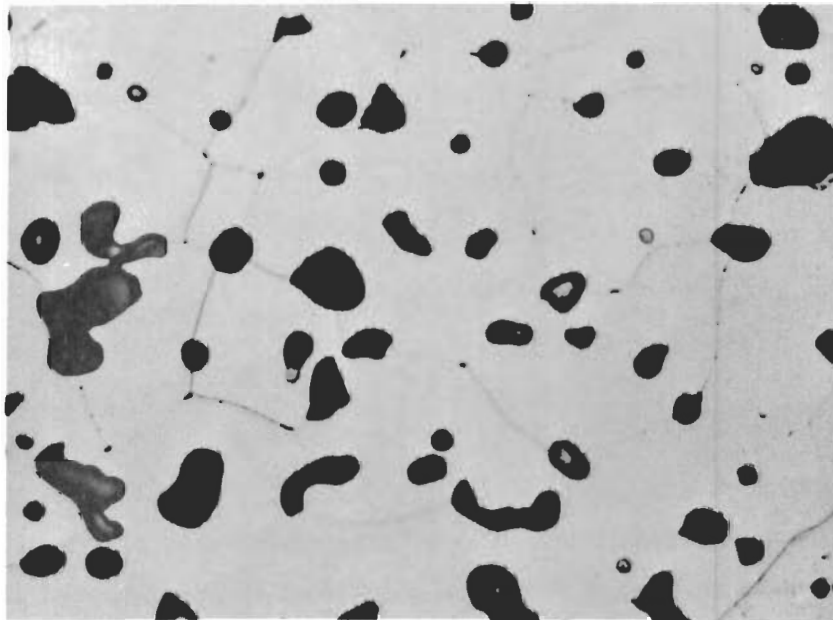


Figure 166. Hf-B-C (51-4-45 At.%), Quenched at Approximately 80°C per Second from 3200°C.

X500

Single Phase Monocarbide Solution Hf(C,B) and Pores (Dark).

Boride precipitation from the carbon-saturated monocarbide phase occurs considerably faster than from substoichiometric composition, and usually could not be prevented at cooling rates lower than 100°C per second (Figure 167). The amount of precipitate phase increases upon lowering the cooling rates (Figure 168 a and b), indicating that the monocarbide phase

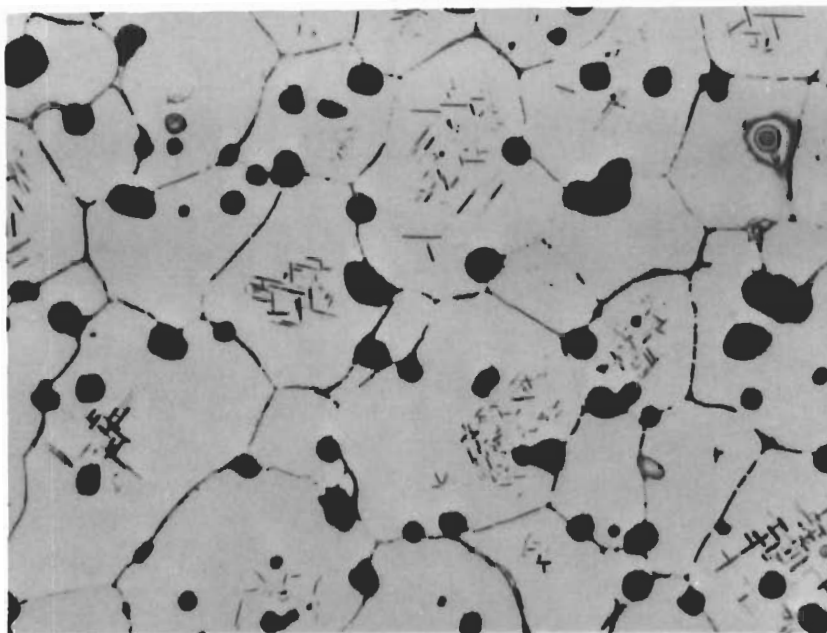


Figure 167. Hf-B-C (48-4-48 At.%), Quenched at Approximately 80°C per Second from 3200°C. X500

Monocarbide Solution with Intragranular, Localized Diboride Precipitations, and Scant Traces of Graphite at the Grain Boundaries.

boundary within the two-phase field $\text{Hf}(\text{C}, \text{B})\text{C}_{1-x} - \text{HfB}_2$ must be located at still lower boron concentrations. A maximum boron exchange of ~ 22 atomic percent was observed at a carbon defect of approximately 7 atomic percent, and an alloy Hf-B-C (57-10-33 At.%), was retained single-phased by tin-quenching the sample from 3100°C (Figure 169). The lattice parameter measured, $a = 4.649 \text{ \AA}$, is compatible with the value to be expected from the extrapolated parameters for a cubic hafnium monoboride⁽⁵⁹⁾.

Contrails

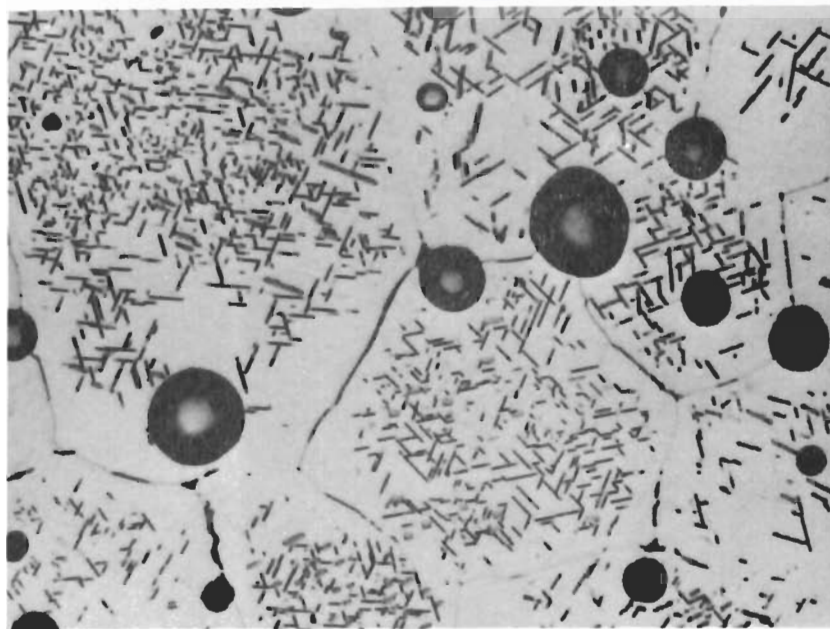


Figure 168(a) X800

Sample from Figure 166, Re-equilibrated at 3200°C, and Cooled at Approximately 10°C per Second.

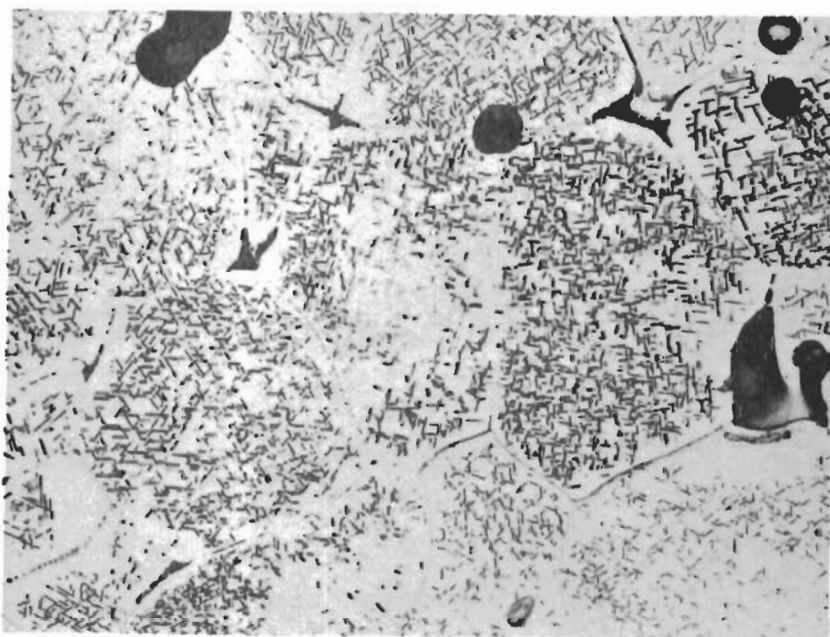


Figure 168(b) X500

Sample from Figure 167, Re-equilibrated at 3200°C, and Cooled at Approximately 10°C per Second.

Figure 168(a) and (b).

Increased Diboride Precipitations from the Monocarbide Solution Following Slow Cooling from 3200°C.

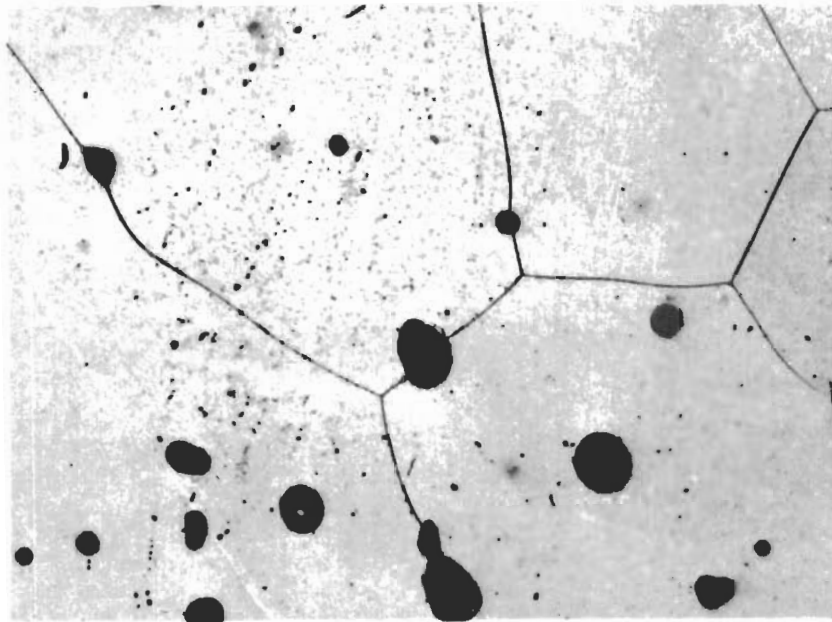


Figure 169. Hf-B-C (57-10-33 At. %), Tin-Quenched from X700
3100°C After Melting.

Single Phase Monocarbide Solution with Pores (Dark)

X-ray: Single Phase, $a = 4.649 \text{ \AA}$

3. The Pseudobinary Section Hafnium Diboride-Graphite

From previous work⁽¹⁾ as well as the lower-temperature equilibration treatments carried out in this work (Figure 131), the existence of an equilibrium diboride-graphite was ascertained. X-ray analysis of the melted samples further showed (Figure 152) that both phases form a true pseudobinary system of the eutectic type. The isothermal reaction temperature was determined to $2515 \pm 10^\circ\text{C}$ from a series of melting point samples located along the concentration diboride-graphite (Figure 170). Due to the presence of large amounts of solid diboride, incipient melting in the alloys located close to the hafnium-boron edge binary was difficult to observe and usually not noted, until temperatures considerably above the eutectic line

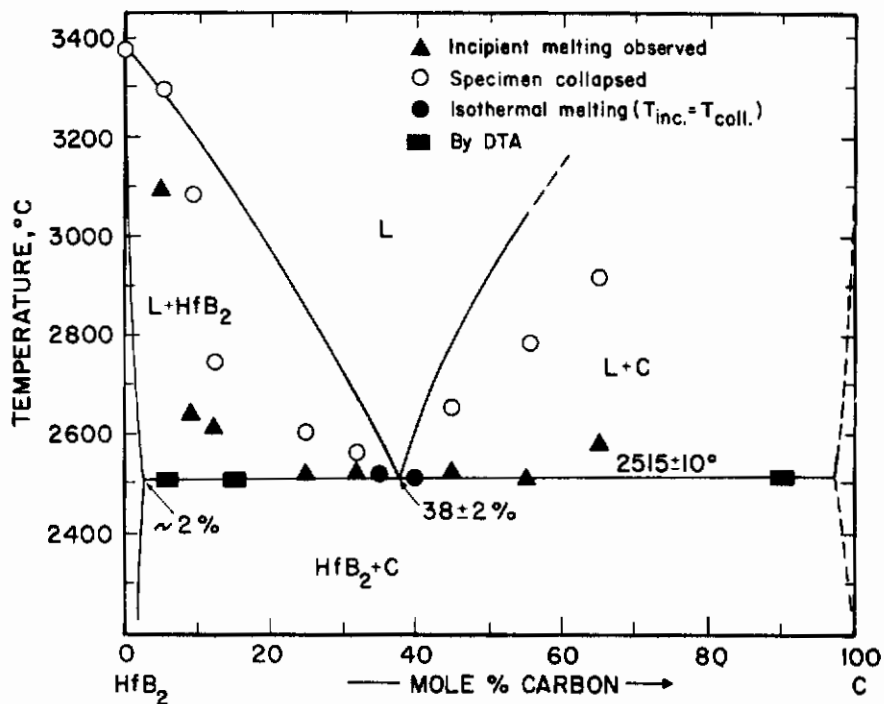


Figure 170. Melting in the Pseudobinary System HfB₂-C.

were reached; nevertheless, heterogeneity at the eutectic temperature at carbon concentrations less than 6 atomic percent was derived from measurements carried out differential-thermoanalytically (Figures 170 and 171), as well as by microscopic inspection of the melted alloys. Micrographic techniques also were used to bracket the pseudobinary eutectic composition to within the composition limits 38 ± 2 mole percent carbon (Figures 172 through 175).

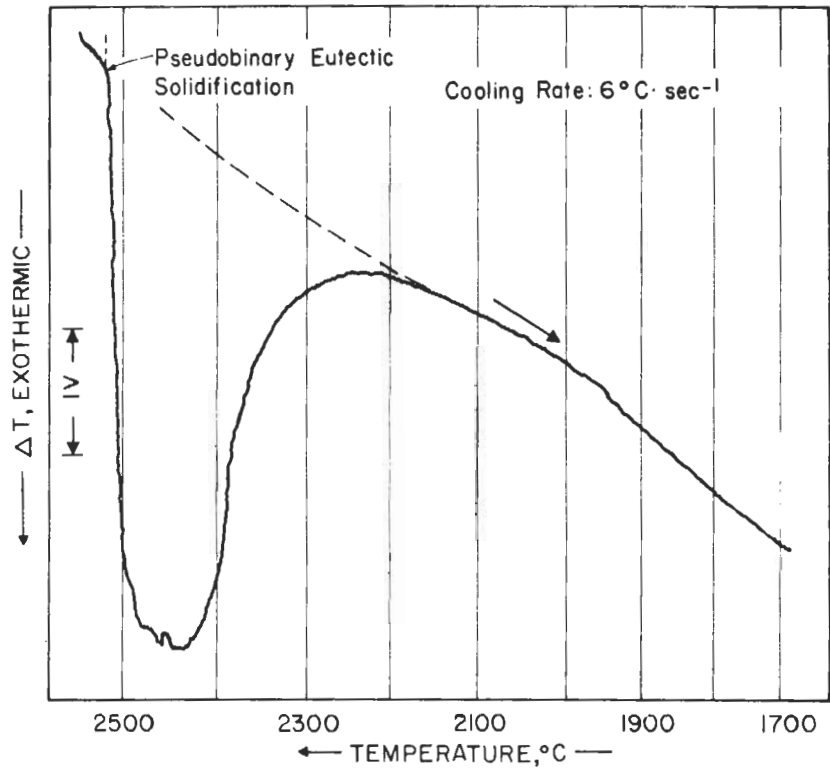


Figure 171. DTA-Thermogram (Cooling) of a Hf-B-C (31-63-6 At.%) Alloy, Showing Pseudobinary Eutectic Solidification Along the Section HfB_2 -C.

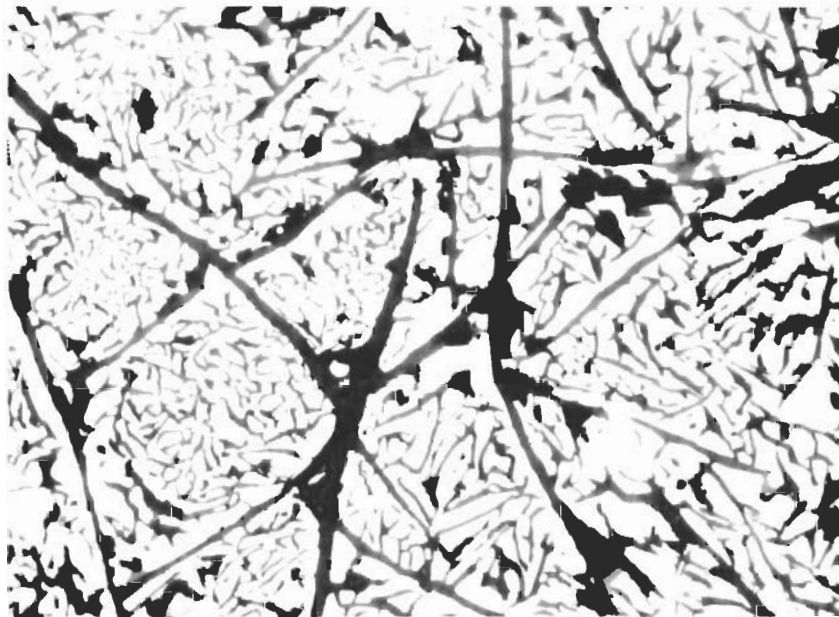


Figure 172. Hf-B-C (18-36-46 At.%), Quenched from 2650°C . X600 Primary Graphite in a Pseudobinary $\text{HfB}_2 + \text{C}$ Eutectic Matrix.

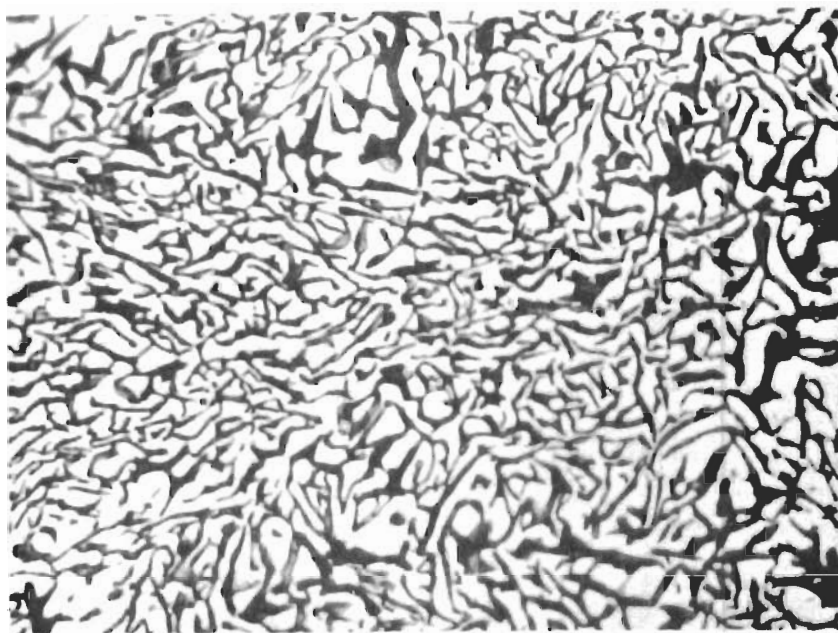


Figure 173. Hf-B-C (20-40-40 At.%), Quenched from 2512°C. X1000
Traces of Primary Graphite in a Eutectic Matrix.

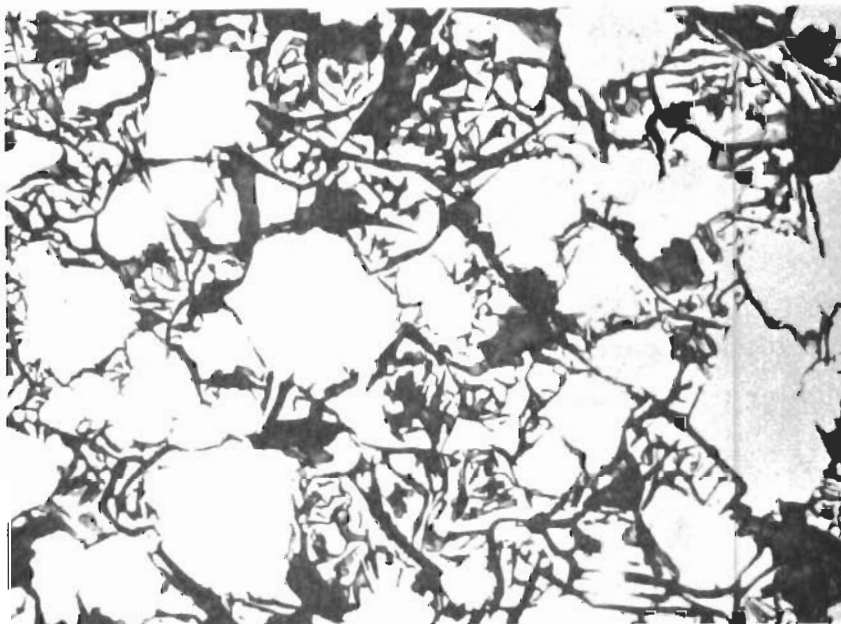


Figure 174. Hf-B-C (22-44-34 At.%), Rapidly Cooled from 2517°C. X600
Primary Hafnium Diboride in a $\text{HfB}_2 + \text{C}$ Eutectic.

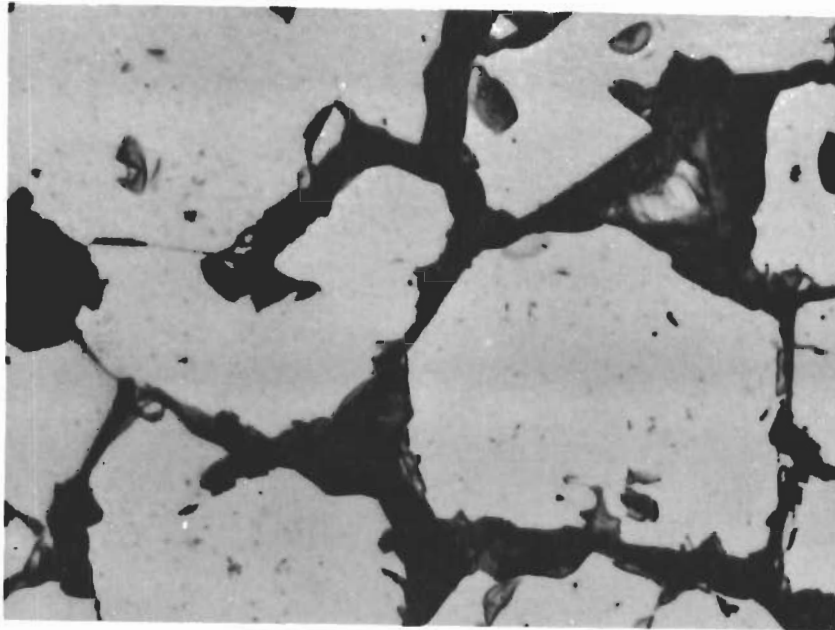


Figure 175. Hf-B-C (28-57-15 At.%), Cooled at 2°C per Second from 2580°C.

X1000

Primary Diboride with Grain Boundary Graphite
(Eutectic Recrystallized.)

4. The Pseudobinary Section Diboride-Boron Carbide

The existence of a eutectic reaction isotherm between hafnium diboride and boron carbide was established by melting point as well as DTA-techniques (Table 34, Figures 176 and 177).

The eutectic composition was derived from the micrographic analysis of the quenched alloys. Typical microstructures from alloys from the pseudobinary section, which also reveal the eutectic to consist of fibrillous diboride, embedded in a continuous boron carbide matrix, are shown in Figures 178 through 180. According to the metallographic findings (Figure 180) as well as the X-ray diffraction results (Table 34), the ternary solubility ranges for both phases are small.

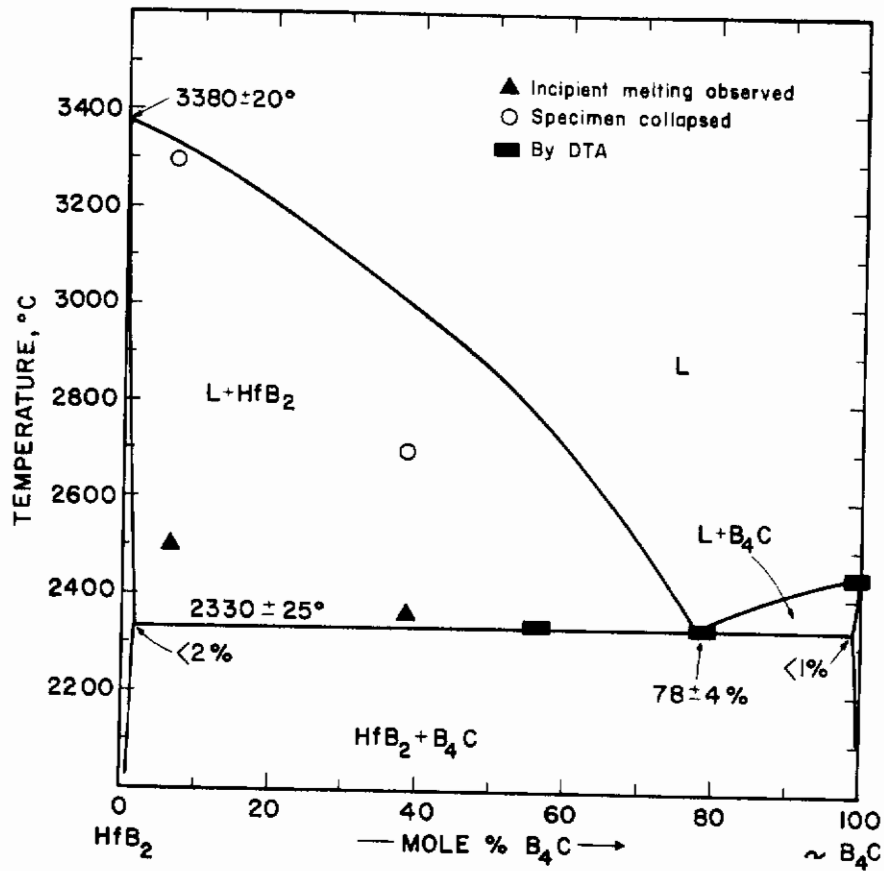


Figure 176. Melting Along the Pseudobinary Section HfB₂-B₄C.

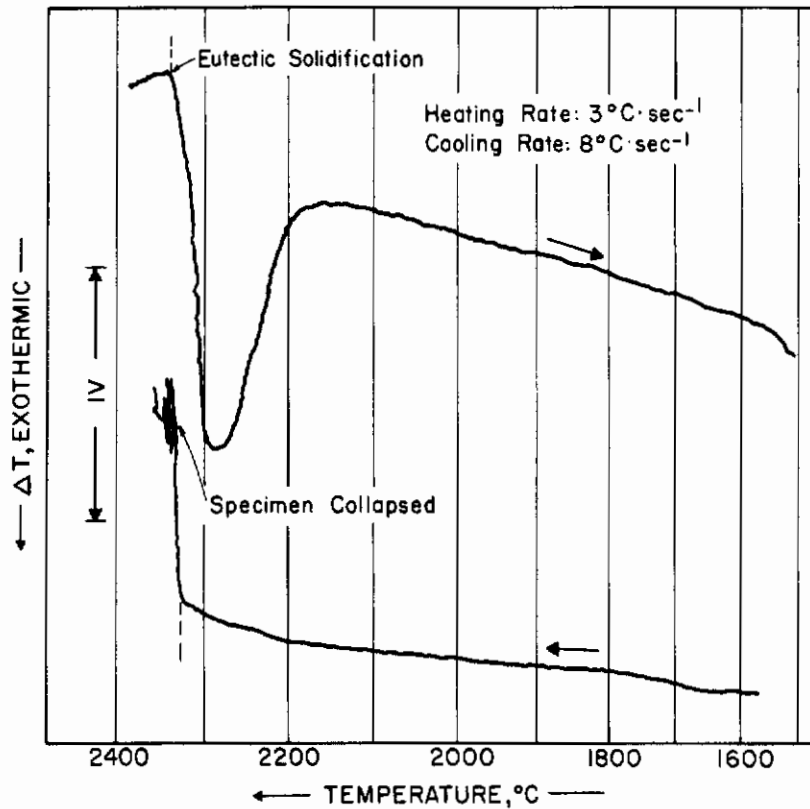


Figure 177. DTA-Thermogram of a Hf-B-C (7-78-15 At.%) Alloy, Showing Eutectic Melting (Heating) and Solidification (Cooling) Along the Section $\text{HfB}_2\text{-B}_4\text{C}$.

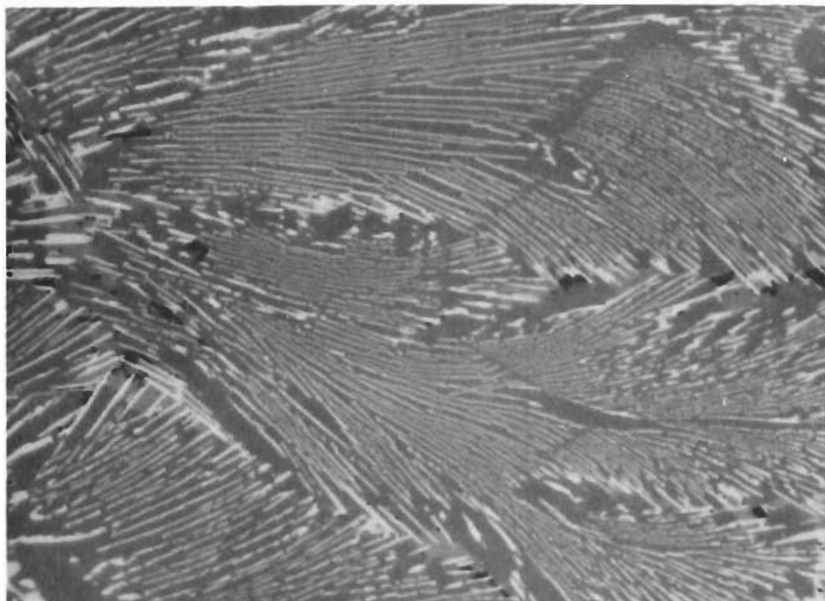


Figure 178(a) X680

Quenched from 2340°C.
HfB₂ + B₄C Eutectic.

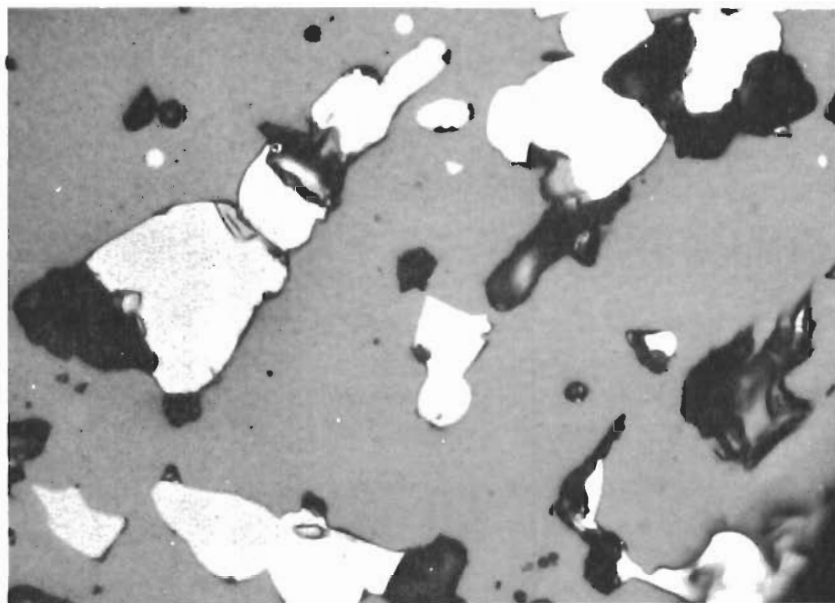


Figure 178(b) X1000

Sample from Figure 178(a),
After Annealing at 2200°C.
(Pores are Due to Break-
out of Diboride During the
Metallographic Preparation.)

Figure 178 (a) and (b). Eutectic Alloy Hf-B-C (7-78-15 At.%).

- (a) Quenched from 2340°C.
- (b) After Annealing at 2200°C.

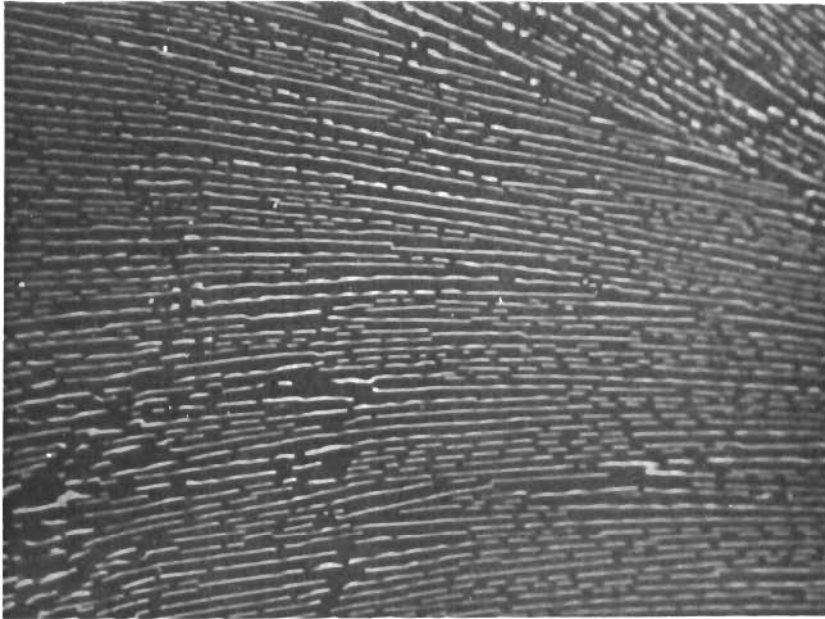


Figure 179(a) X950

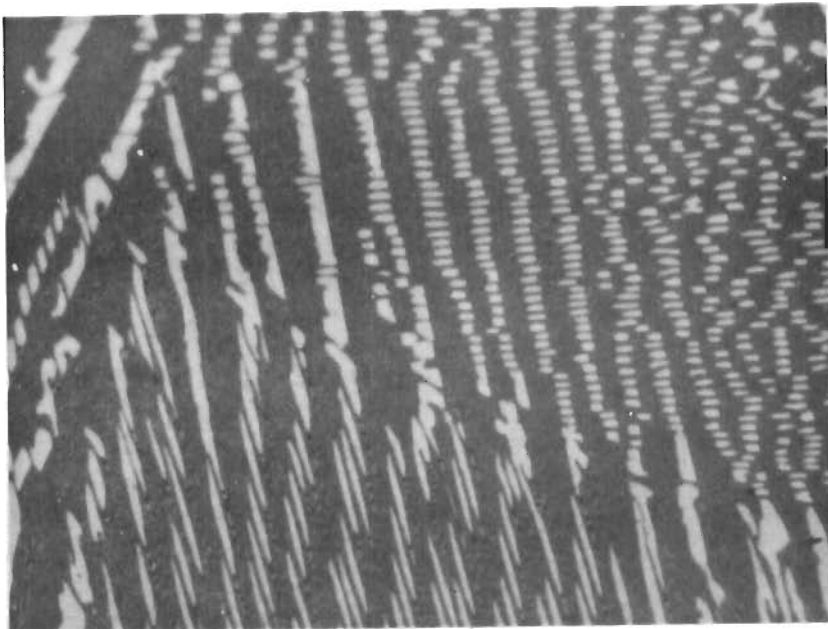


Figure 179(b) X800

Figure 179(a) and (b). Alloy: Hf-B-C (10-77-13 At.%), Cooled at
Approximately 20°C per Second from 2350°C.

HfB₂ + B₄C Eutectic Colonies.

Continuous, Dark Phase: B₄C
Light : HfB₂

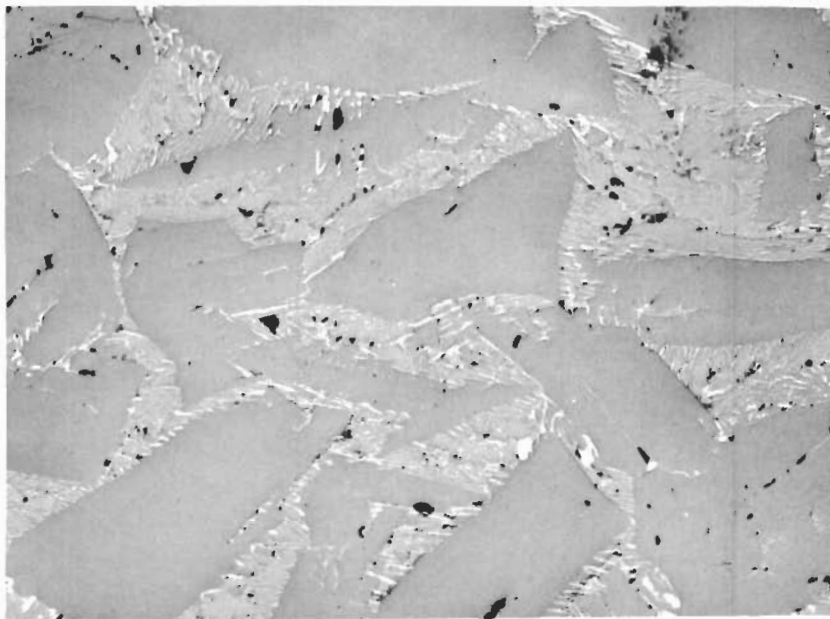


Figure 180. Hf-B-C (4-79-17 At.%), Quenched from 2360°C. X100
Primary Boron Carbide in a $\text{HfB}_2 + \text{B}_4\text{C}$ Eutectic Matrix.

5. Equilibria in the Composition Region
HfC-HfB₂-B-C

From the existence of pseudobinary sections $\text{HfB}_2 + \text{B}_4\text{C}$, $\text{HfB}_2 + \text{C}$, and $\text{HfB}_2 + \text{HfC}$, and the appearance of simple eutectic equilibria in the boundary systems, ternary eutectic equilibria are to be expected to form within the three phase fields $\text{HfB}_2 + \text{B}_4\text{C} + \text{B}$, $\text{HfB}_2 + \text{B}_4\text{C} + \text{C}$, and $\text{HfB}_2 + \text{HfC} + \text{C}$.

The reaction isotherms for the latter two were determined by melting point (Table 34), as well as DTA-techniques (Figures 181 and 182), and the eutectic composition derived from metallographic inspection of the as-melted and quenched alloys (Figure 183, 184, and 185).

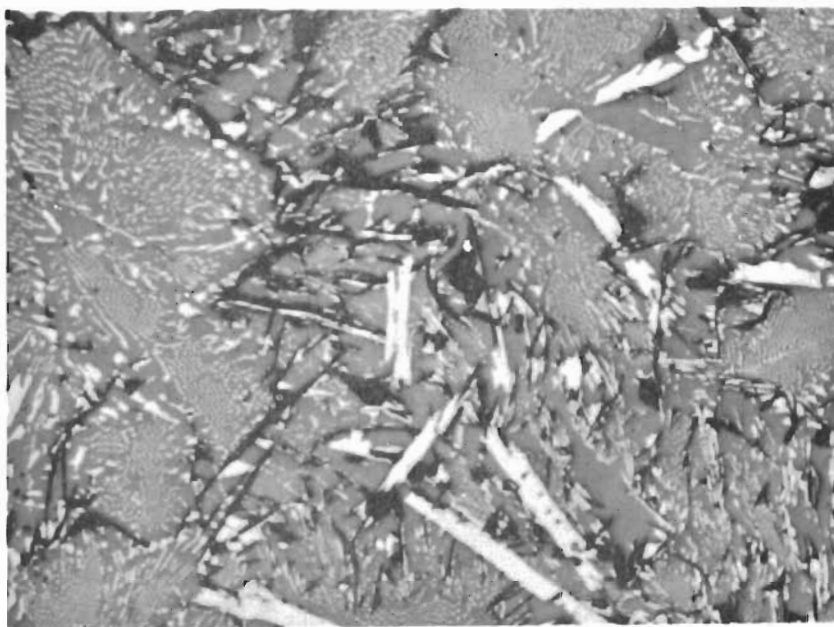


Figure 183. Hf-B-C (10-67-23 At.%), Quenched from 2270°C. X240
Small Amounts of Primary Diboride (Light, Elongated Crystals) in a Predominantly Eutectic Matrix $\text{HfB}_2 + \text{B}_4\text{C} + \text{C}$.

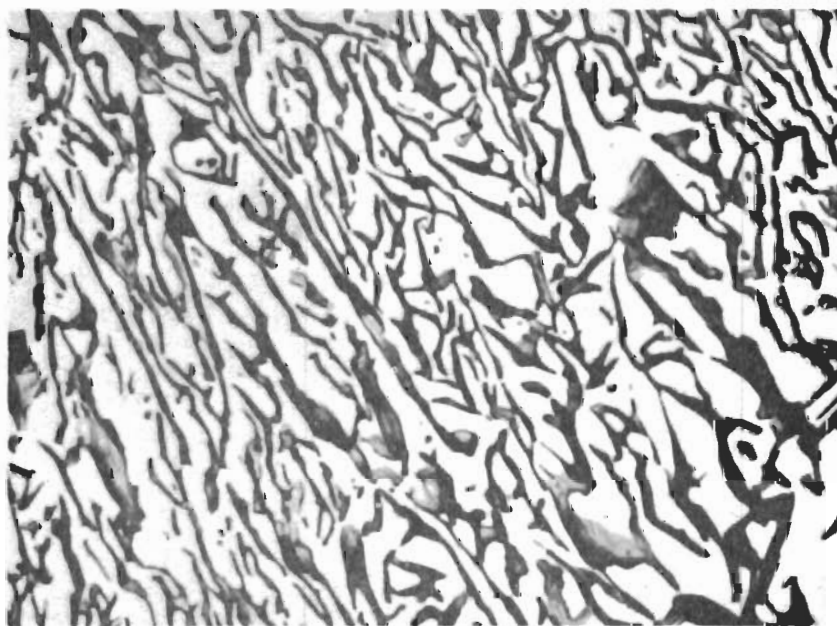


Figure 184. Hf-B-C (23-40-37 At.%), Quenched from 2500°C. X1000
Ternary Eutectic $\text{HfB}_2 + \text{HfC} + \text{C}$.
Note: The Ternary Eutectic Contains Only Very Small Quantities of Monocarbide.

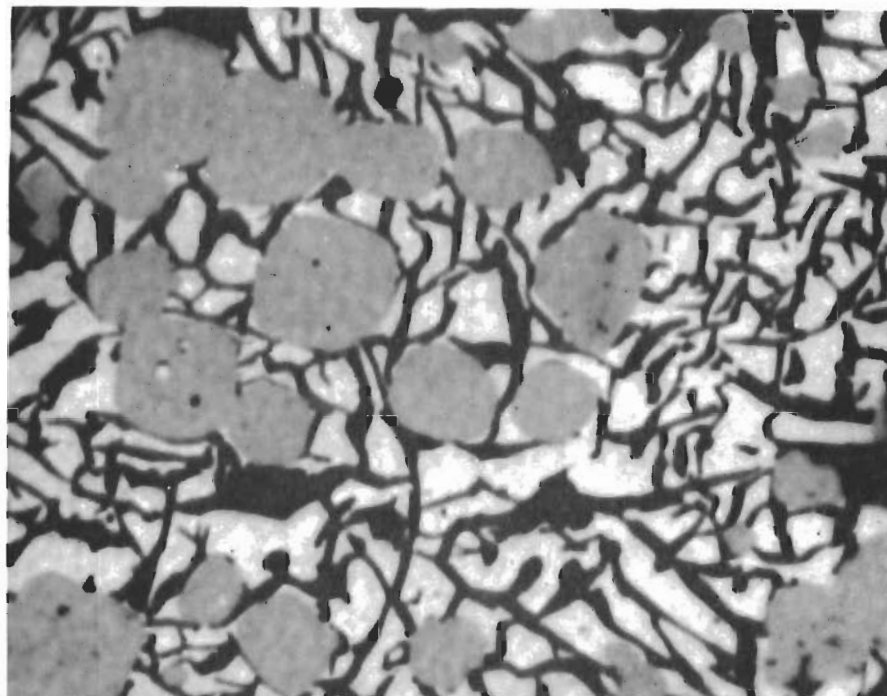


Figure 185. Hf-B-C (25-35-40 At.%), Quenched from 2507 °C. X1000

Primary Monocarbide (Round Elongated Crystals)
and Graphite, in a Matrix of Ternary Eutectic $\text{HfB}_2 + \text{HfC} + \text{C}$.

The poor electrical conductivity of the specimens prohibited the use of the Pirani technique in excess boron-containing alloys. The finally accepted eutectic temperature of 1950°C, therefore, was based on DTA-results obtained on an alloy containing 4 At.% hafnium, 90 At.% boron, and 6 At.% carbon (Figure 186).

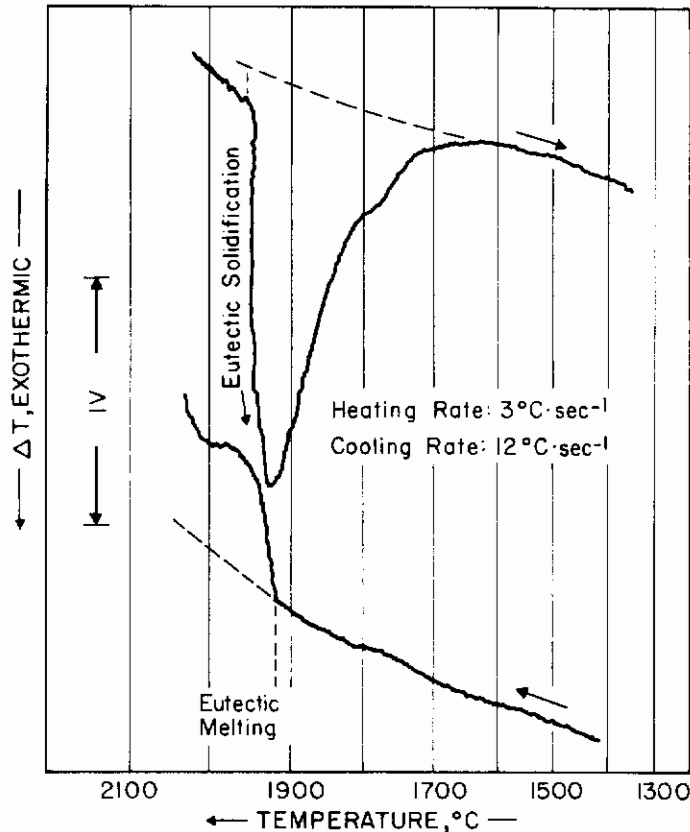


Figure 186. DTA-Thermogram of an Hf-B-C (4-90-6 At.%) Alloy. Formation of the Ternary Eutectic $\text{HfB}_2 + \text{B}_4\text{C} + \text{C}$ at 1950°C .

6. Assembly of the Phase Diagram

The results gained in the course of the experimental work have been combined in the phase diagram assembly shown in Figure 12; binary and ternary isothermal reactions, as well as the phases entering and emerging from the nonvariant equilibria, are summarized in the reaction diagram after Scheil-Schultz (Figure 13). Although the liquidus isotherms incorporated into Figure 17 lack high precision, it was felt, that the estimates based on the melting behavior of the alloys, together with the incipient freezing data gained in the differential-thermoanalytical studies, should represent sufficiently close the actual conditions as to warrant their recording.

For the ease of consultation of the ternary phase equilibrium data, a series of isothermal sections have been prepared from the smoothed experimental data; they are shown in Figures 187(a) through 187 (j).

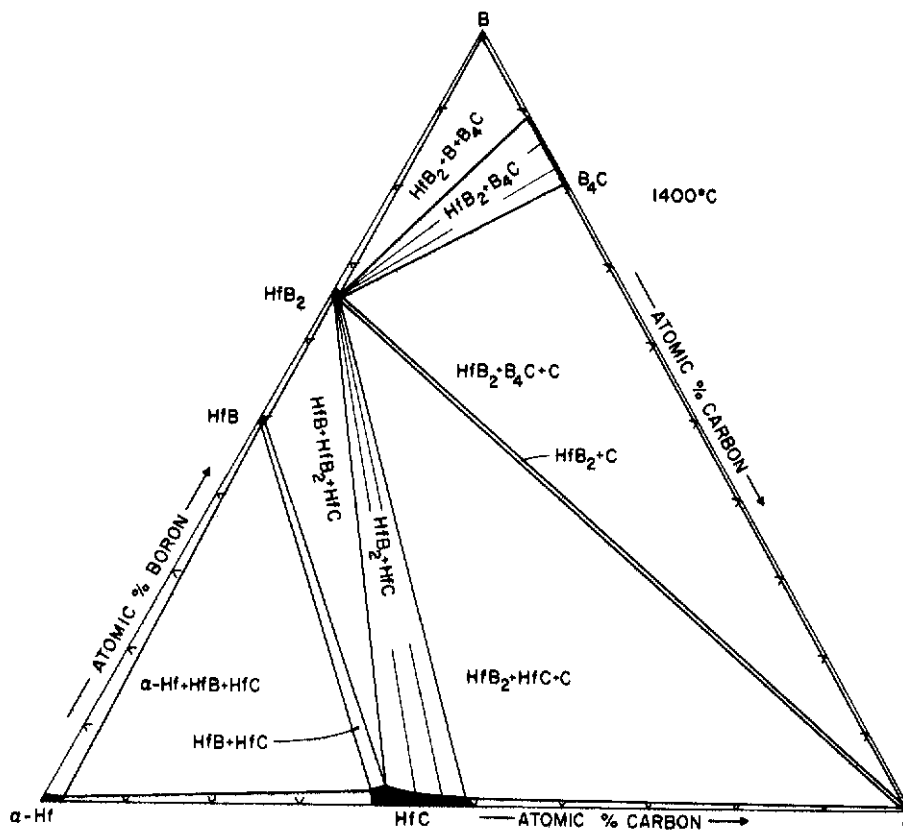


Figure 187(a). Isothermal Section at 1400°C.

Vertical sections (isopleths) are useful in determining the thermal behavior of specific alloy compositions or of alloys located along given concentrations; three such sections, covering all the essential equilibria in the system, were prepared from the temperature sections, and are illustrated in Figures 14, 15, 16.

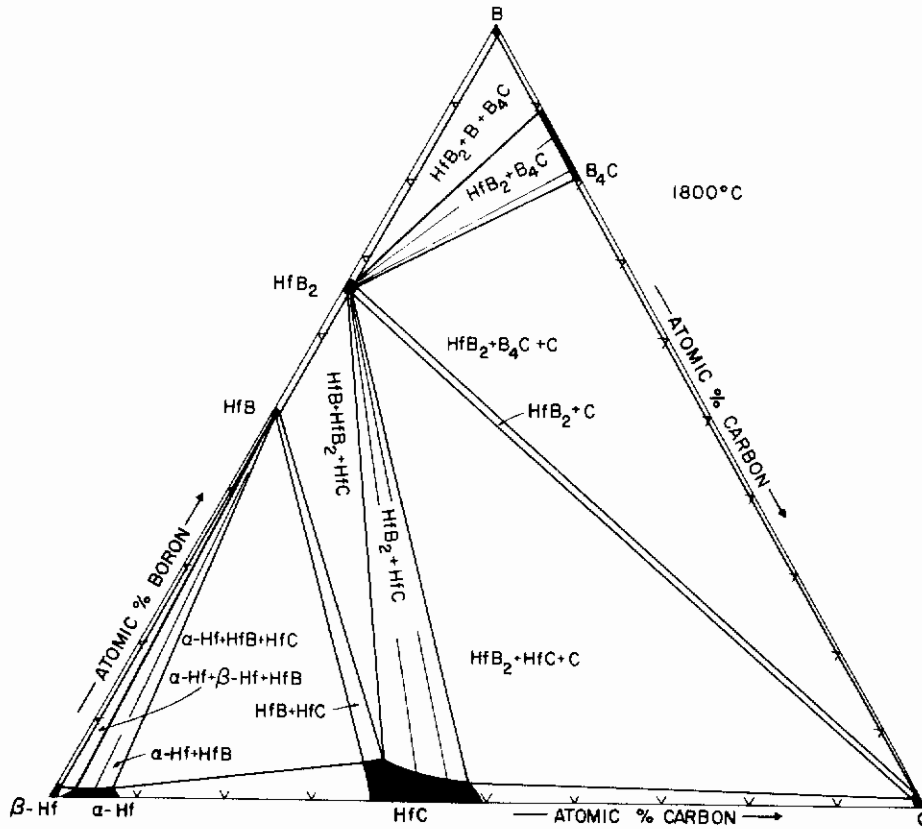


Figure 187(b). Isothermal Section at 1800°C.

Finally, the composition data for the nonvariant melts ($p = \text{const}$), as well as the melting troughs in this alloy system have been combined to yield the projection diagram shown in Figure 188.

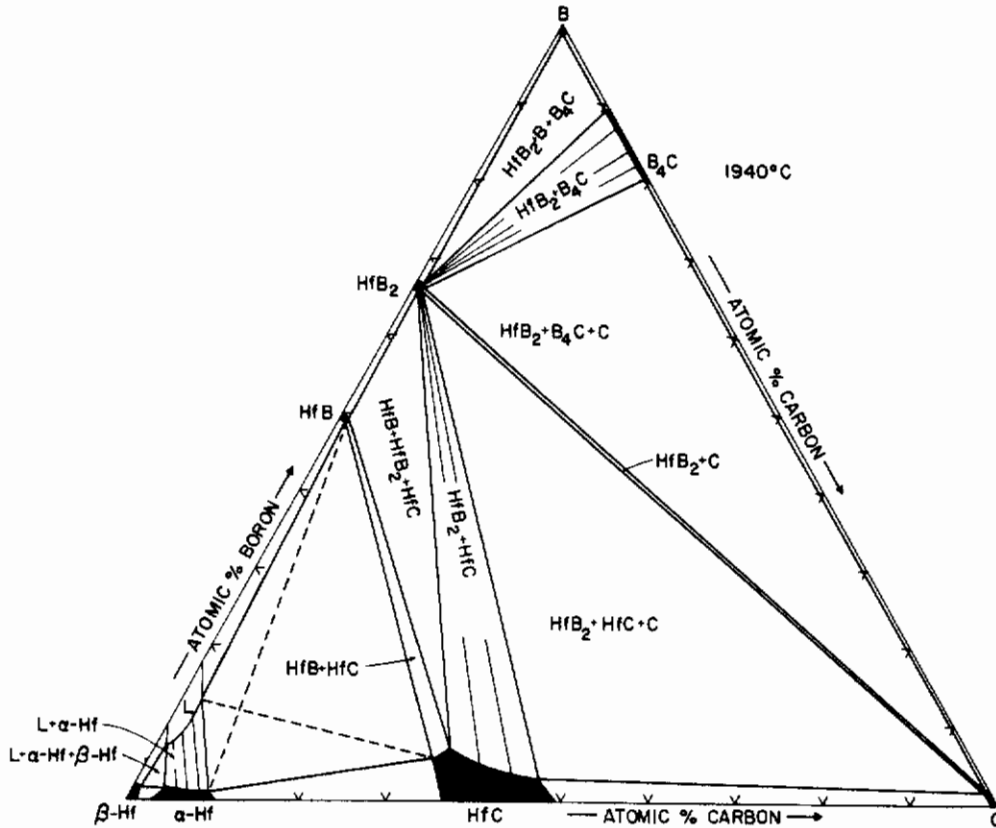


Figure 187(c) Isothermal Section at 1940°C.

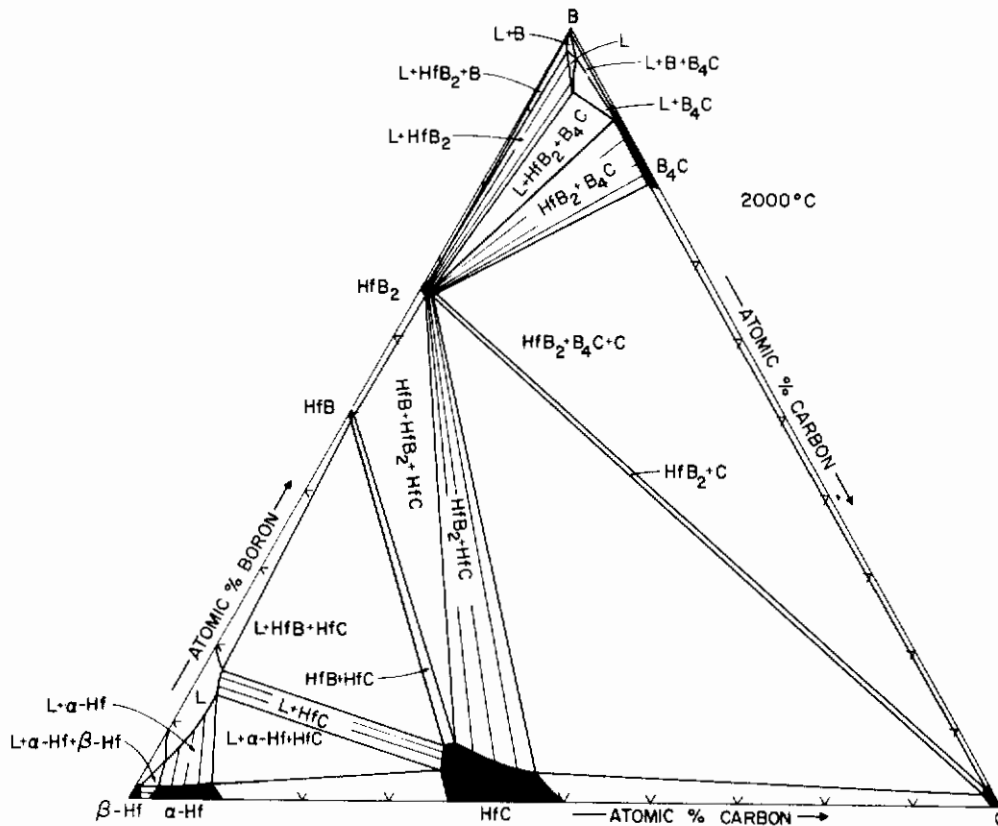


Figure 187(d). Isothermal Section at 2000°C.

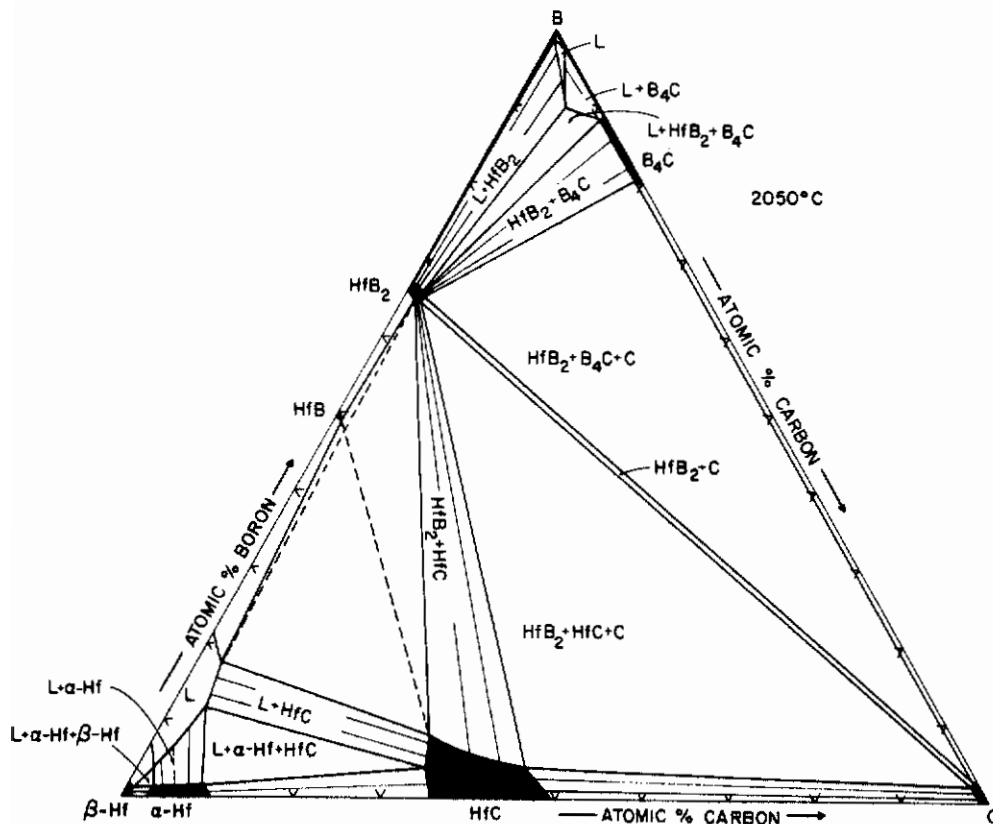


Figure 187(e). Isothermal Section at 2050°C.

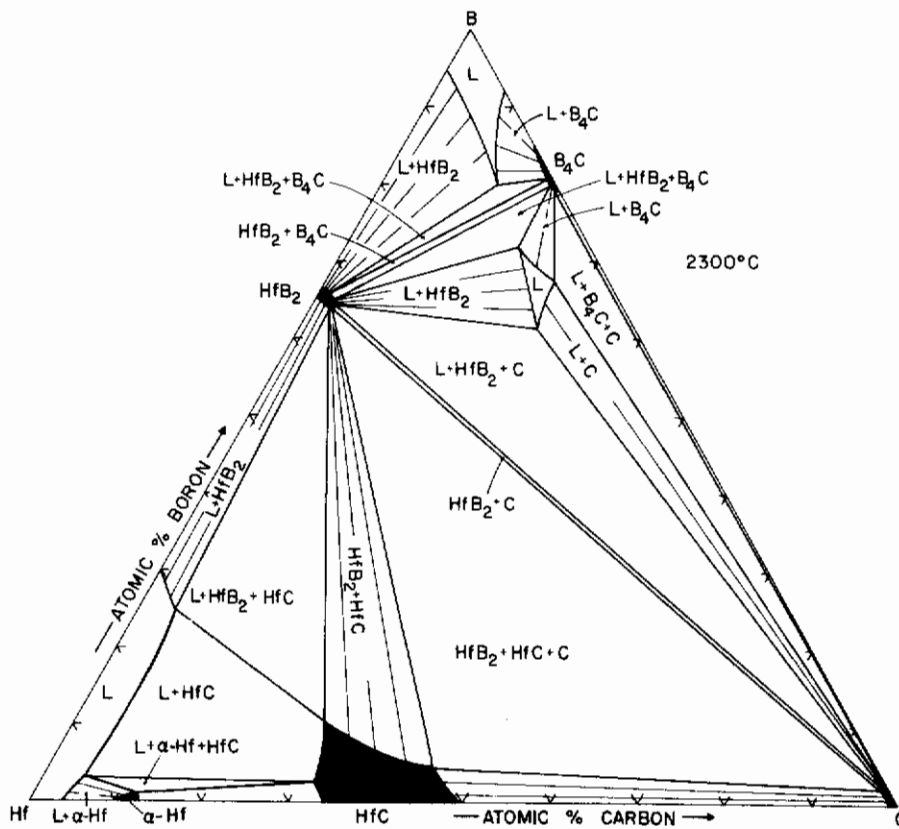


Figure 187(f). Isothermal Section at 2300°C.

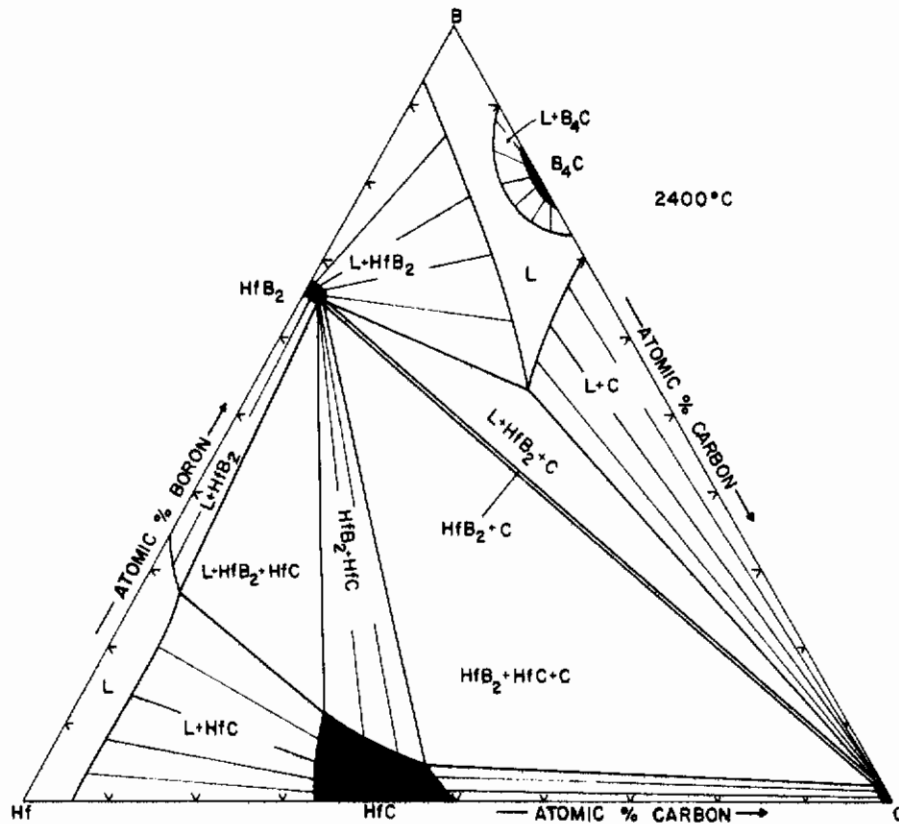


Figure 187(g) Isothermal Section at 2400°C.

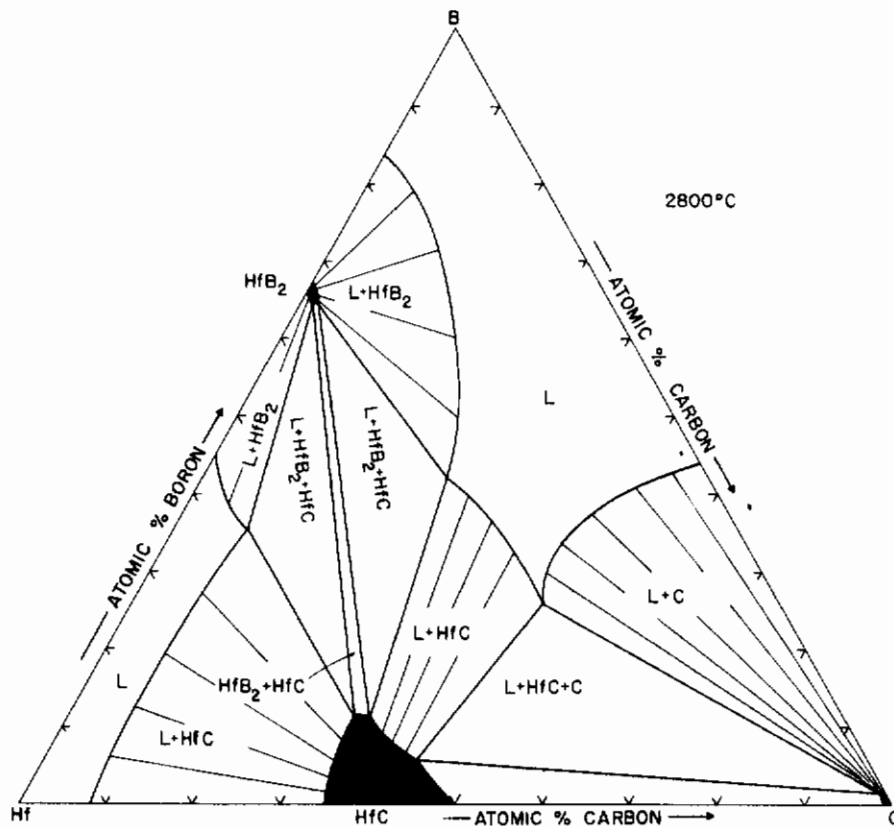


Figure 187(h). Isothermal Section at 2800°C.

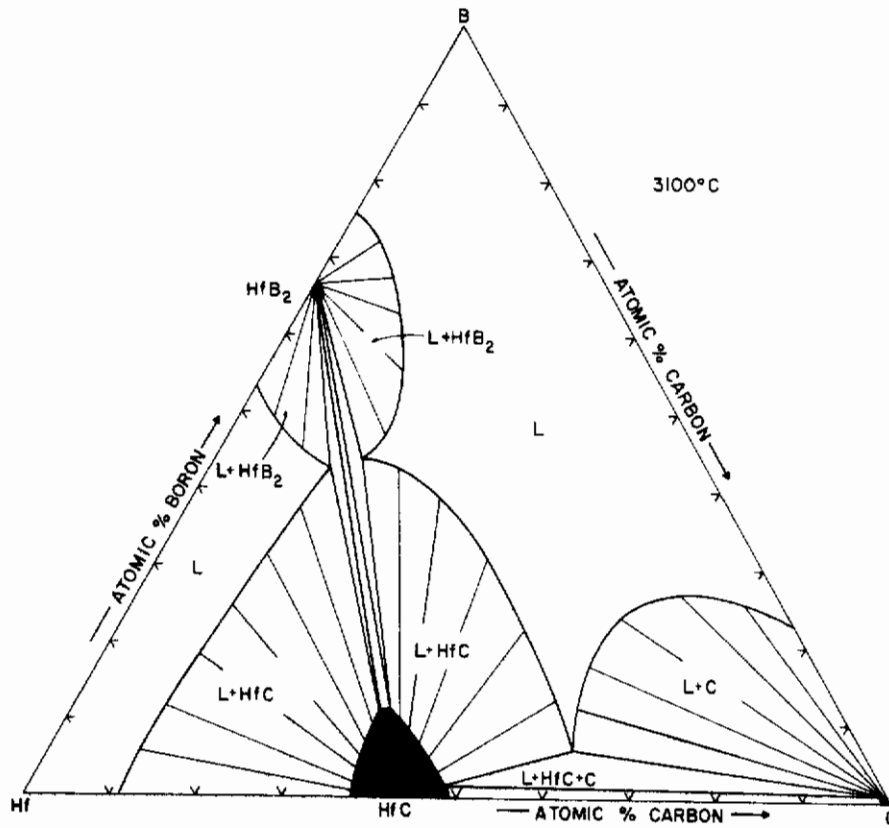


Figure 187(i) Isothermal Section at 3100°C.

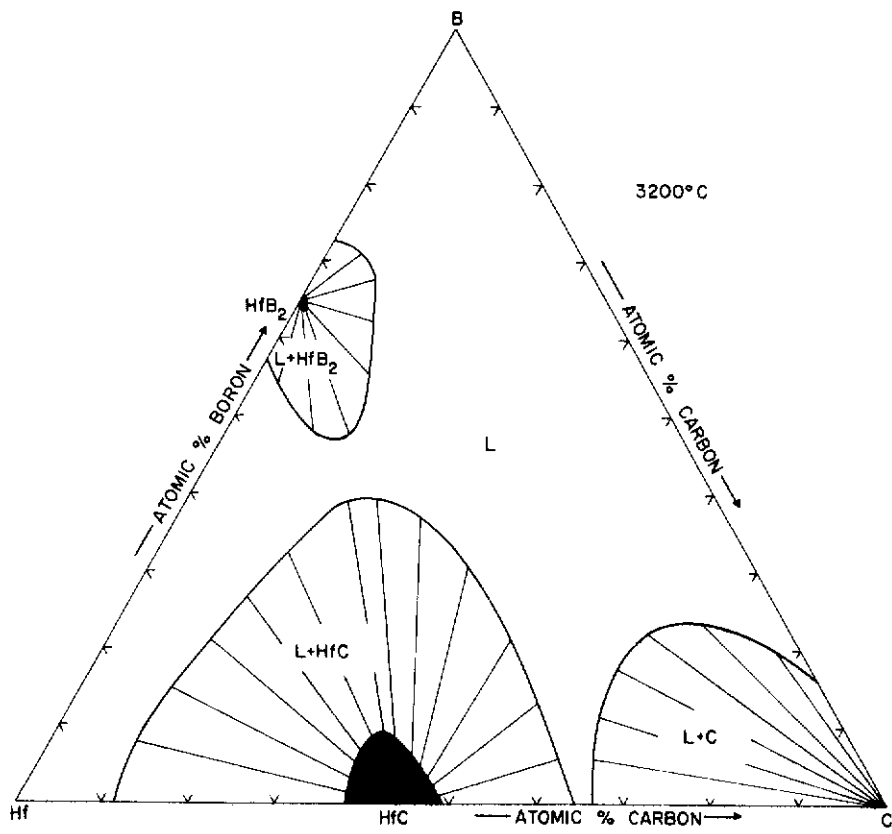


Figure 187 (j). Isothermal Section at 3200°C.

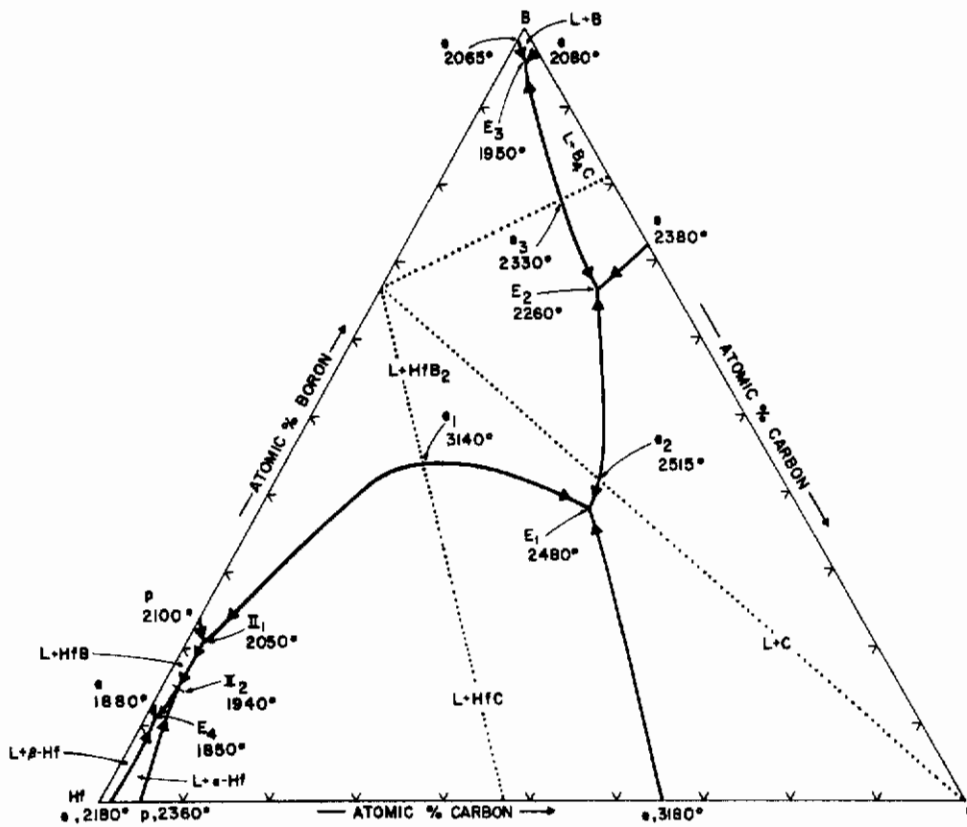


Figure 188. Melting Troughs and Compositions of the Nonvariant (p = const) Melts in the Hf-B-C System.

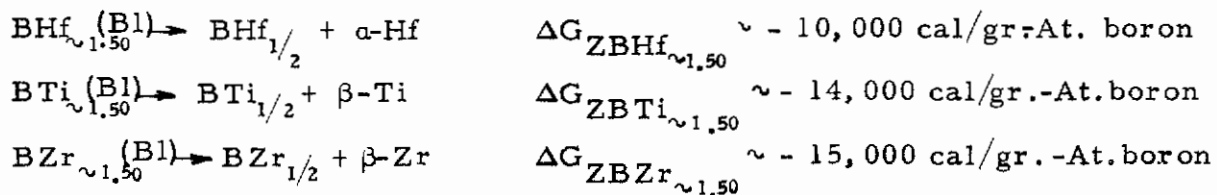
V. DISCUSSION

A. PHASES AND PHASE EQUILIBRIA

Basically, the phase relationships in all three systems are very similar: Pseudobinary sections are formed between the diboride phases and boron carbide, graphite, and the monocarbides; the ternary solid solubility ranges of all borides are small.

The existence of monoborides in the systems Ti-B and Hf-B accounts for one additional four-phase reaction plane in the metal-rich regions of these systems, and the appearance of the high temperature phase ZrB_{12} results in two isothermal ternary reactions in the zirconium-boron-carbon-system. The metal-rich equilibria in the ternary Hf-B-C are further complicated by the carbon-stabilization of the α -hafnium modification in the binary hafnium-carbon. The investigations of the ternary phase relationships showed, however, that the effect of carbon is quickly annihilated by boron additions, i.e. the α -Hf-solid solution is confined to compositions close to the hafnium-carbon binary.

The boron-exchange in the cubic monocarbides is a measure for the relative stability of a face-centered cubic monoboride in the respective binary metal-boron systems; hence, from the observed phase relationships, one would derive a somewhat higher stability for a (hypothetical) cubic hafnium monoboride, than for the B1-compounds in the titanium and zirconium-boron systems. Nevertheless, a simple calculation⁽⁹⁶⁾ shows that the relative thermodynamic stability of cubic monoborides in all three systems is quite low: as an average, the following free enthalpies of disproportionation were obtained (1800°K):



Apart from the direct experimental evidence, these data quite clearly indicate the appearance of fcc monoboride phases in the group IV metal-boron systems as very unlikely.

To a certain degree, the phase relationships in the metal-boron-carbon systems are closely related to the corresponding ternaries Me-B-N⁽⁵⁹⁾. The larger ternary homogeneity ranges of the B1-phases observed in the later systems probably will have to be explained by a comparatively stronger interaction of the interstitial elements as a result of charge transfer reactions. The ultimate formation of carbide-like structures $[(N-B) \equiv (C-C)]$ at a B:N exchange ratio of approximately 1 seems to be confirmed by the experiment⁽⁵⁹⁾.

B. HIGH TEMPERATURE APPLICABILITY OF GROUP IV METAL-BORON-CARBON ALLOYS

Several phase equilibrium-features are of technical interest:

In the zirconium-boron-carbon system, the concentration area metal + diboride + monocarbide suggests the possibility of zirconium cementation of diboride-carbide mixtures for wear-resistant parts. Although the comparatively poor oxidation behavior of zirconium, but especially of the zirconium carbide, at elevated temperatures might appear little attractive, certain improvements could be achieved by alloying additions, such as hafnium, or titanium.

In Ti-B-C alloys, cementation by Ti is only possible for the phases TiB and TiC_{1-x}. The merit of such composites mainly will depend upon the (unknown) mechanical and thermal properties of TiB. A similar situation is encountered with Hf-B-C alloys, although in this case the formation of significant quantities of monoboride could be prevented by rapid cooling from temperatures above 2050°C. The main difficulty in obtaining tough composites, however, arises from the participation of the carbon-embrittled α -Hf-solid solution in the ternary equilibria. Improvement of the ductility of the binder phase by eliminating

the high carbon solubility in the metal phase by alloying additions, such as titanium and zirconium, would be a necessity.

The phase combination $MeC + MeB_2$ might be of interest in lower temperature ($< 1500^\circ C$) application, but its high temperature potential seems to be limited. The temperature-dependent boron exchange reactions in the monocarbides are associated with significant volume changes, and even small-level precipitations of diboride, traversing the carbide grains along specific crystal planes tend to disrupt the carbide matrix and result in bodies with poor mechanical properties.

From the application point of view, probably the most interesting equilibria in the three systems are those formed between the diborides and graphite, and between the diborides and boron carbide.

Although the eutectic temperatures of the pseudobinary sections diboride-graphite do in neither case* exceed approximately $2500^\circ C$, the microstructures obtained suggest interesting possibilities for the development of diboride-graphite composites for high temperature applications. A close control of the microstructure by controlled solidification processes will in each case be advantageous in order to avoid segregation and agglomeration of the graphite phase at the boundaries of the boride grains.

Similarly, the microstructures obtainable for two-phased $MeB_2 + B_4C$ or for three-phased $MeB_2 + B_4C + C$ alloys, should warrant a somewhat closer look upon their characteristics and their technical usability.

*Preliminary results obtained on other pseudobinary sections, such as VB_2-C , NbB_2-C , and TaB_2-C , indicate that the eutectic temperatures for all three systems are also in the range from 2400° to $2500^\circ C$.

REFERENCES

1. H. Nowotny, E. Rudy, and F. Benesovsky: Mh.Chem. 92 (1961), 393.
2. H. Nowotny, E. Rudy, and F. Benesovsky: Mh.Chem. 91 (1960), 693.
3. E. Rudy, F. Benesovsky, and L. Toth: Z. Metallkde, 54 (1963), 345.
4. H. Nowotny, F. Benesovsky, C. Brukl, and O. Schob: Mh.Chem 92 (1961), 403.
5. E. Rudy and St. Windisch: AFML-TR-65-2, Part II, Vol. III (1965); Part I, Vol. VII to X (1965).
6. C. E. Brukl: AFML-TR-65-2, Part II, Vol. VII (1966).
7. C. E. Brukl: AFML-TR-65-2, Part II, Vol. X (1966).
8. J. S. Umanski, and S. S. Khidekel: Zr. Fiz. Khim. SSSR 15 (1941), 983.
9. P. Ehrlich: Z. anorg. Chemie 259 (1949), 1
10. I. Cadoff, J. P. Nielsen and E. Miller: Plansee Proc. (1955), 10
11. I. Cadoff and J. P. Nielsen: J. Metals 5 (1953), 248.
12. H. Bittner and H. Goretzki: Mh.Chem. 93 (1962), 1000.
13. Compare the exhaustive literature compilation in R. Kieffer and F. Benesovsky, Hartstoffe (Wien, Springer, 1963).
14. E. K. Storms: Critical Review of Refractories, LA-2942 (1964).
15. E. Rudy, D. P. Harmon, and C. E. Brukl: AFML-TR-65-2, Part I, Vol. II (May 1965).
16. L. Stone and H. Margolin: WAL-401/85-21 (1953).
17. J. T. Norton and R. K. Lewis: NASA-CR-321.
18. R. I. Bickerdike and G. Hughes: J. Less-Common Metals 1 (1959), 42.
19. J. L. Engelke, F. A. Halden, and E. P. Farley: WADC-TR-59-654 (1960).
20. P. Schwarzkopf and R. Kieffer: "Refractory Hard Metals" (McMillan Company, New York, 1953).
21. E. Friedrich and G. Sittig: Z. anorg. allg. Chemie 144 (1925), 169.

Contrails

REFERENCES (Cont'd)

22. C. Agte and K. Moers: Z. anorg. allg. Chemie 198 (1931), 233.
23. G.A. Geach and F.O. Jones: 2nd Plansee Seminar, Reutte, Tirol (1955), 80.
24. J.S. Umanski: Hard Carbides, Metallurgizdat, Moscow (1947), 32.
25. A.E. Kovalski and T.G. Marareko: Microhardness, Akad. Nauk SSSR, (1951), 187.
26. G.V. Samsonov and N.S. Rozinova: Izvest. Sekt. Fiz. Khim. Anal. 27 (1956), 126.
27. F. Benesovsky and E. Rudy: Planseeber. Pulvermet. 8 (1960), 66.
28. J. Farr: Unpublished work, quoted by E.K. Storms, LAMS-2674 (1962).
29. R.V. Sara, C.E. Lowell, and R.T. Dolloff: WADD TR 60-143, Part IV (1963).
30. R.V. Sara: J. Am. Ceram. Soc. 48 (1965), 243.
31. E. Rudy: AFML-TR-65-2, Part I, Vol. IV (Sept. 1965).
32. R.V. Sara and C.E. Lowell: WADD-TDR-60-143, Part V. (Oct. 1964).
33. M.I. Copeland: U.S. Bureau of Mines Progr. Report USBM-U-952 (June 1964).
34. R.G. Avarbe, A.L. Augustinnik, Yu. N. Vilks, Yu.D. Konrashov, S.S. Nikolskii, Yu.A. Omelchenko, and S.S. Ordanyan: J. Appl. Phys. USSR 35 (1962), 1899.
35. C. Agte and H. Alterthum: Z. Techn. Phys. 11 (1930), 182.
36. R.P. Adams and R.A. Beall: U.S. Bureau of Mines, Report of Investigation 6304 (1963).
37. G.V. Samsonov and J.S. Umanski: Hard Compounds of Refractory Metals (Moscow, 1957), 118.
38. B.F. Decker and J.S. Kasper: Acta Cryst. 7 (1954), 77.
39. E. Rudy and St. Windisch; AFML-TR-65-2, Part I, Vol. VII (Jan 1966).
40. P. Ehrlich: Z. anorg. Chem. 244 (1949), 1.
41. J. Norton, H. Blumenthal, and S.J. Sindeband: Trans. AIME, 185 (1949), 749.

REFERENCES (Cont'd)

42. B. Post and F. W. Glaser: J. Chem. Phys. 20 (1952), 1050.
43. A.E. Palty, H. Margolin and J.P. Nielsen: Trans. Am. Soc. Met. 46 (1954), 312.
44. F. W. Glaser: J. Met. 4 (1952), 391.
45. H. Nowotny: Radex Rundschau, 2 (1953), 41.
46. L. Brewer, D.L. Sawyer, D.H. Templeton, and C.H. Danken: J. Am. Ceram. Soc. 34 (1951), 183.
47. H.M. Greenhouse, O.E. Accountivs, and H.H. Sigler: J. Amer. Chem. Soc. 73 (1951), 5086.
48. C.M. Craighead, O.W. Simmons, and L.W. Eastwood: Trans. AIME 188 (1950), 485.
49. H.R. Ogden and R.I. Jaffee: Trans. AIME 191 (1951), 335.
50. R.M. Goldhoff, H.L. Shaw, C.M. Craighead, and R.I. Jaffee: ASM 45 (1953), 941.
51. C. Agte: Thesis, Technische Hochschule Berlin, 1931.
52. K. Moers: Z. anorg. allg. Chemie 198 (1931), 262.
53. F.W. Glaser and B. Post: Trans. AIME 197 (1953), 1117.
54. R. Kiessling: Acta Chem. Scand. 3 (1949), 90.
55. W. Zachariasen: Acta Cryst. 2 (1949), 94.
56. F.W. Glaser: Trans. AIME 194 (1952), 391.
57. E. Rudy and St. Windisch: AFML-TR-65-2, Part I, Vol. VIII (Jan 1966).
58. W. Schedler: Thesis, Technische Hochschule Graz, 1951.
59. E. Rudy and F. Benesovsky: Mh.Chem. 92 (1961), 415.
60. V.A. Epelbaum and MA. Gurewitsch: Zhur. Fiz. Khim. 31 (1957), 708.
61. P. Duwez: Trans. AIME 191 (1951), 765.
62. C.T. Baroch and T.E. Evans: J. Metals 7 (1955), 908.
63. F.W. Glaser, D. Moskowitz, and B.W. Post: J. Metals 5 (1953), 1119.

REFERENCES (Cont'd)

64. R. Kieffer, F. Benesovsky, and E.R. Honak: *Z. anorg. allg. Chemie* 268 (1952), 191.
65. E. Rudy and St. Windisch: AFML-TR-65-2, Part I, Vol. IX (Jan 1966).
66. E. Rudy: Thesis, Technische Hochschule Wien (1960).
67. R.R. Ridgeway: *Trans. Electrochem. Soc.* 66 (1934), 117.
68. G.A. Meerson and G.V. Samsonov: *Izvest. Sekt. Fiz. Chim. Anal.* 22 (1952), 92.
69. G.V. Samsonov, N.N. Zuravlev, and I.G. Amnuel: *Fiz. Metallov Metalloved.* 3 (1956), 309.
70. G.V. Samsonov: *Zur. Fiz. Chim.* 32 (1958), 2424.
71. G.V. Samsonov, *High Temperature Materials* (English Translation, Plenum Press, New York, 1964).
72. R.T. Dolloff: WADD Techn. Rep. 60-143 (July 1960).
73. R.P. Elliott: ARF 2200-12 Final Report (Jul 1961) (AEC Contr. No. AT (11-1)-578).
74. J.H. Westbrook and E.R. Stover: Gen. Electr. Rep. No. 60-RL-2565M (Nov. 1960).
75. N.G. Sevastianov: *Khim. Referat. Zhur.* 5 (1940), 47.
76. F. Laves: *Nene Folge* 1 (1934), 57.
77. H.S. Zhdanov and N.G. Sevastianov: *Compt. send. Akad. Nauk. SSSR* 32 (1941), 432.
78. H.K. Clark and J.L. Hoard: *J. Am. Chem. Soc.* 65 (1943), 2115.
79. A.W. Lanbengayer, D.T. Hurd, A.E. Newkirk, and J.L. Hoard: *J. Am. Chem. Soc.* 75 (1953), 3582.
80. R.D. Allen: *J. Am. Chem. Soc.* 75 (1953), 3582.
81. F.W. Glaser, D. Moskowitz, and B. Post: *J. Appl. Phys.* 24 (1953), 731.
82. J. Economy, V.I. Matkovich, and R.F. Giese, Jr: Office of Naval Research Contract No. Nonr-4075(00), Rept.No. 6 (Nov. 1964).

REFERENCES (Cont'd)

83. B.F. Decker and J.S. Kasper: Acta Cryst. 12 (1959), 503.
84. E. Rudy, St. Windisch, and Y.A. Chang: AFML-TR-65-2 (Jan 1965).
85. W.J. Engel: Nat. Adv. Comm. Aeronaut. Tech. Note 2187 (Sept.1950).
86. C.G. Goetzel, Treatise on Powder Metallurgy, Vol. II, 747 (New York 1950).
87. K.I. Portnoi, G.V. Samsonov, and K.I. Frolova: J. Appl.Chem. USSR 33 (1960), 577.
88. G.A. Geach and F.O. Jones: 2nd Plansee Seminar, 1955, Reutte, Tirol, p. 80.
89. G.V. Samsonov: Problems in Powder Metallurgy, Vol. 7, 72 (Kiew, 1959).
90. H. Nowotny, F. Benesovsky, C. Brukl, and O.Schob: Mh. Chem. 92 (1961), 403.
91. L. Brewer and H. Haroldsen: J. Electrochem. Soc. 102 (1953), 399.
92. W.B. Pearson: "Handbook of Lattice Spacings and Structures of Metals and Alloys" (Pergamon Press, New York, 1958).
93. E. Rudy: AFML-TR-65-2, Part I, Vol. I (Sept 1965).
94. E. Rudy and G. Progulski: Planseeber. Pulvermet (in preparation for print).
95. H. Heetderks, E. Rudy, and T. Eckert: AFML-TR-65-2, Part III, Vol. I (May 1965); Planseeber. Pulvermet. 13 (1965), 105.
96. Compare E. Rudy: Z.Metallkde 54 (1963), 112.

DOCUMENT CONTROL DATA - R&D		
<i>(Security classification of title, body of abstract and indexing annotation must be entered when the overall report is classified)</i>		
1. ORIGINATING ACTIVITY (Corporate author) Aerojet-General Corporation Materials Research Laboratory Sacramento, California		2a. REPORT SECURITY CLASSIFICATION Unclassified
		2b. GROUP N.A.
3. REPORT TITLE Ternary Phase Equilibria in Transition Metal-Boron-Carbon-Silicon Systems. Part II. Ternary Systems. Volume XIII. Phase Diagrams of the Systems Ti-B-C, Zr-B-C, and Hf-B-C.		
4. DESCRIPTIVE NOTES (Type of report and inclusive dates)		
5. AUTHOR(S) (Last name, first name, initial) Rudy, E. Windisch, St.		
6. REPORT DATE April 1966	7a. TOTAL NO. OF PAGES 212	7b. NO. OF REFS 96
8a. CONTRACT OR GRANT NO. AF 33(615)-1249	9a. ORIGINATOR'S REPORT NUMBER(S) AFML-TR-65-2 Part I, Vol. VI.	
b. PROJECT NO. 7350	9b. OTHER REPORT NO(S) (Any other numbers that may be assigned this report) N.A.	
c. Task No. 735001		
d.		
10. AVAILABILITY/LIMITATION NOTICES This document is subject to special export controls, and each transmittal to foreign governments or foreign nationals may be made only with prior approval of Metals & Ceramics Div., AF Materials Laboratory, Wright-Patterson AFB, Ohio		
11. SUPPLEMENTARY NOTES	12. SPONSORING MILITARY ACTIVITY AFML (MAMC) Wright-Patterson AFB, Ohio 45433	
13. ABSTRACT The ternary alloy systems Ti-B-C, Zr-B-C, and Hf-B-C have been investigated by means of X-ray, metallographic, melting point, and differential-thermoanalytical techniques. The experimental alloy material comprised of hot-pressed and sintered, arc- and electron-beam molten, as well as high temperature equilibrated and quenched, specimens; each phase of the experimental work was supported by chemical analysis. The results of this investigation are discussed and possible fields of application outlined.		
<p><i>This document has been approved for public release and sale; its distribution is unlimited.</i></p> <p><i>USAF Systems Command Letter dated Aug 22 1968 Capt Marchisando U 837117</i></p>		

14.	KEY WORDS	LINK A		LINK B		LINK C	
		ROLE	WT	ROLE	WT	ROLE	WT
	Ternary Phase Equilibria Borocarbides Ti-B-C Zr-B-C Hf-B-C						

INSTRUCTIONS

1. **ORIGINATING ACTIVITY:** Enter the name and address of the contractor, subcontractor, grantee, Department of Defense activity or other organization (*corporate author*) issuing the report.
- 2a. **REPORT SECURITY CLASSIFICATION:** Enter the overall security classification of the report. Indicate whether "Restricted Data" is included. Marking is to be in accordance with appropriate security regulations.
- 2b. **GROUP:** Automatic downgrading is specified in DoD Directive 5200.10 and Armed Forces Industrial Manual. Enter the group number. Also, when applicable, show that optional markings have been used for Group 3 and Group 4 as authorized.
3. **REPORT TITLE:** Enter the complete report title in all capital letters. Titles in all cases should be unclassified. If a meaningful title cannot be selected without classification, show title classification in all capitals in parenthesis immediately following the title.
4. **DESCRIPTIVE NOTES:** If appropriate, enter the type of report, e.g., interim, progress, summary, annual, or final. Give the inclusive dates when a specific reporting period is covered.
5. **AUTHOR(S):** Enter the name(s) of author(s) as shown on or in the report. Enter last name, first name, middle initial. If military, show rank and branch of service. The name of the principal author is an absolute minimum requirement.
6. **REPORT DATE:** Enter the date of the report as day, month, year; or month, year. If more than one date appears on the report, use date of publication.
- 7a. **TOTAL NUMBER OF PAGES:** The total page count should follow normal pagination procedures, i.e., enter the number of pages containing information.
- 7b. **NUMBER OF REFERENCES:** Enter the total number of references cited in the report.
- 8a. **CONTRACT OR GRANT NUMBER:** If appropriate, enter the applicable number of the contract or grant under which the report was written.
- 8b, 8c, & 8d. **PROJECT NUMBER:** Enter the appropriate military department identification, such as project number, subproject number, system numbers, task number, etc.
- 9a. **ORIGINATOR'S REPORT NUMBER(S):** Enter the official report number by which the document will be identified and controlled by the originating activity. This number must be unique to this report.
- 9b. **OTHER REPORT NUMBER(S):** If the report has been assigned any other report numbers (*either by the originator or by the sponsor*), also enter this number(s).
10. **AVAILABILITY/LIMITATION NOTICES:** Enter any limitations on further dissemination of the report, other than those

imposed by security classification, using standard statements such as:

- (1) "Qualified requesters may obtain copies of this report from DDC."
- (2) "Foreign announcement and dissemination of this report by DDC is not authorized."
- (3) "U. S. Government agencies may obtain copies of this report directly from DDC. Other qualified DDC users shall request through _____."
- (4) "U. S. military agencies may obtain copies of this report directly from DDC. Other qualified users shall request through _____."
- (5) "All distribution of this report is controlled. Qualified DDC users shall request through _____."

If the report has been furnished to the Office of Technical Services, Department of Commerce, for sale to the public, indicate this fact and enter the price, if known.

11. **SUPPLEMENTARY NOTES:** Use for additional explanatory notes.
12. **SPONSORING MILITARY ACTIVITY:** Enter the name of the departmental project office or laboratory sponsoring (*paying for*) the research and development. Include address.
13. **ABSTRACT:** Enter an abstract giving a brief and factual summary of the document indicative of the report, even though it may also appear elsewhere in the body of the technical report. If additional space is required, a continuation sheet shall be attached.

It is highly desirable that the abstract of classified reports be unclassified. Each paragraph of the abstract shall end with an indication of the military security classification of the information in the paragraph, represented as (TS), (S), (C), or (U).

There is no limitation on the length of the abstract. However, the suggested length is from 150 to 225 words.

14. **KEY WORDS:** Key words are technically meaningful terms or short phrases that characterize a report and may be used as index entries for cataloging the report. Key words must be selected so that no security classification is required. Identifiers, such as equipment model designation, trade name, military project code name, geographic location, may be used as key words but will be followed by an indication of technical context. The assignment of links, rules, and weights is optional.